Development of Bismuth Oxyhalide Nanostructures for Photocatalytic and Energy Harvesting Applications

THESIS SUBMITTED BY

RATNA SARKAR

THE DEGREE OF DOCTOR OF PHILOSOPHY
(SCIENCE)

Thin Film and Nanoscience Laboratory
Department of Physics
Jadavpur University
Kolkata 700 032, India
2022

Development of Bismuth Oxyhalide Nanostructures for Photocatalytic and Energy Harvesting Applications

THESIS SUBMITTED FOR THE DEGREE OF DOCTOR OF PHILOSOPHY (SCIENCE)

Of

JADAVPUR UNIVERSITY

By

Ratna Sarkar

Thin Film and Nanoscience Laboratory
Department of Physics
Jadavpur University, Kolkata 700 032, India

June 2022

JADAVPUR UNIVERSITY
KOLKATA – 700 032, INDIA
Telephone: +9133-24146666

Ref. No. _____

FACULTY OF SCIENCE
DEPARTMENT OF PHYSICS

Dated: 20.06.2022

CERTIFICATE FROM THE SUPERVISORS

This is to certify that the thesis entitled "**Development of Bismuth Oxyhalide Nanostructures for Photocatalytic and Energy Harvesting Applications**" submitted by **Ratna Sarkar**, who got his name registered on **16/02/2018** for the award of **Ph.D. (Science) degree of Jadavpur University**, is absolutely based upon her own work under the joint supervisions of **Dr. Subrata Sarkar** and **Prof. (Dr.) Kalyan Kumar Chattopadhyay** and that neither this thesis nor any part of it has been submitted for any degree/diploma or any other academic award anywhere before.

Subrata Sarkar
20/06/22

Dr. Subrata Sarkar
Signature of the Supervisor
Date with Office Seal

Dr. Subrata Sarkar
Assistant Professor
Department of Physics
Jadavpur University
Kolkata-700 032

Chattopadhyay 20.6.22

Prof. (Dr.) Kalyan Kumar Chattopadhyay
Signature of the Supervisor
Date with Office Seal

Prof. Kalyan Kr. Chattopadhyay
Professor and Head
Department of Physics
Jadavpur University
Kolkata – 700 032

"Statement of Originality"

I **Ratna Sarkar** registered on 16/02/2018 do here by declare that this thesis entitled "**Development of Bismuth Oxyhalide Nanostructures for Photocatalytic and Energy Harvesting Applications**" contains literature survey and original research work done by the undersigned candidate as part of Doctoral studies.

All information in this thesis have been obtained and presented in accordance with existing academic rules and ethical conduct. I declare that, as required by these rules and conduct, I have fully cited and referred all materials and results that are not original to this work.

I also declare that I have checked this thesis as per the "Policy on Anti Plagiarism, Jadavpur University, 2019", and the level of similarity as checked by iThenticate software is 9 %.

Signature of Candidate: Ratna Sarkar

Date: 20/06/2022

Subrata Sarkar 20/06/22

Dr. Subrata Sarkar
Signature of the Supervisor
Date with Office Seal

Dr. Subrata Sarkar
Assistant Professor
Department of Physics
Jadavpur University
Kolkata-700 032

Prof. (Dr.) Kalyan Kumar Chattopadhyay
Signature of the Supervisor
Date with Office Seal

Prof. Kalyan Kr. Chattopadhyay
Professor and Head
Department of Physics
Jadavpur University
Kolkata – 700 032

Dedicated To My Beloved

Maternal Grand Mother (Dida)…

My Sincere Gratitude
To All My Teachers…

Education is not preparation for life
Education is life itself…

--- By John Dewey

Acknowledgements

The opinion on the extremity of my Ph.D. thesis submission, I discover in my opinion that enormously honoured to have the prospect to thank lots of persons, they have lend a hand me in countless phases of my entire research work in the last few years, without their help, support and guidance this work would not have been done.

I avail myself of the opportunities with great pleasure in acknowledging my deepest sense of gratitude to Prof. (Dr). Kalyan Kumar Chattopadhyay, HOD, Department of Physics, Jadavpur University (JU) for selection of problems, valuable guidance, constant supervision, encouragement, suggestions and painstaking efforts throughout the period of research and preparation of this dissertation.

My sincere gratitude goes out to another supervisor Dr. Subrata Sarkar, Assistant Professor of Department of Physics, Jadavpur University for his continuous support and guidance throughout the course of my research. My research work was completed efficiently because he gave me enough freedom. I gained knowledge and experience from his valuable suggestions.

I am deeply grateful to my ex-supervisor and ex-HOD of the Department of Physics, Jadavpur University, Prof. (Dr.) Tapas Ranjan Middya, for providing me with the opportunity to complete my research with his group. His scientific advice, patient supervision, and encouragement for independent and insightful research I received from him, will always be very much appreciated.

I am indebted to the Department of Physics, Jadavpur University, and all the faculty members; and also the Officers and Staffs of the Ph.D. cell and Research Sections of Jadavpur University.

I convey my heartiest greetings to all the faculty members of the School of Materials Science and Nanotechnology, JU. Specially, I am thankful to Dr. Sourav Sarkar and Dr. Chandan Kumar Ghosh of for their supports; and special thanks to Dr. Ghosh for being my RAC's member.

I am also thankful to Dr. Ruma Ray, HOD of the Department of Physics, Gurudas College, Kolkata, for her invaluable contributions to my academics and research area.

I wish to my heartiest thanks to Dr. Amit Kumar Charkrabary, from Nabawdip Vidasagar College, Nadia, for his continuous support, encouragement, discussing different ideas, and academic as well as non-academic affairs. He helps me at every ups and downs, and pushing up for forwards.

I would also like to express my gratitude to my senior collaborator Dr. Anuradha Mitra (Anu di) for giving me her unconditional support throughout this entire process. Not only is she my senior, but she has also continuously motivated me (till day) for good work. In addition to her in-depth knowledge of materials science, manuscript writing skill, and good representation, she is extremely helpful to me.

I wish to personally thank you, Ms. Dimitra Das (Dimi di), for treating me like your own sister rather than my senior lab colleague. The dedication she has towards research and the welcoming nature of her personality has not only helped me become a motivated researcher, but also a decent human being. I was also inspired by her every step of the way during my research. Through this entire journey, her suggestions have helped me feel confident that I can overcome any obstacles that I face.

I must special thanks to Dr. Nirmalya Sankar Das for his fantastic art work and great skill in using Photoshop that inspire me to be more creative with graphics in my manuscripts.

All my senior lab mates, past and present, have been of great help to me; Bikram da, Biplab da, Biswajit da, Dipayan da, Karamjyoti da, Kausik da, Nripen da, Partha da, Saikat da, Samrat da, Soumen da, Subhasish da, Supratim da, Tufan da, Madhupriya di, Missisipi di, Moumita di, Promita di, Rimpa di, Rituparna di, Sayantani di, Shrabani di. I am also thankful to my junior lab colleagues; Anibrata, Ankita, Arnab, Arya, Nabamita, Nabanita, Moumita, Pulok, Souvik, Suvankar. I am very much thankful to the M. Tech. project students; Abhirupa, Riaz, Sohel, Sagardip for their cooperation. Especially, I am gratefulness to Sohel, for his big support. I am thankful to my colleagues; Antika, Brahami, Dipanwita, Dipayan, Kausik, Suvankar, Suvra for their continuous encouragement and support.

I also thankful to my friends, they help me every stapes in my life Subhamita, Tantia, Somnath, Debjit, Ankita, Shatadru, Dhiraj, Tanmoy, Panchanan, Rupa, Sudipta, Triparna, Banishikha, Simantini.

In this context, I am grateful for the fellowships which I received from Council for Scientific and Industrial Research (CSIR), Government of India for awarding me junior and senior research fellowship [File Number: 09/096(0872)/2016-EMR-I] during my PhD studies. Additionally, I would like to thank the University with Potential for Excellence scheme (UPE-II), Department of Science and Technology (DST) and TEQIP programme for funding various projects. Furthermore, I would wish to thanks the Department of Physics, Jadavpur University for throughout my M. Sc. to Ph. D. journey.

Over and above, the most precious people in my life are grandparents and parents. My gratitude cannot be adequately expressed in words for their unconditional love, affection and care. I have been inspired by them throughout my life. They always encourage and pray for me to excel at every step of my life. It means a lot to me to be supported and sacrificed by them to achieve this goal. My brother, Bipro, deserves special recognition for his continued support during my hard journey. I would like to mention my maternal uncles, especially Mr. Sukesh Adhikary for his constant support throughout my arduous journey.

Finally, I want to dedicate this thesis to my beloved maternal grandmother ‘Dida’ the person who always remains close to my heart.

June, 2022 Ratna Sarkar

Department of Physics

Jadavpur University, Kolkata 700 032

List of publications

This thesis is based on the following publications/communicated articles (1-4)

1. Hollow Micro-spherical Bismuth Oxy-chloride for Superior Visible Light Induced Dye-sensitized Photocatalytic Activity and its Theoretical Insight
Ratna Sarkar, Dimitra Das, Bikram Kumar Das, Anuradha Mitra, Nirmalya S. Das, Subrata Sarkar and Kalyan K. Chattopadhyay*
Materials Research Bulletin, 125 (2020) 110778.

2. Morphology Tuning of Bismuth Oxychloride Nano-Crystals By Citric acid Variation: Application in Visible light Assisted Dye Degradation and Hydrogen Evolution by Electrochemical Method
Ratna Sarkar, Dipayan Roy, Dimitra Das, Subrata Sarkar and Kalyan K. Chattopadhyay*
International Journal of Hydrogen Energy, 46 (2021) 16299-16308.

3. Hydrothermal synthesis of GO wrapped BiOCl nanosheet and its application in visible light assited catalytic degradation of Rhodamine B dye
Ratna Sarkar, Dimitra Das, Kausik Chanda, Brahami Das, Subrata Sarkar and Kalyan Kumar Chattopadhyay*
Materials Chemistry and Physics, 279 (2022) 125796.

4. Grain size dependent catalytic mechanism of sheet like BiOCl nanoparticle dye degradation under UV-light
Ratna Sarkar, Nirmalya Sankar Das, Dimitra Das, Kausik Chanda, Brahami Das, Subrata Sarkar and Kalyan Kumar Chattopadhyay*
Communicated at **Surfaces and Interfaces**

5. Sonochemical Synthesis of Bismuth Oxyiodide Nanocrystal for Wastewater Remediation by Visible-light Photocatalysis
Ratna Sarkar, Dimitra Das, Subrata Sarkar and Kalyan Kumar Chattopadhyay*
Communicated at **Macromolecular Symposia**

Additional list of other publications:

6. Copper and nickel decorated g-C_3N_4 as superior catalysts for reduction of toxic pollutants: A combined experimental and theoretical approach
Dimitra Das, Bikram Kumar Das, **Ratna Sarkar**, Somnath Mukherjee and Kalyan Kumar Chattopadhyay*
Applied Surface Science, 580 (2022) 152137.

7. Enhanced field emission properties of rGO wrapped Ga_2O_3 micro/nanobricks: Experimental investigation with theoretical validation
Brahami Das, Biswajit Das, Nirmayla Sankar Das, Suvra Pal, Bikram Kumar Das, **Ratna Sarkar**, Rimpa Khan, Subrata Sarkar and Kalyan Kumar Chattopadhyay*
Journal of Alloys and Compounds, 902 (2022) 163726.

8. Manipulating dielectric relaxation via anisotropic field deviations in perovskite titanate grain–grain boundary heterostructure: a joint experimental and theoretical venture
Souvik Bhattacharjee, **Ratna Sarkar**, Pratik Chattopadhyay, Anibrata Banerjee, Nirmalya Sankar Das, Dimitra Das and Kalyan Kumar Chattopadhyay*
Applied Physics A, 128 (2022) 501.

9. Highly exfoliated graphitic carbon nitride for efficient removal of wastewater pollutants: Insights from DFT and statistical modelling
Dimitra Das, Bikram Kumar Das, **Ratna Sarkar**, Somnath Mukherjee and Kalyan Kumar Chattopadhyay*
Environmental Research, 221 (2023) 115263.

10. Morphology Tuned Ga_2O_3 Nanostructures for Visible Light Assisted Dye Sensitized Photocatalytic Water Remediation
Brahami Das, Nirmalya S. Das, Biswajit Das, **Ratna Sarkar**, Subrata Sarkar and Kalyan Kumar Chattopadhyay*
Materials Today Communications, 35 (2023) 105849.

11. Enhanced HER Performance by Controlling Crystallinity at the Interface of MoS_2 and Nitrogen Doped Carbon
Kausik Chanda, Partha Bairi, Soumen Maiti, Anjana Tripathi, Ranjit Thapa, Shrabani Ghosh, Karamjyoti Panigrahi, **Ratna Sarkar** and Kalyan Kumar Chattopadhyay*****
Communicated

12. Facile Preparation of CuCo@MnO_2 for Highly Efficient Visible-light Photocatalytic Degradation
Kausik Chanda, **Ratna Sarkar**, Soumen Maiti and Kalyan Kumar Chattopadhyay*
Communicated

Publications in conference proceedings:

1. Faceted Growth of Morphologically Tuned BiOCl
Ratna Sarkar, Dimitra Das, Anuradha Mitra, Subrata Sarkar and Kalyan Kumar Chattopadhyay*
Materials Today: Proceedings, 18 (2019) 1086-1095.

2. Efficient Photocatalytic Activity of Bismuth Oxyhalides with preferentially oriented (210) facets under Visible light
Ratna Sarkar*, Dimitra Das, Brahami Das, Subrata Sarkar and Kalyan K. Chattopadhyay*
AIP Conference Proceedings, 2220 (2020) 020030.

3. Impact of Morphological Change on Improvement of Photo-catalytic Behavior of Co_3O_4 Based System
Dipanwita Mitra*, **Ratna Sarkar**, K. K. Chattopadhyay and Paramita Chattopadhyay*
AIP Conference Proceedings, 2220 (2020) 020029.

4. Facile Preparation of Porous Ga_2O_3 Nano/microbars for Highly Efficient Photocatalytic Degradation
Brahami Das*, Biswajit Das, Suvra Pal, **Ratna Sarkar**, Nirmalya Sankar Das, Subrata Sarkar and Kalyan Kumar Chattopadhyay*
AIP Conference Proceedings, 2220 (2020) 020013.

5. Sodium Borohydride Assisted Reduction of Toxic Pollutants by Silver Coordinated Melamine Based Polymeric Material
Dimitra Das*, **Ratna Sarkar**, Somnath Mukherjee and Kalyan Kumar Chattopadhyay
Materials Today: Proceedings, 46 (2021) 433-438.

Publications in book chapter:

1. Structural Tuning of BiOCl Nano-crystals: PVP Modulated Visible Light Stimulated Photocatalytic Dye Degradation
Ratna Sarkar*, Dimitra Das, Brahami Das, Subrata Sarkar and Kalyan Kumar Chattopadhyay
Emerging Trends and New Horizons in Applied Sciences (New Delhi Publishers), ISBN: 978-81-940943-5-7.

2. Morphological tuning of low dimensional β-Ga_2O_3 for enhanced photocatalytic performance
Brahami Das*, Biswajit Das, Nirmayla Sankar Das, **Ratna Sarkar**, Suvra Pal, Subrata Sarkar and Kalyan Kumar Chattopadhyay
Basic and Applied Sciences into Next Frontiers (New Delhi Publishers), ISBN: 978-81-948993-0-3.

Papers presented in National and International Conferences

1. Recent Trends in Condensed Matter Physics **(RTCMP 2017).**
Venue: Bose Institute, Kolkata, India. (Date: October 31- November 3, 2017).
Presentation mode- **Poster presentation**

2. International Conference on Nanotechnology: Ideas, Innovations & Initiatives- 2017 **(ICN:3I 2017).**
Venue: Indian Institute Of Technology, Roorkee, India. (Date: 06-08 December, 2017).
Presentation mode- **Poster presentation**

3. Recent Trend in Frontier Research in Physics (**RTFRP-2018**).
Venue: Jadavpur University, Kolkata, India. (Date: 6th March, 2018)
Presentation Mode- **Poster presentation**

4. National Seminar on 'Physics at Surfaces and Interfaces of Soft Materials' (**PSISM-2019**)
September 26-27, 2019
Venue: Organised by Department of Physics, Jadavpur University, Kolkata, West Bengal.
Presentation Mode- **Oral presentation**

5. International Conference on Condensed Matter & Applied Physics (**ICC-2019**)
October 14-15, 2019
Venue: Govt. Engineering College, Bikaner, Rajasthan.
Presentation Mode- **Poster presentation**

6. International Conference on Condensed Matter Physics **(IEMPHYS-2019)**
November 14-16, 2019
Venue: Department of Basic Science and Humanities, Institute of Engineering & Management, Kolkata, West Bengal.
Presentation Mode- **Poster Participations**

7. 2nd International Conference on Nanoscience and Nanotechnology **(ICNAN-2019)**
November 29 -December 1, 2019
Venue: Centre for Nanotechnology Research, Vellore Institute of Technology, Vellore, India.
Presentation Mode- **Oral presentation**

8. XXth International Workshop on Physics of Semiconductor Devices **(IWPSD-2019)**
December 17-20, 2019
Venue: Novotel Hotel And Residences, Kolkata, India.
Presentation Mode- **Poster presentation**

9. Workshop on 'Writing Quality Research Article for Publication'
January 13-14, 2020
Vanue: Gandhi Bhavan, Jadavpur University, Kolkata, India.
Presentation Mode- **participated and completed**

10. One Day National Seminar on **'NEW DIRECTIONS IN PHYSICAL SCIENCES'**
February 25, 2020

Venue: Organised by Department of Physics, Jadavpur University in association with Indian Photobiology Society K. P. Basu Memorial Hall, Engineering Science Building
Presentation Mode- **Poster presentation**

11. International Conference on Nano Science and Technology **(ICNSAT-2020)**
March 5-7, 2020
Venue: S. N. Bose National Centre for Basic Sciences, Kolkata for the year 2020 and going to be held in Biswa Bangla Convention Centre, New Town, Kolkata, India.
Presentation Mode- **Poster presentation**

12. Online Course on **'An Introduction to Materials Characterization Techniques'**
June 22-28, 2020
Organization: Department of Physics, K. J. Somaiya College of Science and Commerce, Mumbai, India.

13. Certificate Course in **'Organic Optoelectronics & Spintronics: Fabrication, Modelling and Experimental Techniques'**
July – September, 2020
Organization: Kazi Nazrul University, Kalla (C.H.), Asansol, Paschim Barddhaman, West Bengal, India.

14. Two-day International Conference on **'Resent Trends in Basic and Applied Sciences (VirtCon2020)'**
July 06-07, 2020
Organization: Department of Physics, Bhairab Ganguly College and Dam Dam Matijhil College, Kolkata, West Bengal, India.
Presentation Mode- **Oral presentation**

15. International Web Conference on **'Recent Advances in Nanoscience & Nanotechnology for High-end Applications (IWCRANHA-2020)'**
July 25-26, 2020
Organization: Department of Applied Science and Humanities, Assam University, Silchar, Assam, India.
Presentation Mode- **Oral presentation**

16. **'National Conference on Materials and Devices (NCMD-2020)'**
December 18 -19, 2020
Organization: Department of Physics, Faculty of Engineering and Computing Sciences Teerthanker Mahaveer University, Moradabad
Presentation Mode- **Oral presentation**

17. **'**6th International conference on Nanoscience and Nanotechnology **(ICONN-2021)'**
February 01–03, 2021
Organization: Department of Physics and Nanotechnology, SRM Institute of Science and Technology, Kattankulathur – 603 203
Presentation Mode- **Oral presentation**

Thesis title: Development of Bismuth Oxyhalide Nanostructures for Photocatalytic and Energy Harvesting Applications

Abstract

Index No: 62/18/Phys./25

One of the major aims of nanotechnology related research is to use the improved properties of tailored materials for mitigating some of the prominent problems the world is facing currently. Production and utilisation of clean energy and environmental issues are the major concerns for sustainable development. However, for exploiting the huge potential of the nanomaterials for the application in above areas, the utmost need is to synthesise predesigned nanostructures with controlled morphology, structure, phase crystallinity etc. This research was directed to design and develop some controlled route for the synthesis of bismuth oxyhalide nanostructures for fruitful utilisation in the mentioned fields. To address the associated complexities of the synthesis process, property evaluation extensive analyses of the obtained data have to be performed and this was done.

Recent years have seen many advances in research and a variety of approaches aimed at developing efficient, pollution-free technologies to cope with highly polluted and toxic water contaminants and turn them into non-toxic waste removal products. The photocatalysis technology is one of many technologies that has been found to be efficient and environmental friendly because it uses sunlight as a source of artificial light to demineralize pollutants in a sustainable and cost-effective manner. In addition to removing organic pollutants such as organic textile dyes, this pocess can also be used to treat pesticides, herbicides, phenolic compounds, heavy metals, and pathogens like bacteria and fungus. The photocatalysis can also greatly accelerate the biodegradation of organic pollutants. It is also capable of being used in solar harvesting methods.

A new group of material called bismuth oxyhalides has captivated many researchers to its impressive photocatalytic properties. It is a wide band gap (3.2 ~ 3.6 eV) material with layeard tetragonal matlocatic structure. In addition, it has many other lucrative properties including high stability, low cost, and magnetic separation. This group of material has been tested for efficiency, affordability, water spliting and photocatalytic activity in the visible as well as UV spectrum.

As described in this thesis, bismuth oxyhalides and bismuth based materials were synthesised for use in photocatalysis and energy harvesting. The thesis begins with an introduction to the field of nanoscience and nanotechnology (chapter 1), semiconductors, bismuth oxyhalides, catalysis, as well as a quick overview of the synthesis and processing of materials and their various physical properties as well as various applications in catalysis and energy harvesting. In chapter 2, literature is reviewed on the photocatalytic and energy-harvesting applications and synthesis methods of bismuth oxyhalides. An overview of the basic working principles and the essential tools used in all courses of study are discussed in chapter 3.

Contaminated water by various sources such as by textile wastewater can't be used for drinking. In addition to being highly carcinogenic, sewage-polluted water poses a serious threat to human health. There is an urgent need for the degradation and transformation of these harmful pollutants into harmless ones. The purification of wastewater has been accomplished by a variety of strategies. Photocatalysis has been widely accepted among them due to its high efficiency, non-selectivity, and low cost. High recombination rates of photogenerated carriers limit the photocatalytic activity of wide band gap semiconductors. The development of new hybrids with semiconductor coupling, from the perspective of a moderate application perspective, is one of the strategies used to improve the catalytic performance. Chapter 4 describes a simple hydrothermal synthesis strategy to develop sheet like nanocomposite semiconductors composed of bismuth oxychloride and graphene oxide (BOC-GO) that can have spatial separation and absorb light, with efficient photocatalytic degradation about 99.59 % at 60 minutes under visible light irradiations. In chapter 5, bismuth oxychloride (BiOCl) was synthesised by hydrothermal method by variation of citric acid percentage in the precursor which resulted different morphologies. These materials were evaluated for hydrogen evolution reactions with high overpotential about 72 mV/dec (w.r.t. Platinum) and photocatalytic activity about 97.64 % at 10 minutes illumination under visible light for the best material. The chapter 6 presented synthesis of time and temperature varied pure bismuth oxychloride (BiOCl) by heating method (oil bath) with 3D hollow microspheres like structure for highly efficient dye-sensitisation catalytic performance about 98.92 % degradation for only 6 minutes irradiation for the best sample under visible light. The (110) crystal facetes were predominantly exposed and the corresponding lattice planes are the most water absorber, which is calculated from the density functional theory (DFT). In chapter 7, results of photocatalytic dye degradation under UV light illuminations by the pure bismuth oxychloride (BiOCl) nanomaterial synthesised for different times are presented. An impressive performance of about 99.21 % degradation in only 15 minutes was achieved.
Chapter 8 presents a grand summary of the major findings of the thesis and scope of future research work.

Keywords: Bismuth Oxychloride, Graphene Oxide, Nano-composite, Citric Acid, Textile Dye, Hydrogen Evolution, DFT Calculation, Visible-light, UV-light, Photocatalysis, Dye Sensitization, Water Remediation.

Signature of Candidate: Ratna Sarkar

Date: 20/06/2022

Subrata Sarkar 20/06/22

Dr. Subrata Sarkar
Signature of the Supervisor
Date with Office Seal

Dr. Subrata Sarkar
Assistant Professor
Department of Physics
Jadavpur University
Kolkata-700 032

20.6.22

Prof. (Dr.) Kalyan Kumar Chattopadhyay
Signature of the Supervisor
Date with Office Seal

Prof. Kalyan Kr. Chattopadhyay
Professor and Head
Department of Physics
Jadavpur University
Kolkata – 700 032

List of Abbreviations

Abbreviations	Original Phrase
1D	One Dimention
2D	Two Dimention
3D	Three Dimention
BE	Binding Energy
BET	Brunauer Emmett Teller
BiOCl	Bismuth Oxychloride
BiOBr	Bismuth Oxybromide
BiOI	Bismuth Oxyiodide
BiOX	Bismuth Oxyhalide
BJH	Barret Joyner Halenda
CA	Citric Acid
CB	Conduction Band
CBD	Chemical Bath Deposition
CVC	Chemical Vapour Condensation
CVD	Chemical Vapour Deposition
DFT	Density Functional Theory
DI	Deionized
DRS	Diffused Reflectance Spectroscopy
EIS	Electrochemical Impedance Spectroscopy
EDS	Energy Dispersive X-ray Spectroscopy
ET	Energy Transfer
EDTA-2Na	Ethylene Diamine Tetra Acetate Disodium
EB	Eosin B
FESEM	Field Emission Scanning Electron Microscopy
FTIR	Fourier Transform Infra-Red Spectroscopy
FWHM	Full Width Half Maxima
GO	Graphene Oxide
HER	Hydrogen Evolution Reaction
HOMO	Highest Occupied Molecular Orbita
HR	High Resolution

HRTEM	High Resolution Transmission Electron Microscopy
IPA	Isopropyl Alcohol
IR	Infra Red
LUMO	Lowest Unoccupied Molecular Orbital
LSV	Linear Sweep Voltammetry
MB	Methyl Blue
MO	Methyl Orange
NHE	Normal Hydrogen Electrode
OV	Oxygen Vacancy
PH	Potential of Hydrogen
PL	Photo Luminescence
PVP, K30	Poly Vinyl Pyrrolidone
RhB	Rhodamine B
ROS	Reactive Oxygen Species
SAED	Selected Area Electron Diffraction
VB	Valance Band
UV	Ultra Violet
XPS	X-ray Photoelectron Spectroscopy
XRD	X-Ray Diffraction

List of Chemical Reagents

Chemical Name	Company name (Purity)
Absolute Ethanol (99.99 %) [CH_3CH_2OH]	Sigma-Aldrich (99.9 %)
Ammonium Hydroxide Solution (25 %) [NH_4OH]	Merck (99.9 %)
Barium Sulfate [$BaSO_4$]	Sigma-Aldrich (99.9 %)
Bismuth Nitrate Pentahydrate [$Bi(NO_3)_2 \cdot 5H_2O$]	Merck (99.9 %)
Citric Acid Monohydrate [$C_6H_8O_7 \cdot H_2O$]	Merck (99.9 %)
Ethylene Diamine Tetra Acetate Disodium [$C_{10}H_{14}N_2Na_2O_8$]	Loba Chemie
Graphite Powder [C]	Merck (99.9 %)
Hydrochloric Acid (37%) [HCl]	Merck (99.9 %)
Hydrogen-Peroxide Solution (30 %) [H_2O_2]	Merck (99.9 %)
Isopropyl Alcohol [C_3H_8O]	Merck (99.9 %)
Nafion [$C_7HF_{13}O_5S \cdot C_2F_4$]	Sigma-Aldrich (5 wt.%)
Nitric acid (98 %) [HNO_3]	Merck (99.9 %)
N-Methyl-2-pyrrolidone [C_5H_9NO]	Sigma-Aldrich (99.5 %)
Ortho-Phosphoric Acid (98 %) [H_3PO_4]	Merck (99.9 %)
p-Benzoquinone [$C_6H_4O_2$]	PubChem
Poly Vinyl Pyrrolidone [$(C_6H_9NO)_n$]	Loba Chemie
Potassium permanganate [$KMnO_4$]	Merck (99.9 %)
Rhodamine B [$C_{25}H_{31}ClN_2O_3$]	Loba Chemie
Sodium Nitrate [$NaNO_3$]	Merck (99.9 %)
Sodium Sulfate [Na_2SO_4]	Merck (99.9 %)
Sulfuric Acid (98 %) [H_2SO_4]	Merck (99.9 %)
t-Butanol (99 %)[$C_4H_{10}O$]	Sigma-Aldrich (99.9 %)

Contents

Chapter 1

Introduction

Nanoscience, nanotechnology and nanomaterials are defined and explained in this chapter. It illustrates why the nano world is fascinating, and why students should be interested in this area of science.
To extend the nanoscale boundaries, biologists, chemists, physicists, and mechanical engineers all work together in nanotechnology. A molecular system is essentially the engineering of functional systems. The subject encompasses both the current state of the art and new concepts. Nanotechnology refers to the capability of constructing items from the bottom up, utilising existing tools and techniques to create complete, high performance products, according to its definition in its original meaning.

1.1 Nanoscience and Nanotechnology

Professor Norio Taniguchi introduced nanotechnology in 1974, but the concept was introduced by the Nobel Laureate physicist Richard Feynman in his lecture "There's Plenty of Room at the Bottom: An Invitation to Enter a New Field of Physics" on 29th December 1959 at the California Institute of Technology. In his lecture, Feynman described a technique for manipulating individual atoms and molecules. So that's why Richard Feynman is known as the "Father of Nanotechnology"[1]. However, most researchers and authors often ask themselves how to explain and differentiate between the terms "Nanoscience" and "Nanotechnology". The most commonly used nanoscience definition is as follows:

Nanoscience refers to the study of phenomena and the manipulation of materials that occur at scales smaller than atoms, molecules and macromolecules, in which properties differ considerably from those of larger scales.
In the U.S. National Nanotechnology Initiative (NNI), nanotechnology is defined as follows:
In nanotechnology, unique phenomena enable novel applications by explaining how matter behaves at dimensions between 1 and 100 nanometres[2]. Nanotechnology includes the study, measurement, modelling, and manipulation of matter on a nanoscale. It encompasses science, engineering, and technology on an extremely tiny scale.
During the 1980's, K. Eric Drexler popularised the concept of nanotechnology, referring to machines that could be built on the scale of molecules, as small as a few nanometres across-motors, robot arms, and even whole computers smaller than human cells. During the next ten years, Drexler described and analysed these incredible devices, as well as responding to claims that they were science fiction. On the other hand, mundane technology was developing the capability of building simple structures at the molecular level. In the process of becoming an accepted concept, nanotechnology has taken on a broader meaning that now includes easier forms of nanotechnology. This kind of nanotechnology is

something that the U.S. National Nanotechnology Initiative searches, for any material smaller than 100 nanometres with novel properties are included. A theoretical capability similar to this was envisaged by Richard Feynman in 1959.

I want to build a billion tiny factories, models of each other, which are manufactured simultaneously… The principles of physics, as far as I can see, do not speak against the possibility of manoeuvering things atom by atom. It is not an attempt to violate any laws; it is something, in principle, that can be done; but in practice, it has not been done because we are too big.—Richard Feynman, Nobel Prize winner in physics[3].

1.1.1 A Brief History of Nanotechnology

- **2000 years ago:** In ancient Greece and Rome, sulphide nanocrystals were used to dye hair.
- **1000 years ago (middle ages):** Various sized gold nanoparticles were used in stained glass windows to produce different colours.
- **1959:** "There's plenty of room at the bottom" was the title of Richard Feynman's revolutionary lecture at an American Physical Society meeting.
- **1974:** In a first time use of the term "nanotechnology", Professor Norio Taniguchi describes nanotechnology[4].
- **1981:** Microscopes that scan tunnels are developed by IBM[5].
- **1985:** 'Buckyball'- Discovery by scientists at Rich University and the University of Sussex shows Fullerene (C_{60}) is a material with extraordinary properties[6].
- **1986:** 'Engines of Creation'- Introducing nanotechnology in the first book by K. Eric Drexler[7-9]. Atomic Force Microscope designed by Binning, Quate, and Gerbe.
- **1989:** The IBM logo crafted from atoms.
- **1991:** A carbon nanotube has been discovered by S. Ijima.
- **1999:** 'Nano medicine'- This is the first book devoted to nanomedicine by R. Freitas.
- **2000:** 'National Nanotechnology Initiative' launching from U.S.

Nanotechnology consists of designing, analysing, constructing, producing and using devices, structures, and systems by controlling their shape and size on a nanometre scale.

In defining nanoscience and technology, let us first examine the meaning of "nanometre scale".

1.1.2 Nanometre Scale

A dwarf is a person with the prefix 'nano' from Greek. In general, the nanoscale is defined as being between 1 and 100 nanometres, with a nanometre equivalent to a billionth of a metre (10^{-9} metres). A minimum of 1 nm is usually imposed in order to prevent, for example, individual atoms or very small groups of atoms from being labelled nano-objects. Therefore, nanoscience and nanotechnology are concerned with molecules whose groups are at least 1 nanometre in size. From looking at the above scale, one will be able to understand how small 1 nm is. The user can easily compare it with the size of a micron. However, you can also relate a nanometre's size to the following examples:

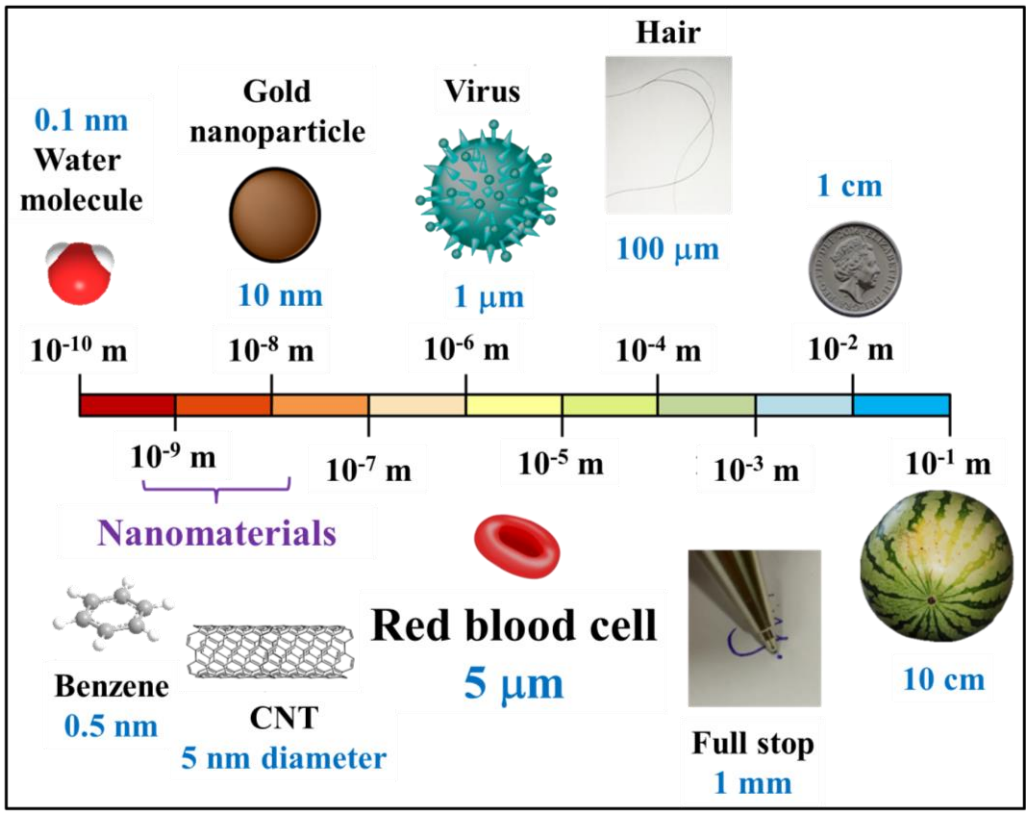

Figure 1.1: Area of nanoscience and technology

a) Each fingernail grows 1 nanometre a second.

b) There are about 1 million nanometres between the head and the centre of the pin.

c) The diameter of a human hair is approximately 80,000 nanometres.

d) The diameter of the DNA molecule is approximately 1-2 nm.

e) Mycoplasmas, the smallest cells in existence, are approximately 200 nanometres in length.

In comparison with a human hair, nanostructures measure ~ 50,000 nm in diameter, while water molecules are ~ 0.3 nm long and carbon nanotubes are ~ 1.2 nm long[10].

The question that arises is that what is a nanomaterial? Now let's look at what the word nanomaterials means.

1.1.3 Nanomaterials

Any object which has at least 1D within nanometre range (~ 1 - 100 nanometres) is considered a nanomaterial. There are numerous types of nanomaterials, but they can be roughly separated into two groups:

1.1.3.1 Non-Intentionally Made Nanomaterials

Materials that have a nanoscale, such as those naturally found in nature (e.g. proteins, viruses, nanoparticles from volcanic eruptions, etc.) as well as those formed by unintentional human activity (e.g. nanoparticles created by diesel combustion).

1.1.3.2 Intentionally Made Nanomaterials

Intentionally made nanomaterials are those that are manufactured intentionally during a specific manufacturing process. Nanotechnologies include only those intentionally created nanomaterials and exclude non-intentionally created nanomaterials. There are a few examples of nanomaterials that are used in our everyday lives or in industrial applications or laboratories.

There are three types of nanomaterials based on their dimension, which are presented in Table 1.1.

Table 1.1: The classification of category wise nanomaterial

Classification	Examples
Zero dimension (0D) < 100 nm	Particles, quantum dots, hollow spheres, etc.
One dimension (1D) < 100 nm	Nanorods, nanowires, etc.
Two dimension (2D) < 100 nm	Tubes, fibres, platelets, etc.
Three dimension (3D) < 100 nm	Spheres, layered structures, etc.

1.1.3.3 What Distinguishes Nanomaterial from Bulk

Micro-structured materials possess many of the same properties as their bulk counterparts but their nanoscale dimensions make them different from bulk materials and atoms. There are several characteristics of nanomaterials that set them apart from bulk materials and these include:

a) A high proportion of surface atoms,

b) Energy-rich surface,

c) Confinement in space and

d) The number of imperfections that are reduced compared to those found in bulk materials[2].

The following advantages are provided by nanomaterials:

In the first place, all nanomaterials contain very small particles. As a result of nanomaterial and nanotechnology, super miniaturisation is attainable. Nanostructures can be packed tightly together due to their size. In consequence, one can locate more functional nanodevices on a given unit of area, which is essential for nanoelectronics. Moreover, high packing density can lead to higher storage volume and storage area as well as faster information processing (since electrons can move between components in a shorter period of time). The results are more sophisticated and smaller electronic devices, faster and smaller circuits, and substantially lower power consumption due to controlling nanostructure interactions and complexity.

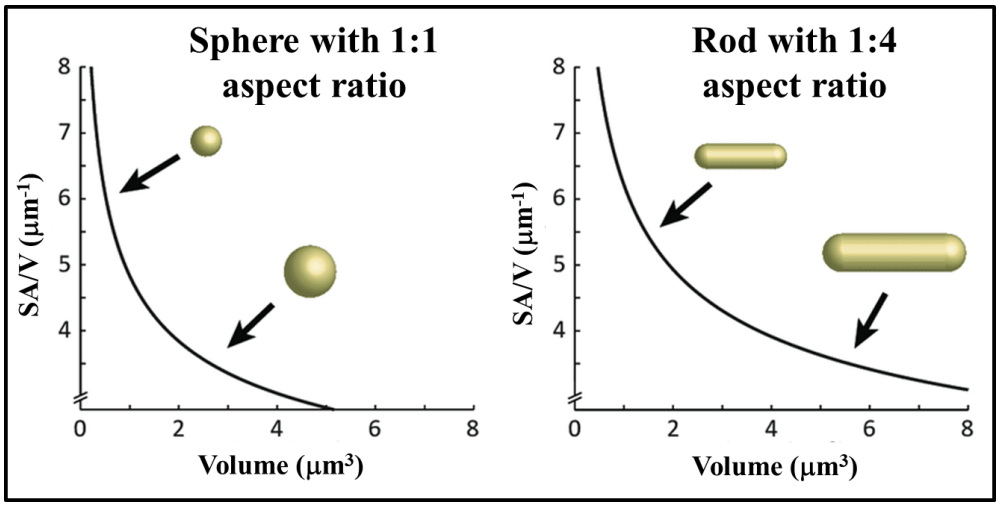

Figure 1.2: The relationship between surface/volume ratio and particle size

In addition, the nanomaterial has a large specific surface area due to their small dimensions, which accelerates their interactions with surrounding environments. The surface area of nanoparticles per unit of mass is much greater than that of larger particles. Considering the fact that growth and catalytic chemical reactions take place at surfaces, nanoparticles will have much higher reactivity than the same mass of a larger particle. In addition to a strong increase in the properties of nanomaterials as a result of particle shrinkage, surface atoms play a significant role in their physical and chemical properties.

The surface area of an object increases only as the second power of its linear dimensions, while the volume of an object decreases as the third power. A nanoparticle has a higher surface-to-volume ratio

(relation between surface and bulk atoms) than a bulk one. The function of particle size, graphs of surface/volume ratio is shown in Figure 1.2[11].

1.1.3.4 Examples of Nanomaterial Used in Our Daily Life

a) In the cosmetics industry, mineral nanoparticles (such as titanium dioxide) are used in sunscreens since conventional sunscreens don't possess the stability needed by chemical long-term UV protection. As a result, students will be protected from UV rays and will be able to avoid undesirable cosmetic bleaching associated with nano form sunscreens.
b) The sports industry uses carbon nanotubes to make baseball bats, which makes them lighter and better performing.
c) In order to identify nanomaterials in products such as towels and carpets used by athletes as a means to prevent bacteria-related diseases, antibacterial nanotechnology is used.
d) Nanomaterials have also been developed for use in military applications. The military is gradually developing the use of removable pigment nanoparticles that enable them to create better camouflage shapes by injecting them into their uniforms. In addition, the military has developed sensors that detect biological agents by using nanomaterials such as titanium dioxide.
e) Additionally, titanium dioxide has been used to create self-cleaning surface coatings (such as plastic reclining chairs). A water film is formed on the lining, and afterward dirt dissolves in the film. After that, the next shower can remove the dirt and clean the chair from top to bottom.

Compared to bulk solids, nanomaterials have many advantages, such as their properties, size, and adaptability, which make them practical in a variety of applications. Additionally, nanomaterials have a high porosity, which increases their demand for applications across a wide array of industries.
So, nanomaterials have become very popular among researchers because of their wide applications and advantages.

1.2 Synthesis and Processing of Nanomaterials

Various types of nanostructures can be synthesised artificially for specific purposes: macromolecules, nanoparticles, bulky balls, nanotubes, etc. As well as using thermodynamic methods, nanostructures can be produced by self-organisation and self-assembly (also called biomimetic processes), which are based on equilibrium or near-equilibrium thermodynamics. It is possible to synthesise material and to arrange it into useful structures for a specific application using these methods. Nanometre is one

billionth of a metre, which is an extremely fine structure. The top-down or bottom-up approach can be utilised to synthesise nanomaterials. Assembling atoms together or disassembling (breaking or dissociating) bulk solids into smaller pieces until they are composed of just a few atoms can be used to synthesis nanomaterials[12]. The different synthesis and processing methods are Mechanical Grinding[13], Sol-Gel Process[14], Solid State Method[15], Gas Phase Synthesis[16], Chemical Vapour Condensation (CVC)[17], Wet Chemical Method[18], Heating Method[19], Chemical Bath Method[20], Hydrothermal Method[21], Solvothermal Method[22], Microwave Synthesis Method[23], Sonochemical Method[24], etc., that produce high quality nanomaterials.

1.3 Properties of Nanomaterials

Materials that are nanoscale have distinct structural characteristics, while atoms and bulk materials have very different properties. The properties of microstructure materials are often similar to those of bulk materials. Although nanoscale materials are very different from bulk materials and atoms, they have similar properties. It is mainly for this reason that they are made from nanometre-sized materials:

i) A large number of surface atoms,
ii) A high surface energy,
iii) A space constraints and
iv) A reduction in defects that do not exist in their bulk equivalents.

Small sizes give nanomaterials a great deal of surface area, which means the surface or interface atoms are larger, which means that the material will have more surface characteristics. If the material's length and size are similar, then its surface characteristics will affect the whole material. Nanomaterials with the characteristic size of nanomaterials can have a limiting effect on the material and can alter its properties. A metal nanoparticle may serve as a highly active catalyst, for example nanowires and chemical nanoparticles can also be used as sensors, where the sensitivity and selectivity of the sensor can be increased[25].

1.3.1 Optical Properties

Nanomaterials have many interesting and useful properties, including their optical properties. These materials can be used to make optical detectors, photocatalysis, solar cells, lasers, sensors, displays, phosphors, photoelectrochemistry and biomedicine. The gap is usually caused by changes in network parameters caused by tempering or doping with impurities, parameters like component shape, size, surface characteristics, and interaction with other nanostructures are also considered.

1.3.2 Electrical Properties

Interesting techniques that can be used to prove step conductivity is mechanically thin the nanowire and measure the current applied with a constant voltage has been demonstrated in the paper "The electrical properties of nanoparticles". Nanotubes and nanotubes' electrical conductivity, the photoconductivity of nanotubes and nanorods, and the electrical conductivity of nanocomposite materials were discussed. Due to the well-defined quantization step in which the nanowires are mainly sized according to their diameter, the smaller the wire diameter, the fewer the number of electromagnetic waves that contribute to conductivity. In case of gain boundary the grain boundary effect plays a very important role, because the interface contains defective elements, such as vacancies, bonds dangling, groups of vacancies, etc.

1.3.3 Mechanical Properties

Metals and ceramics are bulk materials that demonstrate the mechanical properties of nanoparticles, with the effects of porosity, grain size, super plasticity, coated polymers, particle-filled polymers, platelet-filled polymer-based nanocomposite. The carbon nanotube compounds being partially of fundamental interest, in view of the difficulty of producing macroscale bodies with high densities and grains smaller than 100 nm. Although, the two materials that are not formed by pressing and sintering, but which are certain to gain industrial importance. However, it captures the most interest. Material having such properties is polymers that contain nanoparticles or nanotubes, and metals that have amazing properties when severely deformed.

1.4 Applications of Nanotechnology

Nanotechnology is a way to solve big problems with very small solutions. It has many practical applications and many researches are underway in multiple areas of application. The following are some areas where use of nanotechnology, Biomedicine, Electronic goods, Solar energy, Food packaging, Textile industry, Environment purification such as ionic air purification, wastewater treatment with nanospheres, or heavy metals filtration, etc.

1.5 Semiconductor

A semiconductor is a solid chemical that conducts electricity under certain conditions, but not under others, so they are good conduits for controlling electricity. Infrared, visible light, ultraviolet light, and X-rays can all cause thin films of lead to conduct, depending on the electric current or voltage applied to the control electrode. Group IV of the periodic table contains some semiconducting elements (such as germanium and

silicon). Several binary compounds, especially those formed between elements of groups II-VI, III-V, IV-VI, as well as compounds containing two elements of group IV and certain ternary compounds have semiconducting properties. Impurities, or dopants, are the substances contained within a semiconductor that determine its specific properties. The conduction of current in an n-type semiconductor is similar to that in wires, with negatively charged electrons carrying most current. On the other hand, a p-type semiconductor carries current primarily in the form of electron and holes. An electron has negative electric charge and a hole has positive charge. The hole flow occurs in semiconductor materials in the opposite direction to electron flow[26]. Conductive metals are highly electrically conductive, while insulating materials are highly electrically resistive. But semiconductors can exhibit electrical conductivity variations up to several orders of magnitude. Semiconductors have been crucial to the development of modern electronic technology because of this unique property. As transistors and microprocessor chips were discovered, human life-style was forever changed. The semiconductor field has experienced rapid and significant advancements in the past century. Several useful practical applications of semiconducting materials have prompted a great deal of interest including solar cells[27], photo-electrochemical cells[28], sensors[29], photo-luminescence devices[30], photocatalysts[31], etc. As well as providing fundamental insights into electronic processes, they also provide fundamental insights into the electronics themselves. Materials processing has similarly grown in importance through research.

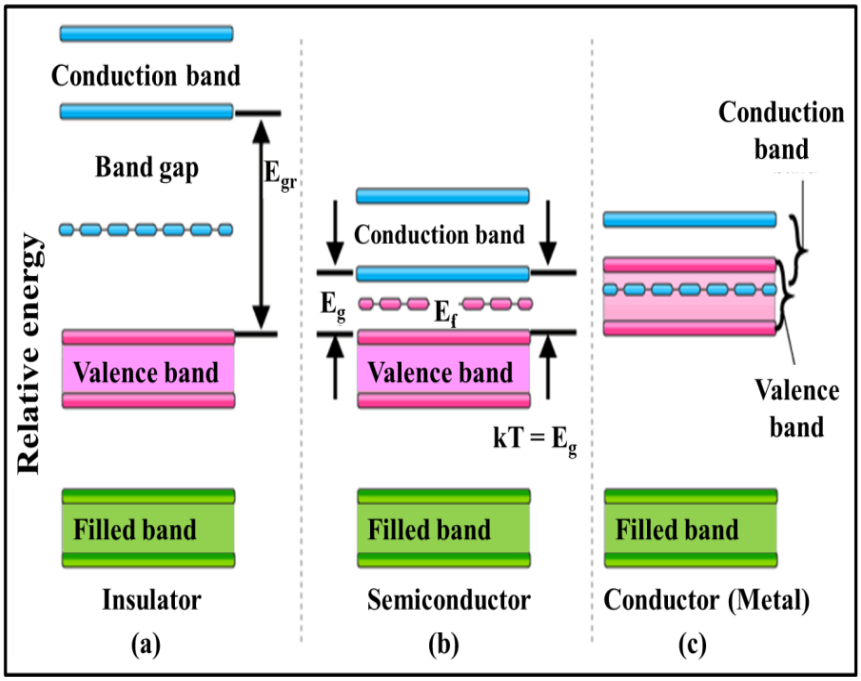

Figure 1.3: The diagram of energy band (a) insulator, (b) semiconductor and (c) conductor (metal)

A variety of new materials are now available that can be used for specific purposes. The major constraint to new technological advancements is often limited material resources. The synthesis of materials with multifunctional high performance properties is now of particular interest to material scientists, as is determining how to synthesise them at a low cost and with high yield.

1.6 Introduction to Bismuth Oxyhalide Nanoparticle

The first thing that comes to mind; what is bismuth oxyhalide? Moreover, why are interested in it? In addition, why is bismuth oxyhalide such a hot topic among researchers? Those questions will be addressed in this section.

1.6.1 Background

In photocatalysis, one can speed up the photoreaction by using a photocatalytic substance, the catalytic reaction is based on the electron and hole pair formation of the catalyst, which induces free radicals such as hydroxyl radicals (OH^- ions) that can enter the secondary reaction. Splitting water by doing this produces hydrogen by splitting water into H^+ and OH^- ions and subsequently producing hydrogen using unlimited solar energy. The photo-reducing CO_2, it can also produce carbon based fuel that can be used for everyday needs. Therefore, there is much research being conducted towards the discovery of the photocatalytic materials to increase the efficiency of photocatalysis. There are many photocatalytic substances that have been discovered so far, TiO_2 is one of the most popular.

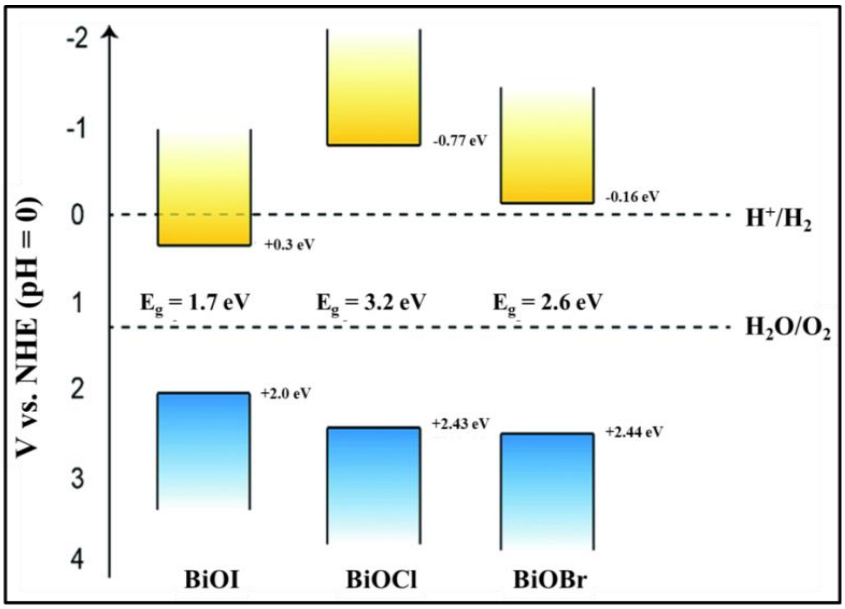

Figure 1.4: The bands of bismuth oxyhalide films are shown compared to the possibilities of water splitting at pH-0, respectively, for the BiOI, BiOCl and BiOBr films

However, it has a very important drawback. It has a bandgap that only extends to the UV spectral region, which limits its ability to absorb sunlight in the UV-B range, allowing for only 6 % of solar energy to be harvested. So many scientific researchers have been directed to finding a suitable material that will work appropriately on the visible light spectrum range of the sun, so that solar energy can be harnessed to its maximum degree. As an addition to TiO_2, bismuth oxyhalide (Chloride, Bromide and Iodide) has emerged as a very promising photocatalytic material. A layered bismuth oxyhalide exhibits an attractive energy band structure and can be used to convert solar energy[32].

1.6.2 Definition and Importance of Bismuth Oxyhalide

It has been proven to be an excellent photocatalytic material for water purification since materials based on bismuth compound are common, less toxic, and cost effective and shown a high photocatalysis due to the formation of a favourable hybrid valence band between Bi (III) and the Bi 6s level in O 2p levels. In BiOX, layers of [X-Bi-O-Bi-X] are stacked and supported by halogen atoms that relate to the Wade wall and are covalently bonded, providing outstanding optical, electrical, and mechanical properties. BiOX nanostructures, such as nanowires, nanofibers, nanosheets, nanoplates, nanodisks, nanoflakes, nanoparticles, nanonuts, nanoflowers, nanoribbons, hollow microspheres, etc., have been synthesised in several different chemical ways, and each layer displays asymmetric decahedral symmetry, due to the fact that each bismuth atom appears surrounded by two oxygen atoms and two halide atoms, with many variations. Recent studies have highlighted the effectiveness of using BiOX materials in photocatalytic degradation because their free electrons have indirect band gaps, an open structure, and an electrical field that is perpendicular to the layer that separates the photogenerated electron hole pairs[33].

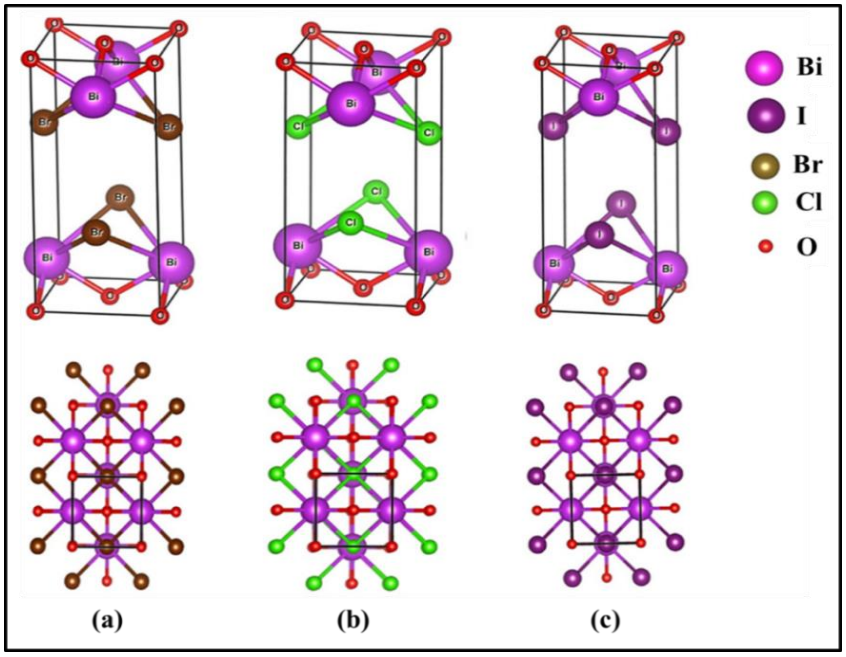

Figure 1.5: The unit cells of bulk (a) BiOBr, (b) BiOCl and (c) BiOI material

However, bismuth oxychloride has been demonstrated to be an excellent photocatalytic material. The ability to absorb visible light is closely associated with its shape, size, crystal plates and dimensions. Thus, in order to construct such a remarkable photocatalytic material that must apply different techniques of synthesis, such as 1D, 2D, 3D, hollow and nanostructures that results in an appropriate band gap structure. The synthesis of bismuth oxyhalides can be achieved in many ways, but studies show that solvothermal and hydrothermal methods are the most efficient and effective methods. The adjusting the thermodynamic parameters of the synthetic system, the characteristics of bismuth oxyhalides can be controlled.

1.6.3 Characteristics of Bismuth Oxyhalide

Research has been concentrated on BiOX nanocrystals due to their unique energy band structure that allows them to absorb sunlight for photocatalysis. However, these materials also have inherent limitations, such as their inability to generate charge carriers under visible sunlight and high tendency to recombine. The characteristics of this material in much greater depth in the subsequent chapters in this thesis, including its photocatalytic activity and the techniques used to overcome its limitations. Including the manipulation of the electric field induced by its single-layered structure, with increasing the photocatalytic activity by transferring and separating charge carriers[34].

1.6.4 Synthesis Techniques of Bismuth Oxyhalide

Since growth mechanisms of BiOX are strongly dependent on synthesis techniques and some parametres. Hydrothermal/Solvothermal, Hydrolysis, Template, reverse microemulsion Method, etc., are some of the common methods of synthesis, which will be discussed one by one for better understanding on the above topics[34].

1.6.4.1 Mechanical Grinding Method

Mechanical grinding has become popular as a method for monocrystalline materials synthesising due to its simplicity, low equipment requirements, and ability to synthesise almost all types of materials. 'Top down' synthesis of nanomaterials relies on the destruction of coarse grains because of distortion, rather than cluster assembly, as the final fabric is made. In mechanical milling, refractory or steel balls are used, which provide energy by vibrating, causing the powder to spin, which determines the ball-to-powder mass ratio, and which produces nanoparticles when under shear action. This method reported by Tadjarodi et al. for synthesis of BiOCl samples for catalytic degradation application[13].

1.6.4.2 Sol-Gel Process

Gel formation is achieved by forming a colloidal suspension in a continuous liquid phase and gelatin the sol to form a network. These colloids are synthesised using metals or metalloids covered with ligands, and they are dispersed in acid or water after they are transformed into oxides. The liquid is removed from the sol during a transition from sol to gel or from gel to sol. Sol-gel is produced by calcining the gel to produce oxide. The BiOCl-TiO_2 composite was synthesised by this method, Sánchez-Rodríguez et al. using this method to prepare the catalyst, for phenol degradation application[14].

1.6.4.3 Solid State Method

To produce nanoparticles, a crucible used for producing nanoparticles is heated to 2000 °C to attain the desired vapour pressure. Materials with high vapour pressures can be analysed using this method. Normally precursors were ground in an agate mortar with CH_3OH at a stoichiometric ratio and some time in an agate mortar. Xie et al. synthesised BiOCl sample by this method at room temperature, for catalytic degradation application[15].

1.6.4.4 Wet Chemical Method

At room temperature, Chen et al. synthesise hierarchical nanostructured bismuth oxychloride within some time. On ambient temperature and pressure, a series of three-dimensional (3D) structures including BiOCl nano-flowers with nano-plates of about 30 nm thickness have been successfully grown. Anisotropic growth is observed along the (110) faces during the synthesis of the samples[18].

1.6.4.5 Heating Method

A hierarchical precursor has been hydrolysed with 80 °C heat and a hierarchical precursor has been transformed to many types of nanocrystals made of BiOCl, including nanoflakes and hollow microspheres (HMSs). The obtained BiOCl was composed of sub-microcrystalline crystals, ranging from monocrystals to polycrystals. Nest-like and hollow structures were induced during the experiment[19].

1.6.4.6 Chemical Bath Method

Ye et al. successfully synthesised the mixture of chemicals by stirring and heating in a low-temperature chemical bath method such as an 80 °C water bath for a prolonged period. A filtration step and cooling step followed the reaction. In the oven, the precipitate was dried at 80 °C for 24 hours after being cleaned with absolute ethanol and deionized water three times[20].

1.6.4.7 Hydrothermal Method

According to Zhan et al. different types of surfactants were introduced into the hydrothermal process with the introduction of different types of bi-functional bicarbonate crystals and their nano-disk like architectures with exposed (001) facets. According to BiOCl products, the sample possesses substantial disk-like structures that have diameters between 100 - 300 nm and thickness between 15 - 30 nm. In addition, study results demonstrate that the type of surfactant, concentration of the reducing agent, concentration of the reactants, and the reaction temperature all contribute to the nano-architecture and morphology of the products[21].

1.6.4.8 Solvothermal Method

Using a solvothermal approach aided by mannitol, Tian et al. have successfully synthesised hierarchical 3D BiOCl nanostructures constructed by interconnected 2D nano-plates with a thickness of about 35 nm, for the dye adsorption application[22].

1.6.4.9 Microwave Synthesis Method

Through a microwave-assisted approach in the presence of deionized water (DI) in low temperature of 70 °C for 15 minutes, Dash et al. were able to successfully produce nano-flakes such as BiOCl. In the creation of nanostructured materials, microwaves have proven to be outstanding technologies, largely because of all the advantages it offers[23].

1.6.4.10 Sonochemical Method

Ultrasonically dispersing the chemicals in 25 mL DI water at 30 °C for 30 minutes was achieved for synthesised BiOX (X= Cl, Br and I) samples. After that, to remove any trace impurities, precipitate was centrifuged after it had been thoroughly washed with DI water and ethanol. Furthermore, the precipitate was drying overnight at 80 °C, and obtained purified material for catalytic degradation application[24].

1.6.4.11 Hydrolysis Method

It is possible to use the same compound as the source of bismuth and halide in hydrolysis method for example to produce BiOCl nanoparticles, Armelao et al. hydrolyzed $BiCl_3$ at 65 °C intended for 6 hours as a source of Bi and Cl, however, this case it was not stabilised; then used acetyl acetone as an auxiliary solvent and added HCl to provide an acidic environment for stabilising it[35]. Different materials can be used to prepare BiOX, and for instance the irregular BiOCl nanosheets formed by Song et al. can have a thickness of 21 to 85 nm and are prepared from $Bi(NO_3)_3$ and HCl, respectively. Furthermore, a pH adjustment of about 2 was performed by adding Na_2CO_3, following the sample was hydrolyzed at room temperature for about 30 min[36].

1.6.4.12 Other Preparation Method

There are several ways to synthesise BiOX and depending on requirement, other methods are used, such as Henle et al. used reverse microemulsion method to generate BiOCl nanoparticles, and also used heptane, non-ionic surfactant, and saline solution, for the ion precipitation. Additionally, reverse micelles which can be used to regulate the size of the nanoparticles[37].

An ionic liquid assisted ultrasound method was used in Yang et al.'s study to generate BiOCl. Reaction conditions for this process are straightforward and simple. Irradiating an ionic liquid with ultrasound for 10 minutes after 20 minutes mixing the $Bi(NO_3)_3$ and ionic liquid supplies the Cl source. A switch in the reaction solvent can produce BiOCl with different morphologies[38].

In situ chemical conversion was used to prepare small, zero-dimensional BiOCl nanoparticles by in-situ chemical conversion. Nanosheets of $Bi_4Ti_3O_{12}$ were used as a substrate and HCl as a source of Cl. Obtaining the BiOCl nanoparticle requires an agitation procedure at room temperature for some time[39].

1.6.5 Applications of Bismuth Oxyhalide

The photocatalytic property of bismuth oxyhalides makes them very useful materials. However, the discussion in this chapter will cover several applications of BiOX, a detailed explanation of which will follow in the following chapter.

1.6.5.1 Application as Photocatalytic Material

To remove organic pollutants, nanomaterials are usually used as catalysts to destroy harmful dyes under sunlight, visible and ultraviolet light. Textiles, cosmetics, paper, leather, pharmaceuticals and other industries generate large amounts of dye as waste, and these dyes pollute the soil from water, and these dyes cause health problems for humans. Since modern people are becoming more dependent on industry. Photocatalysis has gained an increasing amount of attention in recent years, and numerous nanomaterials exist that possess photocatalytic properties, among which bismuth oxyhalide has drawn considerable interest because of its wide band width. The main application of bismuth oxyhalides is a photocatalytic material which is used to degrade organic or inorganic pollutants in aquatic ecosystems. In the water splitting process, it helps to purify water by separating toxic materials from polluted environments.

1.6.5.2 Application as Secondary Battery

The bismuth oxyhalides, Metal-air batteries are used in a huge amount of industrial applications. The primary benefits of metal-air batteries include their low emissions, high energy density, low weight, portability, and extremely low sound and vibration levels. Oxygen reductions are the process that takes place in the metal-air battery or fuel cell. Here, two electrons are absorbed by O_2 to create H_2O_2 and four electrons are absorbed by O_2 to form H_2.

1.6.5.3 Application as Gas Sensor

Photocatalytic material has been used for many years in solid analytical sensors for measuring harmful gases such as ozone, SO_2, NO_2, CO, CO_2 and other dangerous gases, and the organo-phosphorus pesticide biosensor can also be used as a photocatalytic material in agricultural applications.

1.6.5.4 Application as Solar Cell

Research has traditionally focused on semiconductor nanomaterials as the basis for photovoltaic systems (such as dye-sensitive solar cells), since these nanomaterials have a number of advantages and present excellent potential for photovoltaic applications. Recently, researchers have developed solar cells using bismuth oxyhalides in photovoltaic research.

1.7 Introduction of Graphene Oxide

1.7.1 Graphene (C)

Carbon molecules are bonded together into hexagonal patterns to make graphene, a material composed of carbon atoms. Since graphene is so thin, it is considered a 2D structure. The hexagonal honeycomb pattern of graphene leads to many unusual properties, including the fact that it has the highest strength of any material, is best at conductivity, is transparent, and is the lightest material available. A wide variety of industries (like electronics, medicine, aviation, and more) can benefit from graphene[40,41].

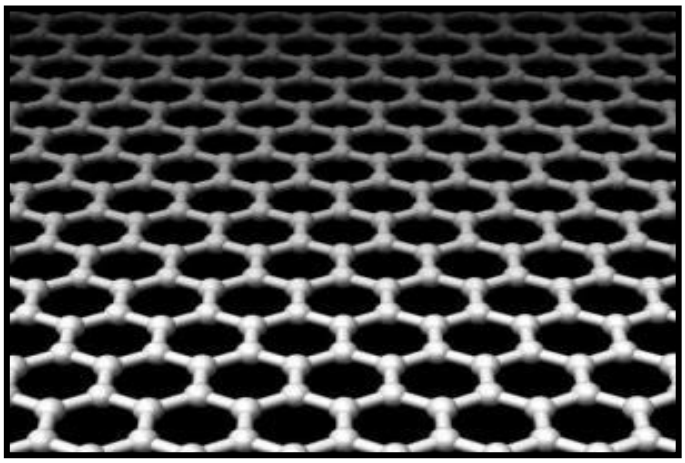

Figure 1.6: A sheet of graphene

1.7.2 Graphene Oxide (GO)

In light of the difficulties and cost of manufacturing graphene, great effort is made to make graphene derivatives or related materials which are effective and inexpensive. An example of such a material would be graphene oxide (GO), which formed through the powerful oxidation of graphite. This is an abundant and cheap material. Carbon-containing groups are infused into graphene oxide, an oxidised form of graphene. As a dispersible material, graphene can be processed easily with water (and other solvents). There are processes that can enhance graphene oxide's properties, but it is not an excellent conductor. Most commonly, it is sold as a powder, dispersed, or as a coating on substrates[38].

1.7.3 Uses of Graphene Oxide (GO)

A graphene oxide film, which can be converted to a conductor, can be deposited on nearly any substrate. The transparency of transparent conductive films makes GO especially suitable for use in electronic devices, solar cells, chemical sensors, and many other applications. Even GO has been studied as a replacement for tin-oxide (ITO) in batteries and touch screens[41]. GO can be used for solar cells, batteries, and capacitors due to its large surface area and the heat it dissipates, because GO can be produced more cheaply and easily than graphene, it may be available at a faster rate and can be used more quickly.

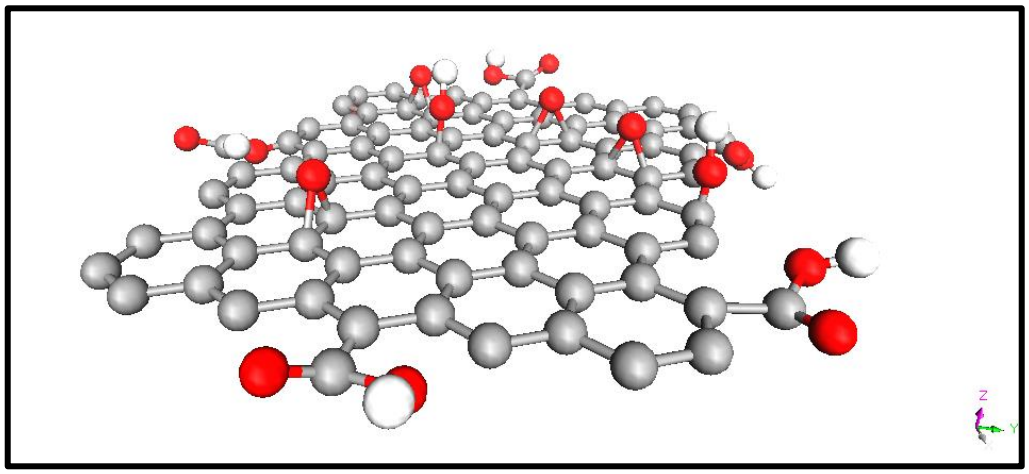

Figure 1.7: Atomic structure of graphene oxide (GO)

1.8 Catalysis

Chemistry describes catalysis as modifying the rate of a chemical reaction by adding a material that is not expended in the reaction. Chemical reaction rates, or velocities, are determined by many factors, including the chemical composition of the reacting species and the external conditions to which they are exposed.

Thousands of chemical protocols are based on catalysis, ranging from academic research in laboratories to the chemical industry. A chemical transformation cannot take place without catalysis. Several chemical protocols are based on catalysis. In addition to lowering temperatures and reducing reagent waste, using catalytic reagents allows a reaction to be more selective, avoiding unwanted by products for a more environmentally friendly solution. Green chemistry is the philosophy of reducing or eliminating chemicals, and the chemical processes that have negative environmentally impacts by following twelve guidelines Anastas and Warner[42] recommended in 1998. Green chemistry is largely concerned with developing ideal catalysts. These principles suggest that stoichiometric reagents are

inferior to catalytic reagents (as selective as possible). Stoichiometric reagents work only once but catalytic reagents can rework a reaction repeatedly. Working like nature is at the heart of green chemistry. Micro-organisms and/or enzymes were designed by nature to carry out environmentally benign reactions.

Many products, such as medicines, fine chemicals, polymers, fibres, fuels, paints, and lubricants, would be impossible to produce without a catalyst. Chemical transformations are facilitated by catalysis, making it possible to create commercially viable materials through chemical reactions. Utilising catalysts can therefore be used to make manufacturing more economic, environmentally friendly and sustainable[43]. Industrial applications are found more often for softer substances such as zeolites, phase transfer catalysts, e.g., crown ethers, as opposed to heavy metal catalysts, which are not usually recoverable.

Enzymatic catalysis is the most efficient and environmentally friendly type of catalysis among the three types of well-known catalysis such as homogeneous, heterogeneous and enzymatic. There are advantages and disadvantages to homogeneous and heterogeneous catalysis, which is why a new catalyst is urgently needed. In catalysis is active like homogeneous catalysis, but is also easy to recover like heterogeneous catalysis[44]. In contrast to homogeneous and heterogeneous catalysts, nanocatalysts have a number of benefits. A nano-catalytic system reduces the chemical reaction time, increases the yield, and allows easier separation and recovery of the catalyst. Any catalyst that is acceptable for green chemical manufacturing processes must allow for catalyst recovery from the process before being accepted for use. Nanoscale catalysts have a large surface area, which results in a dramatic increase in the amount of reactions taking place between the catalyst and the reactants (similar to homogeneous catalysis). Catalysts are insoluble in reaction solvents, so that they separate easily from the reaction mixtures (similar to heterogeneous catalysis)[45-49].

It is important because many industrial processes rely on catalysis for completion, and fundamentally, life as know it would be impossible to imagine without the biological catalysts known as enzymes. Theoretically, catalysis is very intriguing because it illustrates the basic nature of chemical reactions, practically, catalysis is important because many industrial processes functioned effectively as catalysts.

1.8.1 Nano-Catalysis

Since the beginning of nanoparticle development, nanocatalysis has been among the most pioneering applications. Nanocatalysts have been derived from a variety of substances, including aluminium, iron, TiO_2, silica and clay. The remarkable catalytic properties of nanoparticles are still not sufficiently

explained. Nanoparticles have a large active surface area, which directly affects their reaction rate. In addition, this may explain its catalytic properties. Nanoscale materials also have properties based on their structure and shape that can influence their catalytic activity in addition to their configuration (bi-metallic, core-shell, or supported), size and shapes. These parametres have enabled more selective nanocatalysts to achieve greater conversion rates. It is necessary to examine how nanoparticles' physical properties influence their catalysis, as well as how fabrication parametres affect them. Scientists can engineer nanocatalysts with high activity, high selectivity, and high resistance by better understanding these three phenomena. These benefits enable industrialised chemical reactions to consume less energy, produce less waste, and reduce resource consumption and energy consumption, hence reducing negative environmental impacts[50-54]. Nanoparticles are known to be significant industrial catalysts for the production of chemicals and energy conversion and storage. Nanoparticles differ from bulk catalysis because of their heterogeneity and variances in size and shapes. These differences result in varying and particle-specific catalysis. Analysing the intrinsic properties of nanomaterials is essential to understanding the concept of nanocatalysis (Figure 1.8)[55-59]. Catalytic nanomaterials are characterised by their intrinsic properties as follows:

a) Nanostructured solids undergo densification and surface relaxation as the lattice contractures; mean lattice constant, atomic density, and binding energy are all directly linked to bond length.
b) Cohesive energy is crucial for atomic dislocation, diffusion, and chemical reactions in nano-solids, and it is crucial for the growth of self-organising nanostructures, thermal stability, coulomb blockade, critical temperatures for phase transitions, and the melting of a nano-solid.
c) Band structures, including band gap, core level energy, photo-absorption and emission that are affected by binding energy density in the relaxed continuum region.
d) An atomic cohesive energy and binding energy density are two

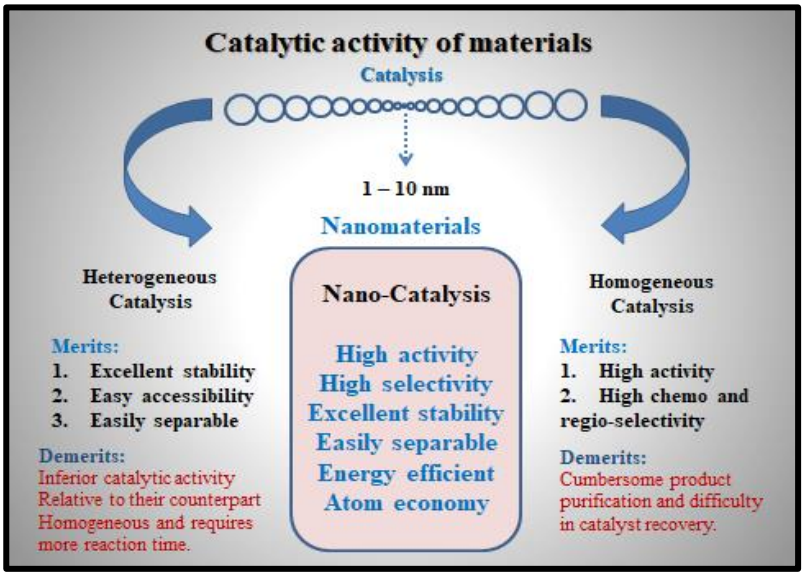

Figure 1.8: The comparative efficiency of heterogeneous, homogeneous and nano-catalysis

essential characteristics of nano-solids such as mechanical strength, Young's modulus, surface energy, surface stress, extensibility and compressibility[60].

There are a number of ways in which catalysis could be classified, but in common there are two types of catalysis:

(a) Heterogeneous Catalysis and

(b) Homogenous Catalysis.

1.8.2 Heterogeneous Catalysis

These heterogeneous catalytic reactions include reactions between gases and liquids and reactions among solid catalysts. It is known that many catalytic reactions do not occur in the same matter state as the catalyst and reactant, those are known as heterogeneous catalysis. Surfaces are prepared by increasing a large area per unit of a catalyst since reaction takes place at the surface, in modern heterogeneous catalytic treatments, all the metals, metal gauzes, incorporated metals, and metal films are used or converted to oxide, sulphide, or halide species.

1.8.2.1 Electrocatalysts

The electrode reactions that make up a fuel cell are accelerated by the use of metal-containing catalysts in electrochemistry, more precisely in fuel cell engineering. An electrocatalyst for fuel cells that uses nanoparticles of platinum or carbon particles is commonly used. If it is in contact with one of the electrodes in a fuel cell, platinum increases the amount of oxygen that is reduced into water, hydroxide, or hydrogen peroxide.

Energy conversion and storage devices, such as fuel and electrolysis cells, have been key drivers of electrocatalysis development over the last few decades. It has been determined that hydrogen electrode reactions (HER and HOR) are the most studied electrode reactions. Oxygen evolution (OER) and oxygen reduction (ORR) are also studied, as is the carbon oxidation reaction (CO_2R) on electrodes containing carbon, as well as the oxidation of a variety of organic and inorganic fuels (methanol, ethanol, etc.) in acid and base media[61].

1.8.3 Homogenous Catalysis

The lead chamber process is an example of homogeneous catalysis, where the catalyst and the reactants are gases, as a catalyst for oxidising sulphur dioxide. When the catalyst and reactants occur in a single state of matter, usually gas or liquid, the reactions are classified as homogeneous catalysis.

1.8.3.1 Organocatalysis

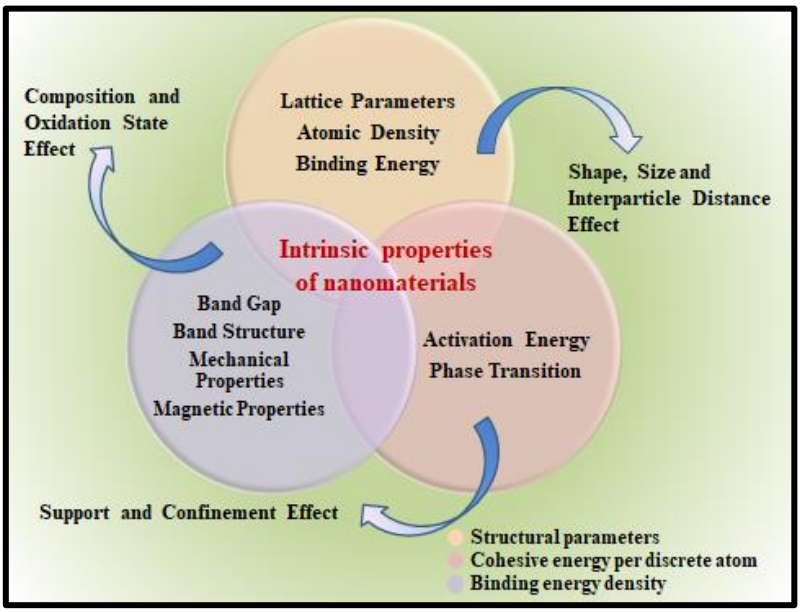

Figure 1.9: A study of the catalytic activity of nanomaterials based on their intrinsic properties

In the study of catalysis, transition metals are sometimes the focus. Many enzymes lacking transition metals also show catalytic properties when containing small organic molecules without metals. It tends to be more difficult to source organic catalysts in bulk, but they are often more affordable than transition metal catalysts because of their loading (amount of catalyst per unit amount of material reacting), expressed in moles percent. It used to be considered that organocatalysts were the "new generation" of catalysts, and they were competitive with traditional metal (-ion)-containing catalysts. An organic catalyst is deemed to function similarly to metal-free enzymes by using for instance, hydrogen bonding as a noncovalent interaction. Organisms perform catalysis through both covalent (e.g., proline) and noncovalent (e.g., thiourea) catalysts whose interactions and bindings with their substrates are different[62].

1.8.3.2 Enzymes and Biocatalysts

Catalysts for metabolism and catabolism are enzymes in biology. There are several types of biocatalysts, most of which are enzymes, but ribozymes and synthetic deoxyribozymes also possess catalytic properties. While technically, soluble enzymes act as homogeneous catalysts, membrane-bound enzymes perform heterogeneously. Despite this, biocatalysts lie on the border between the two types of catalyst. The temperature, pH, enzyme, substrate, and product concentrations are all factors that affect enzyme (and other catalysts) activity. Enzymatic reactions require water as an essential reagent. In addition to being a bond-forming reaction product, myoglobin is also a bond-breaking reaction reactant[63].

In biocatalysis, enzymes are used to produce high-fructose corn syrup and acrylamide. A monoclonal antibody can serve as a weak catalyst by lowering the activation energy of the chemical reaction when

bound to a stable molecule of the transition state of a chemical reaction. "Abzymes" are sometimes used as a name for such catalytic antibodies[64].

1.8.3.3 Photocatalysis

Photocatalysts use visible and UV light to promote their excited state, it reverts to its ground state without being consumed after intersystem crossing with the starting material. If direct illumination is applied to the starting material, it is likely to undergo reactions that are not normal. A common example of this is the production of singlet oxygen via photocatalysis. Solar cells containing dye-sensitised catalysts are also known as photocatalysts.

A photocatalyst is a substance that changes the rate of chemical reactions when exposed to light, and this process is referred to as photocatalysis. Photocatalysts are light and chemically reactive materials that change the rate of chemical reactions in their presence. As a result, they change the rate of chemical reactions in their presence by changing the rate of photon absorption, and by doing so, they change the rate of chemical reaction. Photocatalysis occurs when semiconductors absorb light and create electron-hole pairs as catalysts. Semiconductors become photocatalysts when exposed to light. As a result of photocatalysis, electrons are released because of holes created in semiconductors.

It is a light-sensitive catalyst that accelerates a reaction. Most commonly, a semiconductor is used for the catalyst. In the conduction band (CB) and valence band (VB), the catalyst reacts with light having sufficient energy (or with a given wavelength).

$$Catalyst + h\nu = h_{VB}^{+} + e_{CB}^{-} \qquad (1.1)$$

Photocatalysis generates electrons and holes in the same manner, as shown in Figure 1.10.

1.8.3.3.1 Reaction Mechanism of Photocatalysis

The photocatalytic response is defined as one involving light and some substance, either a catalyst or a catalyst precursor that influences the reaction in some way. The term photocatalysis can be used to refer to any process requiring light and substances. A parameter which is acceptable and attainable must be used to prove that the reaction is catalytic. The reaction can be classified as oxidative photocatalysis or dehydrogenative photocatalysis after titanium dioxide has served as a catalyst.

The photocatalyst will produce electrons and holes when it absorbs visible light (sunlight) or ultraviolet light (fluorescent lamps). As a catalyst is illuminated by light, the electron in its valence band is excited. The electron is driven into the conduction band of the catalyst by the excess energy of the

excited electron. Negative electrons (e^-) and positive holes (h^+) are formed in this way. A semiconductor's 'photo-excitation state' is often referred to as this stage. 'Band Gaps' or energy differences between the conduction and valence bands are a property of semiconductors. In order to photo-excite materials, the required wavelength for light is 1240 (Planck's constant, h)/E_g (Energy band gap).

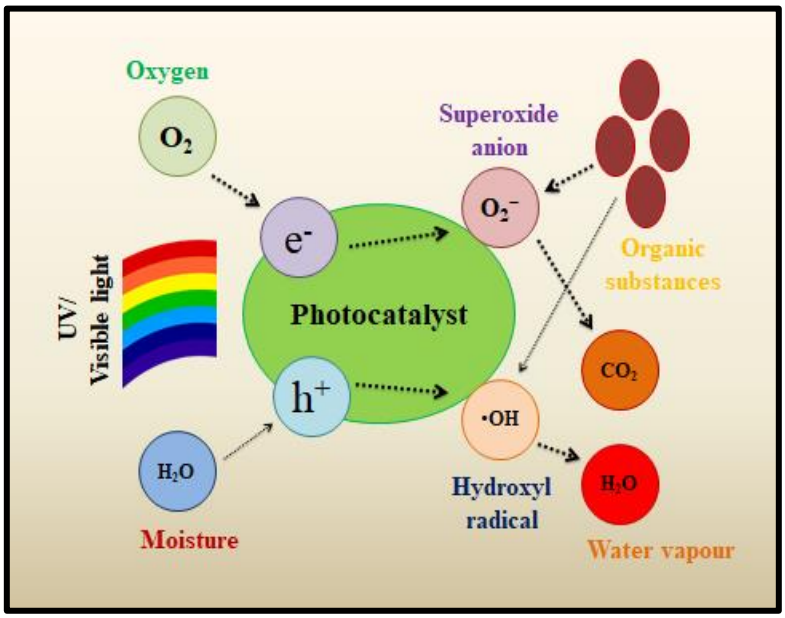

Figure 1.10: Schematic diagram of Photocatalysis mechanism

Electrons and holes present on the catalysis surface react with oxygen and water absorbed onto the surface to form reactive oxygen species (ROS) that can affect the photocatalytic oxidation reaction. According to the above reactions, the ROS (•OH, $•O_2^-$, •OOH) produced in the photocatalysis reaction further reacts with pollutants to oxidise them to CO_2 and water via a few intermediate steps.

$$e_{CB}^- + h_{VB}^+ \rightarrow h\nu \quad (1.2)$$

$$H_2O + h_{VB}^+ \rightarrow \bullet OH + H^+ \quad (1.3)$$

$$O_2 + e_{CB}^- \rightarrow \bullet O_2^- \quad (1.4)$$

$$OH + pollutant \rightarrow H_2O + CO_2 \quad (1.5)$$

$$\bullet O_2^- + H^+ \rightarrow \bullet OOH \quad (1.6)$$

$$\bullet OOH + \bullet OOH \rightarrow H_2O_2 + O_2 \quad (1.7)$$

$$\bullet O_2 + pollutant \rightarrow CO + H_2O \quad (1.8)$$

$$\bullet OOH + pollutant \rightarrow CO_2 + H_2O \quad (1.9)$$

During a photochemical reaction, a catalyst will neither change nor become a by-product. One way to define photosensitisation is by saying that it is the result of photochemical changes occurring within molecular entities of one type after radiation is absorbed by another molecular entity, termed the photosensitizer. Photochemicals such as chlorophyll are involved in photosynthesis. A photocatalyst,

light, and water are necessary for photocatalysis instead of photosynthesis, which converts H_2O and CO_2 into O_2 and $C_6H_{12}O_6$.

$$Dye_{(ads)} + h\nu \rightarrow Dye^{*}_{(ads)} \quad (1.10)$$

$$Dye^{*}_{(ads)} + Catalyst \rightarrow Catalyst(e^{-}_{CB}) + Dye^{+\bullet}_{(ads)} \quad (1.11)$$

$$\bullet OH + Dye_{(ads)} \rightarrow CO_2 + H_2O \quad (1.12)$$

$$Dye^{+\bullet}_{(ads)} + \bullet OH/\bullet O_2^{-} \rightarrow CO_2 + H_2O \quad (1.13)$$

The development of visible-light-responsive photocatalysis for H_2 production, organic dye sensitisation has been considered to be an effective method because it allows tunable HOMO and LUMO states. It is low-cost, and it offers a broad range of possibilities. Catalysts for producing H_2 have up to now been sensitised by a variety of organic dyes[65].

1.8.3.3.2 Photocatalyst or Photocatalytic Material

Photocatalysis is being used for a range of industrial as well as biological applications, including the production of gases (O_2, H_2, etc.) and the purification of the environment. The use of photocatalysis to purify our environment is currently being studied in several research studies. A photocatalytic material capable of degrading environmental contaminants has been searched for by researchers. There have been a number of materials reviewed, but bismuth oxyhalide (Chloride, Bromide and Iodide) has gained attention.

1.8.3.3.3 Importance of Photocatalyst on Environment

A number of industrial and biological applications can be achieved through photocatalysis. However, it can also be used for a number of environmental processes, including the degradation of dyes, pesticides, herbicides, and phenols. A photocatalyst that can degrade the environmental pollutant must therefore be able to perform a photocatalysis reaction, and many studies on various photocatalysts have been conducted, such as TiO_2, ZnO, bismuth oxyhalides, bismuth based materials, etc. The important applications of photocatalysts are self-cleaning surface, self-cleaning photocatalytic surfaces, super hydrophilic surfaces, air purification, destruction of warfare agents, hydrogen production by water cleavage, etc.

1.8.3.3.4 Bismuth Oxyhalide as a Photocatalytic Material

The term photocatalysis refers to the process of decomposing materials with visible or ultraviolet light, so bismuth oxyhalide has been reported to decompose RhB, MO, MB, EB, etc. dyes under the visible

or UV light, indicating it has photocatalytic properties. Moreover, many research papers have been published in which the enhanced photocatalytic properties of bismuth oxyhalides. There have been many developments of experimental methods which have been able to optimise its photocatalytic performance in both the visible and ultraviolet ranges.

1.9 Aims and Objectives

The purpose of this thesis is to investigate and characterise bismuth oxyhalides and bismuth-based composites with different morphologies for energy related application and photocatalysis. Additionally, different synthesis methods will be developed for making nanostructures from these materials. This thesis reports on the catalytic activity and water remediation applications of these inorganic halide nanomaterials. The following are the primary aims and objectives of the thesis:

a) To develop a two-step synthesis procedure involving chemical treatment followed by hydrothermal technique. The development of a nanocomposite bismuth oxychloride-graphene oxide (BOC-GO) material, based on bismuth oxychloride (BiOCl) and graphene oxide (GO). Synthesis of graphene oxide (GO) by modified Hummer's method will be performed for making composite.
b) To synthesise pure bismuth oxychloride (BiOCl) nanomaterial with different morphology by different chemical routes like hydrothermal and heating methods.
c) To study the electrochemical water-splitting (HER) related applications by synthesised pure materials (BiOCl).
d) To study photocatalytic activity by the materials under visible and UV light irradiations.
e) To study the dye-sensitised catalysis application by pure material (BiOCl) in presence of visible light.
f) To study different types of dye degradation and wastewater remediation applications.
g) To understand the various physical processes associated with different properties of the studied nanomaterials and to develop simple models for understanding the same.

References

[1] C. Binns, *John Wiley & Sons*, 14, 2021.
[2] S.L. Brock, *Imperial College Press (London)*, 2004, ISBN 1-86094-415-9.
[3] T. Hendrickson, S. Galley and F. Lamb, *Engineering and Science*, 29(2), 1965, 10-12.
[4] N. Taniguchi, *Proceedings of the International Conference of Production Engineering (Japan Society of Precision Engineering)*, 1974, 8-23.
[5] G. Binning, H. Rohrer, C. Gerber and E. Weibel, *Physical Review Letters*, 49, 1982, 57.

[6] R.E. Smalley, *Reviews of Modern Physics*, 69(3), 1997, 723.
[7] K.E. Drexler, *Oxford University Press, Oxford (New York: Anchor Books)*, 1986.
[8] K.E. Drexler, C. Peterson and G. Pergamit, *William Morrow and Company. Inc.(New York, NY, USA)*, 1991.
[9] K.E. Drexler, *John Wiley & Sons, Inc. (New York)*, 1992.
[10] S. Iijima, *Nature*, 354(6348), 1991, 56-58.
[11] L.K. Harris and J.A. Theriot, *Trends in microbiology*, 26(10), 2018, 815-832.
[12] D. Vollath, *Environmental Engineering and Management Journal*, 7(6), 2008, 865-870.
[13] A. Tadjarodi, O. Akhavan, K. Bijanzad and M.M. Khiavi, *Monatshefte für Chemie-Chemical Monthly*, 147, 2016, 685-696.
[14] D. Sánchez-Rodríguez, M.G.M. Medrano, H. Remita and V. Escobar-Barrios, *Journal of environmental chemical engineering*, 6(2), 2018, 1601-1612.
[15] J. Xie, Y. Cao, D. Jia, H. Qin and Z. Liang, *Catalysis Communications*, 69, 2015, 34-38.
[16] D.S. Kim and N.M. Hwang, *Journal of Physics D: Applied Physics*, 51(46), 2018, 463002.
[17] H.A. Le, S. Chin and J. Jurng, *Powder Technology*, 225, 2012, 167-175.
[18] L. Chen, R. Huang, M. Xiong, Q. Yuan, J. He, J. Jia, M.Y. Yao, S.L. Luo, C.T. Au and S.F. Yin, *Inorganic Chemistry*, 52(19), 2013, 11118-11125.
[19] K. Zhang, J. Liang, S. Wang, J. Liu, K. Ren, X. Zheng, H. Luo, Y. Peng, X. Zou, X. Bo and J. Li, *Crystal Growth & Design*, 12(2), 2012, 793-803.
[20] L. Ye, J. Liu, C. Gong, L. Tian, T. Peng and L. Zan, *ACS Catalysis*, 2(8), 2012, 1677-1683.
[21] X. Zhang, X.B. Wang, L.W. Wang, W.K. Wang, L.L. Long, W.W. Li and H.Q. Yu, *ACS Applied Materials & Interfaces*, 6(10), 2014, 7766-7772.
[22] F. Tian, J. Xiong, H. Zhao, Y. Liu, S. Xiao and R. Chen, *CrystEngComm*, 16(20), 2014, 4298-4305.
[23] A. Dash, S. Sarkar, V.N. Adusumalli and V. Mahalingam, *Langmuir*, 30(5), 2014, 1401-1409.
[24] R. Sarkar, D. Das, B. Das, S. Sarkar and K.K. Chattopadhyay, *AIP Conference Proceedings*, 2220, 2020, 020030.
[25] M.A. Gatoo, S. Naseem, M.Y. Arfat, A. Mahmood Dar, K. Qasim and S. Zubair, *BioMed Research International*, 2014, 2014, 1-8.
[26] M.D. Newton, *Electron Transfer in Chemistry*, 2001, 2-63.
[27] A. Jager-Waldau, *Solar Energy Materials and Solar Cells*, 95(6), 2011, 1509-1517.
[28] K. Aryal, B.N. Pantha, J. Li, J.Y. Lin and H.X. Jiang, *Applied Physics Letters*, 96(5), 2010, 052110.
[29] L.P. Oleksenko, N.P. Maksymovych, E.V. Sokovykh, I.P. Matushko, A.I. Buvailo and N. Dollahon, *Sensors and Actuators B: Chemical*, 196, 2014, 298-305.
[30] A. Ohtomo, M. Kawasaki, T. Koida, K. Masubuchi, H. Koinuma, Y. Sakurai, Y. Yoshida, T. Yasuda and Y. Segawa, *Applied Physics Letters*, 72(19), 1998, 2466-2468.
[31] R. Abe, K. Sayama and H. Sugihara, *The Journal of Physical Chemistry B*, 109(33), 2005, 16052-16061.
[32] J. Li, Y. Yu and L. Zhang, *Nanoscale*, 6(15), 2014, 8473-8488.
[33] M.A. Gondal, C. Xiaofeng and M.A. Dastageer, *Springer India*, 2017.
[34] Z. Wang, M. Chen, D. Huang, G. Zeng, P. Xu, C. Zhou, C. Lai, H. Wang, M. Cheng and W. Wang, *Chemical Engineering Journal*, 374, 2019, 1025-1045.
[35] L. Armelao, G. Bottaro, C. Maccato and E. Tondello, *Dalton Transactions*, 41(18), 2012, 5480-5485.
[36] Z. Song, D. Xuelin, W. Nan, Z. Lihua, L. Zhihong, F. Jindong and X. Caihua, *Chemical Engineering Journal*, 317, 2017, 925-934.

[37] J. Henle, P. Simon, A. Frenzel, S. Scholz and S. Kaskel, *Chemistry of Materials*, 19(3), 2007, 366-373.
[38] C. Yang, F. Li, M. Zhang, T. Li and W. Cao, *Journal of Molecular Catalysis A: Chemical*, 423, 2016, 1-11.
[39] Y. Liu, G. Zhu, J. Gao, M. Hojamberdiev, H. Lu, R. Zhu, X. Wei and P. Liu, *Journal of Alloys and Compounds*, 688, 2016, 487-496.
[40] H. Tang, Y. Ao, P. Wang and C. Wang, *Materials Science in Semiconductor Processing*, 27, 2014, 909-914.
[41] R. Sarkar, D. Das, K. Chanda, B. Das, S. Sarkar and K.K. Chattopadhyay, *Materials Chemistry and Physics*, 279, 2022, 125796.
[42] P.T. Anastas and J.C. Warner, *Green chemistry: Theory and Practice*, 29, 1998.
[43] V. Polshettiwar and R.S. Varma, *Green Chemistry*, 12(5), 2010, 743-754.
[44] M.B. Gawande, P.S. Branco and R.S. Varma, *Chemical Society Reviews*, 42(8), 2013, 3371-3393.
[45] S.G. Babu and R. Karvembu, *Catalysis Surveys from Asia*, 17(3), 2013, 156-176.
[46] P.K. Tandon and S.B. Singh, *Journal of Catalyst and Catalysis*, 1, 2014, 21-34.
[47] K. Yan, G. Wu, T. Lafleur and C. Jarvis, *Renewable and Sustainable Energy Reviews*, 38, 2014, 663-676.
[48] K. Yan, G. Wu, C. Jarvis, J. Wen and A. Chen, *Applied Catalysis B: Environmental*, 148, 2014, 281-287.
[49] H. Luo, H. Jiang, T. Klande, Z. Cao, F. Liang, H. Wang and J. Caro, *Chemistry of Materials*, 24(11), 2012, 2148-2154.
[50] K. Yan, T. Lafleur and J. Liao, *Journal of Nanoparticle Research*, 15(9), 2013, 1-7.
[51] Y. Qiao, H. Li, L. Hua, L. Orzechowski, K. Yan, B. Feng, Z. Pan, N. Theyssen, W. Leitner and Z. Hou, *ChemPlusChem*, 77(12), 2012, 1128-1138.
[52] K. Yan, C. Jarvis, T. Lafleur, Y. Qiao and X. Xie, *RSC Advances*, 3(48), 2013, 25865-25871.
[53] Z. Cao, H. Jiang, H. Luo, S. Baumann, W.A. Meulenberg, H. Voss and J. Caro, *Catalysis Today*, 193(1), 2012, 2-7.
[54] K. Yan, T. Lafleur, G. Wu, J. Liao, C. Ceng and X. Xie, *Applied Catalysis A: General*, 468, 2013, 52-58.
[55] K. Yan, G. Wu, J. Wen and A. Chen, *Catalysis Communications*, 34, 2013, 58-63.
[56] S.L. Candelaria, Y. Shao, W. Zhou, X. Li, J. Xiao, J.G. Zhang, Y. Wang, J. Liu, J. Li and G. Cao, *Nano Energy*, 1(2), 2012, 195-220.
[57] K. Yan and A. Chen, *Energy*, 58, 2013, 357-363.
[58] H. Luo, T. Klimczuk, L. Müchler, L. Schoop, D. Hirai, M.K. Fuccillo, C. Felser and R.J. Cava, *Physical Review B*, 87(21), 2013, 214510.
[59] K. Yan, T. Lafleur, C. Jarvis and G. Wu, *Journal of cleaner production*, 72, 2014, 230-232.
[60] B.R. Cuenya, *Thin Solid Films*, 518(12), 2010, 3127-3150.
[61] E.R. Savinova and A.G. Oshchepkov, *Comprehensive Inorganic Chemistry III (Third Edition)*, 2023, 492-550.
[62] "The Nobel Prize in Chemistry 2021". NobelPrize.org.
[63] D.C. Nelson and M.A. Cox, *Worth Publisher, New York*, 16, 2000, 567-597.
[64] Catalytic Antibodies Simply Explained. Retrieved on 2015-11-11.
[65] F. Deng, J.P. Zou, L.N. Zhao, G. Zhou, X.B. Luo and S.L. Luo, *Nanomaterials for the removal of pollutants and resource reutilization* (Elsevier), 2019, 59-82.
[66] http://nanopinion.en/sites/default/files/observatorynano_briefing_no.10_applications_for_photocatalysts.

Chapter 2

Review of Past Work

2.1 General Idea

It has already been discussed that bismuth oxyhalide is a very significant photocatalytic material, which has been used for water purification, solar cells, and batteries. So it has become a very essential topic in the scientific community and many studies have been conducted to improve its photocatalytic behaviour and semiconductor properties, as well as its band gap energy. It was briefly emphasised that the synthesis technique, characterization and applications of bismuth oxyhalide had been examined, but here looking at some additional past work in much greater detail. The papers were reviewed and elaborated on the progress that took place in this regard, and also seen what research going on and what new applications had been discovered which will clear our perception for this material. Several studies have been conducted on the different types of synthesis methods used which optimise the structural, morphological and properties of bismuth oxyhalide. Since bismuth oxyhalide has excellent properties in UV irradiation range and limited properties in visible light range, so many studies have been performed to improve its photocatalytic behaviour in visible light and UV light range. Additionally, studies have examined how piezo-catalysis and photocatalysis can be combined to achieve high efficiency dye decomposition. In Ismail et al.'s work, bismuth oxychloride was synthesised and they combined it with piezo-catalysis to decompose dye dissolved in water. Similar to previous research, that will discuss many of these investigations[1].

2.2 Some Works on Traditional Bismuth Oxyhalide

Despite the unique layered structure of bismuth oxyhalide, the wide band gap makes it an inefficient photocatalyst. However, scientists have conducted several studies to modify the semiconductor to enhance the absorption of light for a wide variety of applications. Generally, this involves doping bismuth oxyhalide with metallic and non-metallic elements, as well as combining it with other materials so that heterostructure composites can be formed and introducing oxygen vacancies (OVs) and other technologies short of using any other materials.

There are three factors that affect photocatalytic efficiency:

a) Light absorption,
b) Load sharing and
c) Photocatalytic reaction.

In addition, in these methods, bismuth oxyhalide is no longer available, resulting in reduced light absorption, separation efficiency, charge transfer, or increased active surface area, allowing the presence of many reaction sites and improving photocatalytic performance. Furthermore, in the

manufacturing process, morphology and structure are altered, affecting photocatalytic activity.

It is widely known that pure and modified bismuth oxychloride photocatalysts are effective at controlling pollution. While some advances have been made in the research of bismuth oxychloride and its derivatives and bismuth-based materials, some important and practical issues remain. As a first step, many studies have been conducted on organic pollutants, including dye toxins such as RhB, EB, MO, MB, etc. as well as antibiotics (e.g., tetracycline, penicillin). In contrast, few studies have taken into account heavy metals and determined organic toxins, both of which pose serious health risks to aquatic environments and humans. Secondly, the study of the removal of metal ions from pollutant water can be useful to study the purification of water from metal ions in the future. As a result, most of the work on bismuth oxyhalide is a one-time application. Although some synergistic methods have been researched with piezoelectric catalysis and photocatalysis, as well as with chemical-catalysis, synergistic Fenton decomposition, and synergistic effects of photocatalysis and ozonation, and it would be worthwhile to study other methods that utilise photo-degradation efficiency. In addition to recyclability, most modified bismuth oxyhalide materials have excellent stability and reusability, but the article fails to mention how bismuth oxyhalide works in addition to energy, but it will be worthwhile examining how bismuth oxyhalide is used in energy applications, for example hydrogen production, and other solar applications. It's currently unknown how sunlight will be used to initiate photocatalysis and how photocatalyst particles will be deposited on other materials for actual sewage treatment and recycling, and these factors are of great significance to how bismuth oxyhalide will be applied in environmental purification and energy consumption in the future, and some experiments will be necessary to study the mechanism of photocatalysis. By using theoretical calculations, here uncover the path of decomposition. As the technologies advance, it will be easier and cheaper to synthesise bismuth oxyhalide and the materials based on bismuth oxyhalide, and this will cause a lot of attention regarding the use of bismuth oxyhalide. Bismuth oxyhalide based materials for decomposing organic pollutants in actual wastewater treatment[2].

In sum, the following aspects can be highlighted for a highly efficient device that can be designed and fabricated with bismuth oxyhalide photo-catalysts by controlling morphological structure, tuning of internal electric field, and modification of surface. Following are some past work on control of morphological structure, tuning of internal electric field, and surface modification.

2.2.1 Morphological Control

In addition to their specific properties, morphology also affects the specific properties of materials. In

fact, other research has been done that suggests Bi_5O_7I is able to degrade pollutants and activate molecular oxygen based on its shape and its surface structure. As well as 2D nanosheets, hollow structures made of 3D materials have the advantage of improving light absorption through multiple reflections. Though bismuth oxyhalide hollow structures are rarely mentioned today, this material is a good alternative to 2D nanosheets. By using a template method of synthesis coupled with a solid support device, which is the most commonly used method for the manufacturing of hollow or core-shell structural photocatalysts. In addition, the type of reagent will also contribute to the product's shape. Using materials with approximately functional organic ligand alignment can aid in forming photocatalysts that have certain shapes. It can be utilised to prepare some organic halides and photocatalysts.

2.2.2 Tuning of Internal Electric Field

Bismuth oxyhalides photocatalytic activity can be increased by adjusting the electric field within the layers. This can result in improved separation of media. Throughout layered bismuth oxyhalide, the internal electric fields efficiently separate and transfer charge.

The principle of conservation of charge, bismuth, can be replaced by some strange thinking elements in order to increase the electrostatic potential difference between the $[Bi_xO_y]$ and $[X_z]$ layers and make the internal electric field stronger. A semiconductor photocatalyst can alter its atomic environment with impurity doping by creating localised electronic states in the band gap. Development of a model for precise doping of $Bi_xO_yX_z$ is necessary to improve the internal electric field since it shows that the non-bonding interactions are weaker between X [Cl, Br & I] than between Bi and O, that means nonmetallic doping $Bi_xO_yX_z$ tends to replace Cl. An initial hydrothermal carbonization and subsequent heat treatment led to a significant improvement in the internal electric field of Bi_3O_4Cl nanosheets[3].

In addition, the electronic structure of $Bi_xO_yX_z$ can affect the nanosheet thickness, and theoretical calculations indicate that the distance between the exposed areas increases with decreased thickness. The increase in interplanar spacing between the crystals results in more space for the polarisation of the orbital and bound atoms, and this enables a large difference in the charge density between the plates. As a consequence, delamination or intercalation can be used to manufacture ultra-thin sheets for laminate materials with a larger $Bi_xO_yX_z$ internal electric field. The $Bi_xO_yX_z$ internal electric field can be increased. Additionally, solvents and surfactants can also influence the thickness of 2D glasses. The viscosity of the solvent has been shown to affect the thickness of bi-oxygen nanosheets in certain experiments in the [001] direction. It was suggested that this might impact the ion diffraction

efficiency.

The internal electric field runs in a certain direction, so its vertical component also makes it possible for photogenerated electrons and holes to be separated spatially, which is conducive to oxidation and reduction reactions. This vertical direction can also be achieved by combining the same $Bi_xO_yX_z$ with different aspects of exposure in order to produce a heterojunction at the interface between the two $Bi_xO_yX_z$ photocatalysts and the vertical direction of the internal electric field.

2.2.3 Surface Modification

As part of the reaction process, the surface properties of the catalyst are critical in photocatalysis. Oxygen molecules on the surface, modification of functional groups, and co-catalysts alter the surface reaction environment and make it more potent.

A factor affecting the physical and chemical properties of nanomaterials is the presence of defects due to their layered structure and low formation. $Bi_xO_yX_z$ under the influence of external force can form oxygen vacancies relatively readily, enhancing its photoreactivity and allowing extended reaction times. According to the above photocatalytic activity, Bi_5O_7Br with oxygen vacancies exhibits significantly better performance in fixing N_2. There are few studies that have evaluated the photoreactivity of $Bi_xO_yX_z$ with oxygen vacancies. Therefore, here investigate the photoreactivity of other $Bi_xO_yX_z$ with oxygen vacancies. The oxygen vacancy is usually produced by exposure to ultraviolet rays that emit oxygen atoms, or by the interaction between reducing solvents or surface atmospheres (H_2, NH_3, etc.). The interaction between the carboxylate anion and Bi^{3+} can also be used to promote the release of oxygen from the surface, thereby destabilising the Bi_2O bond and leaving the oxygen vacancy on the surface.

Various organic modifications of $Bi_xO_yX_z$ surfaces can capture electrons and selectively adsorb substrates for greater photocatalytic performance, corresponding to the fact that conductive polymers show a high stability and charge carriers. Recently, certain organic modifications on the surface of $Bi_xO_yX_z$ have been utilised as photocatalysts. In photocatalytic materials, a polymer must be conductive and permit the movement of electrons in certain directions, so polyaniline, polypyrrole, polythiophene and other conjugated polyene will be good candidates in the role of electron capture agents.

In recent years, conductive polymers have attracted a lot of interest because they are highly stable and charge carriers. In addition, they can selectively adsorb substrates and capture electrons for better performance. In photocatalytic materials, the electron capture agents must be conductive polymers that

enable electrons to move freely. This role is expected to be suited for conjugated polyene such as polyaniline, polypyrrole, polythiophene, and others with a conjugated structural arrangement.

Catalyst supports act as charge trapping sites, thus contributing to photocatalytic activity. The photogenerated promoter derivatives (PbO_2, MnO_x, IrO_x, CoO_x, NiO) which are directly deposited on semiconductor photocatalysts (MoS_2, Ni) can improve the efficiency of reduction and oxidation reactions through space selective charging.

The preparation of bismuth oxyhalide photocatalyst has also been plagued with difficulties. In order to create pure bismuth oxyhalide, complicated formulas must be used. Hydrothermal alkalinization and thermal calcination are only the two most popular methods of preparing it. Another unique photocatalyst, $Bi_xO_yX_z$ is triggered by a slight change in pH or temperature. Additionally, only $Bi_4O_5X_2$ (X = Br and I) has been synthesised using a molecular precursor approach, so a more efficient synthesis route needs to be investigated. This is the critical factor in developing $Bi_xO_yX_z$ photocatalysis. Solar fuel production is also an important use of photocatalyst. $Bi_xO_yX_z$ photocatalysts are used to produce solar fuel instead of BiOX to decompose organic pollutants. Water splitting, CO_2 conversion, and N_2 fixation are achieved through use of these devices. This is an impressive improvement. The use of $Bi_xO_yX_z$ photocatalyst for bacterial inactivation and organic material synthesis is uncommon, but these applications could be enhanced by this catalyst in the future. However, for a deeper understanding of the photocatalytic mechanism of $Bi_xO_yX_z$, it would be best to use sophisticated characterization techniques. A synchrotron beam can produce infrared spectroscopy in situ[4].

2.3 Properties and Characteristics of Bismuth Oxyhalide

There are two very important properties of bismuth oxyhalide that will be reviewed in this chapter, namely, photocatalytic and optical properties. Apart from these two properties, bismuth oxyhalide also has semiconductor properties, which will be reviewed in this chapter.

2.3.1 Optical Properties of Semiconductor

As a semiconductor, the valence band is occupied to full capacity and the conduction band is unoccupied. The energy band is in general what is created by the combination of many molecular orbitals to form a completely degenerate energy level. The solid materials have several energy bands, but the upper bands (conduction band and valence band) concern us. A molecule's outer orbitals, where electrons are less natural by their surroundings, form discrete energy levels. However, external electrons, which are also known as valence electrons, can only move to the upper edge of their valence

band before they must return to their atom of origin. Through thermal, optical, or electrical energy, electrons are transferred from the VB to CB. A semiconductor device's design is dependent on the band gap energy. Band gap energy is the energy difference between a valence band's and its conduction band's uppermost point.

In order to differentiate between direct and indirect band gap semiconductor materials, one has to consider their optical properties. For semiconductor materials with direct band gaps, electron momentum is the same at both the most VB and least CB levels. Higher or lower moments are found for electrons in the lower VB than electrons in the higher CB. This is because they are in indirect band gaps. During photon excitation, electron holes are created. Since electrons do not have to undergo a moment change in wide band gap semiconductors, this process is simplified. A photon's energy makes it necessary for electrons to undergo a substantial moment change in indirect band gap semiconductors. Electron-hole pairs are formed much faster in direct semiconductors because electrons and holes interact with both photons and phonons. In conventional semiconductors, electron-hole pairs are formed much slower since electrons, photons, and phonons interact with 3D materials. Indirect semiconductors have a broader band gap than direct semiconductors, which makes recombination easier when electron-hole pairs recombine to form photons.

2.3.2 Reflectance/Absorption Spectra of Bismuth Oxyhalide

Reflectance/Absorption spectroscopy and photoluminescence spectroscopy are two optical characterization techniques used to study semiconductor materials. Electronic band gap energy can be found out by using the former equation. A recombination process is determined by the lower energy of the excited photon, as long as the band gap energy of the semiconductor material is less than its energy. During absorption of the photon, after an electron leaves the valence band, it moves to the conduction band. The semiconductor is then left with two electron holes. This creates a charged hole within the VB. The photon passes through a band gap and at this wavelength (or photon energy), its energy equals that of the material's band gap.

It is called the diffuse reflection spectrum because light hitting the semiconductor (powder sample) will scatter in every direction, resulting in the determination of the band gap energy. A sphere collects the light that is reflected by the particles and directs it onto the detector because of the different shapes of the particles. A specular reflection is when the particles have a highly mirror-like surface, displaying the law of reflection directly. In diffuse reflection, the particles have a variety of shapes and orientations. Therefore, they reflect in a variety of directions, which is also reflected in the transmission

spectrum at wavelengths at which the particle has been abducted. The diffuse reflection signal is significantly lower than in the case of specular reflection.

In a reflection spectrum[5], it can be used to calculate the optical absorption spectrum near the edge of the band of bismuth oxyhalide. In BiOCl, BiOBr, and BiOI, these values correspond to white, light yellow and red colours, respectively. These mathematical equations describe the absorption at the band edge:

$$\alpha h\nu = A(h\nu - E_g)^n \qquad (2.1)$$

where,

$\alpha =$ Coefficient of absorption or reflectance,

$h\nu =$ Photonic energy,

$A =$ Proportionality constant and

$E_g =$ Energy band gap.

In addition, n varies according to the characteristics of semiconductors. In an indirect band gap[6] semiconductor known as BiOX, n equals 2. By plotting the straight portion of versus photon energy, the band gap energy (E_g) of BiOCl, BiOBr, and BiOI are approximated by using a tangent to the X-axis.

2.3.3 Photoluminescence Spectra of Bismuth Oxyhalide

Spectroscopy electronics is a useful tool to evaluate photoluminescence, as mentioned above, semiconductors have a variety of energy bands with different energy levels. The molecular and atomic energies necessary for the absorption and emission of UV-Vis light under appropriate conditions. When the energy of the photon of the excitation source exceeds the energy of the forbidden band, the excess energy is absorbed by the electrons in the VB. This leaves a gap with a positive charge in the VB. As a result, electrons migrate into the CB, causing a gap where light can be released as positive energy. This is the process of photoluminescence, which can be measured by using a photoluminescence spectrometer. This is the process of photoluminescence, which can be measured by using a photoluminescence spectrometer. Photogenerated excitons' lifetimes depend on many semiconductor properties, such as the lattice structure, concentration and type of impurities as well as crystallographic defects. Radiation processes other than exciton recombination contribute to the appearance of photoluminescence. These include band-to-band recombination, which occurs due to the attachment of excitons to donors, the attachment of electrons to acceptors, and the recombination of donor-acceptor pairs as well.

It is also possible for electrons and holes to transition within their energy levels as a result of Coulomb's attraction between electron and hole. The energy of this attraction is lower than that of the gap. As with other radiation processes, even with an exciton attached to a donor, acceptor, or a pair of donors and acceptors, other radiation processing can also be done. There are usually no obvious defects present in the sample of non-equilibrium carriers, which affect the lifetimes and concentrations of nonequilibrium holes and electrons[7].

Under a 364 nm excitation wavelength, the BiOCl nanoplate colloidal solution shows a strong blue photoluminescence, and the same is true under a 365 nm UF lamp reported by Deng et al. Comparing the experimental data with a standard sample, it is estimated that the photoluminescence quantum yield is roughly equal to 0.04. Additionally, they estimate that the decay curve at room temperature and time is estimated to be a bi-exponential function of the QDs with an emission at 455 nm, and average decay times are found around 6.7 ns. A fast part of the calculation lasts 1.949 ns, followed by a slow part of 8.448 ns[8].

Two emission peaks were observed at 485 nm and 526 nm in the spectra[9]. The study concluded that the different PL intensities of the different BiOX structures correlated. As a result, the nanoplate structure has the highest PL intensity, whereas the hollow microspheres and flower-shaped microspheres have lower PL intensities.

2.4 Review of Synthesis Methods and Growth Mechanism of Bismuth Oxyhalide

This section will examine several synthesis methods for bismuth oxyhalide and discuss the consequences, advantages and characteristics of each method. Synthesis methods covered include: hydrolysis method, hydrothermal method, solvothermal method, vapour phase synthesis, heat treatment method, template method, wet chemical method and special source-induced synthesis methods.

It has been a great topic among the researchers to find the optimal method of synthesis of bismuth oxyhalide, several methods have been discovered so far, but it is hard to determine which the optimum method. However, as the technology has evolved, there have been many tools discovered which have been utilised for characterising the synthesised sample and that have allowed us to modify our method of synthesis to fit our requirements. In the last few years, discussion about notable progress in the controlled synthesis of bismuth oxyhalide, due to the development of these characterization tools. This section contains a discussion of the most efficient and effective method of synthesising bismuth oxyhalide.

2.4.1 Synthesis by Hydrolysis Method

2.4.1.1 Bi^{3+}–X^{-} (X = Cl, Br & I) Aqueous System

In recent years, Bi^{3+}–X^{-} has been widely employed to synthesise bismuth oxyhalide (Chloride, Bromide and Iodide) with high purity compounds. First, bismuth salts such as $BiCl_3$, $Bi(NO_3)_3$, and Bi_2O_3 are dissolved in aqueous hydrogen halide solution, or it may be a metal halide to form a Bi^{3+}–X^{-} system with very low pH values. Alkali solution is added into the Bi^{3+}−X^{-} system after which NH_4OH is added for pH maintenance at 2 to 3. Meanwhile, precipitation is collected and washed to remove X^{-} ions, and the dried product is obtained by roasting it in an oven for a few minutes.

As the temperature increased, the required concentration ratio for the residue phase of distillation of $BiCl_3$–HCl–H_2O decreased. The theoretical calculation of their research indicates that hydrolysis can be achieved at temperatures exceeding 128 °C[10].

An analysis BiOCl occupies the narrowest thermodynamic region when the concentration of $c_0(Cl^{-})$ decreases from 3.0 to 0.3 mol/L, when hydrometallurgy of Bi in Cl solutions is investigated. As $c_0(Cl^{-})$ is decreased from 3.0 to 0.3 mol/L, the pH in the BiOCl formation drops from 3 to 2. This means that one must control the pH value of aqueous solution to get a pure BiOCl, along with the low values of $c_0(Bi^{3+})$ and $c_0(Cl^{-})$ in aqueous solution that occur during the formation of BiOCl. Since the pH is lower for the formation of BiOCl than for the formation of Bi_2O_3[11].

The temperature and time-controlled TG-MS measurements of in situ PXRD, which showed that the intermediate hydrate $BiCl_3$•H_2O is produced during $BiCl_3$ transformation hydrolysis (in water vapour)[12]. By studying the change of mass of $BiCl_3$ as a function of reaction time, they found 4.6 and 3.8 wt. % respectively. It is formed by the reaction of $BiCl_3$•H_2O with ambient humidity to give intermediate followed by the formation of BiOCl. A transitional hydrate was formed at 277 and 40 °C, representing the development of mass[13]. The highest weight gain of the sample can be seen from the XRD patterns at 27 °C. This indicates that a volatile phase called $BiCl_3$•H_2O is the main component, whereas $BiCl_3$ and BiOCl are also present in small amounts. TG-MS shows a simultaneous increase in the ion concentration at m/z = 18 (H_2O^{+}) from approx. A dilute solution of $BiCl_3$ in H_2O reaches 50 °C, which indicates hydrolysis.

2.4.1.2 Other Hydrolysis Synthesis Process

BiOCl has been prepared Novokreshchenova et al, by reacting NH_4Cl and bismuth (III) trihydrate oxohydroxonitrate $\{[Bi_6O_5(OH_3)](NO_3)_5 \bullet 3H_2O\}$ with ammonium carbonate under normal conditions (23 and 60 °C)[14]. From the bismuth containing HNO_3 solution, they prepared the precursor

bismuth trihydrate oxohydroxonitrate, which can then be converted into bismuth oxychloride by using the following:

$$[Bi_6O_5(OH_3)](NO_3)_5 \bullet 3H_2O + 6NH_4Cl \rightarrow 6BiOCl + 5NH_4NO_3 + NH_4OH + 4H_2O.$$

A thermo-gravimetric/differential thermal analysis (TG-DTA) of bismuth trihydrate oxohydroxonitrate indicates that the dehydroxilation process begins at 270 °C followed by endothermic peaks centred at 330, 375, 440, 520, and 600 °C. This is a culmination of dehydroxilation, 5 nitrate ions devastation, and Bi_2O_3 phase formation, characterised by a peak endothermic temperature of 730 °C resulting from the transformation of a-Bi_2O_3 to d-Bi_2O_3. According to their study, bismuth can be extracted into BiOCl to a level of 99.99 % using NH_4Cl and 99.94 % using HCl. Following is a possible mechanism that can show the equation below:

$$[Bi_6O_5(OH_3)](NO_3)_5 \bullet 3H_2O + 6HCl \rightarrow 6BiOCl + 5HNO_3 + 5H_2O.$$

BiOCl has been synthesised using a novel thermal hydrolysis method developed by Ye et al.. These authors used $Bi_n(Tu)_xCl_{3n}$ as the precursor material, which exhibits a flower-like hierarchical structure[15]. The synthesis of BiOCl in this process takes only 30 seconds using $Bi_n(Tu)_xCl_{3n}$ as a precursor material, they prepared the molecular precursor by combining $BiCl_3$ and Tu (Tu = thiourea) as follows:

$$nBi^{3+} + mTu \rightarrow Bi_n(Tu)_xCl_{3n}.$$

2.4.2 Synthesis by Heat Treatment

Bismuth oxyhalides have been prepared by thermally treating BiI_3 at 260 and 350 °C for 16 and 3 hours at a rate of 5 °C/min, but Liu et al. prepared highly symmetrical BiOI single-crystal nanosheets by annealing directly at same time and temperatures[16]. This method has been found to have a much better (001) BiOI peak than the traditional method. The method implies that there will be a significantly higher percentage of crystals with (001) faces. According to their research, the main reaction occurs between 300-420 °C, followed by 302-560 °C, and finally 120-160 °C.

$$2BiI_3 + O_2 \rightarrow 2BiOI + 2I_2 \uparrow (Approximately\ weight\ loss\ 40.50\ \%)$$

Afterwards, a reaction occurs between the two products,

$$2BiI_3 \rightleftharpoons 2Bi + 3I_2 \uparrow (appear\ weight\ loss\ 52\ \%)$$

There are then weight-loss regions among 300 to 420 °C,

$$5BiOI + O_2 \rightarrow Bi_5O_7I + 2I_2\ (Approximately\ appear\ 28.89\ \%)$$

Finally, in the region at 610-750 °C,

$$2Bi_5O_7I + \frac{1}{2}O_2 \rightarrow 5Bi_2O_3 + I_2 \uparrow (Approximately\ appear\ 6.6\ \%).$$

Here the heat treatment maintains the phase of BiOI till 350 °C. They conducted TG-DSC (Thermo-gravimetric and Differential scanning calorimetry) to demonstrate this.

In addition, Ueda and colleagues[17] have demonstrated that BiOCl can be synthesised by heating $BiCl_3$ at 650-850 °C for 20 hours. In order to obtain the crystal of $Bi_{24}O_{31}C_{l0}$ was obtained by 1:1 mixture of BiOCl and metal oxide at 800 °C for 5 hours heating.

2.4.3 Hydrothermal Synthesis Method/Growth Process

Generally, starting materials for growing BiOX are $BiCl_3$ or $Bi(NO_3)_3$. A halide source (halide salt) gives more accurate results. This is the most commonly used method for synthesising BiOCl as it is straightforward and gives high quality results. $Bi(NO_3)_3$ and saturated NaCl solution were used as starting materials in a mannitol-assisted hydrothermal synthesis method to prepare square crystal edge BiOCl nanoplates[18]. Additionally, when mannitol is present, the direction [001] of BiOCl's layering tends to develop rapidly. A normal square nanoplate is created as a result of hydrogen bonds between hydroxyl groups.

To control particle size (both in-plane and thickness), Deng et al. developed a hydrothermal 2D structure process for preparing BiOX using PVP and H_2O_2 mixture[19]. The chemical sources of bismuth and halide are metal bismuth powder and NaX (X = Cl, Br, and I). Under hydrothermal conditions, bismuth metal undergoes an oxidation reduction reaction with H_2O_2, resulting in bismuth oxyhalide:

$$2Bi + 3H_2O_2 + 2NaX \rightarrow 2BiOX + 2NaOH + 2H_2O.$$

XRD patterns of spherical polycrystalline nano-particulates of the bismuth oxhydrochloride are not indexed to date in the literature survey. The particles produced by hydrothermal reaction are spherical and measure between 5 and 20 nm. As the hydrothermal temperature and concentration increase, and 2D bismuth oxyhalide crystals are pillaged, the size of bismuth oxyhydrohalide/BiOX particles may grow from nanoscale to microscale.

Siao et al. synthesised and characterised ternary bismuth oxyhalide photocatalysts using controlled hydrothermal reactions, constituting a systematic synthesis study on bismuth oxyhalides[20]. A synergetic effect of layered structures, a high BET surface area, heterojunction formation, and low energy band structures were found to give rise to enhanced photocatalytic activity. A photocatalytic step follows both the photoionization degradation and the photocatalysis step. The main active samples in

photoionization were OH^- and h^+.

2.4.4 Solvothermal Synthesis Method/Growth Process

2.4.4.1 Alcoholic-Mediated Process

Zhu et al. first reported that they prepared bismuth oxyhalides by solvothermal processes at 100 – 200 °C in absolute ethanol[21]. The $BiCl_3$ study was used as a base material for the preparation of polycrystalline and single-crystalline BiOCl. The process of hydrolysis takes place when the reaction temperature of BiOCl crystals is raised from 120 to 150 °C. The crystal structure of BiOCl has evolved from polished crystals to single crystals due to trace amounts of water in the pure ethanol solution.

Using activated carbon fibres as reaction templates and anhydrous ethanol as a solvothermal medium, Yuan et al. created BiOCl fibres using similar processes by $BiCl_3$ reactions and anhydrous ethanol media[22]. However, in their study they concluded that the ethanol mediated solvothermal process is necessary to produce lava like surfaces and solid interior structures. The solvothermal process itself was also modified when acetone instead of ethanol used, resulting in the formation of fibres with completely different morphologies of BiOCl. Also, the morphology of BiOCl fibres reveals the presence of many lamellae in the inner shell of the fibre. In spite of the fact that the reason for the unusual morphology of such materials remains unclear, EG (Ethylene glycol) medium-mediated self-assembly processes have been extensively studied as a means of preparing 3D nanostructures[23, 24].

$Bi(NO_3)_3$ is heated during the solvothermal process and EG reacts with Bi^{3+} to form BiOX, bismuth alkoxide, and HNO_3. These are byproducts of this coordination reaction. Due to the hydrogen bonds between the hydroxyl groups on EG, it can act as a soft template. Solvents are also used for the preparation of nanoparticles via solvothermal methods[25]. In the presence of HNO_3, the formation of additional bismuth alkoxide and BiOCl is prevented by bismuth alkoxide precipitating and creating the nuclei.

A Solvothermal preparation route was first reported for BiOCl in 2002[21]. However it took several years for a reawakening of interest in this process. With the development of a hierarchy of solvothermal synthesis treatments using ethylene glycol mediated. $Bi(NO_3)_3$ and halide salts (KCl, NaBr and KI) as starting materials for BiOX synthesis, a hierarchy of successful synthesis treatments has been described[26, 27].

Zhu et al. construct 3D BiOCl hierarchies via a solvothermal process mediated by EG and urea[28]. This process can create a steady flow of hydroxyl ions without template or surfactant use. This mechanism is thought to further support coordination reactions between Bi^{3+} and EG when urea is used to

neutralise HCl byproducts. Under identical solvothermal methods, a-Bi_2O_3 crystals were observed in the absence of urea. $Bi_{12}O_{17}C_{l2}$ crystal phase was observed when the urea/Bi^{3+} molar ratio was increased from 5 to 10. There is significant crystal phase dependence upon the urea/Bi^{3+} molar ratio.

2.4.4.2 Other Solvothermal Method

BiOCl is formed by the reaction of pyridine mediated solvothermal solvation with pyridine and adsorbed water on $BiCl_3$ as the starting media in the study by Song et al., according to their findings, the thickness of the BiOCl nanoplates, which contain a hierarchy of molecule sizes, depends on the volume ratio of water to pyridine[29]. A decrease in volume ratio leads to a decrease in the thickness of BiOCl nanoplates. They also found that every six-membered pyridine ring contains one nitrogen atom that replaces a C–H group. Furthermore, a basic electron pair from the nitrogen atom competes with a basic electron pair from the oxygen atom when forming BiOCl, influencing its morphology.

2.4.5 Synthesis by Vapour-Phase Method

The vapour of bismuth oxyhalides, such as BiOCl, BiOBr, or BiOI, to mix with water vapour and pass through a reaction chamber kept at 700-800 °C, crystals of BiOCl can easily be obtained. In early 1973, discovered the N_2O or helium gas was introduced to the reaction chamber by Silvestri et al., and the bicarbonate crystals are readily formed[30].

A direct vapour-phase transfer technique for synthesis of controllable morphological BiOCl nanostructures can also be employed with $AuCl_3$/Bi mixtures or $BiCl_3$ reported by Peng et al.[13] The starting materials to prepare BiOCl can be either $AuCl_3$/Bi or $BiCl_3$. This process occurs between 160 and 250 °C:

$$AuCl_3 \rightarrow AuCl + Cl_2\,, Cl_2 + Bi \rightarrow BiCl_3.$$

At 234 °C, the melting point of $BiCl_3$, vaporised by a stream of inert gas, is reached. The vaporised $BiCl_3$ undergoes hydrolysis to become BiOCl, as shown below:

$$BiCl_3 + H_2O \rightarrow BiOCl + 2HCl.$$

A stoichiometric mixture of Bi_2O_3 and $BiCl_3$ can also be synthesised in an evacuated system, as shown by the work of Keramidas et al.[31]. Bi_2O_3 and $BiCl_3$ are heated together at 820 °C at a vacuum of 106 Torr. The resulting thin plates are cooled gradually to room temperature, increasing the mechanical strength of the thin plates.

The method used by Ganesha et al.[32] to synthesise BiOI crystals entails starting with a very pure (99.999 %) mixture of BiI_3 and Bi_2O_3 and continuing annealing for 4 days at 450 °C.

2.4.6 Special Halide Source-Induced Preparation

2.4.6.1 Reactive Ionic Liquid (Template Method)

It is well known that halide containing components such as sodium/potassium halide have been used for halide sources in the preparation of BiOX compounds since 2010. In ionothermal synthesis, a solvent is used, a template provides a shape for crystallisation, and a directing force is used to guide the process. As well as serving as templates and solvents for ionothermal synthesis, ionic liquids (IL) can also influence chemical reactions. Ionothermal method produces ultrathin BiOCl nanoflakes (18 nm) containing $Bi(NO_3)_3$ and 1-hexadecyl-3-methylimidazolium chloride $[C_{16}Mm]Cl$, as raw materials, reactants, and templates[33].

The solvothermal reaction in a mixture of 2-methoxyethanol and 1-hexadecyl-3-methylimidazolium bromide $[C_{16}Mim]Br$ ionic liquid (IL), uniform hollow microspheres of BiOBr can be prepared[34]. It is common to use $[C_{16}Mim]Br$ as a starting material for BiOBr preparation as well as the previous method. It has been demonstrated that $[C_{16}Mim]Br$ and 2-methoxyethanol are only slightly miscible, and the emulsions form before the solvothermal reaction. The miniemulsions surrounded by 2-methoxyethanol containing Bi^{3+} form a microemulsion chamber. The 2D BiOBr nanosheets produced by the reaction of Bi^{3+} with IL in the presence of $[C_{16}Mim]Br$. The subsequent growth of flower-like hollow microsphere structure was produced by one-pot ethylene glycol assisted solvothermal method[35].

2.4.6.2 Reactive Surfactant

The preparation of bismuth oxyhalide compounds has been carried out under hydrothermal and solvothermal conditions using halide containing cationic surfactants, such as cetyl trimethyl ammonium chloride or bromide (CTAC/B). BiOBr in aqueous phase has been prepared by hydrothermal reaction using CTAB ($C_{16}H_{33}(CH_3)_3N$-Br-Bi^{3+}) as a source of Br and template, reported by Shang et al. The following reaction occurred:

$$Bi^{3+} + C_{16}H_{33}(CH_3)_3N - Br \rightarrow C_{16}H_{33}(CH_3)_3N - Br - Br^{3+}$$

$$C_{16}H_{33}(CH_3)_3N - Br - Br^{3+} + H_2O \rightarrow BiOBr + C_{16}H_{33}(CH_3)_3N^{+} + 2H^{+}.$$

In aqueous solution, yellow suspension formed when acidic Bi^{3+} and CTAB were mixed together and can be attributed to a complex of Bi^{3+} and CTAB. Furthermore, BiOBr nucleates, after which the lamellar structure grows and is shaped using CTAB as the soft template[36].

Xiao et al. used a hydrothermal process to produce BiOBr with hierarchical structures[37], similarly also reported by Shang et al.'s[36]. In this case, OH is added to the aqueous phase of the reaction. In the

absence of NaOH, only BiOBr nanoflakes were obtained. The morphology of the product is therefore affected by the amount of NaOH used in the reaction system. This reaction is currently unknown, but the following is proposed:

$$Bi(NO_3)_3 + H_2O \rightarrow BiONO_3 + 2H^+ + 2NO_3^-$$
$$BiONO_3 + Br - (CTAB) \rightarrow BiOBr + NO_3^-$$

The formation of $BiONO_3$ may be initiated by hydrolysis of $Bi(NO_3)_3$. Then NO_3 and Br (from CTAB) undergo ion exchange reactions. There are some differences between this reaction and the one proposed by Shang et al.[36]. Therefore, the formation of complexes between Bi^{3+} and CTAB cannot be disregarded.

Furthermore, the nature of the solvent also significantly impacts the morphology of the product in addition to the effect of NaOH on BiOBr morphology. Using ethylene glycol as the solvent instead of water can result in a completely different morphology. It has already been demonstrated that BiOBr with hierarchical structures can be synthesised through a solvothermal process using alcohols (such as ethylene glycol or ethanol, etc.) involving $Bi(NO_3)_3$ and CTAB in nearly identical amounts to the reference material[36].

Using EEG-mediated solvothermal methods, Hongqi et al. and Chen et al. used $Bi(NO_3)_3$ and CTAC, respectively, as sources of bismuth and chloride[38,39]. Examined and discussed the formation mechanism, providing an explanation for the hierarchical formation of BiOBr.

2.4.7 Other Synthesis Technique

There have been other synthesis methods, such as electrospinning[40], ultrasound[41], microwave[42], reverse microemulsion[43], as well as others, investigated to obtain the desired morphology, improving the yield of corresponding compounds of bismuth oxide halide series.

2.4.8 Growth Mechanism of Bismuth Oxyhalide

The different morphologies of BiOCl arise due to the variation in the concentration of the precursors and different synthesis conditions. The main precursors used during synthesis of BiOCl are citric acid (CA) and PVP (Poly Vinyl Pyrrolidone), apart from the $Bi(NO_3)_3$ and HCl. CA is a structure-directing agent which induces the growth of different morphological architectures, whereas PVP is a surfactant which helps in the typical attachment of the nanomaterials to assemble into different morphologies like hollow, nut or nest-like structures of BiOCl. This type of PVP-induced attachment is termed as

imperfect oriented attachment. CA is also an important biological chelating agent for metal ions, forming strong complexes with Bi^{3+}, Al^{3+}, Ca^{2+}, Fe^{3+}, Zn^{2+} and Mg^{2+}.

It is known that the crystal structure of BiOCl is layered, with slabs of $[Bi_2O_2]$ interleaved by double slabs of Cl atoms. The work described in the thesis presents a window of the different parameters and correct combinations of precursors such as pH, concentration, temperature, growth time etc, to obtain the desired structures. The plausible formation of BiOCl can be speculated as follows:

(i) When $Bi(NO_3)_3$ is dissolved in hydrochloric acid, Bi^{3+} is produced.

(ii) Free Bi^{3+} cations can interact with citric anions via the chelation effect to produce $[C_6O_7H_5]^{3-}Bi^{3+}$.

(iii) When $Bi(NO_3)_3$ solution is added drop-wise into the reaction solution, Bi^{3+} cations will be slowly released from the $[C_6O_7H_5]^{3-}Bi^{3+}$ complex, thus gradually converting to BiOCl.

(iv) This conversion occurs through self-hydrolysis process since BiOCl has a much higher stability in solution as compared to $[C_6O_7H_5]^{3-}Bi^{3+}$.

(v) The origin of various microstructures of BiOCl results from its intrinsic nucleation and anisotropic growth.

The reactions are given below:

$$Bi(NO_3)_3 \rightarrow Bi^{3+} + 3NO_3^-$$

$$Bi^{3+} + [C_6O_7H_8] \rightarrow [C_6O_7H_5]^{3-}Bi^{3+} + 3H^+$$

$$[C_6O_7H_5]^{3-}Bi^{3+} + H_2O + H^+ + Cl^- \rightarrow BiOCl + C_6O_7H_8$$

$$HCl \rightarrow H^+ + Cl^-$$

After the formation of BiOCl crystals, as the concentration of acid increases in the growth media, the probability of combination of neighbouring BiOCl crystals via hydrogen bonding also increases. This in turn leads to formation of BiOCl plates. Further increment of acid concentration and number of hydrogen bonding sites gradually cause the plates to attach with each other leading to formation of nano/micro spheres.

If the concentration of acid is increased further, the already prepared BiOCl may be corroded to metallic chloride of bismuth which is easily water soluble. This is washed away during sample cleaning leaving behind sheet like structures of formerly spheres.

The purpose of CA is thus evident from the above discussion. Without the presence of this agent, non-uniform crystal growth with large-sized nanoflakes of BiOCl is formed resulting in agglomeration. Self-assembly is an effective technique to form hierarchical superstructures, because self-assembling

results in the formation of thermodynamically stable structures. CA plays an important role in the nucleation, crystal growth, and self-assembly of microcrystalline BiOCl crystals since CA can undergo hydrolysis to form $[C_6O_7H_5]^{3-}$ and H^+. As observed from the above equations, it can be speculated that $[C_6O_7H_5]^{3-}$ ions can chelate with Bi^{3+} ions to form $[C_6O_7H_5]^{3-}Bi^{3+}$. Hydrogen bond formation takes place between the carboxyl group of CA and the hydroxyl ion in $[C_6O_7H_5]^{3-}Bi^{3+}$. Additionally, hydrogen bonds are made between the hydroxyl ions in $[C_6O_7H_5]^{3-}Bi^{3+}$. Alternatively, CA can also get absorbed on the BiOCl surface, and the surface-absorbed CA can combine with $[C_6O_7H_5]^{3-}Bi^{3+}$ present in the reaction solution, thus forming hydrogen bonds. Thus, adjusting citric acid concentration could control crystal growth and self-assembly of BiOCl microcrystals. In presence of low concentration of CA, less number of hydrogen bonds is formed, resulting in the growth of the BiOCl crystals along one direction forming square nanoplates like morphology. However, when the concentration of CA is increased, it is highly probable that the strong hydrogen bonds formed between the adjacent lateral surfaces of the nanoplates which are in contact with each other, function as the integrating force to held together the superstructure. On further increasing the amount of CA, large number of hydrogen bonds is formed in the system, and the interaction between the adjacent nanoplates becomes strong enough to enable the self-assembling of these nanoplates into three-dimensional micro-spherical morphology of BiOCl[44,45].

In presence of both citric acid (1.2 mmol) and PVP, monodispersed hierarchical hollow microspheres of BiOCl were formed. The three-dimensional hollow BiOCl microspheres were composed of a large number of radically grown nanosheets similar to the morphology observed in our case. In absence of CA and in presence of PVP, the as-synthesized BiOCl samples were mainly composed of asymmetric round nanoflakes. Again, in presence of CA and in absence of PVP, only nanoplates and solid microspheres of BiOCl were observed. In conclusion, it can be speculated that the surfactant PVP plays a crucial role in initiating the strong interactions between the nanoplates, resulting in self-assembling of these nanoplates-like structures into hollow microspherical superstructures. The growth mechanism of BiOCl can be attributed to the strong synergetic interaction between CA and PVP. Plausible growth mechanism for such nanostructures was also proposed by other workers[46].

2.5 Review on Application of Bismuth Oxyhalide

The use of bismuth oxyhalide as a photocatalytic material as discussed in this chapter earlier has increased greatly in recent years. This section will discuss in detail the applications of bismuth oxyhalide. In addition to being used for photocatalysis, bismuth oxyhalide is also used for water

splitting, air purification, reducing environmental pollutants, and detecting gases among many other applications, which will be documented in detail one by one.

2.5.1 Application of Bismuth Oxyhalide as Photocatalyst

2.5.1.1 Degradation of Inorganic, Organic and Microorganism Pollutant

Chemical and organic pollutants in water are degraded using it as a photocatalyst. By measuring how well this photocatalytic degrades pollutants or inactivates pathogens, it is possible to measure its effectiveness. Sadly, drinking water is often contaminated with organic pollutants such as noxious gases, noble metal ions, and organic dyes such as tetrabromo-bisphenol A, RhB, EB, MO, MB, etc. In tests with and without a catalyst, as well as tests involving UV and visible light, and even tests using radioactive radiation. It can be determined if BiOX photocatalyst efficiently in the degradation process and if their sole reaction is photocatalytic. The tests will determine if the produced BiOX can perform in pure catalytic degradation, as well as if any other non-photocatalytic reactions are observed. The reason for this is that some organic pollutants and microbes can be deactivated and removed just by coming into contact with UV as well as visible light, and certain chemicals. As the experiment progresses, the concentrations of pollutants and pathogens are measured. The collected data can be used to assess the photocatalytic efficiency of the prepared catalyst.

The degradation of MO dye in 120 minutes was reported by Shi et al.[47], methylene orange dye was also degraded by Wang et al.[48], and MB and MO dyes were degraded by Seddigi et al.[49] under UV light irradiation of the BiOCl materials.

Photocatalytic performance of a BiOCl/TiO_2/diatomite heterojunction was demonstrated by Ao et al. recently showed inferior degradation ability of crystalline BiOCl under visible light[50]. Shan et al.[51] informed that BiOBr exhibited poor photocatalytic activity when used to degrade RhB dye, whereas Han et al.[52] also reported the degradation of p-cresol and RhB dyes with BiOBr. Bai et al.[53] described that pure BiOI performed photocatalysis in the degradation of tetracycline under visible light.

A number of air and water remediation accomplishments have been made using BiOX materials[54], including photocatalytic degradation of MO and RhB dyes by flack materials and particle like materials incorporating BiOBr[55]. Visible light photocatalysis of RhB and MO dyes with rod and plate like materials incorporating BiOI[56].

Recent research has focused on enhancing BiOCl's photo-degradation efficiency. Several studies have reported the synthesis of CdS QDs coupled by BiOCl nanomaterials[57]. Zhang et al. created a BiOCl/$Bi_2O_2CO_3$ nano-composite[58]. Sun et al. demonstrated that the nanocomposite of Ag/BiOCl[59].

Zhang et al. proposed that a novel Z-scheme BiOI/BiOCl nanofiber can be synthesised[60]. Yu et al. proposed C doped BiOCl flowerlike nanomaterial[61], etc. By segregating photoinduced charge carriers, all of these composites have been designed as photocatalysts charge carriers to improve photocatalytic activity. Yuan et al. also demonstrated that Fe(III)-modified BiOBr represented a photocatalytic agent for organic dyes and benzyl alcohol under UV-light[62]. Developing micro-spherical BiOI which catalyses the degradation of RhB with visible light was demonstrated by Wang et al.[63].

Additionally, metals and nonmetals can be doped into BiOX to enhance their catalytic activity or heterojunctions can be formed between them and other semiconductors to get a better performance. In addition, Tian et al. synthesised $BiPO_4$ nanomaterial that showed photocatalytic activity of MB dye under UV-light[64], and also reported efficient photo-degradation of MB dye with Fe doping of BiOCl nanomaterial[65]. Bi_2S_3/BiOCl heterostructure was synthesised by Cao et al. to enhance the photocatalytic degradation of RhB under visible light illumination[66]. Among these works, Cui et al., synthesised a CdS/BiOBr composite with impressive photocatalytic properties[67]. Mehraj et al. reported a p-n heterojunction made from Fe_2O_3/BiOI with excellent visible-light assisted photocatalytic performance[68]. The heterojunction sample with oxygen vacancies in z-scheme $BiO_{1-x}Br/Bi_2O_2CO_3$ was created by Ding et al., enhancing the degradation of antibiotics to 4-MAA, CIP, and others under visible light[69].

In a study on the degradation of bisphenol A, Li et al. developed (001) dominant crystal faces of BiOCl[70]. According to Pan et al.[71], CdS quantum dots were coupled with BiOCl nanosheets. A Mn doped BiOCl was developed by Pare et al.[72]. WO_3/BiOCl heterojunction was developed by Shamaila et al.[73]. In addition to supporting the development of BiOCl/Bi_2O_3 heterojunction by Chai et al.[74]. Liu et al. established a $BiOCl_{1-x}Br_x$ (x=0–1) heterojunction[75]. La-doped BiOCl was synthesised by Xu et al.[76]. A composite with Fe_3O_4/Pr-BiOCl/Luffa was synthesised by Yang et al.[77]. The photocatalytic activity of BiOCl was improved by irradiating it with visible, UV, and solar light. TiO_2/BiOCl used to photocatalytic degradation of Cr(VI) and tetracycline by Hu et al.[78]

Graphene (C) and graphene based composites' unique 2D structures and high conductivity make them highly efficient electron moderators. The latter has drawn the interest of many researchers in recent years as they look for successful implementation in photocatalytic water purification systems. Mahdavi et al. fabricated ZnO/GO nanocomposite by zinc acetate $\{Zn(CH_3CO_2)_2.\ 2H_2O\}$ and graphene oxide (GO)[79]. Tang et al. reported BiOCl and graphene nanocomposite by solvothermal method[80]. Graphene and graphene oxide nanosheets were coupled to BiOBr nanosheets in 2D with a simple and low-cost method proposed by Zhang et al. and his colleges[81]. A one-step hydrothermal method allows

facile preparation of chemically linked bismuth oxyiodide-grapheme (BiOI-C) nano-composites series successfully synthesised by Liu et al.[82]. $BiO_xCl_y/BiO_mBr_n/BiO_pI_q$/GO composites prepared from bismuth oxychloride/bismuth oxybromide/bismuth oxyiodide are reported by Siao et al.[83]. Wang et al. have developed nanosheet composites of reduced graphene oxide (rGO) and ultrathin BiOCl (U)[84]. The hydrothermal method has been employed to form heterostructures by combining GO with BiOBr sheets to produce rGO and exposed [001] facets[85]. Liu et al. developed reverse micro-emulsion of BiOI and rGO nanocomposite, and used solvothermal synthesis, for the synthesis of highly efficient photocatalysts[86]. ZnO quantum dots (QD) are produced in a soft chemical route and effectively fabricated on rGO surfaces[87].

In an experiment by Zhang et al., synthesised BiOBr microspheres by means of ionothermal synthesis, and used the microspheres to deactivate the M-lylae pathogen[88]. In the absence of fluorescent light, the degradation of M-lylae is almost zero, suggesting that it is an indestructible pathogen.

Using a photo-deposition method, Zhu et al. synthesised Ag/BiOI and escherichia coli (E. coli) were used in this study[89]. Liang et al. used an in situ ion exchange reaction in their study of the deactivation of E. coli. A composite of BiOI and AgI with visible light could significantly enhance E. coli neutralisation, showing how composite materials can play a role in any photocatalytic process. Both compounds lack the ability to neutralise E. coli alone in the presence of visible light. Furthermore, the BiOI-AgI composite failed to kill E. coli when no visible light radiation was present. Due to the generation of heterojunction between BiOI and AgI, electron hole recombination was reduced purely by photocatalysis[90].

The degradation of organic and inorganic toxic dyes from water using BiOCl/Bi_3O_4Cl nanocomposite was synthesised by wet-chemical method along with the use of BiOX as photocatalysts[91]. The process was also used to deactivate microbes via photocatalysis. Gaseous 2-propanol (IP) was used in their study for the degradation curves, with a number of ratios of BiOCl and Bi_3O_4Cl, and P25 as a reference. The degradation constant k for the BiOCl/Bi_3O_4Cl nanocomposite with the optimised ratio is 2.1 times that of P25 and 6.6 times that of Bi_3O_4Cl after 2 hours of visible light irradiation. Chang et al. found $NaBiO_3$ to be highly active photocatalysis compared to P25[92]. As a result, they observed 9 % removal with P25 when compared to 90 % removal of visible or xenon lights illumination.

Tian et al. created 3D microspheres via a one-step solvothermal method to remove bisphenol A using photocatalytic activity[93]. However, the bisphenol A (BPA) was found to degrade at a rate of 25.6 % without the use of a photocatalyst after 90 minutes of irradiation. With the presence of light, BiOBr microspheres functioned as a photocatalyst and emitted about 100 % degradation after 90 minutes,

whereas P25 as a photocatalyst only degraded 50.3 % of BPA.

In an experiment using microwave irradiation to synthesise 3D flower-like BiOBr, it was found that the removal rate of Cr(VI) ions was 94 % after two hours[94]. They also found that the removal rate was much higher when using flower-like BiOBr than plate-like structure.

The study of hydrolyzed BiOX to create various BiOX (X = Cl and Br) and synthetic azo dye (MO) as pollutants[95]. Analysis findings indicate that the MO molecule has not been fully photo-mineralized, as the TOC (Total Organic Carbon) depletes much slower than MO dye.

A non-aqueous sol–gel method was used to synthesis BiOBr microspheres, irradiating them with visible light, to remove NO[12]. BiOBr microspheres synthesised using non-aqueous sol-gel material degraded NO by 45 % within 10 minutes, while bulk powder BiOBr synthesised by chemical precipitation material degraded NO only 13 %.

2.5.1.2 Water Splitting

In a classical photocatalytic water splitting reaction, water molecules are oxidised by photogenerated electrons and oxidised them by photogenerated holes. Water spitting can be mediated by semiconductor photocatalysts whose CB bottoms are lower than those of H^+/H_2 and their VB tops are lower than those of O_2/H_2O. BiOX is such a semiconductor photocatalyst that meets these criteria.

Zhang et al. investigated possible water splitting reactions and degradation mechanisms of RhB using a BiOCl/CuPc (copper phthalocyanine) composite[96]. Their findings showed that bi-functional catalysts, such as BiOCl/CuPc, can degrade RhB at a faster rate than metal catalysts. When RhB and methanol are added to the reaction system, more oxygen is produced.

A sandwich structure of I-BiOCl and bipolar membrane has been synthesised by Liu et al. using photoelectro-synergistic catalysis[97]. Additionally, they showed that the sandwich structure made up of I-BiOCl/BPM material generated more H_2 than the pure BPM, and that 35.5 % of its energy was saved at a current density of 200 mA cm^{-2}.

A solid-state method was used to successfully synthesise a BiOCl/β-FeOOH heterojunction. These were then studied in terms of their structure, composition, and photochemical properties. In the HER process demonstrated superior photocatalytic performance by the heterojunction photocatalyst. Under visible light, the HER rate was about 16.64 $mmolg^{-1}h^{-1}$ over six hours of illumination[98].

To prepare Pd-doped BiOCl and 2D BiOCl nanosheets materials were synthesised for CO_2RR via the wet-chemical method. Among the products converted from CO_2 both on BiOCl and Pd-doped BiOCl nanosheets, formic acid is the only one resulting from water reduction[99].

It is proposed that 2D titanium carbide MXene nanocomposites in the form of BiOCl@$Ti_3C_2T_x$ exhibit excellent catalytic performance. The low overpotentials can be used as a catalyst in ambient nitrogen reduction reactions with superior long term stability. The catalyst has produced high faradaic efficiency about 11.98 %, yielding 4.06 $\mu g h^{-1} cm^{-2}$ of NH_3 at -0.10 V (compared to RHE) in 0.1 mol/L HCl[100].

2.5.2 Application of Bismuth Oxyhalide as Secondary Battery

Metal-air batteries are probably the most attractive application for BiOX's technology due to their small size, low emissions, high energy density, light weight, flexible portability, low noise and vibration. Firstly, oxygen reduction occurs by reducing oxygen into H_2O_2 during cathodic reactions in fuel cells and metal-air batteries. Secondly, oxygen reduction is accomplished by reducing O_2 into H_2O_2 using four electrons.

Yuan et al. are able to successfully prepare micro-assembles of BiOCl using a simple hydrothermal reaction[101]. All the samples tested, their BiOCl (0.18 M concentration) samples exhibited the maximum working potential window, at 1.47 eV.

A photo-fuel cell based on TiO_2 and BiOCl as photocatalysts has been created by Fujishima et al., reaching a voltage (V_{oc}) of 1.69 to 1.76 V and a power of 21.11 watts[102]. The researchers managed to achieve an efficiency of 0.024 of the absorbed light per cell current.

A chloride ion battery with metal oxychloride as a cathode was developed by Zhao et al.[103]. During this study they used FeOCl cathode which has 158 $mAhg^{-1}$ discharge capacity in the first cycle and 60 $mAhg^{-1}$ after 30 cycles.

As positive electrode materials, spinel-type $LiMn_2O_4$'s (III, IV) is being studied. Unfortunately, these diodes do not perform well during cycling at high temperatures, so they are ineffective in practical applications. The research has been focused on cation substitution at Mn sites, surface modification, and combining with other materials to overcome these limitations.

2.5.3 Application of Bismuth Oxyhalide as Gas Sensor

Over the years, scientific research has been focused on developing chemical sensors to detect and monitor harmful gases, such as ozone, CO, CO_2, NO_2, SO_2, and other hazardous gases. Moreover, some semiconductors can be used to produce photo-electronically activated biosensors for the detection of organophosphate pesticides, which are widely used in agriculture.

Using surfactant-assisted methods to prepare BiOCl and study reproducible CO gas sensing patterns at 300 °C, reliable patterns of gas sensing in all CO, CO_2, and O_2 gases were derived at 400 °C. Bi-

functional substances also have p-type semiconductors property as a result of their reactions with oxygen and CO_2 gases[104].

2.5.4 Application of Bismuth Oxyhalide as Solar Cell

The use of dye-sensitised semiconductor nanomaterials in solar cells has been in the spotlight for years, and they are a promising prospect for the future. In addition to having excellent photovoltaic properties, these materials are accessible and cheap, and could make excellent photovoltaic materials. The consequence of these developments has been a lot of interest in photovoltaic based on BiOX-based solar cells.

BiOI nanoplate microspheres embedded in the chitosan matrix were used by Zhao et al. to synthesise for BiOI based solar cells[105]. The open circuit potential (Voc) of the BiOI–CHI colloidal solution was -461.1 mV under short-circuit operating conditions. The photocurrent density (Isc) was 20.4 A/cm^2 and with the fill factor (FF) was 0.46.

The solar cell designed by Wang et al. uses aggregates of flakes-like BiOI structures that cross each other[106]. Using the SILAR method, BiOI flakes were developed at room temperature on an FTO glass with a TiO_2 block layer. In a cell made with BiOI nanoflakes, the photocurrent density is 241 Acm^2, the open circuit potential (Voc) is 0.62 V, the fill factor is 0.61, the efficiency is 0.09 %, and the IPCE is 4 %.

2.6 Conclusions

A detailed discussion of various aspects of bismuth oxyhalides synthesis, characterization and various applications were presented in this chapter. The analysis was done here to learn about the various properties of bismuth oxyhalide.

Reference

[1] M. Ismail, Z. Wu, L. Zhang, J. Ma, Y. Jia, Y. Hu and Y. Wang, *Chemosphere*, 228, 2019, 212-218.
[2] L. Yao, H. Yang, Z. Chen, M. Qiu, B. Hu and X. Wang, *Chemosphere*, 273, 2021, 128576.
[3] J. Li, L. Cai, J. Shang, Y. Yu and L. Zhang, *Advanced Materials*, 28(21), 2016, 4059-4064.
[4] X. Jin, L. Ye, H. Xie and G. Chen, *Coordination Chemistry Reviews*, 349, 2017, 84-101.
[5] X. Zhang, Z. Ai, F. Jia and L. Zhang, *The Journal of Physical Chemistry C*, 112(3), 2008, 747-753.
[6] K.L. Zhang, C.M. Liu, F.Q. Huang, C. Zheng and W.D. Wang, *Applied Catalysis B: Environmental*, 68(3-4), 2006, 125-129.
[7] R. Singh and B. Pal, *Journal of Molecular Catalysis A: Chemical*, 371, 2013, 77-85.
[8] Z. Deng, F. Tang and A.J. Muscat, *Nanotechnology*, 19(29), 2008, 295705.
[9] K. Ren, K. Zhang, J. Liu, H. Luo, Y. Huang and X. Yu, *CrystEngComm*, 14(13), 2012, 4384-4390.
[10] G.Q. Zheng and M.T. Tang, *Chinese Journal of Nonferrous Metals*, 10, 2000, 250-252.

[11] Y.Y. Wang, W.J. Peng and L.Y. Chai, *Journal of Central South University of Technology*, 11(4), 2004, 410-413.
[12] A. Wosylus, S. Hoffmann, M. Schmidt and M. Ruck, *European Journal of Inorganic Chemistry*, 2010(10), 2010, 1469-1471.
[13] H. Peng, C.K. Chan, S. Meister, X.F. Zhang and Y. Cui, *Chemistry of Materials*, 21(2), 2009, 247-252.
[14] M.N. Novokreshchenova, Y. Yukhin and B.B. Bokhonov, *Chemistry for Sustainable Development*, 13, 2005, 563-568.
[15] L. Ye, L. Zan, L. Tian, T. Peng and J. Zhang, *Chemical Communications*, 47(24), 2011, 6951-6953.
[16] H. Liu, J. Cai, M. Luo, C. Chen and P. Hu, *RSC Advances*, 10(10), 2020, 5913-5918.
[17] W. Ueda, F. Sakyu, T. Isozaki, Y. Morikawa and J.M. Thomas, *Catalysis Letters*, 10(1), 1991, pp.83-89.
[18] J. Xiong, G. Cheng, G. Li, F. Qin and R. Chen, *RSC Advances*, 1(8), 2011, 1542-1553.
[19] Z. Deng, D. Chen, B. Peng and F. Tang, *Crystal Growth and Design*, 8(8), 2008, 2995-3003.
[20] C.W. Siao, H.L. Chen, L.W. Chen, J.L. Chang, T.W. Yeh and C.C. Chen, *Journal of Colloid and Interface Science*, 526, 2018, 322-336.
[21] L. Zhu, Y. Xie, X. Zheng, X. Yin and X. Tian, *Inorganic Chemistry*, 41(17), 2002, 4560-4566.
[22] R. Yuan, C. Lin, B. Wu and X. Fu, *European Journal of Inorganic Chemistry*, 2009(24), 2009, 3537-3540.
[23] L.S. Zhong, J.S. Hu, H.P. Liang, A.M. Cao, W.G. Song and L.J. Wan, *Advanced Materials*, 18(18), 2006, 2426-2431.
[24] A.M. Cao, J.S. Hu, H.P. Liang and L.J. Wan, *Angewandte Chemie International Edition*, 44(28), 2005, 4391-4395.
[25] Y. Wang, X. Jiang and Y. Xia, *Journal of the American Chemical Society*, 125(52), 2003, 16176-16177.
[26] E. Bárdos, A.K. Király, Z. Pap, L. Baia, S. Garg and K. Hernádi, *Applied Surface Science*, 479, 2019, 745-756.
[27] J. Zhang, F. Shi, J. Lin, D. Chen, J. Gao, Z. Huang, X. Ding and C. Tang, *Chemistry of Materials*, 20(9), 2008, 2937-2941.
[28] L.P. Zhu, G.H. Liao, N.C. Bing, L.L. Wang, Y. Yang and H.Y. Xie, *CrystEngComm*, 12(11), 2010, 3791-3796.
[29] J.M. Song, C.J. Mao, H.L. Niu, Y.H. Shen and S.Y. Zhang, *CrystEngComm*, 12(11), 2010, 3875-3881.
[30] V.J. Silvestri, T.O. Sedgwick and J.B. Landermann, *Journal of Crystal Growth*, 20(2), 1973, 165-168.
[31] K.G. Keramidas, G.P. Voutsas and P.I. Rentzeperis, *Zeitschrift für Kristallographie-Crystalline Materials*, 205(1), 1993, 35-40.
[32] R. Ganesha, D. Arivuoli and P. Ramasamy, *Journal of Crystal Growth*, 128(1-4), 1993, 1081-1085.
[33] J. Ma, X. Liu, J. Lian, X. Duan and W. Zheng, *Crystal Growth and Design*, 10(6), 2010, 2522-2527.
[34] H. Cheng, B. Huang, Z. Wang, X. Qin, X. Zhang and Y. Dai, *Chemistry–A European Journal*, 17(29), 2011, 8039-8043.
[35] J. Xia, S. Yin, H. Li, H. Xu, Y. Yan and Q. Zhang, *Langmuir*, 27(3), 2011, 1200-1206.
[36] M. Shang, W. Wang and L. Zhang, *Journal of Hazardous Materials*, 167(1-3), 2009, 803-809.
[37] P. Xiao, L. Zhu, Y. Zhu and Y. Qian, *Journal of Solid State Chemistry*, 184(6), 2011, 1459-1464.

[38] L.I.U. Hongqi, G.U. Xiaona, C.H.E.N. Feng and Z.H.A.N.G. Jinlong, *Chinese Journal of Catalysis*, 32(1), 2011, 129.
[39] F. Chen, H. Liu, S. Bagwasi, X. Shen and J. Zhang, *Journal of Photochemistry and Photobiology A: Chemistry*, 215(1), 2010, 76-80.
[40] C. Wang, C. Shao, Y. Liu and L. Zhang, *Scripta Materialia*, 59(3), 2008, 332-335.
[41] Y. Chang-Lin, Z. Wan-Qin and J.C. Yu, *Chinese Journal of Inorganic Chemistry*, 27(10), 2011, 2033-2038.
[42] L. Zhang, X.F. Cao, X.T. Chen and Z.L. Xue, *Journal of Colloid and Interface Science*, 354(2), 2011, 630-636.
[43] J. Henle, P. Simon, A. Frenzel, S. Scholz and S. Kaskel, *Chemistry of Materials*, 19(3), 2007, 366-373.
[44] R. Sarkar, D. Roy, D. Das, S. Sarkar and K.K. Chattopadhyay, *International Journal of Hydrogen Energy*, 46(30), 2021, 16299-16308.
[45] R. Sarkar, D. Das, B.K. Das, A. Mitra, N.S. Das, S. Sarkar and K.K. Chattopadhyay, *Materials Research Bulletin*, 125, 2020, 110778.
[46] K. Zhang, J. Liang, S. Wang, J. Liu, K. Ren, X. Zheng, H. Luo, Y. Peng, X. Zou, X. Bo and J. Li, *Crystal Growth & Design*, 12(2), 2012, 793-803.
[47] Z.Q. Shi, WANG Yan, C.M. Fan, Y.F. Wang, G.Y. Ding, *Transactions of Nonferrous Metals Society of China*, 21(10), 2011, 2254-2258.
[48] Y. Wang, Z.Q. Shi, C.M. Fan, X.G. Hao, G.Y. Ding, Y.F. Wang, *International Journal of Minerals, Metallurgy, and Materials*, 19, 2012, 467-472.
[49] Z.S. Seddigi, M.A. Gondal, U. Baig, S.A. Ahmed, M.A. Abdulaziz, E.Y. Danish, M.M. Khaled, A. Lais, *PLOS One*, 12(2), 2017, 0172218.
[50] M. Ao, K. Liu, X. Tang, Z. Li, Q. Peng and J. Huang, *Beilstein Journal of Nanotechnology*, 10(1), 2019, 1412-1422.
[51] L. Shan, Y. Liu, H. Chen, Z. Wu and Z. Han, *Dalton Transactions*, 46(7), 2017, 2310-2321.
[52] A. Han, J. Sun, G.K. Chuah and S. Jaenicke, *RSC Advances*, 7(1), 2017, 145-152.
[53] J. Bai, Y. Li, P. Wei, J. Liu, W. Chen and L. Liu, *Small*, 15(23), 2019, 1900020.
[54] G. Li, B. Jiang, S. Xiao, Z. Lian, D. Zhang, C.Y. Jimmy and H. Li, *Environmental Science: Processes & Impacts*, 16(8), 2014, 1975-1980.
[55] Z. Jiang, F. Yang, G. Yang, L. Kong, M.O. Jones, T. Xiao and P.P. Edwards, *Journal of Photochemistry and Photobiology A: Chemistry*, 212(1), 2010, 8-13.
[56] Y. Wang, K. Deng and L. Zhang, *The Journal of Physical Chemistry C*, 115(29), 2011, 14300-14308.
[57] J. Pan, J. Liu, S. Zuo, U.A. Khan, Y. Yu and B. Li, *Materials Research Bulletin*, 103, 2018, 216-224.
[58] X. Zhang, T. Guo, X. Wang, Y. Wang, C. Fan and H. Zhang, *Applied Catalysis B: Environmental*, 150, 2014, 486-495.
[59] J. Sun, Z.D. Hood, S. Wu, P. Wan, L. Sun, S. Yang and M.F. Chisholm, *Nanotechnology*, 30(30), 2019, 305601.
[60] P. Zhang, H. Liang, H. Liu, J. Bai and C. Li, *Materials Chemistry and Physics*, 272, 2021, 125031.
[61] J. Yu, B. Wei, L. Zhu, H. Gao, W. Sun and L. Xu, *Applied Surface Science*, 284, 2013, 497-502.
[62] M. Yuan, F. Tian, G. Li, H. Zhao, Y. Liu and R. Chen, *Industrial & Engineering Chemistry Research*, 56(20), 2017, 5935-5943.
[63] X. Wang, S. Yang, H. Li, W. Zhao, C. Sun and H. He, *RSC Advances*, 4(80), 2014, 42530-42537.
[64] F. Tian, G. Li, H. Zhao, F. Chen, M. Li, Y. Liu and R. Chen, *Journal of Catalysis*, 370, 2019, 265-273.

[65] F. Tian, H. Zhao, G. Li, Z. Dai, Y. Liu and R. Chen, *ChemSusChem*, 9(13), 2016, 1579-1585.
[66] J. Cao, B. Xu, H. Lin, B. Luo and S. Chen, *Catalysis Communications*, 26, 2012, 204-208.
[67] W. Cui, W. An, L. Liu, J. Hu and Y. Liang, *Applied Surface Science*, 319, 2014, 298-305.
[68] O. Mehraj, B.M. Pirzada, N.A. Mir, M.Z. Khan and S. Sabir, *Applied Surface Science*, 387, 2016, 642-651.
[69] J. Ding, Z. Dai, F. Qin, H. Zhao, S. Zhao and R. Chen, *Applied Catalysis B: Environmental*, 205, 2017, 281-291.
[70] Y. Li, Y. Zhao, G. Wu, H. Ma and J. Zhao, *Materials Research Bulletin*, 101, 2018, 39-47.
[71] J. Pan, J. Liu, S. Zuo, U. A. Khan, Y. Yu and B. Li, *Materials Research Bulletin*, 103, 2018, 216-224.
[72] B. Pare, B. Sarwan and S.B. Jonnalagadda, *Applied Surface Science*, 258(1), 2011, 247-253.
[73] S. Shamaila, A.K.L. Sajjad, F. Chen and J. Zhang, *Journal of Colloid and Interface Science*, 356(2), 2011, 465-472.
[74] S.Y. Chai, Y.J. Kim, M.H. Jung, A.K. Chakraborty, D. Jung and W.I. Lee, *Journal of Catalysis*, 262(1), 2009, 144-149.
[75] Y. Liu, W.J. Son, J. Lu, B. Huang, Y. Dai and M.H. Whangbo, *Chemistry–A European Journal*, 17(34), 2011, 9342-9349.
[76] K. Xu, X. Fu and Z. Peng, *Materials Research Bulletin*, 98, 2018, 103-110.
[77] Q. Yang, Y. Zhai, X. Li and H. Li, *Materials Research Bulletin*, 106, 2018, 409-417.
[78] X. Hu, G. Zhang, C. Yin, C. Li and S. Zheng, *Materials Research Bulletin*, 119, 2019, 110559.
[79] R. Mahdavi and S.S.A. Talesh, *Materials Chemistry and Physics*, 267, 2021, 124581.
[80] H. Tang, Y. Ao, P. Wang and C. Wang, *Materials Science in Semiconductor Processing*, 27, 2014, 909-914.
[81] W. Zhang, F. Dong, T. Xiong and Q. Zhang, *Ceramics International*, 40(7), 2014, 9003-9008.
[82] H. Liu, W.R. Cao, Y. Su, Z. Chen and Y. Wang, *Journal of Colloid and Interface Science*, 398, 2013, 161-167.
[83] C.W. Siao, W.L.W. Lee, Y.M. Dai, W.H. Chung, J.T. Hung, P.H. Huang, W.Y. Lin and C.C. Chen, *Journal of Colloid and Interface Science*, 544, 2019, 25-36.
[84] W. Wang, M. He, H. Zhang and Y. Dai, *International Journal of Electrochemical Science*, 11, 2016, 1831-1839.
[85] L. Allagui, B. Chouchene, T. Gries, G. Medjahdi, E. Girot, X. Framboisier, A.B. haj Amara, L. Balan and R. Schneider, *Applied Surface Science*, 490, 2019, 580-591.
[86] Z. Liu, W. Xu, J. Fang, X. Xu, S. Wu, X. Zhu and Z. Chen, *Applied Surface Science*, 259, 2012, 441-447.
[87] S.K. Mandal, K. Dutta, S. Pal, S. Mandal, A. Naskar, P.K. Pal, T.S. Bhattacharya, A. Singha, R. Saikh, S. De and D. Jana, *Materials Chemistry and Physics*, 223, 2019, 456-465.
[88] D. Zhang, M. Wen, B. Jiang, G. Li and C.Y. Jimmy, *Journal of Hazardous Materials*, 211, 2012, 104-111.
[89] L. Zhu, C. He, Y. Huang, Z. Chen, D. Xia, M. Su, Y. Xiong, S. Li and D. Shu, *Separation and Purification Technology*, 91, 2012, 59-66.
[90] J. Liang, C. Shan, X. Zhang and M. Tong, *Chemical Engineering Journal*, 279, 2015, 277-285.
[91] B. Gao, A.K. Chakraborty, J.M. Yang and W.I. Lee, *Bulletin of the Korean Chemical Society*, 31(7), 2010, 1941-1944.
[92] X. Chang, J. Huang, C. Cheng, W. Sha, X. Li, G. Ji, S. Deng and G. Yu, *Journal of Hazardous Materials*, 173(1-3), 2010, 765-772.
[93] H. Tian, J. Li, M. Ge, Y. Zhao and L. Liu, *Catalysis Science & Technology*, 2(11), 2012, 2351-2355.

[94] G. Li, F. Qin, H. Yang, Z. Lu, H. Sun and R. Chen, *European Journal of Inorganic Chemistry*, 2012(15), 2012, 2508-2513.
[95] Y. Zhiyong, D. Bahnemann, R. Dillert, S. Lin and L. Liqin, *Journal of Molecular Catalysis A: Chemical*, 365, 2012, 1-7.
[96] L. Zhang, W. Wang, S. Sun, Y. Sun, E. Gao and J. Xu, *Applied Catalysis B: Environmental*, 132, 2013, 315-320.
[97] X. Liu, H. Yang, H. Dai, X. Mao and Z. Liang, *Green Chemistry*, 17(1), 2015, 199-203.
[98] W. Li, S.A. He, X. Wang, Q. Ma and C.H. Zhao, *International Journal of Energy Research*, 43(6), 2019, 2162-2171.
[99] P.A. Hsieh, P.J. Chen, L.M. Lyu, S.Y. Chen, M.C. Tseng, M.Y. Chung, W.H. Chiang, J.L. Chen and C.H. Kuo, *ACS Applied Materials & Interfaces*, 13(49), 2021, 58799-58808.
[100] Y. Wang, M. Batmunkh, H. Mao, H. Li, B. Jia, S. Wu, D. Liu, X. Song, Y. Sun and T. Ma, *Chinese Chemical Letters*, 33(1), 2022, 394-398.
[101] J. Yuan, J. Wang, Y. She, J. Hu, P. Tao, F. Lv, Z. Lu and Y. Gu, *Journal of Power Sources*, 263, 2014, 37-45.
[102] Y. Fujishima, S. Okamoto, M. Yoshiba, T. Itoi, S. Kawamura, Y. Yoshida, Y. Ogura and Y. Izumi, *Journal of Materials Chemistry A*, 3(16), 2015, 8389-8404.
[103] X. Zhao, Z. Zhao-Karger, D. Wang and M. Fichtner, *Angewandte Chemie*, 125(51), 2013, 13866-13869.
[104] C.R. Michel, N.L.L. Contreras and A.H. Martínez-Preciado, *Sensors and Actuators B: Chemical*, 160(1), 2011, 271-277.
[105] K. Zhao, X. Zhang and L. Zhang, *Electrochemistry Communications*, 11(3), 2009, 612-615.
[106] K. Wang, F. Jia, Z. Zheng and L. Zhang, *Electrochemistry Communications*, 12(12), 2010, 1764-1767.

Chapter 3

Experimental Techniques

Nanotechnology was revolutionised in the early 1980s, following the invention of two extensive breakthroughs: the development of cluster science and the development of scanning tunnelling microscopes (STMs) that led to the discovery of fullerenes in 1981 and the structural determination of carbon nanotubes in 1991. Physicochemical, optical and thermal properties of nanomaterials can be determined through characterization tools. These properties can be determined through a number of measurements. So let's take a look at Characterization tools for nanomaterials.

3.1 Synthesis Techniques

Morphology controlled bismuth oxychloride (BiOCl) nanomaterial synthesis by hydrothermal and heating method. A combination of an oven and an autoclave is used to execute the hydrothermal process, whereas the heating method occurs by controlling the temperature of the system. The graphene oxide (GO) synthesised by modified Hummers' method, and also BOC-GO composite nanomaterial synthesis with graphene oxide (GO) and bismuth oxychloride (BiOCl) by hydrothermal method.

3.1.1 Autoclave

Autoclaves are pressurised devices used to heat liquids or organic solvents above their boiling point at a pressure that is greater than atmospheric pressure. An autoclave is basically a cylindrical iron chamber with a screw cap. The cap can be tightly attached to the iron chamber so that it is able to withstand very high pressures during reaction. An inert reaction chamber is built inside the iron chamber using a cylindrical Teflon tube and a Teflon cap. An autoclave arrangement used to hydrothermally synthesise BiOCl and BiOCl based composite nanomaterials shown in Figure 3.1.

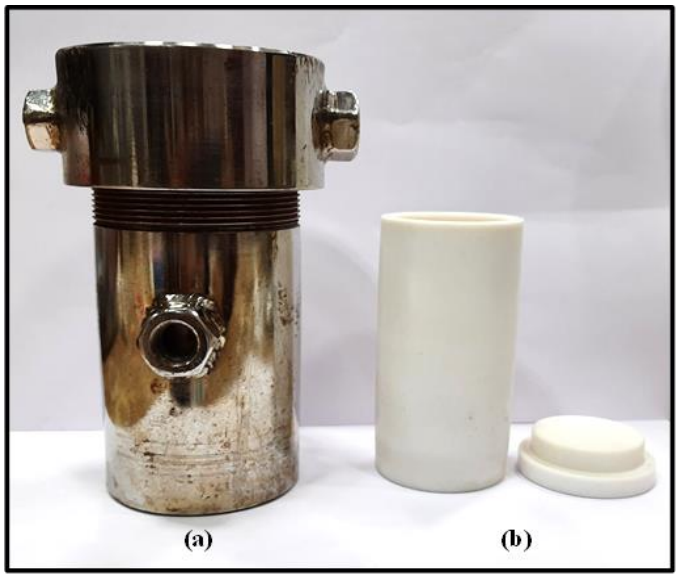

Figure 3.1: Image depicting (a) Autoclave setup and (b) the Teflon tube in the autoclave

3.1.2 Oven

In order to carry out the hydrothermal reaction, an oven is used. In addition to a simple low temperature oven, since the reaction temperature did not exceed 250 °C, the reaction had to be performed at a low temperature. An electronic temperature controller can control the heating rate of the oven to within ± 0.5 °C of accuracy. Additionally to being used for synthesis, the

ovens are also used for drying the samples, and which demonstrate in Figure 3.2(a).

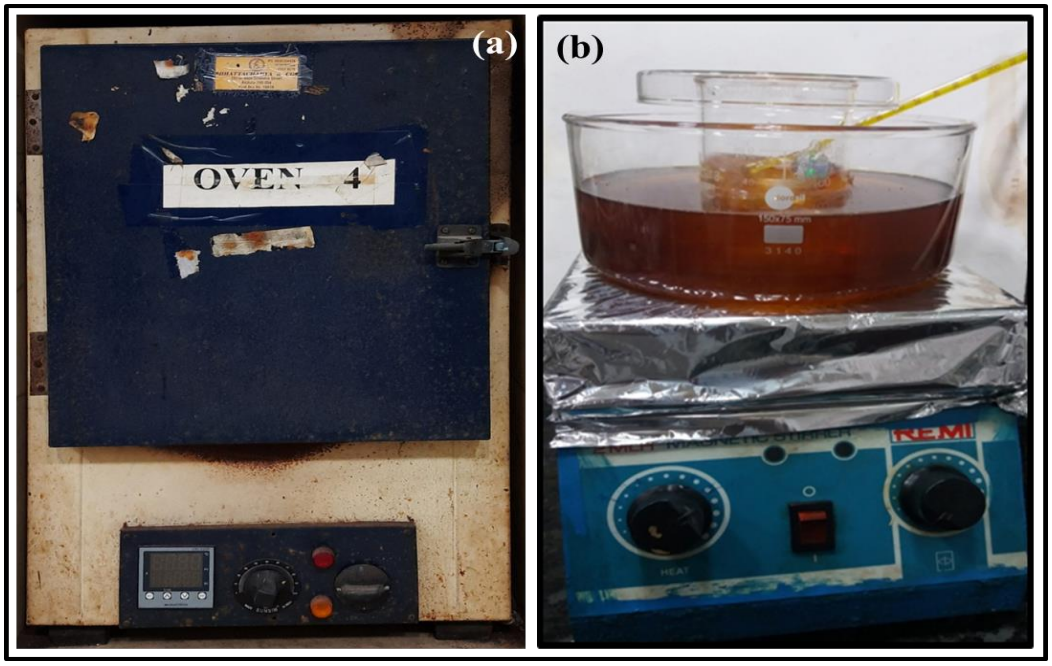

Figure 3.2: Digital image setup of an oven (a) and synthesis setup of Chemical Bath method (b)

3.1.3 Heating/Chemical-Bath Method

Mixture of chemicals were synthesised in this study by agitating them over an oil bath for an extended period of time at temperatures ranging from 40 °C to 200 °C. Following the completion of the reaction, filtration and cooling were performed. The washed precipitate was cleaned with ethanol and deionized water several times and then dried for 24 hours at 80 °C in an oven. This is also shown in Figure 3.2(b).

3.2 Characterization Techniques

3.2.1 X-ray Diffraction Technique

Diffraction of X-rays can be used to characterise crystalline materials in a non-destructive way. In addition to providing information about structure, phase and preferred crystal orientations (texture), it provides additional structural parameters such as average grain size, crystallinity, crystal defects, and deformations. The crystal peaks of XRD are created by Constructive Interference from a monochromatic X-ray beam that scatters at an angle from each set of lattice planes. Crystal lattice position determines the maximum intensity of an atom. Diffraction patterns are replicates of periodic arrangements of atoms within a material. It is possible to identify the phases of various crystal samples by browsing the standard database of powder X-ray diffraction patterns (PXRD)[1].

The development of X-ray technology began in the year 1912, when diffraction by any crystal confirmed X-ray's wave nature. The X-ray diffraction technique can be used to determine the crystal structure at various planes.

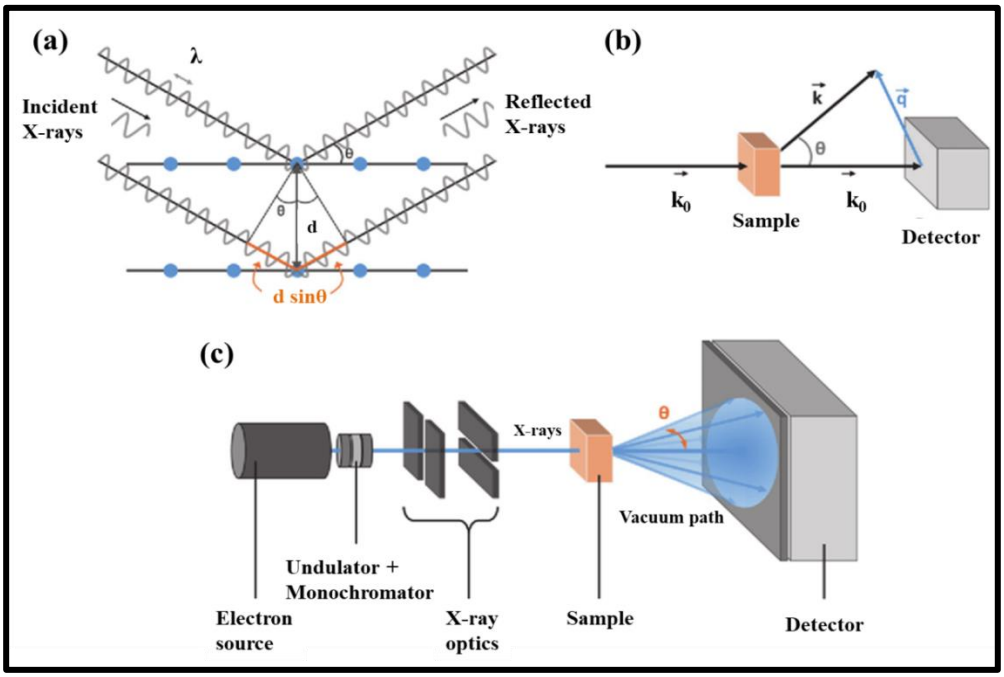

Figure 3.3: (a) The diagram of Bragg equation for X-rays scattering, (b) the outline of geometrically constructed scattering and (c) Diagram of the setup for a small-angle X-ray scattering experiment

Bragg's law is involved in the analysis of structural patterns using the diffraction method. The atoms in a crystal lattice act as scattering sources perpendicular to the monochromatic X-rays they are impinging upon. There are parallel planes of reflection within the crystal lattice. When two reflected waves from different planes are projected at an angle of a certain angle, the intensity of the reflected beam will be maximum, and it is schematically represented in Figure 3.3. The relation that gives rise to this condition is called Bragg's law,

$$2dSin\theta = n\lambda \qquad (3.1)$$

where,

d = inter planar distance,

θ = the Bragg's angle,

n = the diffraction order and

λ = the wavelength of the x-rays.

Figure 3.4: Digital image of X-rays diffractometer to the D8 advance bruker (a), Rigaku (MiniFlex 600) setup (b) and inner chamber of the bench top (c)

An X-ray wavelength in diffraction ranges from approximately 0.5 to 2.5 Å. If the incident beam hits the atomic planes of the crystal at the Bragg angle, it will cause constructive interference. To determine d_{hkl} values, the atomic planes are indexed according to conventional Miller index notation. There could be several parallel lattice plane groups in a crystal structure. An interference peak will be produced by each set of planes due to X-ray diffraction. There will thus be several diffraction peaks in the overall diffraction pattern. Due to its importance, the d value is determined by changing either the θ or λ in the Bragg equation and measuring the other. In terms of structural analysis, there are three methods: Laue technique, rotating crystal method, and powder technique. In these methods the following variables are taken into account and the digital photograph of the setup demonstrated in Figure 3.4(a).

TABLE 1: XRD measurements using different methods

Different types of Diffractometer		
Method	**Wave Length(λ)**	**Incident Angle(θ)**
Laue Method	Variable	Fixed
Rotating Crystal Method	Fixed	Variable (In part)
Power Method	Fixed	Variable

XRD traces for the samples were measured using an Rigaku Mini Flex 600 X-ray diffractometer at 40 KV and 30 mA in the θ-2θ mode with monochromatized CuK_α radiation, (λ = 1.5404 Å), and the digital photograph of the setup can be seen in Figure 3.4(b,c).

3.2.2 Electron Microscope

Microscopically small objects can be observed with an electron microscope. Instead of using visible light, an electron microscope uses an electron beam to focus on objects. The wavelength of De Broglie for electrons is longer for a given energy, as electrons have lower mass than protons and neutrons. This is the reason why electrons are ideal for use in electron microscopes. A wavelength of electrons is much smaller than a visible light wavelength, so features can be differentiated by fractions of a nanometre or even less. Electron microscopes are more advantageous than ordinary microscopes. Instead of traditional lenses, normal microscopes use coil-shaped electromagnets to bend electron beams as they travel through them. As opposed to ordinary microscopes, where an image is magnified, electron microscopes produce an electron micrograph as an image and not as a magnified image. There are three main types of electron microscopes: scanning electron microscopes (SEMs), transmission electron microscopes (TEMs), and scanning transmission electron microscopes (STEMs).

3.2.2.1 Field Emission Scanning Electron Microscopy (FESEM)

The electron microscope can be used for the analysis of material properties, defects, topography (e.g., particle size and shape) and metallographic details of nano-crystalline powders and bulk materials. The magnification ranges between 10 and 300,000 times, and the depth of the field is almost infinite. FESEM produces images with reduced electrostatic distortion, and spatial resolutions between 1 and 0.5 nm, which are comparable to those obtained with conventional Scanning Electron Microscopy (SEM). An electron beam's interaction with a sample can have a wide range of effects as shown in Figure 3.5(a).

3.2.2.1.1 Working Principle

In the scanning electron microscope, the field emission cathode provides a narrow probe beam at low and high electron energies, improving the spatial resolution and minimising sample damage and charging[2]. Some applications require higher magnification than that available through in-lens FESEM, and the schematic illustration of the working principle is demonstrated in Figure 3.5(b). In-lens imaging is used for ultra-high-magnification imaging, and the digital image of the setup is demonstrated in Figure 3.5(c,d).

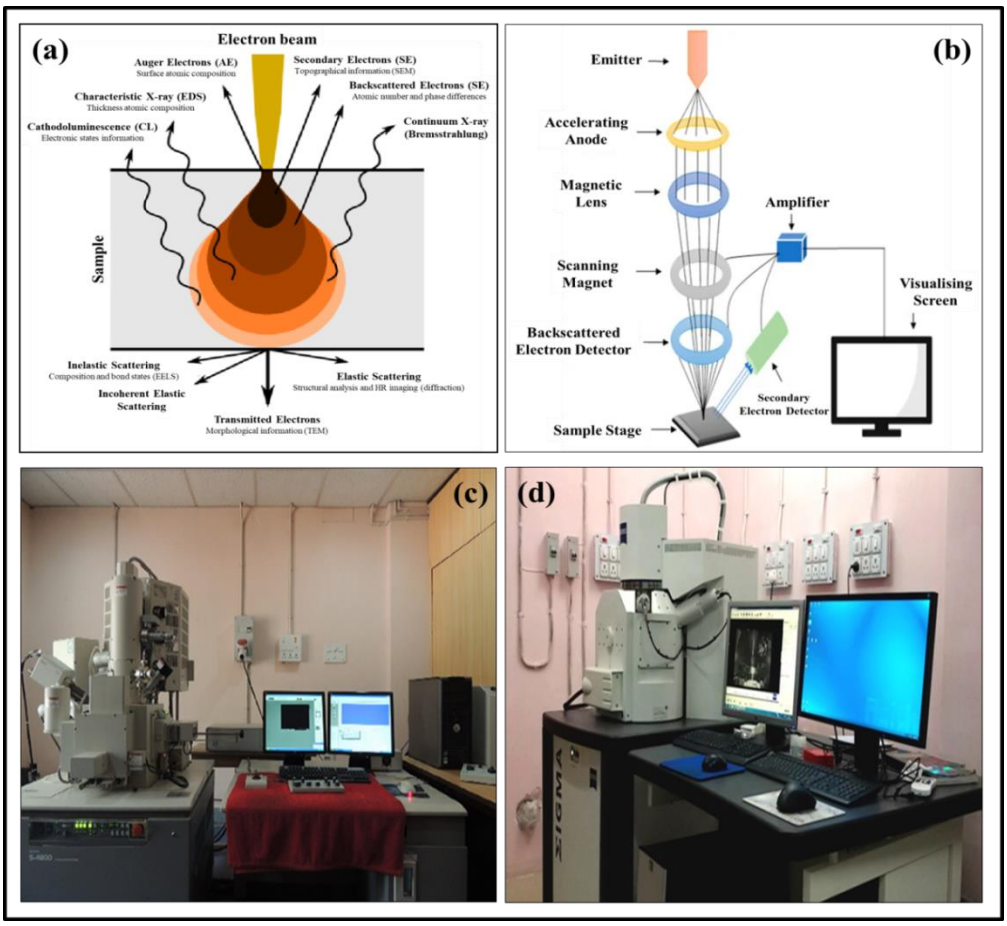

Figure 3.5: The interaction between electron beams and samples can have a variety of effects (a), scanning electron microscope working principle diagram (b), **d**igital photograph of HITACHI S4800 (c) and ZEISS SIGMA FESEM setup (d)

3.2.2.2 Energy Dispersive X-ray Spectroscopy (EDS)

Energy dispersive X-ray spectra (EDS or EDX), is used to determine the physical composition of a sample. An electron beam bombards the samples, interacting with the X-rays to analyse their composition. Each element possesses a unique atomic structure, which is why its electromagnetic emission spectrum features a unique set of peaks. This is the basis for the characterization process. In SEMs, electron beams bombard the sample's surface, which produces electron ejection from its atoms. In order to equalise the difference in energy between these two states of electrons, higher state electrons are inserted into the electron vacancies, producing an X-ray. Radiation of this type of energy gives information about its source.

Solid state lithium-drifted silicon detectors have been used for EDS X-ray equipment. The ratio of X-ray energies to X-ray abundances varies depending on what is emitted. The detector creates a charge pulse when struck by an incident X-ray. In proportion to the energy of the X-ray with the charge pulses

are generated. The voltage pulses (still proportional to X-ray energy) are converted to a charge pulse by a charge-sensitive preamplifier. Once the signal has been sorted by voltage, it is received by a multi-channel analyser. An X-ray is displayed and data evaluated on a computer according to the energy obtained from voltage measurement. Now it can be determined the composition of elements in a sample volume by evaluating the spectral energy level of X-rays versus counts. Figure 3.6 and Figure 3.5(c) shows the schematic representation and digital image of an EDS set-up which attached to the FESEM instrument.

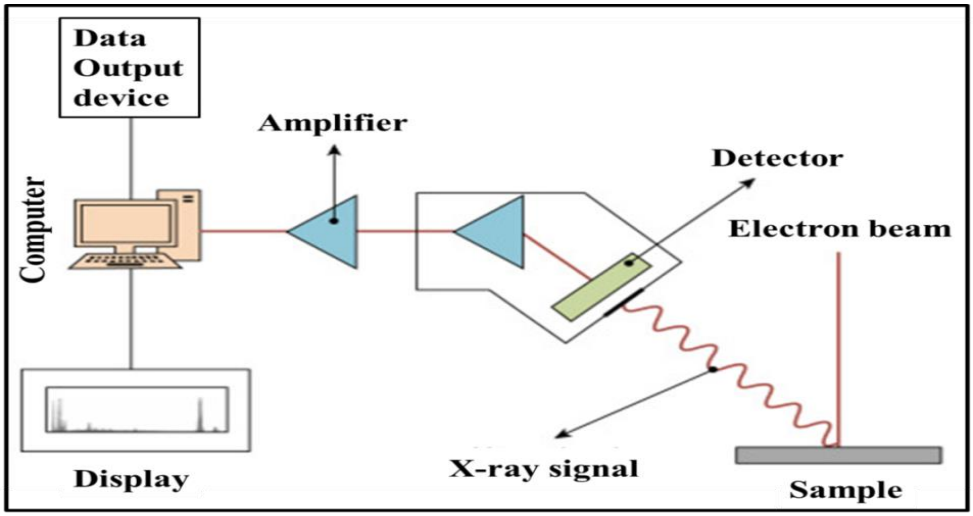

Figure 3.6: Energy Dispersive X-ray Spectroscopy schematic diagram

3.2.2.3 High Resolution Transmission Electron Microscopy (HRTEM)

The crystal structure at the atomic level imaging can be captured using high-resolution transmission electron microscopes. The image is not created by absorption as it is in traditional microscopes. It is instead created by interference in the image plane. This method has high resolution and is a valuable tool in order to study the nanoscale properties of materials. HRTEM uses an accelerating voltage that is very stable in the range of ppms or even higher. This results in a very stable accelerating voltage. High-resolution TEM has the potential to display crystal structure, defects, and single atoms. An array of materials can be examined using HRTEM at the atomic scale in order to determine their crystal structure and lattice defects. It can characterise grain boundaries, point defects, and stack failures.

3.2.2.3.1 Working Principle

The basic properties of HRTEM, the low refractive index direction of a very thin crystal, have been positioned perpendicular to the electron beam. Figure 3.7(a-d) shows how all lattice planes roughly

parallel to the electron beam diffract the main beam corresponding to the Bragg position[2]. The digital photograph of HRTEM setup is demonstrated in Figure 3.7(e).

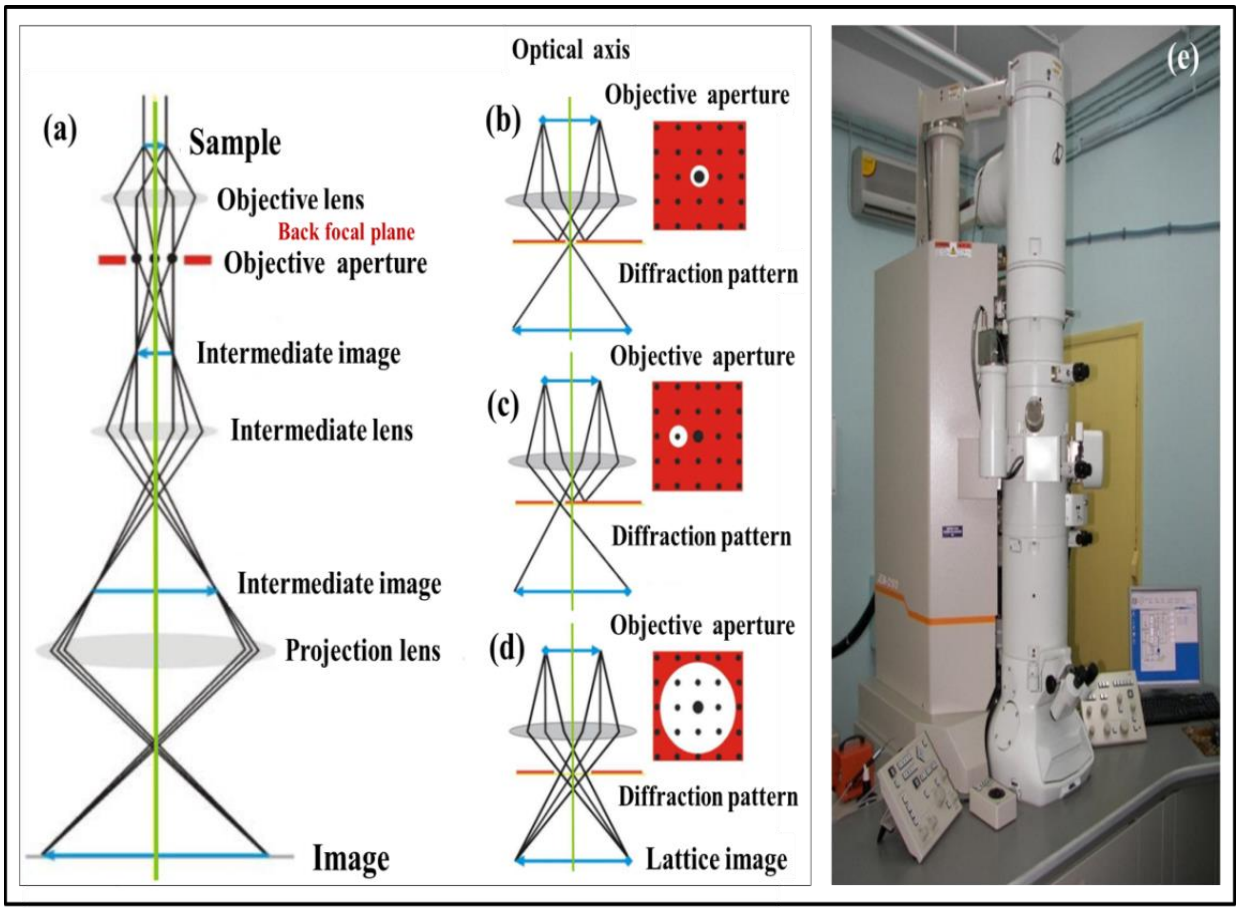

Figure 3.7: Ray diagram of a TEM operating in image mode (a), three basic imaging modes of TEM: bright field image (b), dark field image (c) and high resolution image (d) and digital photograph (e) of HRTEM setup

a) A diffraction pattern is created by transforming the periodic potentials of the 2D electrons. All of the diffracted light and original rays are collected again in the objective lens, and their interference produces an inverse transformation.

b) A typical magnification of 106 times was achieved on the screen by using the following electro-optical system.

3.2.3 Spectroscopy

In electromagnetic radiation, the wavelength or frequency of the radiation affects how it interacts with matter. Spectroscopy is the science that analyses and interprets electromagnetic spectra obtained after measurement of the wavelengths or frequencies of the radiation. There is also the possibility that matter

waves, acoustic waves, and gravitational waves are radiative energies, and the Laser Interferometer Gravitational-Wave Observatory (LIGO) has identified gravitational waves with a spectral signature.
A spectrometer is a device that detects and determines colour based on the properties of visible light and all ranges of electromagnetic radiation. A prism disperses visible light in a gas phase, and the wavelength dependence of absorption by the material is determined. An important tool in physics, chemistry, and astronomy is spectroscopy. In addition to evaluating the structure and composition of matter over a broad range of scales, it can also determine the electronic structure of matter over astronomical distances. Its applications include tissue analysis and medical imaging in the biomedical spectroscopy field.

3.2.3.1 Ultraviolet-Visible-Near-Infrared (UV-Vis-NIR) Spectroscopy

UV-Vis spectrophotometry mainly analyses chemical reactions at ultraviolet or visible wavelengths. These regions of the electromagnetic spectrum are responsible for triggering electronic transitions. In most cases, UV-Vis spectrophotometry is carried out as a quantitative analysis. An ultraviolet or visible lamp for deuterium or tungsten, a source of ultraviolet light and a reference light, a detector, and a monochromatic light are required in this technique. UV light produces the ultraviolet spectrum when exposed to the sample. The cuvette is designed to hold the samples and introduce them into the path of light. Quartz cuvettes are transparent at wavelengths over 180 nm and at wavelengths less than 310 nm, so they are commonly used for ultraviolet measurements. The absorption of plastic and glass cuvettes is lower than this wavelength, and for that reason, it is not possible to measure absorption below this wavelength.

3.2.3.1.1 Working Principle

An UV-Vis-NIR spectrometer measures a sample's reflection, absorbance, or transmission properties, in other words, its optical properties. Molecular absorption of light in the ultraviolet range (200-400 nm) occurs in this spectroscopy. An absorbance function in the UV-Vis region reveals how much light a compound absorbs. An electronic excited state is achieved whenever an ultraviolet photon is absorbed by a molecule. As an electron moves from an height occupied molecular orbital (HOMO) of the molecule to an lowest unoccupied molecular orbital (LUMO), it can also be said that the electron is promoted. HOMO and LUMO both have energy differences which are equal to the energy absorbed by the ultra-violet radiation. A spectroscopic method is based on this principle.

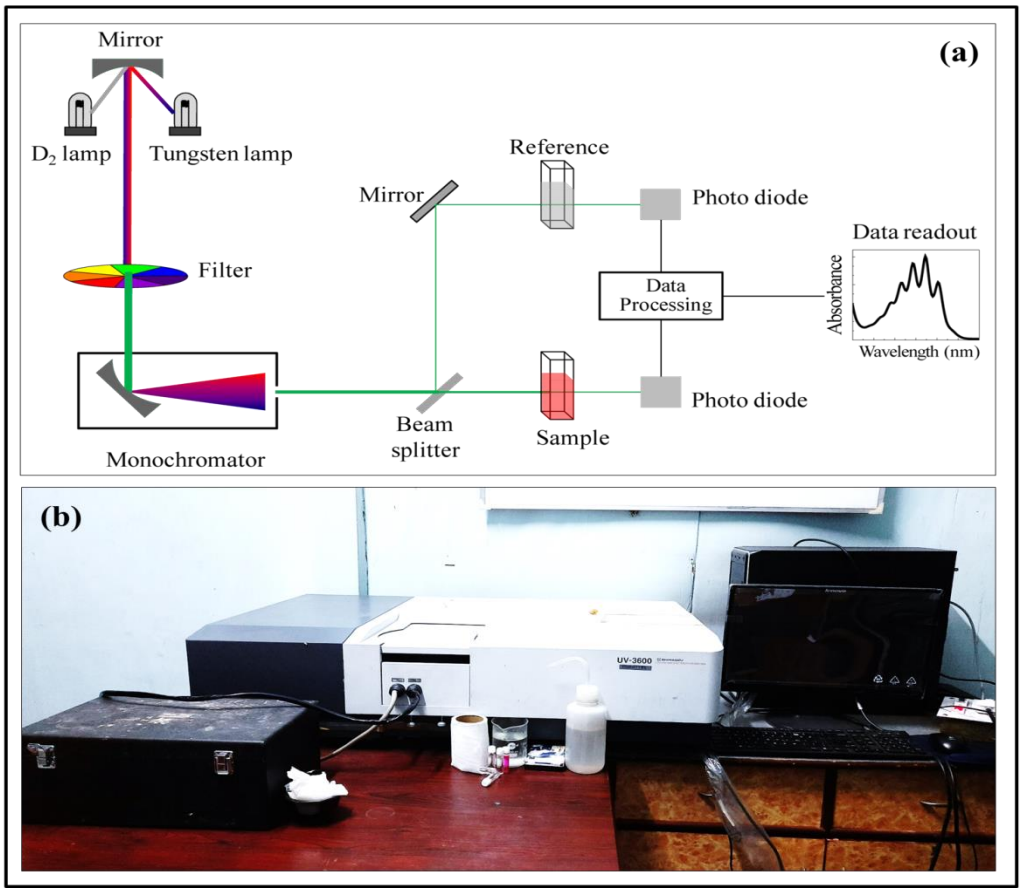

Figure 3.8: The schematic diagram of UV-VIS-NIS Spectrophotometer (a) and digital photograph of UV-VIS-NIS (SHIMADZU UV-3600) Spectrophotometer (b)

Absorption or reflectance measurements can be used to determine parameters such as ionisation energy, electron affinity, and band gap (i.e. absorption energy). A measurement of the band gap of a material is possible by using the experiment because photons with energies greater than the band gap will be absorbed, while photons with energies less than the band gap will be transmitted. To quote Bardeen, for the parabolic band structure, the relationship between the absorption coefficient (α) and the band gap is as follows:

$$(\alpha h\nu) = A(h\nu - E_g)^n \qquad (3.2)$$

where,

n = A band gap is described by an electronic nature represented, n = 1/2 for direct permitted transitions, n = 2 for indirect permitted transitions, n = 3 for indirect forbidden transitions, and n = 3/2 for direct forbidden transitions.

The measure of A is,

$$A = \log(I/I_0) \qquad (3.3)$$

Here, I_0 is the intensity of the incident beam, whereas I is its transmitted beam.

Energy difference E_g between the valence band and conduction band is determined by optical gap and photon energy $(h\nu)$ is determined by incident photon energy. In case of an indirect transition, $(\alpha h\nu)^{1/2}$ is showing a linear relationship with photon energy. $(\alpha h\nu)^{1/2}$ vs. $h\nu$ gives an intercept on the energy axis at $(\alpha h\nu)^{1/2} = 0$, and the optical gap is the intercept at $(\alpha h\nu)^{1/2} = 0$.

In scan-drive mode, the wavelength setting of the monochromator is changed automatically, and the recorder is led by the oscilloscope to record the absorbance and transmittance spectrum of the sample. The schematically illustrated process can be seen in Figure 3.8(a).

Nanoparticles with BiOCl have an absorption spectrum that varies with particle size and dielectric medium, while metal nanoparticles have absorption spectra that shift as particle size increases to longer wavelengths[2]. The most commonly used solvents are water, ethanol, hexane and cyclohexane. The UV-Vis-NIR spectra were carried out by the Shimadzu UV 3600 spectrophotometer, and it demonstrated digital photography in Figure 3.8(b).

3.2.3.2 X-ray Photoelectron Spectroscopy (XPS)

An X-ray photoelectron spectrometer (XPS) and monochromatic Al K_α X-ray (hν = 1486.6 eV) source were used as well as a hemispherical analyser (SPECS HSA 3500) to analyse the constituent atoms. Referenced in the above paragraph is a description of XPS's fundamental mechanism[3]. A photoelectron peak's kinetic energy (KE) and binding energy (BE) are directly correlated because of existing information about the incident x-ray energy. This method provides a way to identify elements and determine their atomic composition using standards. This relation is the basis for the determination of the electron binding energy by the spectrometer:

$$BE = h\nu - KE - \phi_{spc} \qquad (3.4)$$

where,

$h\nu =$ the energy of the incident ray and

$\phi_{spc} =$ the factor of the instrument.

The measurements however, were made from a small piece with a uniform growth area based on CF based materials. Survey scans were performed with pass energy of 40 eV, while HR scans were conducted with pass energy of 20 eV. A 10 kV voltage and 15 mA current are used for operating the X-ray source. The schematic diagram of X-ray photoelectron emission spectroscopy process and digital photograph of XPS are presented in Figure 3.9.

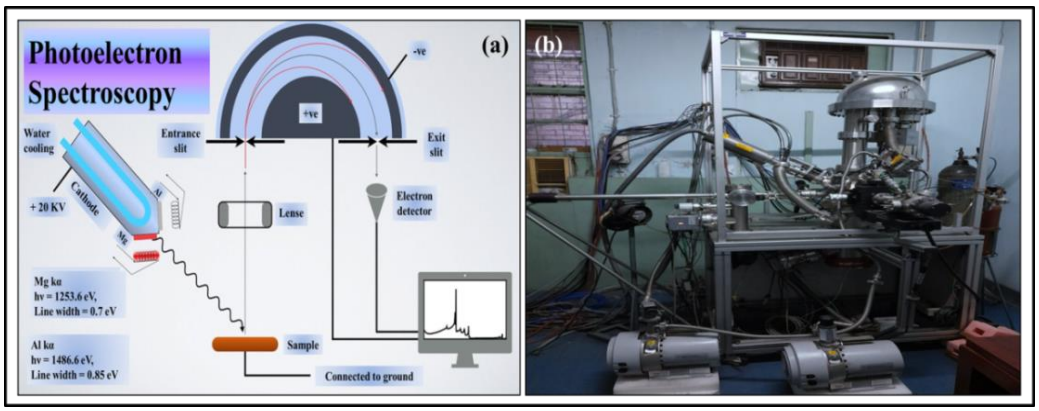

Figure 3.9: (a) Schematic diagram of X-ray photoelectron emission spectroscopy process, and (b) Digital photograph of XPS

3.2.3.3 Raman Spectroscopy

A Raman spectrum is performed to determine a system's vibrational, rotational, and other properties by scattering monochromatic laser light inelastically or via Raman scattering. Information about phonon modes is provided by the shift in energy. This shift in energy occurs when the phonons interact with the laser light. A laser beam illuminates a sample, and the electromagnetic radiation caused by the laser impact is collected by the lens and travels through the collimator. In order to produce Stokes-Raman scattering, the molecule relaxes into a vibrational state. It is important to alter the molecules' polarizability before the Raman scattering occurs. Molecular vibration results in anti-Stokes Raman light scattering, which occurs if the molecules are already vibrating. The Raman spectroscopy method can be extended to stimulate surface enhancement and Raman resonance spectroscopy. It is based on the polarizability change rate as well as the intensity of Raman scattering[4].

3.2.3.3.1 Working Principle

The Rayleigh scattering process occurs when a sample is irradiated with a monochromatic intense light source (usually a laser). The primary scattering occurs from the sample itself and takes place within a wavelength that is similar to the wavelength of the incoming laser radiation. There is a small amount of incoming light, approximately one photon out of a million, which scatters using a wavelength that is different from the original laser wavelength. A Raman spectrum provides both qualitative and quantitative information about the sample. The Raman spectra carried out by WITEC alpha 300R - RAMAN spectroscopy. The diagram of working principle, scattering line and digital photograph are shown in Figure 3.10.

a) The sample is excited by laser light,

b) All directions are scattered by this light,

c) Detectors that record Raman spectra use some of this scattered light and

d) Spectral features unique to the sample including the original laser (Rayleigh) frequency and the Raman spectral characteristics can be seen in this spectrum.

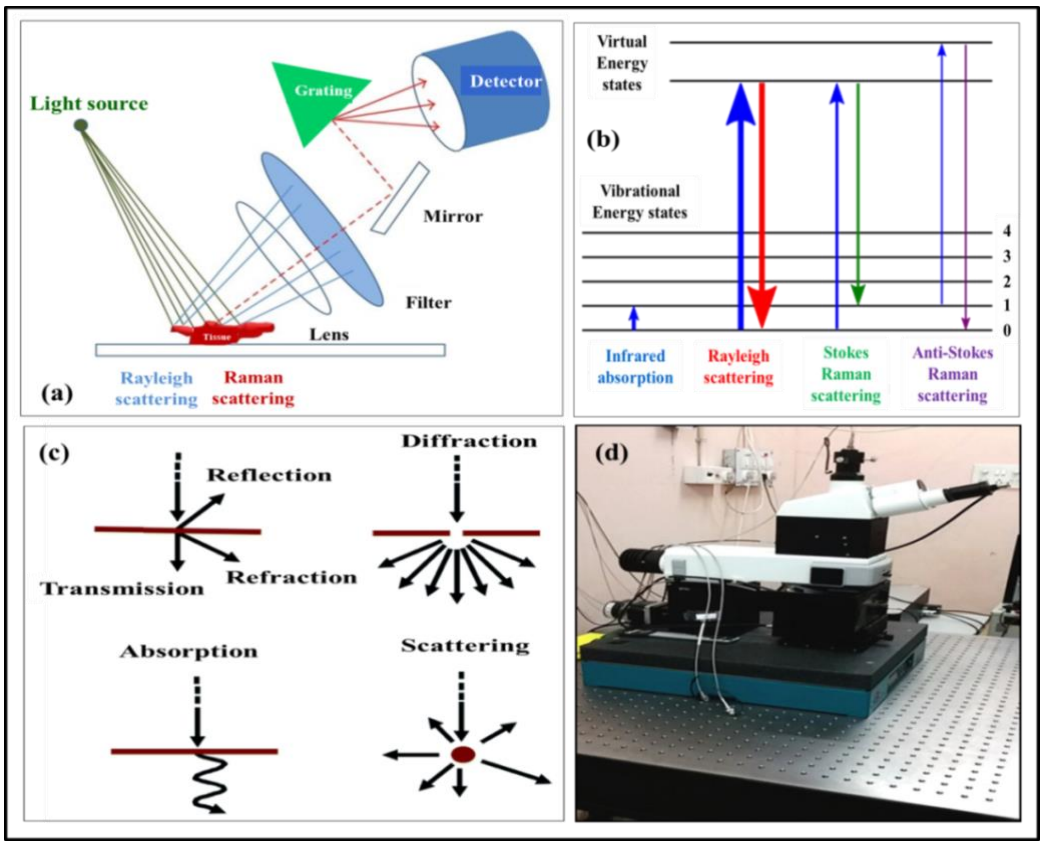

Figure 3.10: (a) Schematically light radiating from the excitation source (green line) induces Rayleigh scattering (blue line) and Raman scattering (red dotted line), Pure Raman scattering is detected in the absence of Rayleigh scattering, (b) energy-level diagram of the states involved, (c) different processes resulting from light-matter interactions and (d) digital photograph of Raman spectrometer

3.2.3.4 Fourier Transform Infrared (FTIR) Spectroscopy

As an analytical technique, Fourier Transform Infrared Spectroscopy (FT-IR) utilises Fourier Transforms to determine the chemical composition of a variety of organic chemicals, polymers, coatings, paints, adhesives, semiconductors, lubricants, gases, biological samples and inorganic materials. In addition to bulk or thin films, liquids, solids, pastes, powders, fibres and other form factors, FT-IR can be applied to analysing a wide array of biological materials. Analysing materials not only qualitatively (identification) but quantitatively (amount) is possible with this technique. The FT-IR technique can be applied to analyses up to ~ 11 millimetres in diameter, as well as to bulk measurements or to measuring sample layers up to ~ 1 micrometre thick. In FT-IR spectroscopy,

broadband spectra are obtained from NIR to FTIR wavelengths. A FT-IR spectrometer measures all wavelengths simultaneously, unlike a dispersive instrument such as a grating monochromator. FT-IR has long been used to obtain infrared spectra. Firstly, an interferogram is generated by using an interferometer, and then a Fourier Transform (FT) is applied to the interferogram to obtain the spectrum. FT-IR spectrometers collect and digitise the interferogram, perform the FT function, and display the spectrum. The FT-IR technique is effective in identifying chemicals because its range of frequencies is 4000 to 400 cm^{-1}, representing each molecule's molecular fingerprint[5]. The schematic diagram and digital photographs of the FT-IR spectrometer are shown in Figure 3.11.

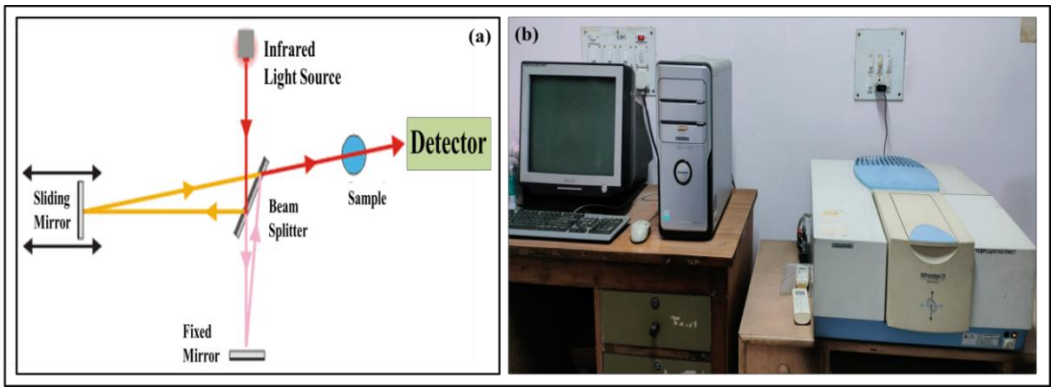

Figure 3.11: (a) Schematic diagram of FTIR and (b) digital photograph of FTIR

3.2.4 Brunauer–Emmett–Teller (BET)

The BET theory explains gas adsorption on solid surfaces, and is one of the most important methods of determining surface areas of materials. Physical adsorption, or physisorption, is also commonly mentioned as the observations. BET theory applies mainly to systems of adsorption that use a probe gas in addition to the adsorbed material (called the adsorptive) to determine specific surface area. Brunauer, Emmett, and Teller presented their theory in 1938 in the Journal of the American Chemical Society[6].

As a gaseous adsorbate, nitrogen is the maximum usually working for probing surfaces. Due to these reasons, the usual BET analysis is commonly accompanied at N_2's boiling point (77 K).

In addition, other probing adsorbents can also be used for surface area measurement, although less commonly, allowing for surface measurements at different temperatures[7]. Adsorbents such as argon, carbon dioxide, and water are examples of such devices. A molecule's adsorption cross section and specific surface area determine its adsorption volume. The specific area is scale-dependent property and has no single true value[8]. Figure 3.12 shows a schematic illustration of BET and a digital image of the device.

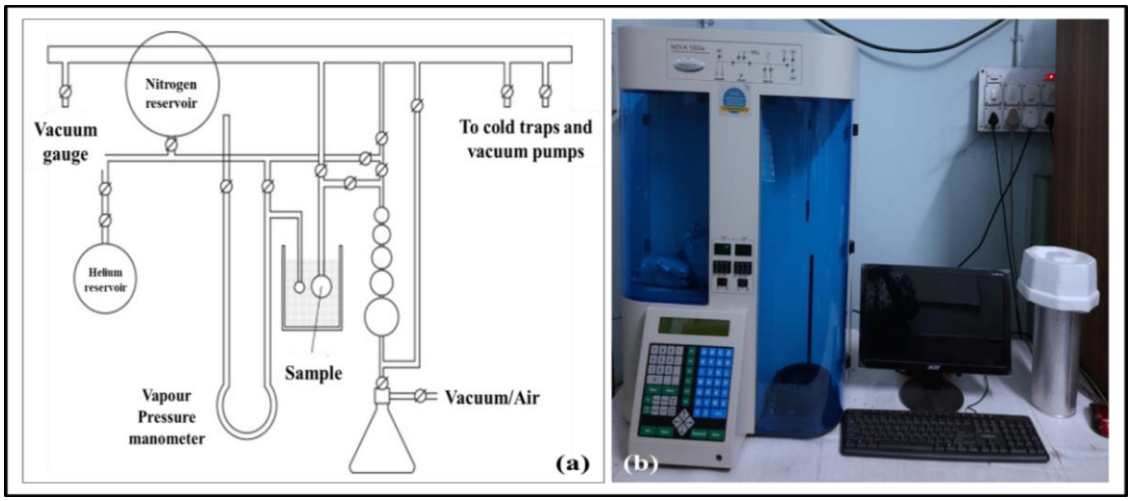

Figure 3.12: (a) The schematic diagram and (b) digital photograph of BET

3.2.4.1 Application

Solid catalysis depends greatly on catalyst surface area for catalytic activity. By applying the BET method, the superficial areas of mesoporous silica and layered clay minerals have been calculated to be hundreds of metres per gram.

3.2.5 Mott–Schottky

According to a Mott–Schottky plot, capacitance is represented by the reciprocal of the square of the capacitance ($1/C^2$), as a function of the potential difference between bulk semiconductors and bulk electrolytes. A linear plot is evident in many theoretical models and experiments. A Mott-Schottky analysis is the process of observing Mott-Schottky plots to determine system properties (such as flat band potentials, doping densities, or Helmholtz capacitances) [9].

The depletion layer (ω) is correspondingly larger when bias voltage (V) is applied,

$$\omega = [\frac{2\varepsilon}{qN_D}(V + V_{bi})]^{1/2} \qquad (3.5)$$

where,

$\varepsilon = permittivity\ (\varepsilon_T \varepsilon_0)$,

$q = elementary\ charge$,

$N_D = doping\ density\ and$

$V_{bi} = built\ in\ potential.$

At the surface of the semiconductor (on the liquid electrolyte side), the positive charge is compensated by ionic negative charge. The interface between the metal and semiconductor forms a dielectric capacitor when the charges separate.

3.2.6 Nyquist

Signal processing and automatic control use a Nyquist plot to visualise frequency responses. Nyquist plots are used most commonly to evaluate the stability of criterion. In cartesian coordinates, the X-axis shows the real portion of the transfer function. On the Y-axis is plotted the imaginary portion. Plots for each frequency can be obtained by sweeping frequency as a parameter. This plot can be described in polar coordinates, where radial coordinates, or gain, are radially centred, and angular coordinates, or phase, are angularly centred. Harry Nyquist, who was once involved with Bell Laboratories, paved the way for the Nyquist plot.

An open-loop system without feedback loop can be used to assess the stability of closed-loop negative feedback systems. An open-loop system can be fitted with the Nyquist stability criterion. The system with delays and other non-rational transfer functions are easily analysed with this method, which is not the case when analysing systems by other methods. Stability can be measured by counting how many times the point has been encircled by other points (-1, 0). Crossings of the real axis, which indicate the range over which the system will be stable, can be used to estimate the gains[10].

3.2.7 Zeta Potential

As a method for defining surface functionality and particle stability, zeta potential measurements have gained in importance over the past few decades. Zeta potential analyses are primarily designed to determine a material's surface charge. Various types of materials may be used, ranging from nanoparticles to membranes or silicon wafers. A zeta potential is a concept that is influenced by the pH value and ionic strength of a medium. Here, discusses the theory behind the zeta potential, the techniques for analysing it, and its use in various applications[11].

3.2.7.1 Working Principle

Zeta potential will be established on any material in contact with a liquid medium. Surface properties include zeta potential. Zeta potential is commonly expressed in millivolts. Surface functional groups of a material react with the surrounding medium when in contact with a liquid. An accumulation of oppositely charged ions occurs when a surface charge is created. The electrochemical double layer is

formed when these counter-ions arrange themselves spontaneously. Zeta potential is equal to the sum of the initial surface charge and the accumulated layer[12].

3.2.8 Photocatalytic property measurement

3.2.8.1 Basics of Photocatalysis

Solar power is the only source of renewable energy in the universe. The world's current annual energy needs are met in one hour by sunlight reaching the earth's surface. Scientists are finding ways to collect, exploit and store solar power directly or indirectly. It has been suggested that plants are the world's largest chemical factory, because photosynthesis is the largest chemical factory in the world. Miniaturisation and nanomaterials are considered key to a sustainable future, which is why nanotechnology has received much attention in recent years. Nano-chemistry equips scientists with the tools required to create nanomaterials that are controlled in size, shape, and surface properties. Therefore, some groups of scientists are currently working on the synthesis of novel non-structural materials. In this process, photon energy is absorbed from the sun and converted into kinetic or electrical energy[13].

Metal complexes and organometallic compounds provide a vast array of reactions that can be induced by light. This is one of the reasons why researchers are interested in photocatalytic reactions. Organic photochemistry, in general, can be adequately described in terms of the properties of the electronic excitation and the resulting reactions if only three participating states are considered. Crossing results in the ground state, first excited singlet state, and the corresponding triplet excited state.

In the following section is described the design of the Photoreactor and its mathematical modelling.

3.2.8.2 Design of Photoreactor

Photoreactors are apparatus and devices that bring photons, photocatalysts, and reagents into contact and collect the reaction products generated by physicochemical reactions. Their shapes and modes of operation are varied and they can operate in different environments. As far as photoreactor design is concerned, one needs to establish its type, mode of operation, size as well as optimal operating conditions. A photoreactor can generally be divided into three types, based on how they are operated:

a) Batch reactors, which exchange matter with the environment during operation,
b) Semi-continuous reactions, which exchange products and reactants with the environment and
c) Continuous reactors, which have a continuous inlet and outlet of equal mass[14].

The radiation and the photoreactor are the main components of a photocatalytic system, while the reactor configuration for a thermal catalytic process is decided based on the

a) Mode of operation,
b) Phases present in the reactor,
c) Flow properties,
d) Heat exchange requirement and
e) The composition and operating conditions of the starting reaction mixture.

Besides the parameters already discussed, the choice of heterogeneous photoreactors also depends on the geometry. The materials used to ensure the penetration of radiation through the reaction mixture, taking into account. Monocrystalline semiconductors affect penetration depth in a sophisticated fashion by absorbing the photon at energy higher than the forbidden band of the photocatalyst.

Photoreactors generally have an internal 400 W high-pressure mercury spotlight (Philips), surrounded by a water-cooled quartz jacket, which is used to contain an ultraviolet filter allowing wavelengths >400 nm. Two 40 W UV (Philips) tubes with an emission wavelength of 254.6 nm (UVC) were used to investigate photocatalyst activity under UV light irradiation, along with a 15 cm distance between the tubes and the photocatalytic media.

Approximately 0.03 g of RhB sample and 40 mL of 10^{-5} M test solution were used in the catalysis media. Different time durations of constant stirring were used for the photocatalysis experiment. Degraded solution was collected after a predefined time period. An absorption study was performed later on these collected solutions. The photocatalytic test for as-synthesised samples was carried out by using RhB, EB and MO as organic dyes. To disperse the sample in dye solution, a 40 mL quartz beaker was prepared for UV light irradiation. Two walled glass beakers were used for visible light illumination. In order to negate the effects of temperature on catalysis, continuous cold water was pumped between the walls. As a result of stirring the mixture from dark to light for an hour, the catalyst samples and dye molecules were able to adsorb and desorb. A sample of the solutions exposed to light was collected about 4 mL at intervals of relevant timer. UV-Vis-NIR Spectrophotometers have been used to monitor dye degradation rate over time. The C_t/C_0 vs. time plot can be used to calculate degradation efficiency (η) of the as-prepared samples using the equation,

$$\eta\,\% = \frac{(\eta_0 - \eta_t)}{\eta_0} \times 100 \qquad (3.6)$$

Dye concentrations are η_0 (initial concentration) and η_t (final concentration) at time t = 0.

3.2.9 Electrochemical Measurement

3.2.9.1 Potentiostats/Galvanostats: Basic Principles (Autolab PGSTAT)

Electrochemical measurements are performed with a potentiostat or galvanostat. The PGSTAT can operate in potentiostatic or galvanostatic mode. The potentiostat/galvanostat is a device that accurately controls the potential difference between the counter electrode and the working electrode, thus ensuring that the value of the potential difference is well-defined and corresponds to the value specified by the user. A current flow between the working electrode and counter electrode is utilised to control and continuously monitor by the galvanostatic mode. Thus, PGSTAT allows the user to accurately control the applied potential or current, at any time during the measurement. This results from the use of a negative feedback mechanism.

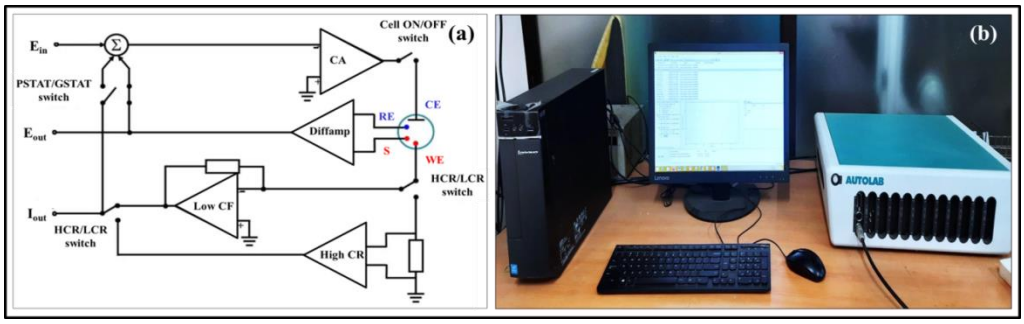

Figure 3.13: (a) Schematic diagram of Potentiostat/Galvanostat (PGSTAT) and (b) digital photograph of Autolab (PGSTAT)

A PGSTAT is illustrated in Figure 3.13(a). A control amplifier (CA) controls the flow of current through the cell through an electronic block referred to as the counter electrode (CE) shown in the Figure. Current follower (low CF) is used to measure low values of current, and a shunt (high CR) is used for measuring high values of current. In a differential amplifier (DA), the electrode potentials are always measured between the reference electrode (RE) and connector S. According to the mode of use (potentiostatic or galvanostatic), the PSTAT/GSTAT switch must be set appropriately. This signal from the summation point (Σ) is fed to the control amplifier, where it is combined with the waveform created by the digital-to-analog converter (Ein).

PGSTAT (M-204) potentiostat/galvanostat connected to computers using Nova 1.11 software was used to perform electrochemical measurements. The resulting digital image is depicted in Figure 3.13(b).

3.2.9.2 Configuration of Three Electrodes in Autolab

In electrochemistry, the most common configuration is a three-electrode setup. Working electrodes (WE), counter electrodes (CE), and reference electrodes (RE) make up this system. Measurements of

current are made between the CE and WE in this configuration. In the WE and CE, potential differences are controlled whereas they are measured in the WE and CE.

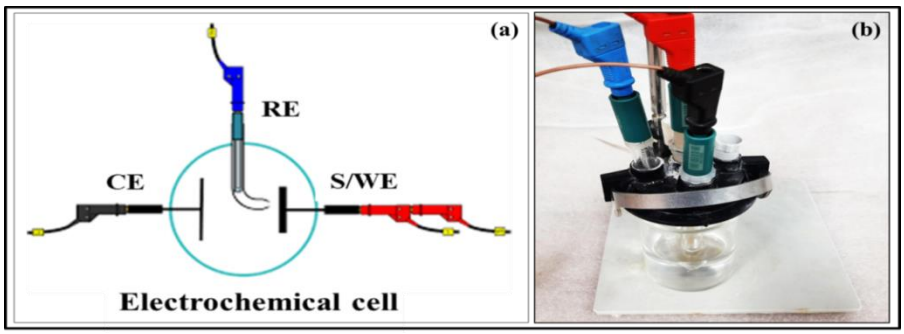

Figure 3.14: Schematic configuration of the three-electrode setup (a) and digital photograph of Autolab (PGSTAT) with three electrodes connected setup (b)

The RE functions as a calibrating and measuring electrode without carrying any current, which helps to calibrate and measure the potential of WE. Low current densities require a constant electrochemical potential for the RE. Due to the low current of the RE, there is often a very small iR difference between the RE and the WE. A very low current goes through the RE, so the difference in resistance between the RE and WE are very low. In order to reduce uncompensated resistance and ohmic losses caused by this resistance, the RE should be positioned as close to the WE as possible. This is not difficult to accomplish with a Luggin-Haber capillary. As seen in Figure 3.14, a three-electrode configuration is schematically and digitally[15].

Our study describes the three-electrode configuration used to measure electrochemical activity in HER. A platinum wire CE was used as a sample electrode and a 3 M KCl saturated AgCl/AgCl electrode was used as a RE. As the acidic electrolyte, all measurements were carried out with H_2SO_4 (0.5 M). Linear sweep voltammetry (LSV) was used to conduct the experiment in acidic solution at a scanning rate 10 mV/s. During all measurements, reversible hydrogen electrodes (RHE) were added to the Ag/AgCl as a RE:

$$E(HER) = E(Ag/AgCl) + 0.27\,V \qquad (3.7)$$

3.3 Conclusions

This chapter examines the instruments or tools used for the characterization of different types of nanomaterials. These instruments are helpful in measuring the surface structure, morphology, compositional, and optical properties of each nanomaterial. Nanoparticles are analysed with most of the materials listed above.

References

[1] A.S. Bolokang, M.J. Phasha, C. Oliphant and D. Motaung, *International Journal of Refractory Metals and Hard Materials*, 29(1), 2011, 108-111.
[2] K.K. Chattopadhyay and A.N. Banerjee, *PHI Learning Pvt. Ltd*., 2009. ISBN Number: 978-81-203-3608-7.
[3] B.V. Christ, *John Wiley & Sons*, 1, 2000.
[4] J.R. Ferraro, K. Nakamoto, C.W. Brown, *Elsevier Science*, 2003. ISBN Number: 978-01-225-4105-6.
[5] C. Berthomieu, R. Hienerwadel, *Photosynthesis Research*, 101, 2009, 157-170.
[6] P.H. Emmett and E.D.W.A.R.D Teller, *Journal of the American Chemical Society*, 60, 1938, 309-319.
[7] D.A. Hanaor, M. Ghadiri, W. Chrzanowski and Y. Gan, Langmuir, 30(50), 2014, 15143-15152.
[8] K.S. Sing, *Advances in Colloid and Interface Science*, 76, 1998, 3-11.
[9] J. Bisquert, *CRC Press (Science)*, 2014. ISBN Number: 978-14-398-3602-6.
[10] H. Nyquist, *Bell Syst. Technical Journal*, 11, 1932, 126-147.
[11] ISO 13099-2, I., *International Organization for Standardization (ISO), Geneva (Switzerland)*, 2012.
[12] https://wiki.anton-paar.com/en/zeta-potential/
[13] R. Ameta, M.S. Solanki, S. Benjamin and S.C. Ameta, *Emerging Green Chemical Technology (Academic Press)*, 2018, 135-175. ISBN Number: 978-0-12-810499-6.
[14] A.E. Cassano, C.A. Martin, R.J. Brandi and O.M. Alfano, *Industrial & Engineering Chemistry Research*, 34(7), 1995, 2155-2201.
[15] A.A.N. EC08, *Metrohm Autolab BV*, 2011, 1-3.

Chapter 4

Hydrothermal synthesis of GO wrapped BiOCl nanosheet and its Application in Visible light assited catalytic degradation of Rhodamine B dye

4.1 Introduction

The discharge of different types of pollution from factories and industries majorly contribute to water contamination that directly affects human life and disrupts the environmental ecosystem to an alarming extent. The photocatalytic technique is generally pursued in water purification from textile dyes due to its cost-effective, non-toxic and chemically stable properties[1]. For a considerable time period, TiO_2 and TiO_2 based materials got ample significance for their effective photodegradation activity besides their low cost, stable and non-toxic nature. On the other hand, TiO_2 could be excited only by UV light arising from its wide bandgap in UV region (3.2 - 3.35 eV) for its rutile and anatase phases, which consequently restrained its realistic application. Therefore cultivating a photocatalyst having a suitable bandgap which might be excited in presence of visible light irradiation has emerged to be an important research area in the present years[2]. Many researches including our group have already developed efficient bismuth oxyhalides (BiOX, X = Cl, Br and I) with layered structures and wide range of bandgap (2.45 - 3.5 eV) and studied their performances in the photocatalytic degradation of harmful dye pollutants[3-5] mediated by photoinduced electron-hole pairs in presences of visible light[6-8]. BiOCl catalysts exhibit large bandgap with high absorption in both visible and UV range[9]. In addition, BiOCl has a distinctive tetragonal structure[1-6,9,10] which has been proved to be highly advantageous for large amount of light-harvesting and beneficial charge carriers[11]. However, pure BiOCl has been modified by many researchers to achieve enhancement of the photodegradation performance. Pan et al. proposed a sequence of CdS QDs coupled BiOCl nanomaterial[12], Zhang et al. fabricated a $BiOCl/Bi_2O_2CO_3$ nano-composite[13], Sun et al. successfully synthesised Ag/BiOCl nanocomposite[14], Zhang et al. proved that a novel Z-scheme BiOI/BiOCl nanofibers[15], Yu et al. proposed C doped BiOCl flowerlike nanomaterial[16] etc., all of these composites have been designed in order to significantly improve the photocatalytic activity of BiOCl by segregation of photo-induced charge carriers.

The exclusive 2D structures and high conductivity of graphene and graphene-based composites have made them efficient electron moderators which in turn have appealed to a massive number of researchers in the current scenario[17-21] for successful implementation in photocatalytic water purification applications[22-25].

Conventional organic dyes have highly toxic, mutagenic and carcinogenic properties, nevertheless they are widely utilised in a large number of industrial sectors like textile, cosmetic, research of agriculture, paper and pulp, fabric, processing of food, leather, medicinal product and electroplating etc. Because of their huge level of production and utilisation, organic dyes are considered to be one of the primary pollutants emitted from innumerable industries resulting in antagonistic reactions to the environmental

ecosystem. Hence water pollution caused by toxic dye pollutants have remained a significant problem through decades which demand immediate and necessary measures of treatment[26]. Photocatalytic dye removal has been an important and effective technique for separation of contaminants and insoluble carcinogenic pollutants from wastewater. In this work, Rhodamine B (RhB), a harmful, toxic, and carcinogenic organic dye has been considered for photocatalytic study and this dye has been successfully removed by photocatalysis procedure for wastewater treatment.

The present work deals with the successful synthesis of pristine BiOCl and a nanocomposite of BiOCl and GO (BOC-GO) having nanosheets like morphology via hydrothermal synthesis route, whereas pure GO was prepared by modified Hammers procedure. The composite nanomaterial presented highly efficient photocatalytic performance due to their excellent charge separation property that can be recommended for water remediation applications.

4.2 Experimental Details

4.2.1 Materials

$Bi(NO_3)_3 \cdot 5H_2O$ (Bismuth nitrate pentahydrate), $C_6H_8O_7 \cdot H_2O$ (Citric Acid Monohydrate) and HCl (Hydrochloric acid, 37 %) was obtained from Merck Group. PVP (Poly Vinyl Pyrrolidone, K30) was purchased from Loba Chemie Pvt. Ltd., Graphite powder (99 %), $NaNO_3$ (Sodium nitrate), H_3PO_4 (Ortho-phosphoric acid, 85 %), H_2SO_4 (Sulphuric acid, 98 %), $KMnO_4$ (Potassium permanganate), and H_2O_2 (Hydrogen peroxide, 30 %) were purchased from Merck Group. NH_3 (Ammonia solution, 25 %), IPA (Isopropyl alcohol) were from Mark Group, and EDTA-2Na (Ethylene diamine tetra acetate disodium, M.W. = 372.24 g/mol) and *p*-BQ (*p*-Benzoquinone, M. W. = 108.096 g/mol) were parched from Loba Chemie Pvt. Ltd. and PubChem. During synthesis of the samples, absolute ethanol (99.99 %) and DI water were used.

4.2.2 Methods

4.2.2.1 Synthesis of Graphene Oxide (GO)

GO (graphene oxide) was prepared from a graphite precursor following the modified Hummers procedure. Initially, 2 g of pure graphite dust (99 %), 2 g of $NaNO_3$, 10 mL of H_3PO_4 (85 %), and 90 mL of H_2SO_4 (98 %) were put together in a beaker and stirred continuously for 24 hours at ambient temperature. After that, the beaker was settled down in an ice bath with a controlled temperature of 5 °C or below, followed by the addition of 12 g of $KMnO_4$ at regular time intervals till a homogeneous solution was achieved. After that the beaker was removed from the ice bath and 100 mL of DI water

was added dropwise into the solution. This resulted in an exothermic reaction along with heat generation which subsequently increased the temperature to approximately 98 °C and the mixture solution turned into a brown colour. Then the beaker was transferred into a water bath and maintained at a temperature of 35 °C for 2 hours with addition of 200 mL of DI. Next, 10-15 mL of H_2O_2 (30 %) was added drop by drop into that solution and the respective solution turned to light yellow colour. The solution was then washed several times with hydrochloric acid (5 %) and DI water, after which it was kept in an oven at 60 °C under vacuum conditions overnight to finally obtain the graphene oxide (GO).

4.2.2.2 Synthesis Procedure of BiOCl and BiOCl-GO Sample

The pristine BiOCl and BiOCl-GO samples were synthesised by the hydrothermal method. All chemicals were used without any purification. At first, 2.5 mL of HCl (37 %) was mixed with 22.5 mL of DD water, and then 2 mmol of $Bi(NO_3)_3 \bullet 5H_2O$ was added into the respective aqueous mixture. The combined mixture was then stirred vigorously till the formation of a homogeneous solution at ambient condition. Another aqueous solution was similarly prepared by mixing citric acid monohydrate (7.02 x 10^{-2} mmol), K30 Poly Vinyl Pyrrolidone (2.08 x 10^{-4} mmol), absolute alcohol (50 mL) and DI water (42 mL), which was subsequently heated up to a temperature of 80 °C. Next, the previous solution was poured into this heated solution. For the formation of the composite sample, this process was followed by the addition of 10 mL of GO solution (30 mg GO dissolved into 10 mL DI water). Finally, this solution was poured into a 60 mL Teflon lined stainless steel autoclave and was subjected to hydrothermal treatment for 3 hours in a preheated oven maintaining a temperature of 160 °C. After completion of this reaction procedure, the system was cooled down naturally to ambient condition, and the precipitates were washed repeatedly with pure DI water and ethanol to achieve a neutral pH (pH = 7). After filtration, the washed precipitates were dried for 10-12 hours in an oven at 60 °C. The synthesised samples were named as BOC (pure BiOCl) and BOC-GO (BiOCl-GO composite).

4.2.2.3 Characterizations of Sample

The as-prepared samples were subjected to several sophisticated techniques. The PXRD (powder X-ray diffraction) was recorded from D8 Bruker advance X-Ray diffractometer with a radiation source of Cu Kα (λ = 1.54 Å) and at a scanning rate of 2θ of 5 $^{\circ}$/min for proper identification of phases, crystallite size, and dimension of samples. The different chemical structure of the pure and composite samples were analysed by XPS (X-ray photoelectron spectroscopy) using an Al K_α source (WF = 4.39 eV) of Thermo fisher (ESCALAB Xi+). The morphology of the samples were perceived from FESEM (Field

emission scanning electron microscopic) images operated at 10 kV accelerating voltage used by Bruker Nano GmbH Berlin, Germany (Esprit 1.9), and the EDX (Energy dispersive X-ray spectra) measurements were used by FESEM instrument (Hitachi S-4800). The HRTEM (High resolution transmission electron microscopic) analysis by JEOL-JEM 2100 PLUS. DRS (Diffuse reflectance spectra) measurements of the samples were carried out by UV–Vis spectrophotometer (Shimadzu 3600 UV-Vis-NIR) using barium sulfate ($BaSO_4$) as standard reflective material. Raman analyses were conducted by Witec Raman spectrophotometer instrument equipped with a laser source having an excitation wavelength of 532.3 nm. Knowledge about the nature of bonds and their formation were obtained from FTIR (Fourier transform infrared spectroscopy) analysis of the samples (Shimadzu FTIR-8400S). The BET (Brunauer-Emmett-Teller) analysis of the samples were measured by Quantachrome instrument NOVAe 1000 nitrogen sorption analyser (Version 11.03) at 77 K and 1 bar for the surface area, pore size and N_2-adsorption-desorption isotherm.

4.2.2.4 Activity of Photocatalysis

The photocatalytic dye degradation property of the fabricated BOC-GO sample was recorded by studying the degradation activity of 10^{-5} M concentration of aqueous solution of organic textile dye Rhodamine B (RhB) under ambient conditions in presence of visible light irradiation and at a neutral pH value (pH 7). The photocatalytic experimental procedure of the as-synthesised sample was carried out in a customised double walled glass beaker with continuous water flow in between the two walls. In this system, 30 mg of as-prepared catalyst was dispersed in 40 mL of aqueous dye (RhB) solution. Then the respective dye solution was continuously stirred for 1 hour to procure the adsorption-desorption equilibrium condition. Thereafter, the entire system was transferred under a visible light source comprising of Hg lamp with an ultraviolet (UV) cutoff filter. At certain periods of time duration, 4 mL of the aqueous solution was taken and immediately centrifuged to separate the catalyst material from the dye solution and the absorbance spectra of this dye solution were then evaluated from UV-Vis spectrophotometer.

4.2.2.5 Variation of different Parametres

The load variations were done by different amounts of catalyst use into the respective aquatic solution like as 0, 15, 30 and 45 mg, and the stability test was done up to 3 cycles by same photocatalytic method repeatedly used, like as 1st cycle was done 3 times for taking 30 mg catalyst for 2nd cycle and then again 1st cycle was done 8 times and 2nd cycle was done 4 times for 30 mg catalyst for 3rd cycle.

The pH variations were done by using HCl (37 %) and NH_3 (25 %) solutions for making an acidic and basic medium. Finally, the scavenger tests were done by using 0.01 mol/L of EDTA-2Na (Ethylene diamine tetra acetate disodium), *p*-BQ (*p*-Benzoquinone) and IPA (Isopropyl alcohol) for the photo-induced hole (h^+), superoxide anion ($\bullet O^-_2$), and hydroxyl radicals (•OH) of the photodegradation activity of the photocatalyst.

4.3 Results and Discussion

4.3.1 Crystal Structure Analysis

The PXRD spectra of the as-synthesised pure BOC and BOC-GO composite samples are demonstrated in Figure 4.1. All the respective diffracted peaks of both the as-synthesised materials were indexed according to the tetragonal primitive lattice P4/nmm phase of BOC (JCPDS-06-0249). The characteristic peaks were sharp and intense which in turn proposed the well crystalline nature of the as-synthesised samples. Since GO usually has a sharp pick at 2θ ~ 11 which may be located at the same place of (001) lattice plane. Additionally, the peak corresponding to the (001) lattice plane significantly increased in intensity for the composite sample as compared to the pristine BOC sample.

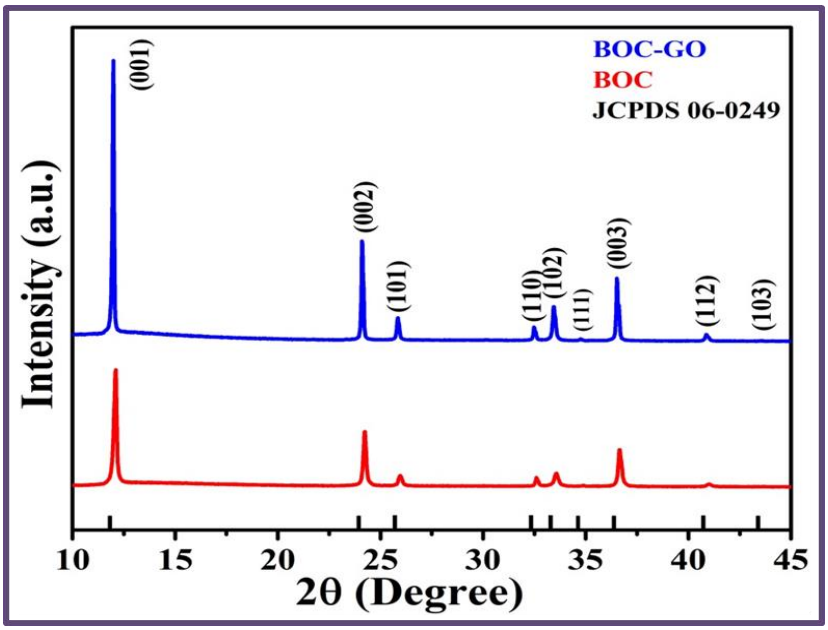

Figure 4.1: The PXRD pattern of the both pure (BOC) and composite (BOC-GO) samples

4.3.2 Compositional Structure Analysis

The X-ray photoelectron spectroscopy (XPS) analysis was carried out for the compositional analysis of bismuth (Bi), oxygen (O), chlorine (Cl) and carbon (C) elements of the BOC and BOC-GO composite were demonstrated in Figure 4.2 and Figure 4.3. The survey spectrum analysis established the existence

of Bi, O, Cl and C elements and that was demonstrated in Figure 4.2(a). The peaks rise at 159. 098 eV was recognised for Bi 4f, at 198.445 eV for Cl 2p, at 529.349 eV for O 1s and at 283.493 eV accredited for environmental C 1s. The environmental C arises as an impurity that comes from atmospheric CO_2[4].

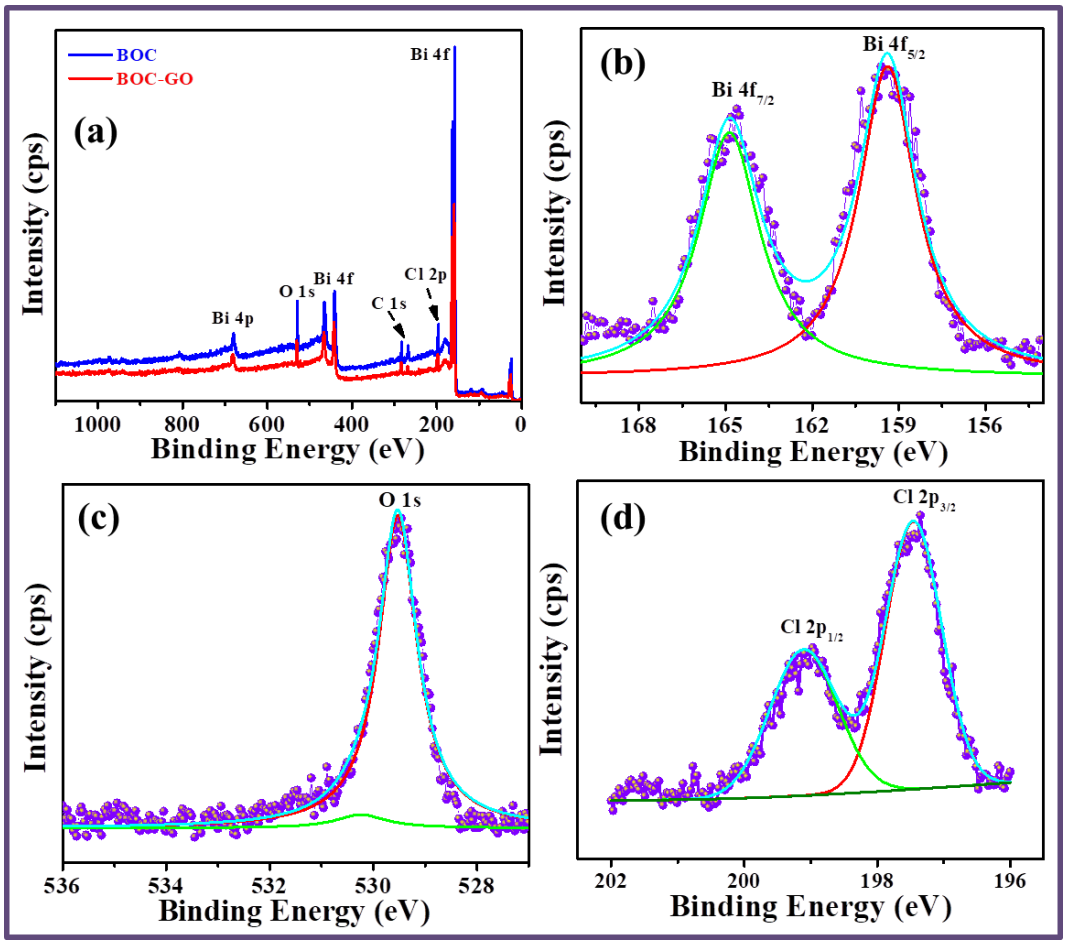

Figure 4.2: The XPS elemental survey scan of BOC and BOC-GO sample (a), Bi 4f spectrum (b), O 1s spectrum (c) and Cl 2p spectrum (d) of the BOC

The accompanying peaks at 159.38, 164.87 and 159.84, 165.18 eV were carried out for Bi $4f_{5/2}$ and Bi $4f_{7/2}$ of the BOC and BOC-GO composite sample for Bi-O bond, which were demonstrated in Figure 4.2(b) and Figure 4.3(a); and the peak at 157.34 eV arises which was called satellite peak. The established the peak for O 1s at 530.26, 529.53 and 531.38, 530.56 eV of pure and composite samples, which arose Bi-O bond for O_2 atom and H_2O atom attached the surface of both sample due to the 1st and 2nd peak in Figure 4.2(c) and Figure 4.3(b)[27]. The peak at 197.46, 199.1 and 198.5, 199.97 eV demonstrated in Figure 4.2(d) and Figure 4.3(c) for Cl 2p spectrum that belongs to Cl $2p_{3/2}$ and Cl $2p_{1/2}$ respectively and that carried out to Cl^- of Bi-Cl bond for both samples. The peak was demonstrated in Figure 4.3(d) at 284.85 (C=C), 285.8 (C-O), 287.8 (C-O), 288.13 (C=O) and 289.69 eV for the C 1s for

the composite material[28]. Therefore the PXRD and XPS analysis supported that the prepared samples were pure BiOCl (BOC) and BiOCl-GO (BOC-GO) composites.

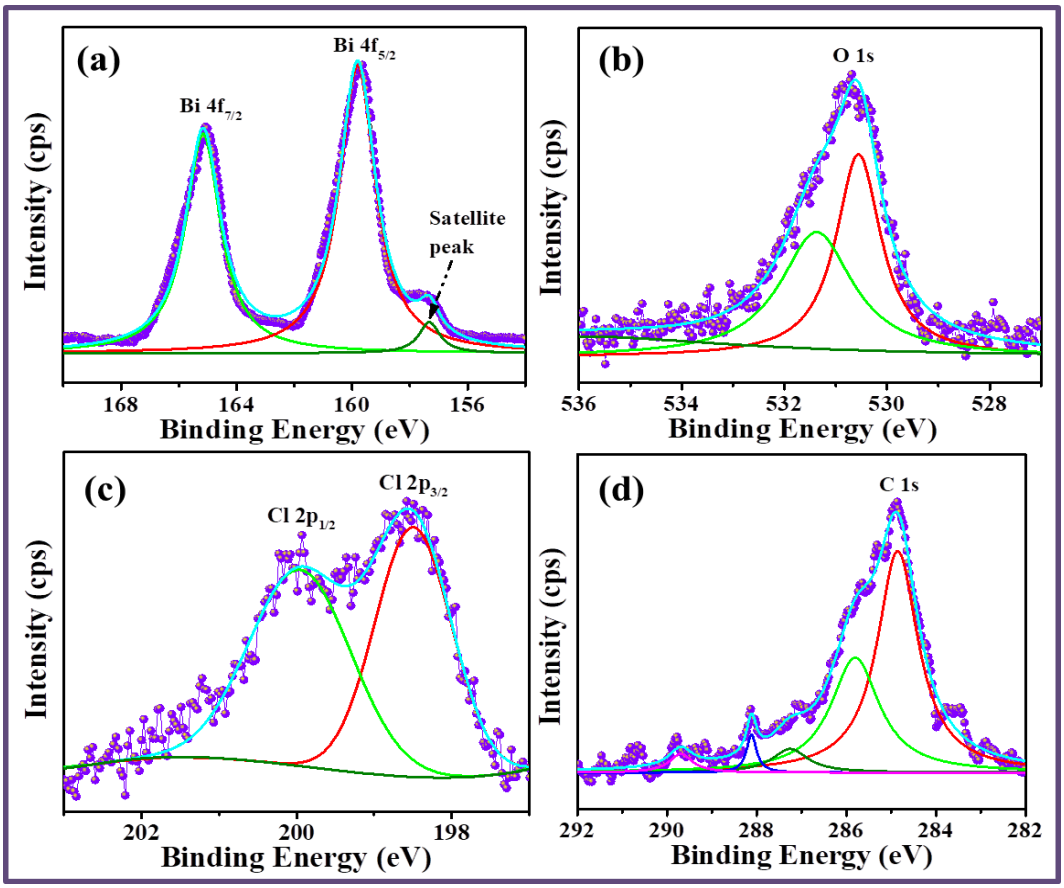

Figure 4.3: The XPS analysis of (a) Bi 4f spectrum, (b) O 1s spectrum, (c) Cl 2p spectrum and (d) C 1s spectrum of BOC-GO composite

The elemental analysis was done by EDX (Energy dispersive X-ray) spectra of the pure (BOC) and composite (BOC-GO) materials and that demonstrated Figure 4.4(a) and Figure 4.4(b). Both the spectra properly showed Bi, O, Cl and only C showed a composite sample, which was also confirmed by XPS analysis. The elemental mapping of both samples demonstrated Figure 4.4(c-l), and the corresponding weight and atomic percentage (%) of Bi, O, Cl and C elements of both samples were given in Table 4.1, the ratio was taken approximately stoichiometric.

4.3.3 Chemical Structural Analysis

The Raman spectra analysis of BOC and BOC-GO was carried out at room temperature and the corresponding spectra are shown in Figure 4.5(a). Raman analysis was performed to have a better insight into the composite formation since the XRD analysis of the pristine BOC and BOC-GO sample

suffered from the coinciding of the (002) lattice plane of pure BiOCl (BOC) with the characteristic peak of GO.

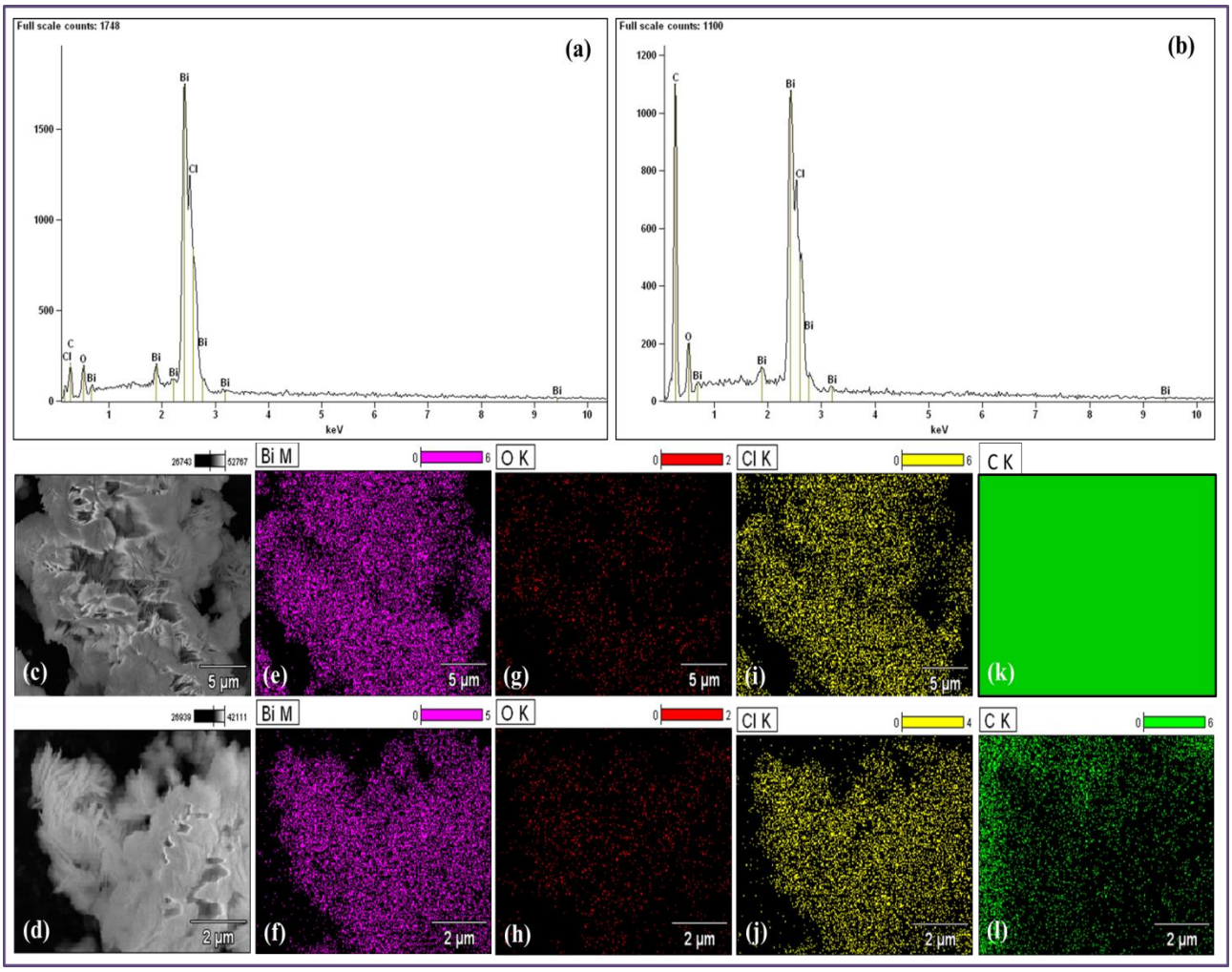

Figure 4.4: Energy dispersive X-ray spectra (EDX) spectrum of BOC (a) and BOC-GO (b) nanomaterials, Morphology of EDS (c,d), and elemental mapping of Bi (e,f), O (g,h), Cl (i,j), blank (k) and C (l) of the BOC and BOC-GO materials

The 108 cm^{-1} band was allotted for the characteristic surface or interface stretching mode of vibration, band at 152 cm^{-1} was allocated to the Bi-Cl internal stretching mode known as A_{1g} vibration, the peaks at 205 and 307 cm^{-1} were assigned to the Bi-Cl external stretching mode, also known as E_g vibration, the bands at 402 and 508 cm^{-1} were consigned to the motion of O-atoms which results in a weak mode of vibration, known as B_g. The spectra clearly demonstrate that the peak positions corresponding to 307 and 508 cm^{-1} suffered from a blue shifting to 205 and 402 cm^{-1} respectively. The peak at 1355 cm^{-1} was assigned to the D band and that at 1505 cm^{-1} was allocated to the G band, which are characteristics of GO in the BOC-GO composite sample. Interestingly, these two peaks are completely absent in the

Raman spectrum of the pristine BOC sample. The appearance of these two peaks in the composite sample strongly confirms the attachment of GO with the BOC material. Our group has already published the synthesis and detailed characterisation of pristine GO samples, so it has not incorporated those data in the present work[29]. The Raman spectrum of pure GO is shown in Figure A5 (Appendix). The G band was allotted to the coplanar bond stretching of the sp^2 bonded carbon (C) atoms, whereas the D band was assigned to the defect states corresponding to the sp^3 bonded carbon species. The ratio of intensity of the D and G bands (I_D/I_G) suggested the disorder in the GO sheet where high value of ratio indicated lesser amount of disorder arising from structural defect. The ratio of intensity (I_D/I_G) for the BOC-GO nanocomposite was near to 1.1, which proposed the evolution of small sized sp^2 areas in GO[30]. This information stipulated the construction of BOC-GO nanocomposite.

Table 4.1: The compositional ratio of the both BOC and BOC-GO samples

Sample Name	Quantitative Result	Bi	O	Cl	C
BOC	**Weight %**	81.18	4.47	14.35	00
	Atom %	36.21	26.06	37.73	00
BOC-GO	**Weight %**	42.50	6.11	7.66	43.72
	Atom %	4.58	8.60	4.86	81.95

The bond formation analysis by Fourier transport infrared spectroscopy (FTIR) spectra of the prepared pure and composite samples was demonstrated in Figure 4.5(b). The peak arising at 528.77 cm^{-1} was for the symmetrical vibrations of the Bi-O bond of both samples. The ring stretching vibration for C-Cl chloro bonds arising at 655.14 and 837.5 cm^{-1} for pure (BOC) samples and at 671.94 and 838.3 cm^{-1} for composite (BOC-GO) samples. The peak at 1085.45 cm^{-1} epoxy broad hump obtained C-O bond for composite sample. The large range at 1291, 1424.57 and 1666.12 cm^{-1} for the pure sample and at 1290.2, 1429.37, 1658.12 and 1730.9 cm^{-1} for the composite sample obtained C-N bond of PVP used capping agent. The peak at 2297.98 and 2300.38 cm^{-1} arises for the C=O bond of PVP carbonyl stretching vibration for pure and composite samples. The bands at 2884.25 and 2953.83 cm^{-1} were raised for the C-H alkane bond due to the composite and pure samples. The broad hump arises at 3461.72 and 3609.69 cm^{-1} for the O-H stretching mode of vibration pure and composite samples. All the arising characteristic peaks confirmed the fruitful fabrication of highly pure and composite nanomaterials[4,10].

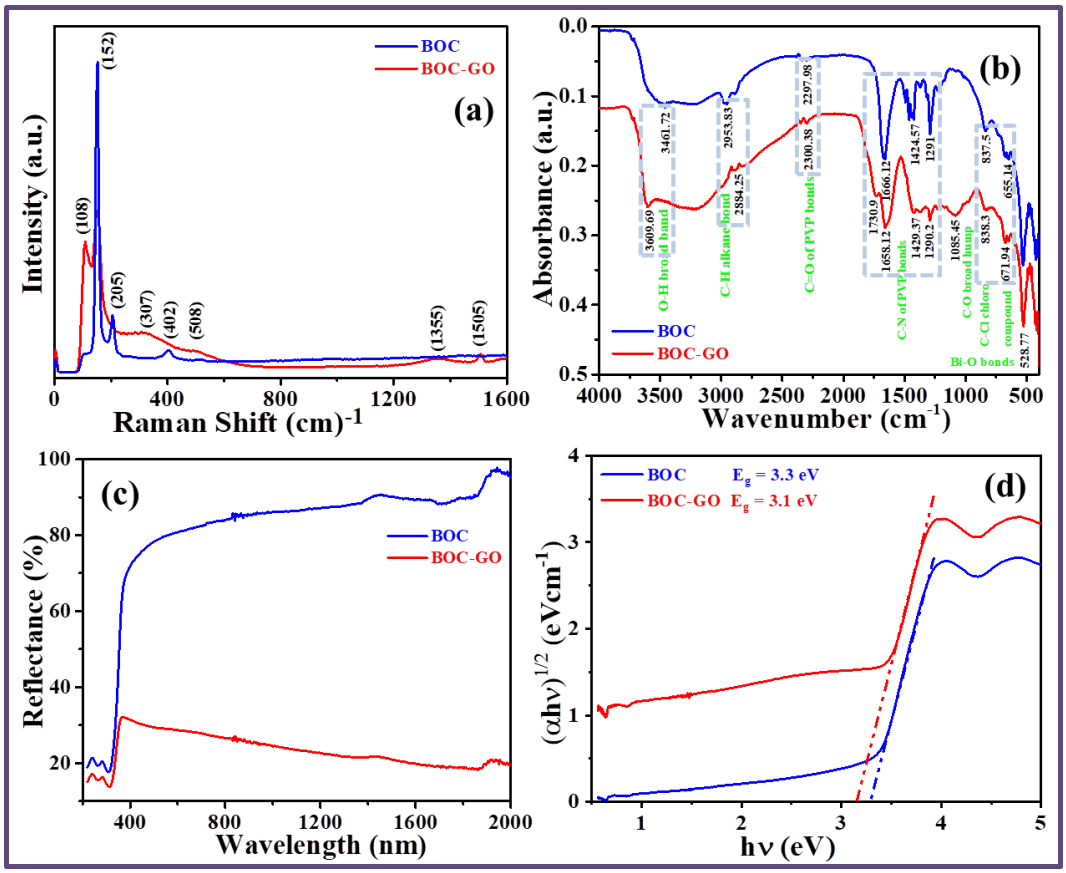

Figure 4.5: (a) Raman shaft pattern, (b) FTIR spectrum, (c) UV-Vis DRS spectra and (d) Calculated Kubelka-Munk function vs. photonic energy plots of both samples

4.3.4 Optical Property Analysis

Figure 4.5(c) shows the UV-Vis diffuse reflectance spectra of the BOC and BOC-GO materials in the range of 200-2000 nm. Both samples exhibited absorption in the visible range with reflectance edge around $\lambda > 400$ nm. The percentage of reflectance of BOC-GO was lower than that of BOC due to the former's dark coloured nature. Figure 4.5(d) shows the indirect bandgap of both the materials plotted as Kubelka-Munk function vs. photonic energy ($h\nu$) and calculated from Kubelka-Munk method[9]. The band gaps (E_g) of BOC and BOC-GO were evaluated to be 3.3 and 3.1 eV respectively. The band gap value decreased slightly for the composite sample than the pure one.

4.3.5 Brunauer Emmett Teller Analysis

The Brunauer-Emmett-Teller (BET) analysis of both prepared samples was carried out by N_2 adsorption-desorption isotherm and also measured the surface area, porosity and the distribution of pore size. Figure 4.6(a) and Figure 4.6(b) demonstrated the N_2 adsorption-desorption isotherm and corresponding pore size distribution of the pure (BOC) and composite (BOC-GO) samples. The

analysed surface area, pore volume and also average pore diameters were calculated by using the Barret Joyner Halenda (BJH) method demonstrated in Table 4.2.

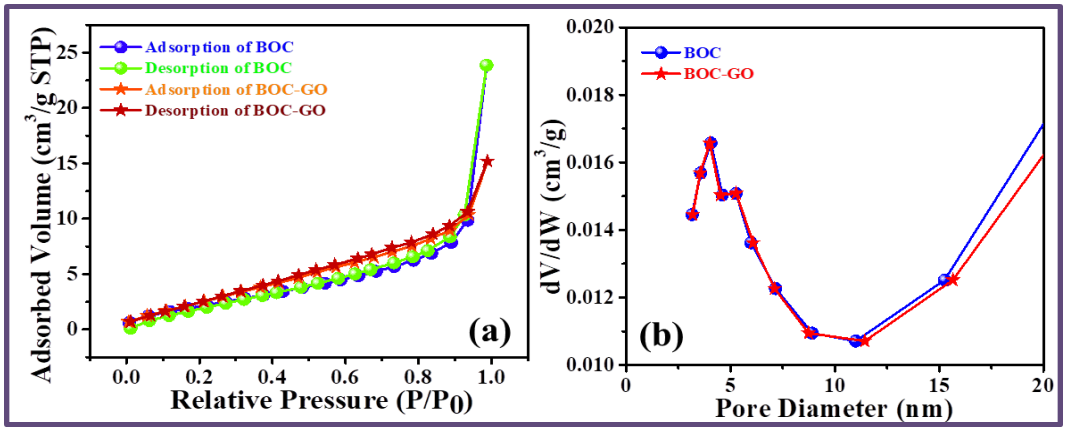

Figure 4.6: (a) N_2-adsorption-desorption isotherms and (b) Pore size distributions of both samples

Here the evaluated results agreed the composite sample has a higher surface area, pore volume and also average pore diameter than the pure sample, which efficiently improved the catalytic performance.

Table 4.2: The comparison of the surface area, average pore diameter and total pore volume of both samples

Samples Name	Surface Area (m^2/g)	Average Pore diameter (nm)	Total Pore Volume (cm^3/g)
BOC	9.150	1.61315e+01	3.690e-02
BOC-GO	11.983	7.84414e+00	2.350e-02

4.3.6 Morphology Analysis

The FESEM images of both the samples have been demonstrated in Figure 4.7. The Figure 4.7(a) and Figure 4.7(b) respectively exhibit the FESEM images of BOC; and in Figure 4.7(c) and Figure 4.7(d) demonstrated FESEM images of BOC-GO material at high and low dimension or magnified image of 1 μm and 500 nm. It can be clearly observed that both the samples display plate-like morphology. The plates of the composite material are significantly demonstrated in the GO layer and properly attached with respective plates. Additionally, the structures of the composite material show a slightly porous nature. The average length and average thickness of the BOC plates are approximately 20 nm to 2 μm and 10 to 50 nm respectively, whereas the average length and thickness of the BOC-GO plates are around 50 nm to 3 μm and 20 to 60 nm respectively.

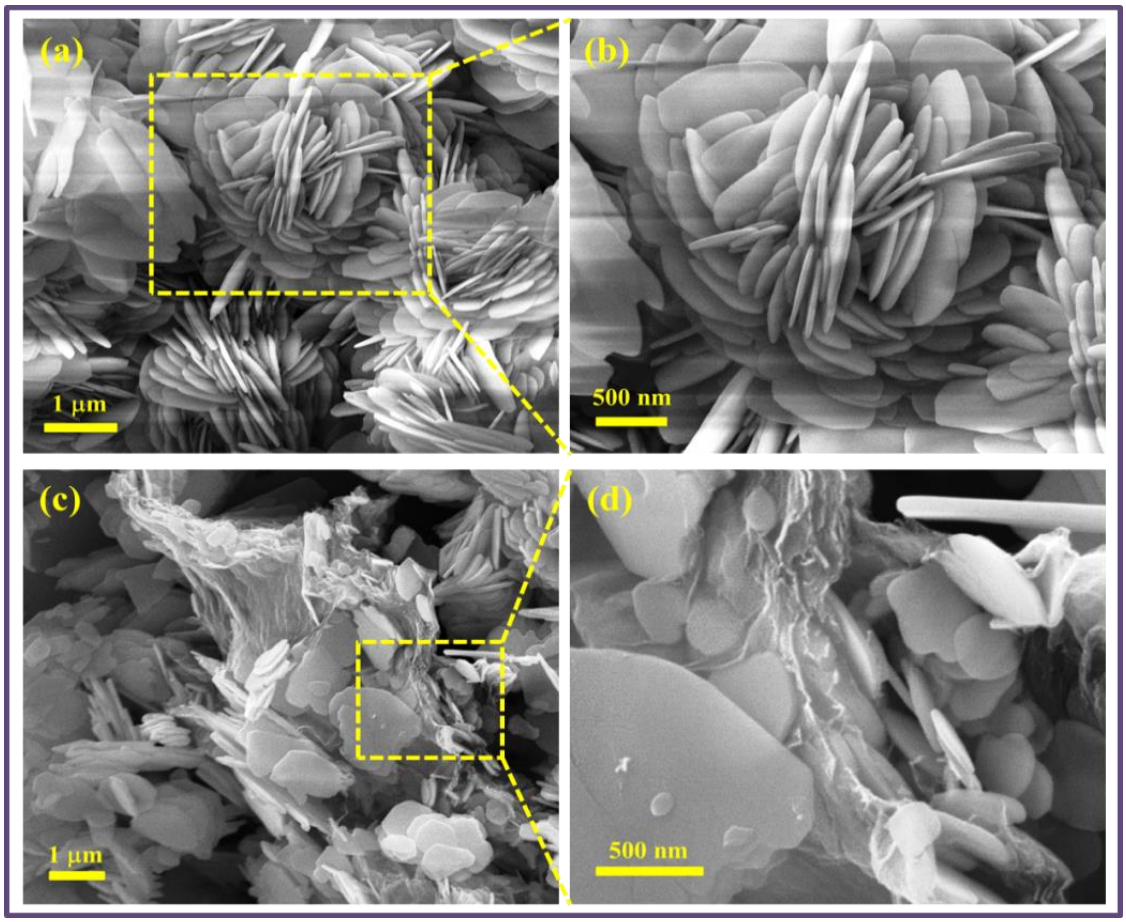

Figure 4.7: FESEM images (a) and (c) high dimension of BOC and BOC-GO materials, (b) and (d) low dimension or magnified image of BOC-GO material

The High resolution transmission electron microscopy (HRTEM) images of the synthesised materials Figure 4.8(a) and Figure 4.8(d) were exposed to the preparation of both sample morphology nanoplate in a solid constellation, which agrees with the corresponding FESEM images. Figure 4.8(d) clearly demonstrated the GO layer attached with the respective plates. The crystal lattice fringes were displayed in Figure 4.8(b) and Figure 4.8(e) which approved the highly crystalline of both materials along with the (001) lattice plane that agrees with the PXRD spectra. Figure 4.8(c) and Figure 4.8(f) were shown the SAED array of the prepared nanomaterials that agreed to the polycrystalline morphology of both samples.

4.3.7 Photocatalytic Performance Analysis

The photocatalytic performances of both the pristine and composite materials were studied by efficiently degrading RhB dye under visible light. Figure 4.9(a) and Figure 4.9(b) demonstrates the optimised absorbance pattern of RhB dye after catalytic reactions by BOC and BOC-GO catalyst

materials, and it can be seen that both the nanomaterials were capable of completely degrading RhB dye by photocatalysis technique within a short time period.

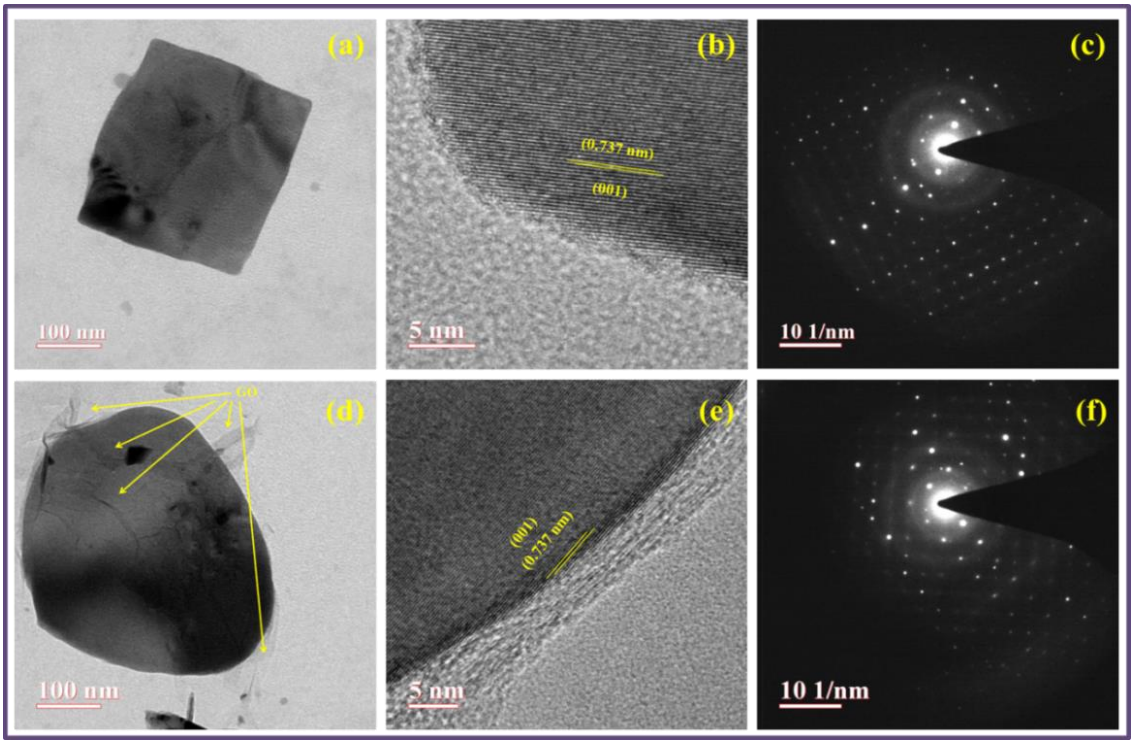

Figure 4.8: (a,d) HRTEM images, (b,e) Lattice fringes and (c,f) SADE pattern of BOC and BOC-GO materials

The composite sample showed 99.59 % photocatalytic degradation within 60 minutes of irradiation by visible light. Figure 4.9(c) shows the C/C_0 vs. irradiation time (t) plot, and the Figure 4.9(d) demonstrated $\ln(C_0/C)$ vs. irradiation time (t) plot and it was also known as the 1st order rate kinetics or constants which were calculated by Langmuir-Hinshelwood's mechanism of the pseudo-first order kinetics and the corresponding equation (4.1) is as follows[9]. The rate constant values were calculated from the linear plot of $\ln(C_0/C)$ vs. irradiation time (t) and the corresponding bar graph for both the samples are shown in Figure 4.9(e).

$$\ln\left({}^{C_0}/_{C}\right) = k_{app}t \qquad (4.1)$$

where,

C_0 = initial concentration of aqueous RhB dye,

C = final concentration of aqueous RhB dye and catalyst solution at time 't',

k_{app} = apparent first order kinetics rate constant and

t = irritation time.

The bar plots of 1st order rate constant (c) and photodegradation efficiency (d) for both materials.

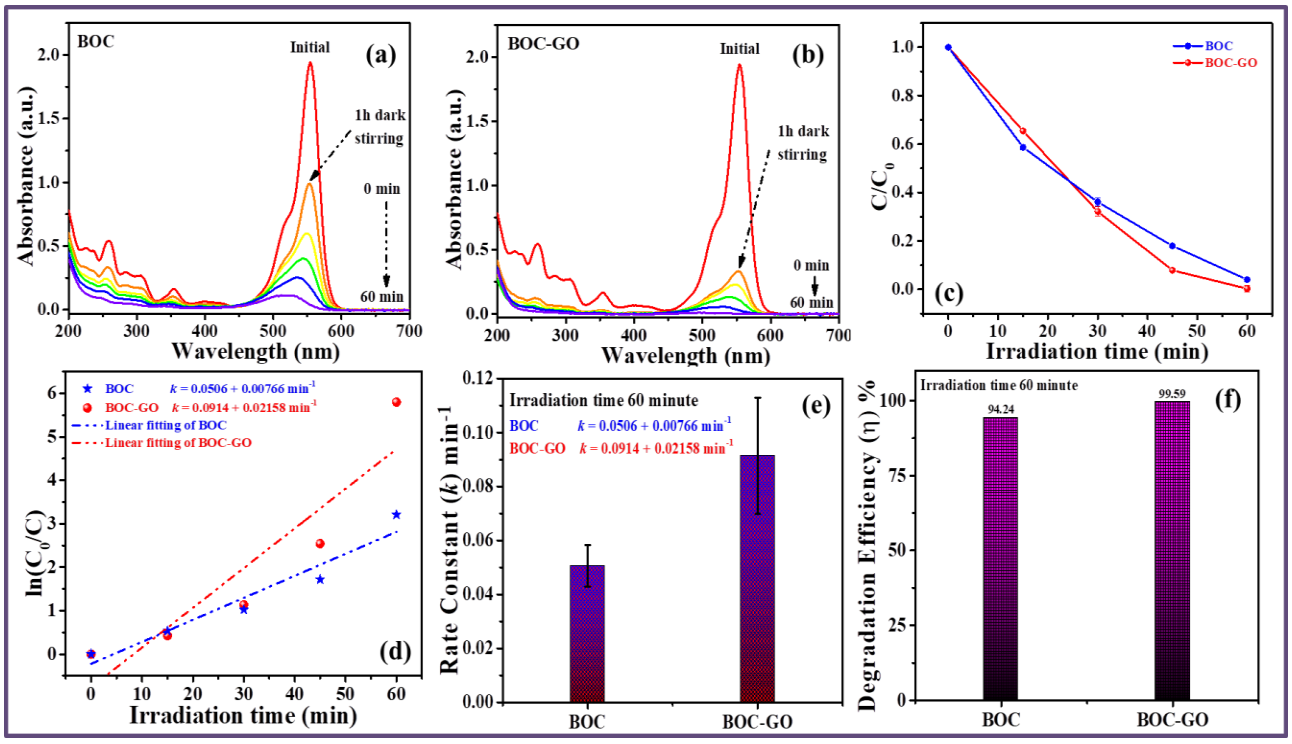

Figure 4.9: Optimized absorbance pattern of BOC (a) and BOC-GO (b) nanomaterials, the C/C_0 vs. irradiation time (t) graphs (c), $\ln(C_0/C)$ vs. irradiation time (t) graphs (d), the bar plots of 1st order rate constant (e) and photodegradation efficiency (f) for both materials

Figure 4.9(f) demonstrated the bar graph of degradation efficiency (η %) of both the samples for 60 minutes irradiation time. The photodegradation efficiency was calculated by equation (4.2)[9].

$$\eta\ \% = \frac{\eta_0 - \eta_t}{\eta_0} X\ 100 \qquad (4.2)$$

where,

η = photodegradation efficiency of the photocatalyst,

η_0= initial absorbance of aqueous RhB dye solution and

η_t = final absorbance of aqueous RhB dye and catalyst solution at the time 't'.

The BOC-GO composite material showed excellent photocatalytic performance and achieved a degradation efficiency of 99.59 % within 60 minutes of visible light irradiation. Both the nanomaterials showed efficient photocatalytic degradation performance in the same time interval, but the composite material was able to completely degrade RhB in contrast to the pristine BOC sample which could not achieve 100 % efficiency within 60 minutes of irradiation.

The effect of load variation of the catalyst on the photocatalytic performance was studied and the corresponding $\ln(C_0/C)$ vs. irradiation time (t) plot is demonstrated in Figure 4.10(a) which proves the gradually increasing in the photocatalytic rate contents with corresponding increase in the catalyst concentration (0, 15, 30 and 45 mg) and corresponding bar plots Figure 4.11(a).

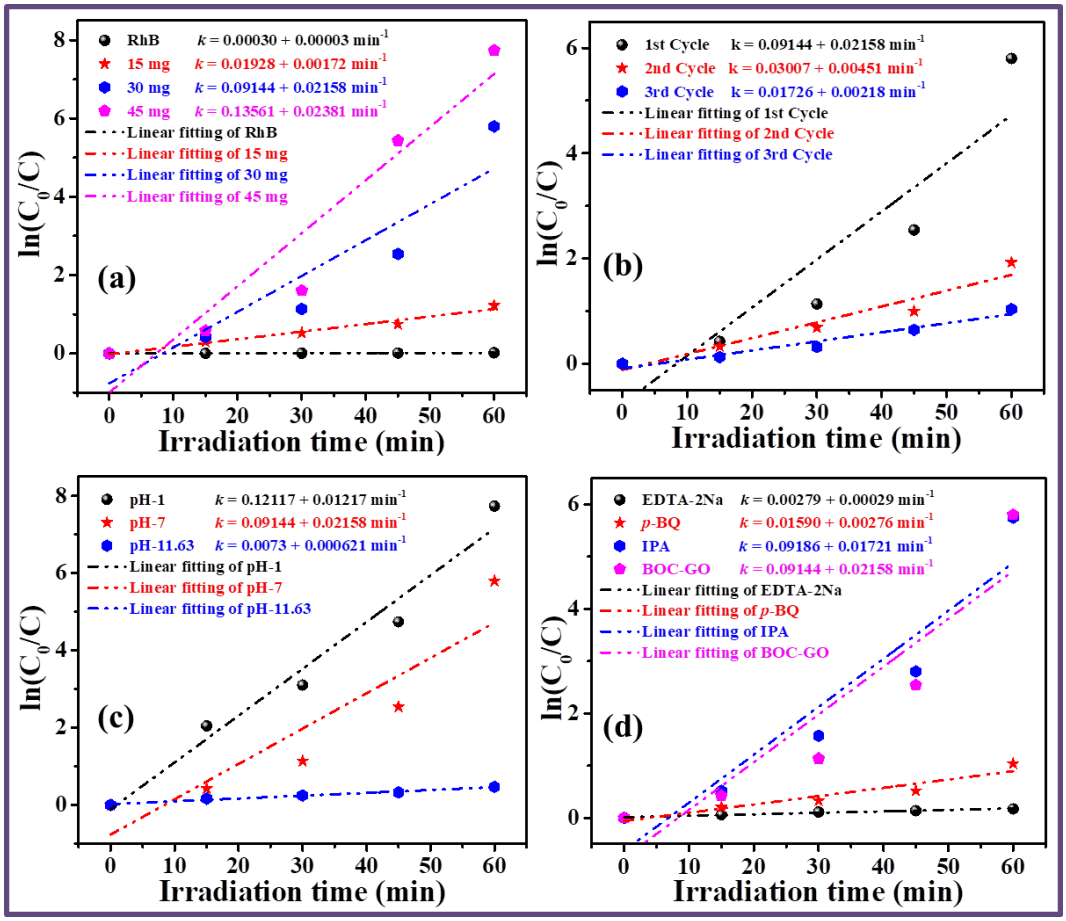

Figure 4.10: The calculated value of 1st order kinetic rate constant for the variation of different parameters had demonstrated the catalytic photodegradation for varying the photocatalyst amount (a), stability test up-to 3rd catalytic cycles (b), pH of system (c) and scavenger test for active radicals (d) for the catalytic activity of BOC-GO composite

Figure 4.10(b) confirms the reusability and stable property of the composite sample by reusing the photocatalyst up to 3 runs. In the reusability test, the used photocatalyst sample was collected after the first photocatalytic cycle, and then centrifuged to remove the catalyst from the dye solution. The collected sample was dried at 80 °C overnight. This dried sample was repeated in the 2nd cycle using the same photocatalytic procedure and the same amount of dye concentration. This method was repeatedly done up to 3 photocatalytic cycles and corresponding bar plots Figure 4.11(b).

Figure 4.10(c) shows the pH variation to study its effect on the photodegradation rate constants of the composite sample. In acidic medium, the photocatalytic rate constants of the composite sample was about 0.12117 + 0.01217 min^{-1}, however in alkaline medium it decreased to a large extent to about 0.0073 + 0.000621 min^{-1} in the same time duration of visible light irradiation and corresponding bar plots Figure 4.11(c).

The catalytic degradation process of dyes involves the essential activity of the elementary photoactive radicals which are photo-induced hole (h^+), superoxide anion ($•O_2^-$), and hydroxyl radicals (•OH) that directly participate in the redox reaction and could easily degrade the organic textile dye (RhB) under a visible light source.

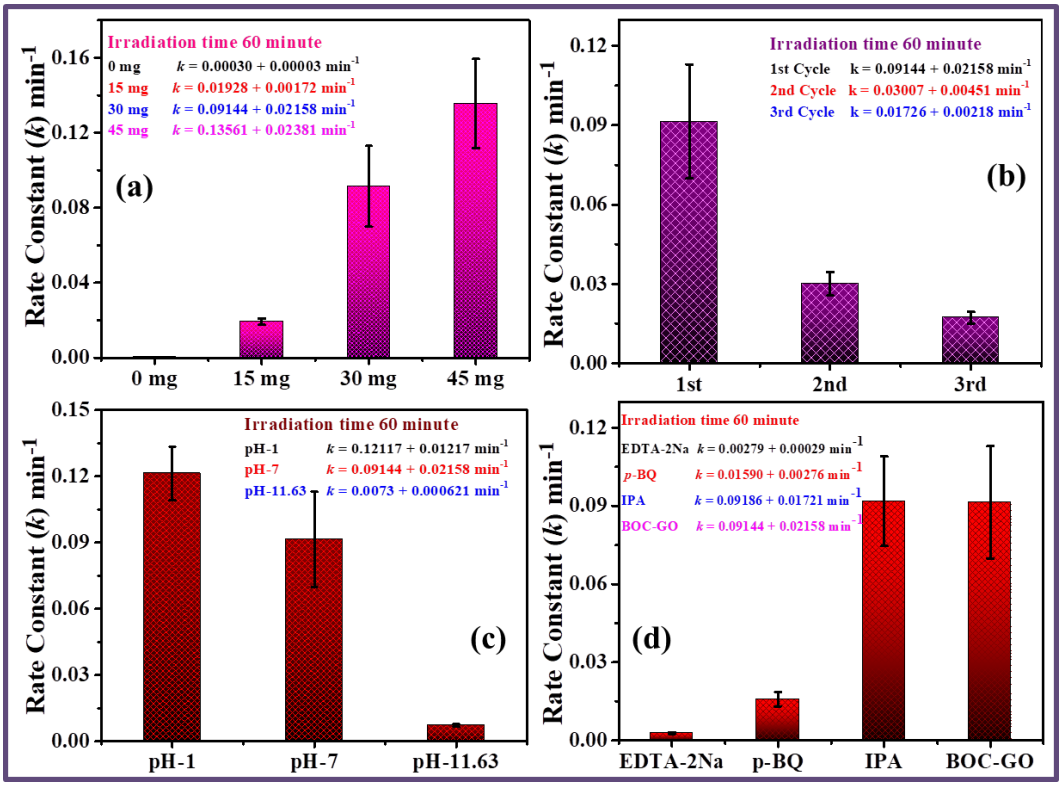

Figure 4.11: The calculated bar graphs had demonstrated of 1st order kinetic rate constant for the variation of different parameter, (a) the photocatalyst amount, (b) stability test up-to 3rd catalytic cycles, (c) pH of system and (d) scavenger test for active radicals for the catalytic activity of BOC-GO composite

Here, the photocatalytic activity is carried out of the BOC-GO composite material by exposing it to different types of scavengers which in turn helps to identify the functioning radicals in the catalytic system. The scavengers used were 0.01 mol/L of EDTA-2Na (Ethylene diamine tetra acetate disodium), *p*-BQ (*p*-Benzoquinone) and IPA (Isopropyl alcohol) to analysis the effects of the scavengers on the photodegradation activity of the photocatalyst. The photo degradation's rate constant

plots are demonstrated in Figure 4.10(d). It is clearly evident that the photodegradation rate constants get drastically hindered due to the addition of EDTA-2Na and p-BQ which are the scavengers of photo-induced holes and superoxide anion radicals respectively. Although the addition of IPA which acted as scavenger for hydroxyl radicals shows no significant changes in the catalytic rate constants as compared to the efficiency when no scavengers were added into the catalytic system. In conclusion, the scavenger test indicates that the most necessary radicals performing in these redox reactions were photo-induced holes and superoxide radicals and corresponding bar plots Figure 411(d).

Figure 4.12 shows the XRD spectra of the composite material before and after the completion of the photocatalytic degradation activity. It can be observed that there are essentially no drastic changes in the characteristic peaks and phases of the BOC-GO material after the photocatalytic redox reaction. However, there is significant reduction in the peak intensities after the reduction reactions.

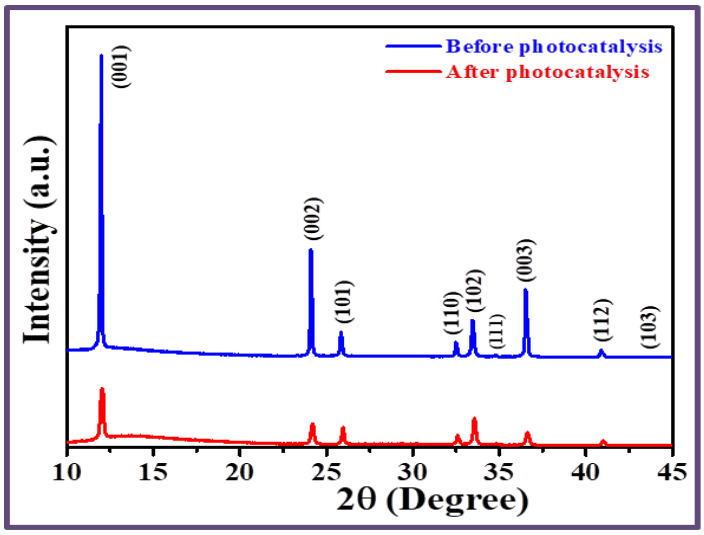

Figure 4.12: The PXRD pattern was shown of the before and after photocatalysis of the BOC-GO composite

4.3.8 Proposed Photocatalytic Mechanism

The proposed visible-light induced photocatalytic mechanism for the dye decomposition procedure by BOC-GO composite sample is shown in Scheme 4.1. Here the bandgap of the BOC-GO material is in the visible region of the UV-Vis spectrum so the visible-light assisted photocatalysis proved to be favorable for the material. The excitation of the nanomaterial transpired in presence of visible light followed by successive production of the photoelectrons in the conduction band (CB), and the photo-induced holes in the valence band (VB) of the BOC-GO nanocomposite photocatalyst. The photo-excitation of the composite catalyst leads to the initiation of photoelectrons in the CB (e^-_{CB}) and photo-induced holes (h^+) in the VB. The formation of the heterojunction between the graphene oxide and the

BiOCl enabled the suppression of recombination of the photo-induced electrons and holes by rapid transfer of the charge carriers from one system to another.

The CB of BOC-GO (0.4 V vs. NHE)[4] is at a positive potential (ve^+) than the redox potential required for the formation of the superoxide anion radical [$O_2/\bullet O_2^-$ (-0.046 V vs. NHE)]; hence this reduction reaction is not conceivable in the CB of BOC-GO. However, the two-reaction pathway via H_2O_2 formation for the production of •OH radical is plausible due to the more positive redox potential of O_2/H_2O_2 (0.69 V vs. NHE) reaction than the CB potential of BOC-GO which in turn benefits the generation of hydroxyl radicals in presence of the photo-induced electrons.

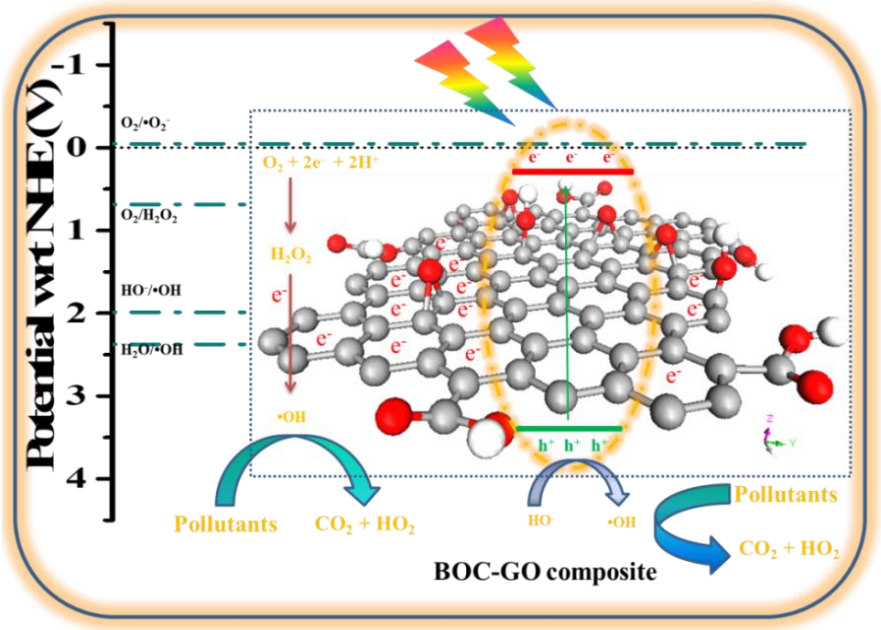

Scheme 4.1: Proposed photocatalytic mechanism was shown of the organic dye degradation by BOC-GO sample

Now the VB potential of BOC-GO composite (3.5 V vs. NHE) is at a higher positive potential than the redox potential of $H_2O/\bullet OH$ (2.37 V vs. NHE), which results in the oxidation reaction necessary for the generation of •OH from OH^- facilitated by the photo-induced holes in the VB of BOC-GO.

Hence the reaction events occurring during the complete photocatalysis procedure are described by the following equations:

$$(BOC-GO) + h\nu \rightarrow (BOC-GO)_{e_{CB}^-} + (BOC-GO)_{h_{VB}^+} \quad (4.3)$$

$$O_2 + 2H^+ + 2e_{CB}^- \rightarrow H_2O_2 \quad (4.4)$$

$$H_2O_2 + e_{CB}^- \rightarrow \bullet OH \quad (4.5)$$

$$OH^- + h_{VB}^+ \rightarrow \bullet OH \quad (4.6)$$

$$\bullet OH + Pollutants \rightarrow CO_2 + H_2O \text{ (Photodegradation products)} \quad (4.7)$$

Finally, the •OH active radicals, along with the photo-induced holes could subsequently degrade the harmful organic RhB dye to non-carcinogenic CO_2 and H_2O.

4.4 Conclusions

In conclusion, to successfully synthesise the BOC-GO nanosheets like composite material by hydrothermal method, and the various properties like identification of phases and chemical structures were efficiently conformed by sophisticated techniques like XRD, XPS, Raman, FTIR, UV-Vis DRS, BET, FESEM and HRTEM etc. The nanocomposite was effectively accomplished in the photodegradation of harmful, organic pollutant Rhodamine B (RhB) dye within a short time period assisted by visible light irradiation, and the photodegradation efficiency of the material was found to be around 99.59 % which supported the composite's highly active photocatalytic nature. Moreover, variations of different parameters such as the amount of catalyst and pH of the medium were analysed to investigate their effects on the photocatalytic performance of the nanomaterial. A feasible mechanism was also suggested to comprehend the reaction events occurring during the catalytic degradation procedure by BOC-GO. In this way the catalyst efficiently performed in the wastewater treatment for removal of toxic pollutants present in aqueous ecosystems.

References

[1] W. Lin, X. Yu, Y. Zhu and Y. Zhang, *Frontiers in chemistry*, 6, 2018, 274.
[2] R. He, S. Cao, D. Guo, B. Cheng, S. Wageh, A.A. Al-Ghamdi and J. Yu, *Ceramics International*, 41(3), 2015, 3511-3517.
[3] K.O.C. Husnu, H. Akkus and A. Mamedov, *Gazi University Journal of Science*, 25(1), 2012, 9-17.
[4] R. Sarkar, D. Das, B.K. Das, A. Mitra, N.S. Das, S. Sarkar and K.K. Chattopadhyay, *Materials Research Bulletin*, 125, 2020, 110778.
[5] R. Sarkar, D. Das, B. Das, S. Sarkar and K.K. Chattopadhyay, *AIP Conference Proceedings*, 2220(1), 2020, 020030.
[6] L. Yao, H. Yang, Z. Chen, M. Qiu, B. Hu and X. Wang, *Chemosphere*, 273, 2020, 128576.
[7] Y. Huo, J. Zhang, M. Miao and Y. Jin, *Applied Catalysis B: Environmental*, 111, 2012, 334-341.
[8] X. Wang, S. Yang, H. Li, W. Zhao, C. Sun and H. He, *RSC Advances*, 4(80), 2014, 42530-42537.
[9] R. Sarkar, D. Roy, D. Das, S. Sarkar and K.K. Chattopadhyay, *International Journal of Hydrogen Energy*, 46(30), 2021, 16299-16308.
[10] R. Sarkar, D. Das, A. Mitra, S Sarkar and K.K. Chattopadhyay, *Materials Today: Proceedings*, 18, 2019, 1086-1095.
[11] D.H. Wang, G.Q. Gao, Y.W. Zhang, L.S. Zhou, A.W. Xu and W. Chen, *Nanoscale*, 4(24) (2012) 7780-7785.
[12] J. Pan, J. Liu, S. Zuo, U.A. Khan, Y. Yu and B. Li, *Materials Research Bulletin*, 103, 2018, 216-224.
[13] X. Zhang, T. Guo, X. Wang, Y. Wang, C. Fan and H. Zhang, *Applied Catalysis B: Environmental*, 150, 2014, 486-495.

[14] J. Sun, Z.D. Hood, S. Wu, P. Wan, L. Sun, S. Yang and M.F. Chisholm, *Nanotechnology*, 30(30), 2019, 305601.
[15] P. Zhang, H. Liang, H. Liu, J. Bai and C. Li, *Materials Chemistry and Physics*, 272, 2021, 125031.
[16] J. Yu, B. Wei, L. Zhu, H. Gao, W. Sun and L. Xu, *Applied Surface Science*, 284, 2013, 497-502.
[17] R. Mahdavi and S.S.A. Talesh, *Materials Chemistry and Physics*, 267, 2021, 124581.
[18] H. Tang, Y. Ao, P. Wang and C. Wang, *Materials Science in Semiconductor Processing*, 27, 2014, 909-914.
[19] W. Zhang, F. Dong, T. Xiong and Q. Zhang, *Ceramics International*, 40(7), 2014, 9003-9008.
[20] H. Liu, W.R. Cao, Y. Su, Z. Chen and Y. Wang, *Journal of Colloid and Interface Science*, 398, 2013, 161-167.
[21] C.W. Siao, W.L.W. Lee, Y.M. Dai, W.H. Chung, J.T. Hung, P.H. Huang, W.Y. Lin and C.C. Chen, *Journal of Colloid and Interface Science*, 544, 2019, 25-36.
[22] W. Wang, M. He, H. Zhang and Y. Dai, *International Journal of Electrochemical Science*, 11, 2016, 1831-1839.
[23] L. Allagui, B. Chouchene, T. Gries, G. Medjahdi, E. Girot, X. Framboisier, A.B. haj Amara, L. Balan and R. Schneider, *Applied Surface Science*, 490, 2019, 580-591.
[24] Z. Liu, W. Xu, J. Fang, X. Xu, S. Wu, X. Zhu and Z. Chen, *Applied Surface Science*, 259, 2012, 441-447.
[25] S.K. Mandal, K. Dutta, S. Pal, S. Mandal, A. Naskar, P.K. Pal, T.S. Bhattacharya, A. Singha, R. Saikh, S. De and D. Jana, *Materials Chemistry and Physics*, 223, 2019, 456-465.
[26] N.B. Singh and A.B.H. Susan, *Polymer-based Nanocomposites for Energy and Environmental Applications*, 2018, 569-595.
[27] J. Rashid, S. Karim, R. Kumar, M.A. Barakat, B. Akram, N. Hussain, H.B. Bin and M. Xu, *Scientific Reports*, 10(1), 2020, 1-11.
[28] S. Kang, R.C. Pawar, Y. Pyo, V. Khare and C.S. Lee, *Journal of Experimental Nanoscience*, 11(4), 2016, 259-275.
[29] M. Mukherjee, U.K. Ghorai, M. Samanta, A. Santra, G.P. Das and K.K. Chattopadhyay, *Applied Surface Science*, 418, 2017, 156-162.
[30] P. Howli, S. Das, S. Saha, B. Das, P. Hazra, D. Sen and K.K. Chattopadhyay, *RSC Advances*, 6(94), 2016, 91860-91869.

Chapter 5

Morphology tuning of Bismuth Oxychloride nano-crystals by Citric acid variation: Application in Visible light-assisted dye degradation and Hydrogen evolution by Electrochemical method

5.1 Introduction

Bismuth oxychlorides (BiOCl) have layered structures which can be tuned into different morphologies for significant variation in their chemical and physical properties leading to their applications in numerous fields like photocatalysis, hydrogen evolution, oxygen reduction, and many more[1]. In recent times, catalytic reactions mediated in presence of light (photo) sources have become an effective method to remove toxic effluents in the wastewater from various chemical and textile industries that would otherwise be released into the environment. The pure BiOCl nanomaterials have impressive photocatalytic properties[1-4] for their large indirect band gaps in the range of 3.2 ~ 3.5 eV along with their unique layered morphology and p-type nature. The indirect band gap of BiOCl can effectively suppress the recombination of photogenerated electron and hole pairs[3] thereby considerably improving their catalytic properties.

There are many reports on the catalytic activity of bismuth oxyhalides (BiOX, X = Cl, Br & I) in their pure form. Xiong et al. developed tunable nanostructures of BiOCl which exhibited highly efficient photocatalytic properties with regard to dye degradation under visible light[5], Huo et al. synthesised flower-like BiOBr crystals which could degrade RhB in presence of visible light[6],Yuan et al. also synthesised hierarchical Fe(III)-modified BiOBr samples which exhibited photocatalysis of organic dyes and benzyl alcohol in presence of H_2O_2 under UV-light[7], and Wang et al. developed micro-spherical BiOI for visible-light assisted photocatalytic degradation of RhB[8]. There are also reports regarding the modification of BiOX by simple doping with metals or non-metals or by forming heterojunctions with other semiconductors to improve their catalytic efficiency. Tian et al. proposed Fe doping of BiOCl nanomaterial for efficient photo-degradation of methyl blue (MB) dye in presence of visible light irradiation[9] and he also synthesised $BiPO_4$ nanomaterial that showed photocatalytic activity of the same textile dye in presence of UV-light[10], Cao et al. developed Bi_2S_3/BiOCl heterostructure for enhanced photocatalytic activity in degrading RhB under visible light irradiation[11], Cui et al. synthesised a novel composite of CdS/BiOBr which exhibited impressive photocatalytic properties[12], Mehraj et al. fabricated Fe_2O_3/BiOI based p-n heterojunction which showed excellent visible-light assisted photocatalytic activity[13] and Ding et al. developed the z-scheme $BiO_{1-x}Br/Bi_2O_2CO_3$ heterojunction sample with oxygen vacancies that improved the photocatalytic activity in degradation of antibiotics (CIP, 4-MAA, etc.) under visible light[14]. These reports prove the efficiency of BiOX in degrading organic toxic pollutants establishing them as prospective materials for water remediation.

Exhaustion of energy sources is the most demanding challenge of the 21st century. Nowadays most researchers are aiming to develop eco-friendly and low-cost renewable sources of energy. In nature there are many renewable energy resources like water, wind, sunlight, tides, geothermal heat etc., all of which are safe and clean and can be exploited without further purification. In this aspect, hydrogen generation[15] by three most productive methods like thermochemical method by solar energy, photochemical and electrochemical has been constantly studied, researched and developed for effective utilisation in practical applications. Energy obtained from hydrogen evolution is capable of being used for energy storage as a substitute for batteries. The photocatalytic water splitting method to evolve oxygen and hydrogen using an efficient and targeted semiconductor material in presence of visible light or UV-light irradiation sources is one of the most supportive procedures for storage of solar energy[16]. Although the photocatalytic water splitting has shown excellent performance in production of hydrogen and oxygen, this process suffers from relatively inferior efficiency in energy conversion, thereby limiting its possibility in wide range industrial applications. Since 1789, there has been a rapid surge in the extensive research and development of water electrolysis to generate hydrogen with impressive purity. This method has gained significant popularity in recent times owing to its appreciable flexibility and efficiency. The electrodes used in this method consist of anode and cathode for oxygen evolution and hydrogen evolution reactions respectively[17]. This method requires more attention in order to develop eco-friendly and low-cost electrolyte and electrodes to sustain long term endurance.

In this work, a simple synthetic strategy has been used to prepare morphology varied (00l) lattice plane exposed pure BiOCl nanomaterials by variation in citric acid concentration which exhibited effective photocatalytic degradation of harmful organic textile Rhodamine B dye in presence of visible light irradiation in the aqueous environment. The material has been further utilised for hydrogen evolution by employing electrochemical measurements and the Tafel slope of the best nanomaterial gives a value of about 72 mV/dec.

5.2 Experimental Details

5.2.1 Materials and Methodology

All precursors were purchased from Merck and utilised without further purification. 1.2 mmol of Bismuth Nitrate Pentahydrate {$Bi(NO_3)_3$, $5H_2O$}, 0.85 mL of Hydrochloric acid (HCl 37 %) and 7.5 mL of DI water were mixed to form solution A. Similarly, various molar ratios (0 mmol, 0.5 mmol, 1.0 mmol and 1.5 mmol) of the capping agent Citric acid ($C_6H_8O_7$), Poly Vinyl Pyrrolidone (PVP, K30), 50 mL of Absolute Ethanol (C_2H_6O) and 42 mL DI water were mixed to form solution B under

vigorous stirring at 80 °C. After that, solution A was drop wise added to solution B followed by continuous stirring for 5 min at 80 °C to make solution C. Thereafter solution C was transferred into a stainless steel PTFE-lined autoclave of 100 mL and subsequently heated for 3 hours at 160 °C. After the reaction was complete, the system was naturally allowed cool down to ambient temperature, and then washed with ethanol and DI water by filtration of the precipitates until the solution pH turned to neutral value of 7. Then the samples were dried overnight at 80 °C in an oven to obtain the powder products. Variation in the molar ratio of the citric acid during the synthesis procedure resulted in the as-prepared samples named as CA-0 (0 mmol), CA-1 (0.5 mmol), CA-2 (1.0 mmol) and CA-3 (1.5 mmol).

5.2.2 Characterizations

The as-prepared materials were characterised by several sophisticated techniques to have a proper insight into the formation of phases, morphology, chemical bonding, electronic band gap and compositional analysis. The phase formation of the catalysts were analysed by X-Ray diffraction (XRD, Bruker D8 advance) accompanied with Cu Kα source (λ = 1.54 Å), at a scan rate of 2 °min^{-1} from the range of 2θ =10 to 60 °. Raman shifts of the samples were analysed by Witec Raman Spectroscopy combined with a laser source of wavelength 523 nm to analyse the chemical bonds of the synthesised samples. The structural morphology of the materials was revealed from the Field Emission Scanning Electron Microscopic study (FESEM, Hitachi S-4800) which was equipped with an Energy Dispersive X-ray Spectroscope (EDS) for the analysis of the compositional ratios of the material. The lattice fringes were obtained from high resolution Transmission Electron Microscopic (TEM) images. The optical band gap of the materials was obtained from the Diffuse Reflectance Spectra (DRS) measured from UV-Vis Spectroscopy (Shimadzu UV-3600).

5.2.3 Photocatalytic Property Measurement

The photocatalytic properties of the as-prepared pure BiOCl citric acid varied materials were measured at room temperature and neutral pH of 7. A two walled glass beaker designed for the circulation of cold water was utilised for the photocatalytic reactions. 30 mg of the as-synthesised samples were dispersed in 10^{-5} M of aqueous solution of Rhodamine B (RhB) dye in 40 mL DI water. The solution was continuously stirred under dark conditions for 1 hour to attain the maximum adsorption-desorption equilibrium stage. After 1 hour the system was placed under a high pressure mercury lamp accompanied with a UV cut-off filter as the source for visible light. 3 mL of the dye solution was extracted at regular time intervals, centrifuged for 5 min to separate the catalyst from the solution and finally subjected to absorption analysis from UV-Vis Spectroscopy.

5.2.4 Electrochemical Property Measurement

The HER, Nyquist and stability tests were measured by the AUTOLAB PGSTAT302N (M-204) equipped with a 3 electrode configuration system and the electrochemical impedance was analysed subsequently by employing 1.1 Nova software. 10 mg of the as-prepared material was dropped on glass carbon after 1 hour of continuous stirring in 100 µL absolute ethanol.

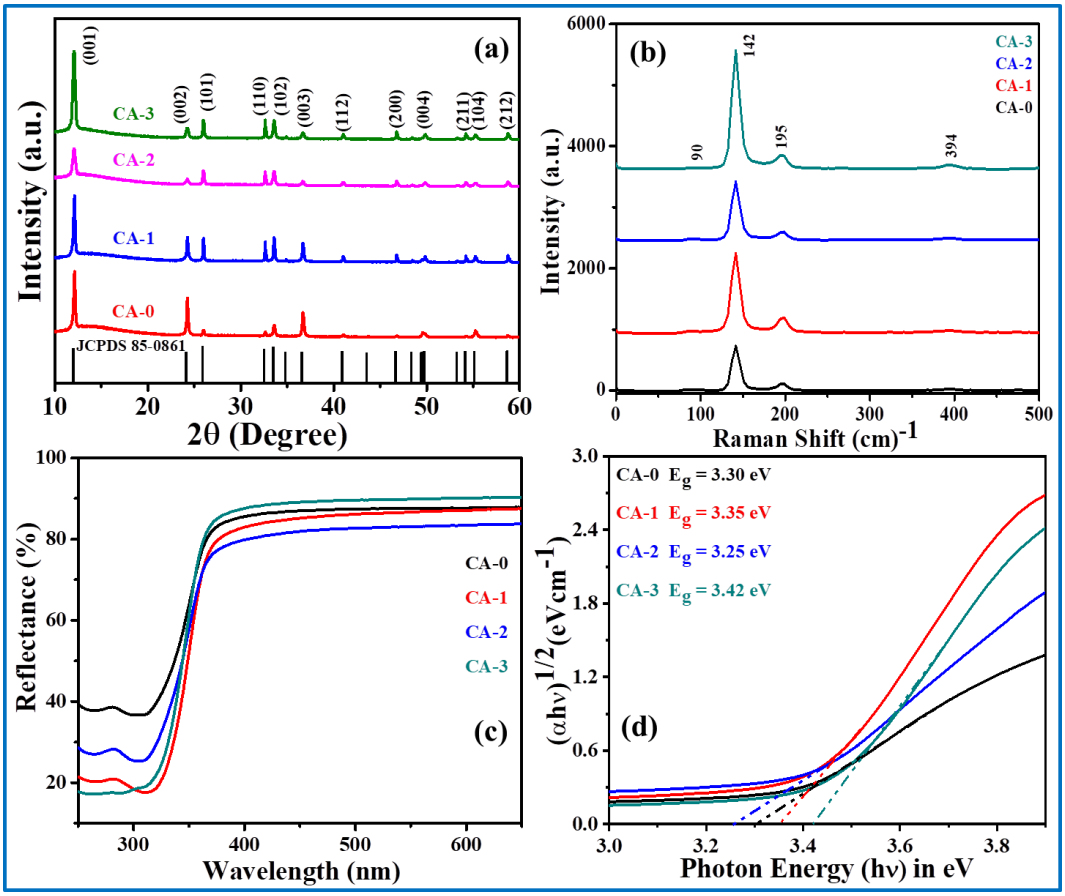

Figure 5.1: XRD patterns of BiOCl synthesised with varying amounts of citric acid (a), Raman spectra of BiOCl samples (b), Diffuse Reflectance Spectra of all the samples (c) and Kubelka –Munk plots for indirect band gap of the BiOCl samples (d)

Pt electrode was used as the counter electrode, Ag/AgCl electrode was used as the reference electrode and 0.5 M H_2SO_4 was utilised as the electrolyte solution.

$$E_{(HER)} = E_{(Ag/AgCl)} + 0.2\,V \qquad (5.1)$$

The acidic electrolyte solution was used for the measurement of the linear sweep voltammetry (LSV) and the stability test. The Nyquist measurement was performed at a stable frequency of 100000 Hz.

5.3 Results and Discussion

5.3.1 Structural Analysis

The XRD patterns of all the as-prepared nanomaterials are shown in Figure 5.1(a). The most intense peak corresponds to the (001) lattice plane. All the observed peaks are well matched with JCPDS card no. 85-0861. It is to be noted that all the samples exhibit good crystallinity in nature.

5.3.2 Chemical Analysis

Raman shifts of as-prepared BiOCl nanomaterials are shown in Figure 5.1(b). The spectra clearly show three peaks which are identified as Raman active mode A_{1g}, E_g and B_g[18-20]. The highest intense peak at 142 cm^{-1} arises due to the internal stretching vibration mode of the Bi- Cl bond and is known as the A_{1g} band, whereas the weak band at 90 cm^{-1} arises due to the first order stretching.

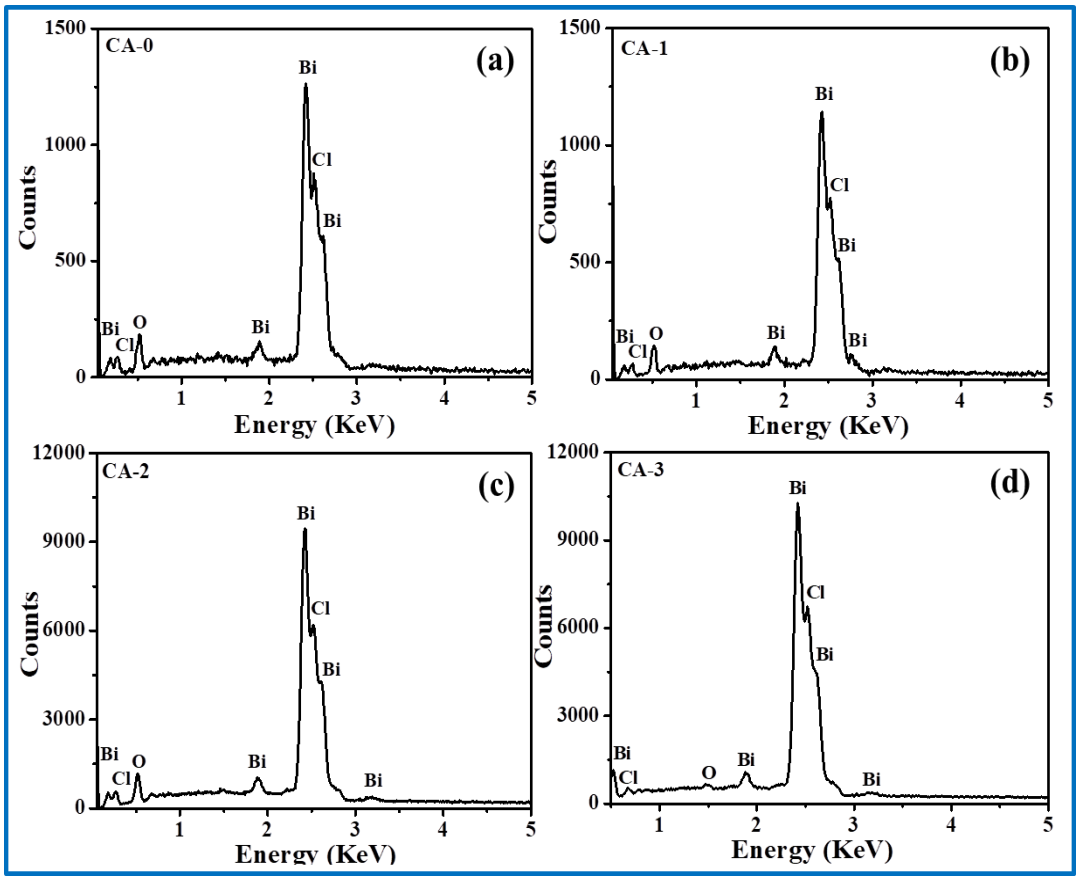

Figure 5.2: Energy Dispersive X-ray Spectroscopy (EDS) pattern of (a) CA-0, (b) CA-1, (c) CA-2 and (d) CA-3 pure BiOCl citric acid varied as-synthesized nanomaterials

The two other prominent peaks at 195 cm^{-1} and 394 cm^{-1} are assigned to the Bi-Cl bond internal stretching vibration mode which is also known as E_g band and the O^{2-} motion of atoms known as B_g

band respectively. No other peaks can be observed in the Raman spectra of the as-synthesised nanomaterials.

5.3.3 Optical Property Analysis

UV- Vis diffuse reflectance spectroscopy (UV-Vis DRS) has been carried out in the range of 250 nm to 650 nm for all the as-prepared white coloured powder samples taking $BaSO_4$ as standard for reflectance. The corresponding reflectance graph is shown in Figure 5.1(c). It can be observed that all samples exhibited high reflectance of about 92 % along with a sharp drop near 310 nm.

Table 5.1: Quantitative results as obtained from EDS analysis

Materials	Quantitative Result	Bi	O	Cl
CA-0	Weight %	79.46	5.07	15.47
	Atom %	33.54	27.98	38.48
CA-1	Weight %	81.91	4.34	13.75
	Atom %	37.29	25.81	36.90
CA-2	Weight %	81.2	4.30	14.50
	Atom %	36.44	25.19	38.37
CA-3	Weight %	80.8	4.97	14.23
	Atom %	35.19	28.27	36.54

The indirect band gaps of the samples are analysed from the reflectance spectra by using the Kubelka-Munk equation and the corresponding plots of the Kubelka-Munk operator vs. Photon Energy (hν) are shown in Figure 5.1(d)[21]. The Kubelka-Munk equation is given by:

$$(\alpha h\nu)^{1/r} = k(h\nu - E_g) \qquad (5.2)$$

where,

$\alpha = (1-R)^2/2R$,

R = Reflectance

$h\nu$ = photon energy in eV,

k = a proportionality constant,

E_g = band-gap energy and

r = 1/2 or 2 depending on the direct or indirect nature of the materials respectively.

Here the calculated band gaps of the nanomaterials lie in the UV region in the range of 3.25 to 3.42 eV as shown in Figure 5.1(d).

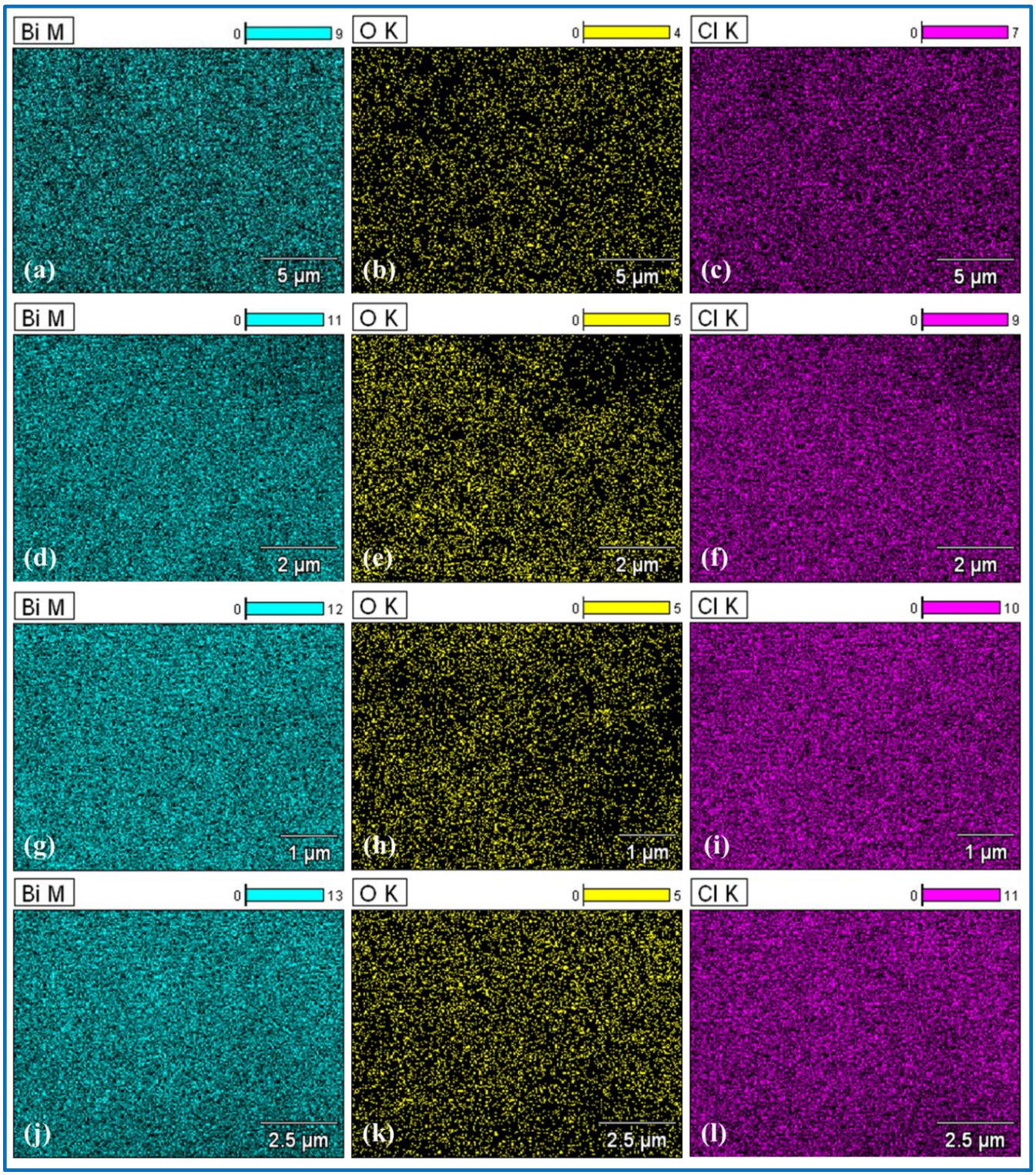

Figure 5.3: Elemental Mapping of the CA-0 (a-c), CA-1 (d-f), CA-2 (g-i) and CA-3 (j-l) nanomaterials

5.3.5 Compositional Analysis

The elemental composition of the BiOCl nanomaterials has been calculated from energy dispersive X-ray spectroscopy (EDS) results which indicate the presence of Bi, O and Cl as shown in Figure 5.2(a-d) and the corresponding elemental mapping is shown in Figure 5.3(a-l). The quantitative results of the samples such as weight and atomic percentages of the respective elements are presented in Table 5.1.

5.3.4 Morphological Analysis

Figure 5.4 shows the morphology of all the synthesised samples as obtained from field emission scanning electron microscopy (FESEM). It can be observed that variation in the concentration of citric acid leads to gradual change in the morphology of the samples. Figure 5.4(a) reveals the chunks of nanosheets with dimensions of 50 nm to 2 μm and thickness of 25 nm to 1 μm. Figure 5.4(b) shows nano-disk morphology with average radii between 100 and 300 nm and it is be evident from Figure 5.4(c) that the nanosheets self-assemble to form nano-nuts with average dimensions of 3 to 5 μm and average thickness of 4 to 5 μm. Figure 5.4(d) shows nano-flakes with average length of 2 nm to 1 μm and average thickness 200 to 500 nm.

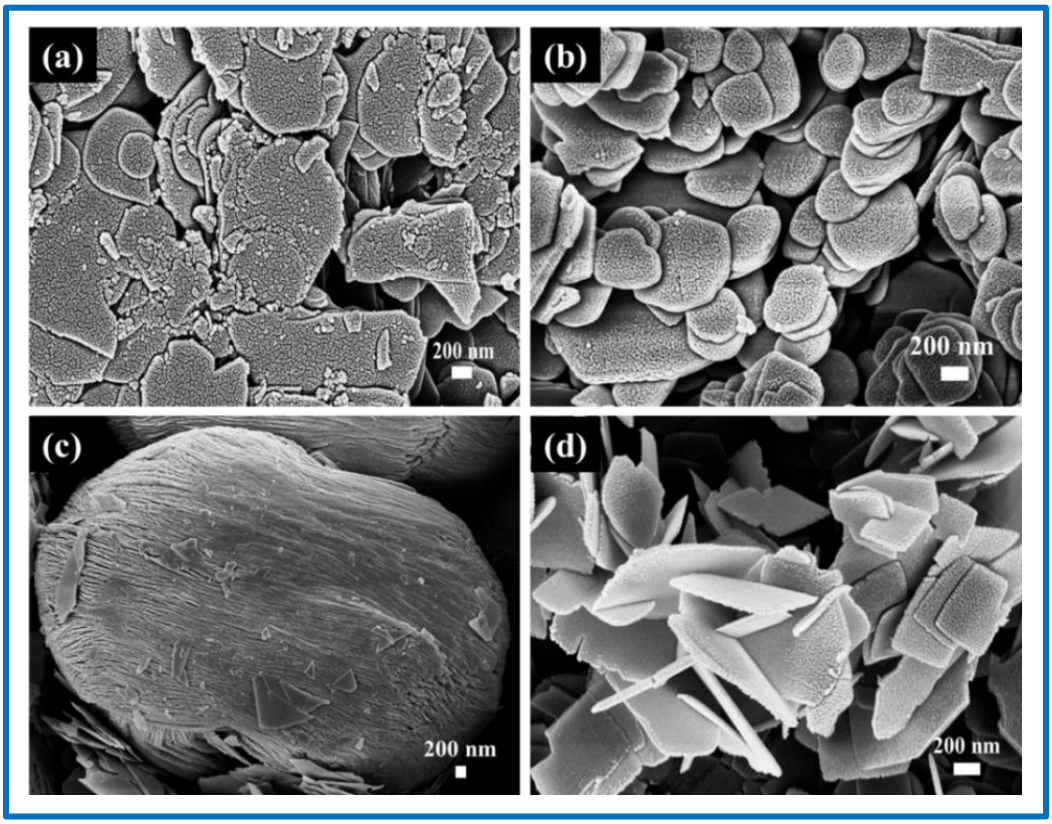

Figure 5.4: FESEM images of BiOCl (a) CA-0, (b) CA- 1, (c) CA-2 and (d) CA-3

Figure 5.5 shows the transmission electron microscopy and high resolution transmission electron microscopy (HRTEM) images of the as-prepared CA-2 BiOCl material. Figure 5.5(a) reveals the arrangement of various nanosheets in a solid cluster. This agrees with the respective FESEM image shown in Figure 5.5(c). The lattice fringes shown in Figure 5.5(b) confirm the high crystallinity of the sample along the (001) plane which corroborates the XRD results. Figure 5.3(c) shows the SAED pattern of the as-synthesised nanomaterial which reveals the polycrystalline nature of the sample.

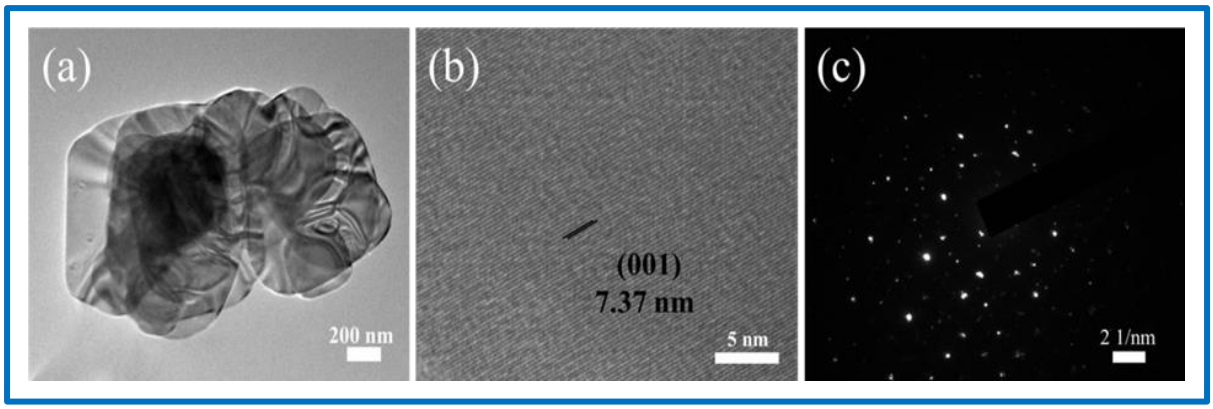

Figure 5.5: TEM image (a), HRTEM image showing lattice fringes (b) and the SAED pattern (c) of CA-2 sample

5.3.6 Photocatalysis Activity Analysis

The photocatalytic performance of the as-prepared BiOCl nanomaterials has been analysed by degrading 10^{-5} M aqueous solution of Rhodamine B (RhB) under visible light irradiation. Figure 5.6(a-d) shows absorption spectra of the RhB dye in presence of all as-prepared catalysts which reveal the efficient degradation within this small time interval. The degradation efficiency of the best sample CA-2 is about 98 % within 10 minutes of visible light irradiation as observed from Figure 5.6(c).

The (C/C_0) vs. irradiation time graphs are shown in the Figure 5.7(a) and the apparent rate constant (k_{app}) values have been calculated from the Langmuir-Hinshelwood pseudo 1st order kinetics equation (5.3) by plotting $\ln(C_0/C)$ vs. time graphs as shown in Figure 5.7(b) for the all BiOCl samples[22, 23].

$$\ln\left(C_0/C\right) = k_{app}t \qquad (5.3)$$

where,

C_0 = RhB dye concentration at the beginning of the reaction,

C = RhB dye concentration at time 't',

k_{app} = apparent rate constant and

t = time.

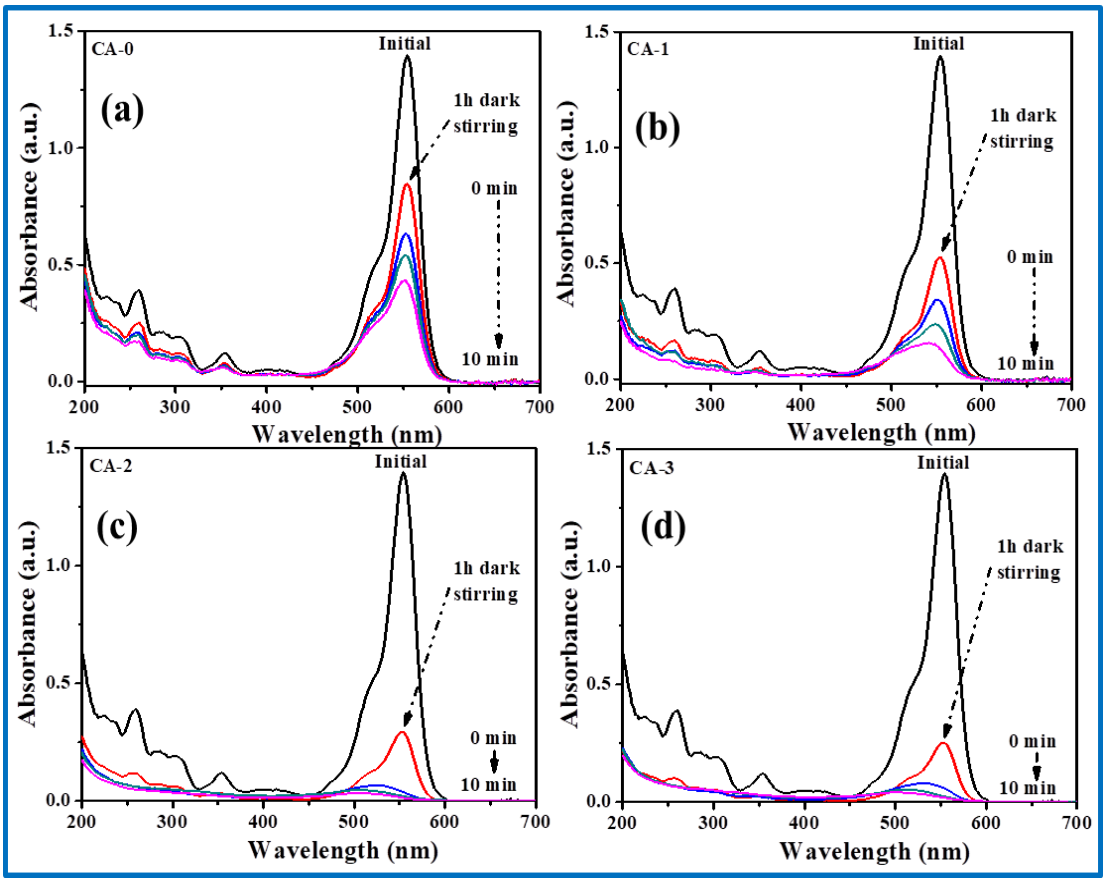

Figure 5.6: Absorption spectra of (a) CA-0, (b) CA-1, (c) CA-2 and (d) CA-3

The bar graphs as shown in Figure 5.7(c) and Figure 5.7(d) respectively correspond to the rate constant (k) values and degradation efficiency (η) values for 10 min of irradiation time. The efficiency of the photocatalysts was analysed by the equation (5.4):

$$\eta\,\% = (A_0 - A_t)/A_0 \times 100 \qquad (5.4)$$

where,

η = degradation efficiency of the photocatalyst,

A_0 = Initial absorbance of the RhB dye solution at the beginning of the reaction and

A_t = Absorbance of the RhB dye solution at time 't'.

The photocatalytic performance rates were succeeding to the 1st order kinetics and the rate constant analysis also tabulated by Table 5.2.

All the nanomaterials showed efficient photocatalytic degradation of harmful RhB in the presence of visible light; however the best sample CA-2 has shown impressive degradation activity of about 98 % in only 10 minutes. The dosage variation on the catalytic activity has been further studied and the

corresponding bar graphs are shown in Figure 5.8(a). It reveals the gradual increase in the degradation efficiency with increase in the catalyst dosage (0, 15, 30 and 45 mg).

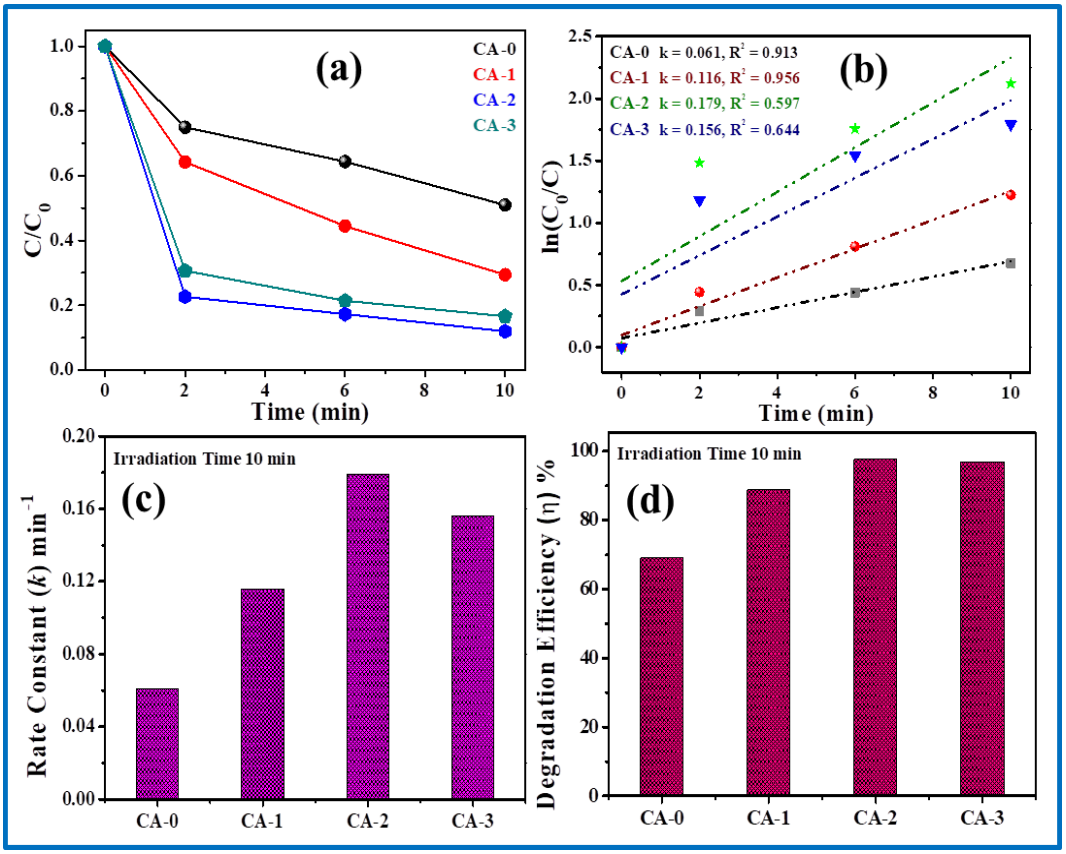

Figure 5.7: The (C/C_0) vs. time plots (a), $\ln(C_0/C)$ vs. time plots for 1st order kinetics (b), bar graph plots of rate constant (c) and degradation efficiency (d) of BiOCl samples

Figure 5.8(b) shows a bar graph plot of variation in the pH which affects the degradation efficiency of the CA-2 catalyst to a considerable extent. In acidic medium the degradation efficiency of the material is 98.42 % whereas in the alkaline medium the efficiency decreases drastically to 35.97 % in the same time interval.

Table 5.2: Rate constant values of time and temperature varied samples

Materials Name	R^2 values	*k* values (min^{-1})	Degradation efficiency (η)%
CA-0	0.913	0.061	69.06
CA-1	0.956	0.116	88.85
CA-2	0.597	0.179	97.64
CA-3	0.644	0.156	96.94

Figure 5.8(c) reveals the stability of as-prepared pure BiOCl sample by recycling the catalyst up to 3

cycles. For the catalyst recycling studies, the used catalyst material obtained after the first catalytic cycle was washed thoroughly with DI water and dried at 60 °C overnight. The dried product was then again utilised for the next catalytic cycle following similar procedures with similar dye concentration. This process was repeated three times.

The effect of the light sources (UV and visible) on the photocatalytic activity are shown in Figure 5.8(d). It shows the catalyst superior efficiency under visible light.

In the photocatalytic dye degradation, the primary active radicals are hydroxyl radical, holes, and superoxide anions whose active involvement in the redox reactions can very efficiently degrade the RhB dye under visible light irradiation. The CA-2 catalyst was subjected to different scavengers of active radicals like *p*-benzoquinone ((BQ) 0.01 mol/L), ethylene diamine tetra acetate disodium ((EDTA-2Na) 0.01 mol/L) and isopropyl alcohol ((IPA) 0.01 mol/L), to analyse the effect of these scavengers on the degradation efficiency of the catalyst. The corresponding degradation efficiency bar graphs are shown in Figure 5.9(a).

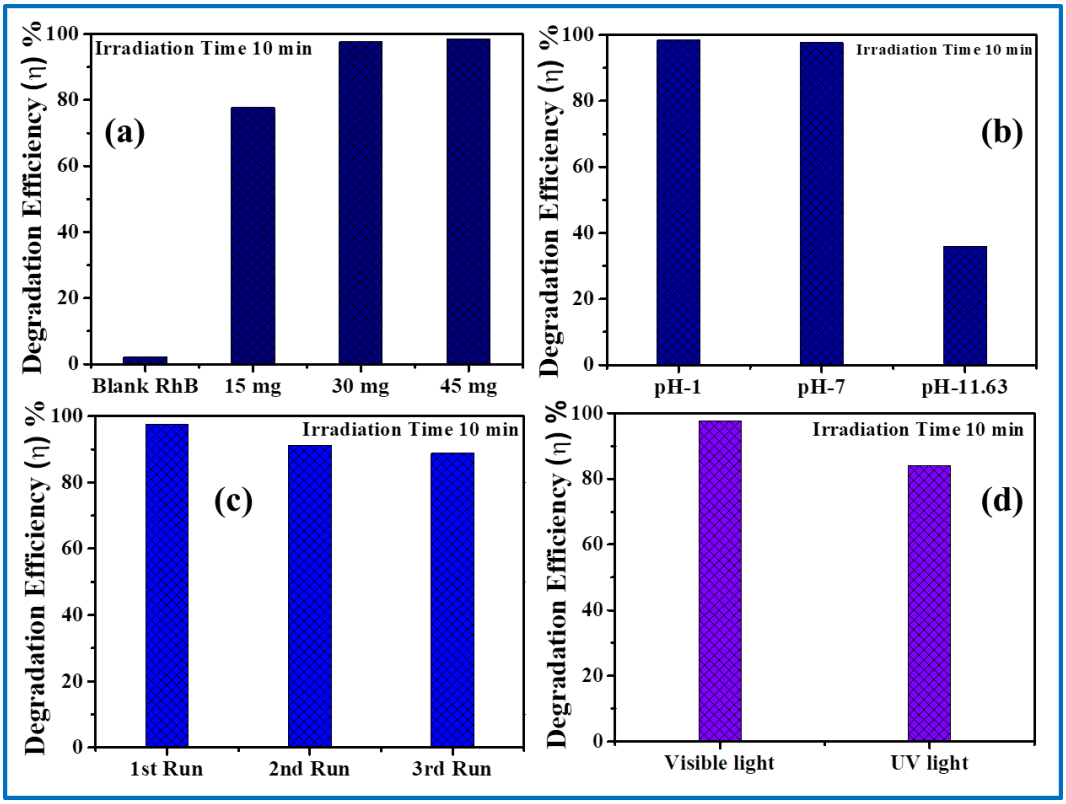

Figure 5.8: Bar graphs showing the change in the photocatalytic degradation efficiency on varying the catalyst dosage (a), pH of the system (b), recycling test up to three times (c) and the variation of the light sources (d) on the catalytic activity of CA-2

It clearly shows that the degradation efficiency significantly changed with the addition of BQ which acted as the superoxide anion quencher, and also on addition of EDTA-2Na which acted as hole scavenger; whereas on adding IPA, the scavenger for hydroxyl radicals, the reaction rate did not change considerably. Thus from these results it can be concluded that the superoxide radical and the photogenerated holes are necessary radicals required for the photocatalytic degradation.

Figure 5.9(b) shows the XRD graph of the CA-2 catalyst before and after photocatalysis which reveals basically no change in the materials due to the reaction. Figure 5.9(c) also shows the FESEM image of the catalyst CA-2 after photocatalysis.

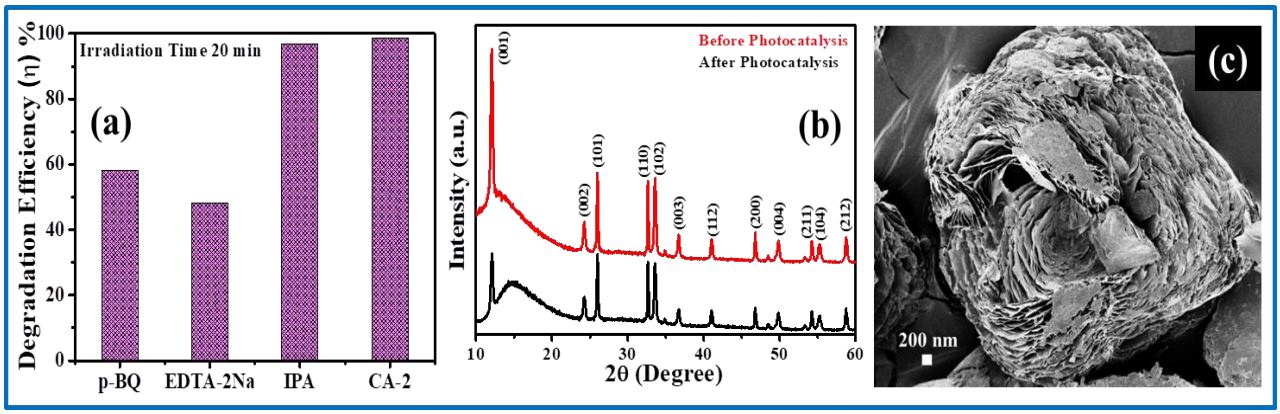

Figure 5.9: Scavenger test for active radicals (a), XRD pattern before and after photocatalysis (b) and FESEM image after photocatalysis (c) of the CA-2 nanomaterial

5.3.7 Proposed Mechanism for Photocatalytic Dye Degradation

A mechanism of dye decomposition in the presence of CA-2 material under visible light irradiation has been proposed in Scheme 5.1. The bandgap of CA-2 lies in the UV region but the sample interestingly exhibits better catalytic properties under visible light irradiation. This phenomenon can be attributed to the dye-sensitisation[24] mechanism where, initially, in presence of visible light, RhB gets excited to an active radical RhB*.

The high adsorptions of RhB on the CA-2 and CA-3 samples as compared to the CA-0 and CA-1 samples are evident from the absorbance spectra (Figure 5.6) from where it can be seen that after 1 hour of dark stirring and with the on-set of light irradiation, there is a significant reduction in the absorption intensity of CA-2 and CA-3 than that of CA-0 and CA-1. With the strong adsorption of the RhB dye on the catalyst surface, photo-degradation occurred more efficiently for the CA-2 and CA-3 samples as compared to the CA-0 and CA-1 samples. This strong adsorption phenomenon suggests the possibility of a dye-sensitisation mechanism during the photocatalytic activity.

Moreover since the lowest unoccupied molecular orbital (LUMO) of RhB is at a more negative potential than the conduction band (CB) of BiOCl, so there will be a transfer of the photogenerated electrons from the LUMO edge of RhB to the CB edge of BiOCl. Following this event, an active radical RhB· is formed from RhB* due to the formal donation of an electron, which can subsequently result in the effective degradation to non-toxic products in presence of $\cdot O_2^-$ or ·OH radicals[1].

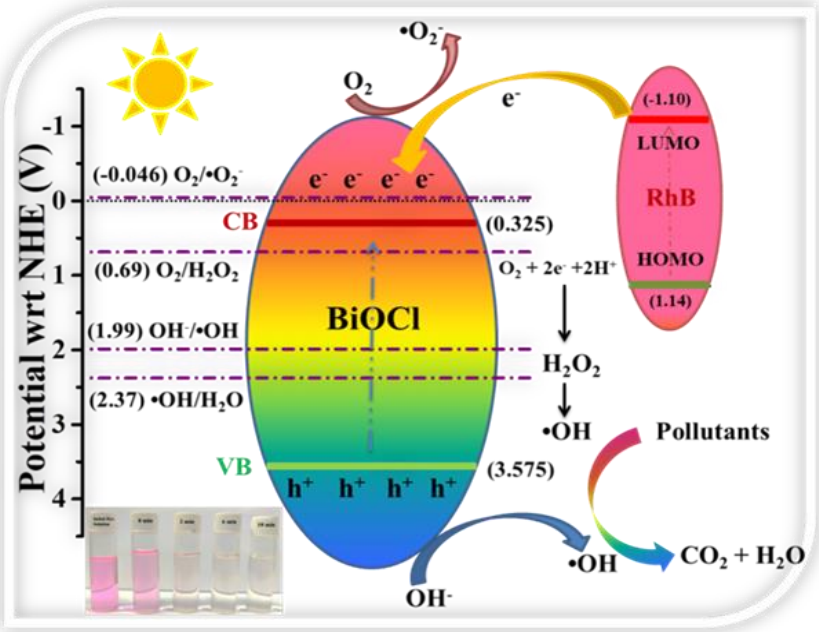

Scheme 5.1: Proposed mechanism of dye degradation by BiOCl (CA-2) sample in presence of visible light

The electrons on the CB of BiOCl can generate superoxide anions ($\cdot O_2^-$) or it can also generate ·OH radicals by H_2O_2 reaction chain. These active radicals can degrade RhB dye into non-toxic end products of CO_2 and H_2O molecules. Also, the holes in the valence band (VB) of BiOCl can directly degrade RhB dyes into CO_2 and H_2O. The unique nano-nut like morphology along with the (001) exposed crystal facet can also result in the enhanced photocatalytic activity of the BiOCl samples. The exposed (001) plane can result in the improved adsorption of dye molecules on the BiOCl sample. A comparison Table 5.3 has been provided in the supporting file to compare the performance of the as-synthesised catalyst material with other existing reports.

5.3.8 Electrochemical Activity Analysis

The electrochemical activity of the CA-2 nanomaterial for hydrogen evolution reaction (HER) by a three electrode compositional set up system was established. Figure 5.10(a) shows the Linear sweep voltammetry (LSV) plots of all CA materials with a scan rate of 10 mV/s. The Figure 5.10(b) shows the comparative polarisation curve CA-2 with Pt tip. The measurement was carried out in acidic medium

(0.2 M H_2SO_4) where the as-prepared sample was deposited on glassy carbon which acted as the working electrode. The calculations and analysis of the LSV plots of CA-2 and commercial Pt tip were done with iR correction.

Table 5.3: Comparison of photocatalysis of different reported pure BiOCl catalysts

Name of Catalyst	Dye degraded and Concentration of Dye	Degradation Time (min)	Catalyst Dosage in 100 mL DI (g)	$k_{relative}$ (min^{-1})	$k_{absolute}$ = $k_{relative}$/Catalyst Dosage (min^{-1})
BiOCl [25]	RhB (4.17 x 10^{-4} M)	120	0.1	0.0670	0.6704
BiOCl NS [26]	RhB (1.04 x 10^{-3} M)	20	0.05	-	-
BiOCl HNS [27]	RhB (10^{-5} M)	15	0.01	-	-
BiOCl [28]	RhB (10^{-5} M)	4	0.1	-	-
BiOCl [29]	RhB (10^{-6} M)	60	0.05	0.112	2.24
BiOCl [30]	RhB (10^{-5} M)	20	0.02	0.272	13.6
BiOCl [This Work]	RhB (10^{-5} M)	10	0.075	0.179	2.387

The Tafel equation describes the overpotential of all samples for a specific current density for sluggish reaction kinetics in Figure 5.10(c). The Tafel parameters (see below) are a means to compare lectro-catalysts. The slope as calculated from the Tafel plot indicates the type of reaction mechanism taking place and the corresponding equation is given below (5.5):

$$X = a + b\ log\ |J| \qquad (5.5)$$

where,

X = overpotential,

a = constant,

b = Tafel slope and

J = current density.

The mechanism of HER and the rate-determine step can be evaluated from the Tafel slope. The values as determined from the Tafel slopes for three types of HER mechanisms, namely, Volmer, Heyrovsky and Tafel are 118, 39 and 29 mV dec^{-1} respectively[31] and the reactions taking place for these three types[32] are given by the following equations (5.6), (5.7) and (5.8):

$$A + e^- + H^+ \rightarrow AH_{ads}\ (for\ Volmer) \qquad (5.6)$$

$$AH_{ads} + e^- + H^+ \rightarrow A + H_2\ (for\ Heyrovsky) \quad (5.7)$$

$$AH_{ads} + AH_{ads} \rightarrow 2A + H_2\ (for\ Tafel) \quad (5.8)$$

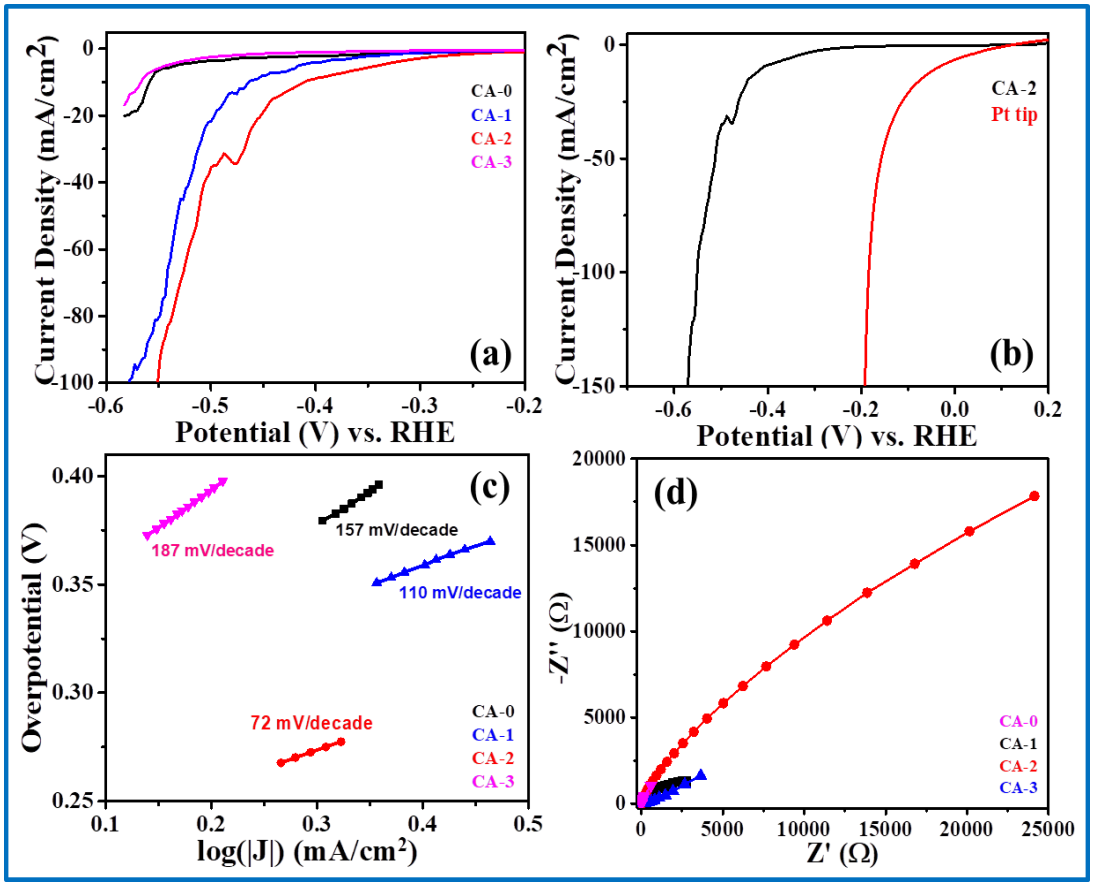

Figure 5.10: The polarisation (iR corrected) curves of all materials with a scan rate of 10 mV/s (a), comparative polarisation (iR corrected) curve CA-2 with Pt tip (b), the Tafel plots (c) and the nyquist plots of all synthesised sample (d)

The well-known commercial Pt tip and the as-synthesised nanomaterial CA-2 have Tafel slopes 72 mV/dec respectively as given in Figure 5.10(c). It is to be noted that usually in HER, the Heyrovsky reaction occurs for electrochemical desorption whereas electrochemical adsorption leads to Volmer reaction. In the present work, the reaction rate as determined from the Tafel slope indicates the occurrence of the Heyrovsky type reaction for the CA-2 nanomaterial.

Figure 5.10(d) shows the Nyquist plot of all the as-synthesised CA nanomaterial measured at a frequency of 100 Hz to 0.1 MHz. The diameter of the semicircle obtained from the Nyquist graph indirectly evaluates the charge transfer resistance which is essential for HER catalysis. It also explains the Nyquist plot of CA-2 which exhibits an almost linear relationship between $Z^{//}$ vs $Z^{/}$. Generally, a small semicircle is the indication of low charge transfer resistance between the electrolyte ions and the

working electrode. In comparison to CA-2 with CA-0, CA-1 and CA-3, that exhibits a large semicircle which implies the higher resistivity to exhibit facile HER performance.

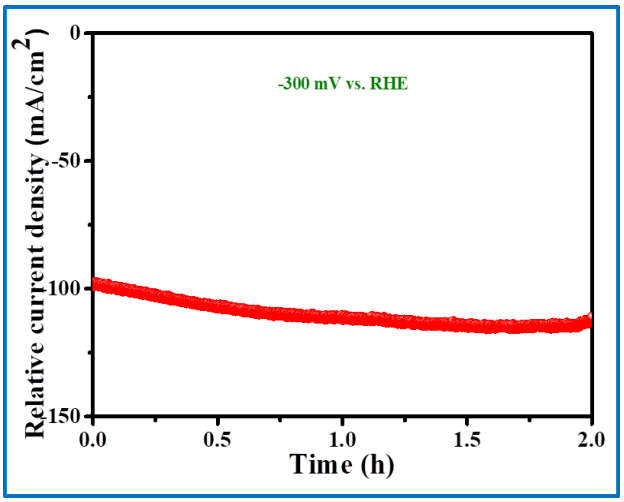

Figure 5.11: The relative stability test of the CA-2 nanomaterials at -300 mV vs. RHE with applied potential to achieve at -100 mA/cm^2 current density

Figure 5.11 shows the relative stability test, also called the long-term chronoamperometric test, of the sample CA-2. A potential of -300 mV (vs. RHE) was applied for 2 hours to accomplish about ~ 100 mA/cm^2 current density. After that the material shows insignificant diversion in current density of about ~ 9.4 % w.r.to initial which proves high stability of CA-2 in HER in acidic medium.

5.4 Conclusions

In conclusion, morphology-tuned BiOCl samples prepared by variation in concentration of the capping agent citric acid were effectively exploited for degradation of toxic Rhodamine B (RhB) dye under visible-light irradiation. The best sample showed impressive degradation efficiency. Further variation in parameters like catalyst dosage, pH and irradiation sources during photocatalysis were analysed to observe the catalysts' performance. The pure material was also successfully used as an electrocatalyst for hydrogen evolution mediated by electrochemical measurement in the acidic medium. The Tafel slope showed a value of about 72 mV/dec for the best sample CA-2 nanomaterial.

References

[1] X. Su, L. Hou, L. Xia, X. Yu, J. Guo, Y. Zhu and Y. Zhang, *Journal of Materials Science*, 54, 2019, 4559-4572.
[2] Y. Xu, S. Xu, S. Wang, Y. Zhang and G. Li, *Dalton Transactions*, 43, 2014, 479-485.
[3] L. Ye, X. Liu, Q. Zhao, H. Xie and L. Zan, *Journal of Materials Chemistry A*, 1(31), 2013, 8978-8983.
[4] F. Tian, Y. Zhang, G. Li, Y. Liu and R. Chen, *New Journal of Chemistry*, 39(2), 2015, 1274-1280.

[5] J. Xiong, G. Cheng, F. Qin, R. Wang, H. Sun and R. Chen, *Chemical Engineering Journal*, 220, 2013, 228-236.
[6] Y. Huo, J. Zhang, M. Miao and Y. Jin, *Applied Catalysis B: Environmental*, 111, 2012, 334-341.
[7] M. Yuan, F. Tian, G. Li, H. Zhao, Y. Liu and R. Chen, *Industrial & Engineering Chemistry Research*, 56(20), 2017, 5935-5943.
[8] X. Wang, S. Yang, H. Li, W. Zhao, C. Sun and H. He, *RSC Advances*, 4(80), 2014, 42530-42537.
[9] F. Tian, G. Li, H. Zhao, F. Chen, M. Li, Y. Liu and R. Chen, *Journal of Catalysis*, 370, 2019, 265-273.
[10] F. Tian, H. Zhao, G. Li, Z. Dai, Y. Liu and R. Chen, *ChemSusChem*, 9(13), 2016, 1579-1585.
[11] J. Cao, B. Xu, H. Lin, B. Luo and S. Chen, *Catalysis Communications*, 26, 2012, 204-208.
[12] W. Cui, W. An, L. Liu, J. Hu and Y. Liang, *Applied Surface Science*, 319, 2014, 298-305.
[13] O. Mehraj, B.M. Pirzada, N.A. Mir, M.Z. Khan and S. Sabir, *Applied Surface Science*, 387, 2016, 642-651.
[14] J. Ding, Z. Dai, F. Qin, H. Zhao, S. Zhao and R. Chen, *Applied Catalysis B: Environmental*, 205, 2017, 281-291.
[15] C.V. Reddy, K.R. Reddy, V.V.N. Harish, J. Shim, M.V. Shankar, N.P. Shetti and T.M. Aminabhavi, *International Journal of Hydrogen Energy*, 45(13), 2020, 7656-7679.
[16] C.V. Reddy, K.R. Reddy, N.P. Shetti, J. Shim, T.M. Aminabhavi and D.D. Dionysiou, *International Journal of Hydrogen Energy*, 45(36), 2020, 18331-18347.
[17] X. Li, X. Hao, A. Abudula and G. Guan, *Journal of Materials Chemistry A*, 4(31), 2016, 11973-12000.
[18] E. Smith and G. Dent, *John Wiley & Sons*, 2005, 129-150.
[19] R.L. McCreery, *Measurement Science and Technology*, 12(5), 2001, 653.
[20] R. Sarkar, D. Das, B.K. Das, A, Mitra, N.S. Das, S. Sarkar and K.K. Chattopadhyay, *Materials Research Bulletin*, 125, 2020, 110778.
[21] K.K. Chattopadhyay and S. Saha, *LAP Lambert Academic Publishing GmbH & Co*, 2012. [22] R. Sarkar, D. Das, A. Mitra, S Sarkar and K.K. Chattopadhyay, *Materials Today: Proceedings*, 18, 2019, 1086-1095.
[23] R. Sarkar, D. Das, B. Das, S. Sarkar and K.K. Chattopadhyay, *AIP Conference Proceedings*, 2220(1), 2020, 020030.
[24] H. Zhao, Y. Zhang, G. Li, F. Tian, H. Tang and R. Chen, *RSC Advances*, 6(10), 2016, 7772-7779.
[25] Q. Wang, J. Hui, Y. Huang, Y. Ding, Y. Cai, S. Yin, Z. Li, B. Su, *Materials Science in Semiconductor Processing*, 17, 2014, 87-93.
[26] X. Li, C. Zhu, Y. Song, D. Du, Y. Lin, *RSC Advance*, 7, 2017, 10235-10241.
[27] J. Xiong, G. Cheng, F. Qin, R. Wang, H. Sun, R. Chen, *Chemical Engineering Journal*, 220, 2013, 228-236.
[28] J. Xiong, G. Cheng, G. Li, F. Qin, R. Chen, *RSC Advance*, 1, 2011, 1542-1553.
[29] K. Shen, M. A. Gondal, A. A. Al-Saadi, L. Li, X. Chang, Q. Xu, *Research on Chemical Intermediates*, 41, 2015, 2753-2766.
[30] D. H. Wang, G. Q. Gao, Y. W. Zhang, L. S. Zhou, A. W. Xu, W. Chen, *Nanoscale*, 4, 2012, 7780-7785.
[31] S. Anantharaj, S.R. Ede, K. Sakthikumar, K. Karthick, S. Mishra and S. Kundu, *ACS Catalysis*, 6(12), 2016, 8069-8097.
[32] R. Khan, M. Samanta, S. Ghosh, N.S. Das and K.K. Chattopadhyay, *International Journal of Hydrogen Energy*, 44(39), 2019, 21315-21323.

Chapter 6

Hollow Micro-spherical Bismuth Oxy-chloride for Superior Visible Light Induced Dye-sensitized Photocatalytic Activity and its Theoretical Insight

6.1 Introduction

Water purification is of utmost importance in modern times owing to the increased discharge of effluents from textile and chemical industries into the water bodies thereby leading to severe detrimental effects on aquatic ecosystem. Around one thousand tons of toxic non-degradable chemical dyes are ejected into the water bodies each year primarily from textile industries. According to the reports by Konstantinou and Albanis[1], dyes and effluents emitted from textile industries forms the primary groups of toxic organic compounds. Water soluble reactive coloured dyes like Rhodamine B and Methyl Orange are the most troublesome dyes to be removed. Rhodamine B dye comprises of nitrogen groups which renders its photolysis-resistant nature and subsequent anaerobic degradation results in carcinogenic and mutagenic products[2]. A study by Leena and Raj[3] revealed that textile dyes possess high stability as compared to other effluents and has the capability to remain unaltered under varying environmental conditions. Moreover those dyes which are properly dispersed in aquatic medium do not possess ionization tendency and can bio-accumulate in aquatic organisms[4]. Hence it is of immense importance to design economically viable photocatalytic materials to effectively degrade toxic dyes in order to achieve a step towards conserving environmental resources.

Significant progress has been achieved in recent time to effectively design semiconductor-based photocatalysts for efficient degradation of toxic dyes to non-toxic degradable products by employing UV or visible irradiation sources. Anatase titanium oxide (TiO_2) has been the most sought after material in this regard because of its impressive photochemical reactivity and relatively insignificant environmental toxicity[5]. However several limitations of TiO_2 like poor utilisation of the visible spectrum and inferior adsorption capability of hydrophobic pollutants hinder its application feasibility[6]. Till then there has been a steady and constant urge to develop some new photocatalytic materials which could overcome the conventional drawbacks and prove to be highly efficient in degradation of toxic pollutants. Photocatalyst system can be broadly classified into oxides-based[7], sulphides-based[8], oxysulfides-based[9], nitrides-based[10] and oxynitrides-based materials[11, 12].

In recent times Bismuth Oxyhalides (BiOX, X= Cl, Br, I and F) has been extensively investigated and employed in photocatalytic activities owing to their layered crystal structure[13] and appropriate band gap. This class of wide band gap (3.2-3.5 eV), V–VI–VII ternary semiconductor materials possessing distinctive opto-electronic features, impressive chemical stability and non-toxicity contributes its applicability in numerous fields. There are several reports on different synthetic strategies of BiOX samples like reverse micro-emulsions, wet chemical methods, low temperature chemical vapour

deposition, sonochemical process etc.[14]. Zhang et al. developed a one-pot solvothermal method utilizing ethylene glycol solvent to synthesise BiOX nanoplate microspheres[15] whereas Michel et al. carried out a non-aqueous surfactant-assisted synthetic technique to develop BiOCl material[14]. Sopha et al. prepared BiOCl having nano-platelet like morphology by breakdown anodization technique[16]. Applications of BiOX materials in multiple areas have been demonstrated in the following reports: Li et al. designed dye-sensitised BiOCl catalyst for efficient air and water purification[17]; Jiang et al. prepared BiOBr flakes for visible light degradation of methyl orange dye[18]; Wang et al. synthesised plate-like BiOI for visible light photocatalysis[19]. Among all the reported BiOX photocatalysts, BiOCl has proved to be the most efficient in degrading pollutants mainly because of its unique layered structure which provides sufficient space to achieve polarization of the corresponding atoms and orbitals which results in the effective separation of photogenerated electron and hole pairs thereby enhancing the photocatalytic property[12]. The theoretical band gap of BiOCl makes it suitable for dye degradation under UV light irradiation. Recently many modifications of pure BiOCl have been performed to employ the material for visible-light assisted dye degradation in order to establish its practical viability. Li et al. developed (001) dominant crystal facets of BiOCl for Biphenol A degradation[20], Pan et al. reported CdS quantum dots coupled BiOCl nanosheets[21], Pare et al. developed Mn-doped BiOCl[22], Shamaila et al. designed WO_3/BiOCl heterojunction[23], Chai et al. synthesised BiOCl/Bi_2O_3 based heterojunction[24], Liu et al. developed $BiOCl_{1-x}Br_x$ (x=0–1)[25], Xu et al. synthesised La-doped BiOCl[26] and Yang et al. reported the synthesis of a composite based on Fe_3O_4/Pr-BiOCl/Luffa[27] to improve the photocatalytic activity of BiOCl under visible, UV and solar light irradiation. Hu et al. fabricated TiO_2/BiOCl composite for photocatalytic degradation of Cr(VI) and tetracycline[28]. Moreover, there are a number of reports regarding the structural modifications of BiOCl for performance enhancement where various groups have synthesised different morphologies like single-crystal nanodisks[29], ultrathin BiOCl nanosheets[30], micro-spheres[31] and flower like structures[32].

The crystal structure of BiOCl is tetragonal bipyramidal. This tetragonal matlockite[33] structure (PbFCl) forms the basic backbone of BiOCl which subsequently undergoes crystallization to give rise to a layered structure comprising of $[Bi_2O_2]^{2+}$ slabs. Non-bonding weak van der Waals interactions aid in the combined stacking of these slabs mediated by halogen (Cl, Br, I and F) atoms[34]. The central bismuth atom in each of the [X–Bi–O–Bi–X] pattern is encompassed by adjacent four oxygen atoms and four halogen atoms which essentially results in asymmetric decahedral symmetry[35]. The significant intralayer covalent bonding along with the associated interlayer van der Waals bonding renders the compelling anisotropic physical, electrical and optical properties of BiOX compounds[36]. Moreover,

BiOCl has unsaturated dangling bonds only at the edges rather than at the surfaces as implied from the bonding anisotropy. The significantly impressive photo-stability of BiOCl arises from the fact that the photo-excited antibonding states cannot weaken the O-Bi-Cl bond[35]. The electronic state configureuration of BiOX compounds reveal that the valence band (VB) is mainly composed of oxygen 2p and Bi 6s hybrid orbitals which are in contrast to metal oxides where only the oxygen 2p orbitals form the VB. The conduction band (CB) is comprised of Bi 6p orbitals[37]. The significantly wide VB as resulted from the largely diffused 6s orbitals of bismuth attributes to the superior mobility of photogenerated charge carriers[38].

In the present work, pure BiOCl with hollow microsphere like morphology and (110) dominant exposed crystal facet has been synthesised following a facile chemical synthesis route. Variation in synthesis time and temperature duration has been performed to study the effect of synthetic conditions on phase formation and morphology of the samples. The samples exhibited superior photocatalytic activity under both visible and UV light irradiation. The best sample could completely degrade Rhodamine B (RhB) dye in a very short time. Different variations in photocatalytic parameters (like pH, dosage variations and source of irradiations) have been performed to study their respective effects on catalytic activity. A detailed mechanism supported by the plausible occurrence of dye sensitisation under visible light has been proposed to understand the impressive photocatalytic activity of pure BiOCl. Extensive first principles calculations were further employed to support the reaction mechanism. Till date, very few of the existing literatures on BiOCl photocatalysts provide an extensive photocatalytic study with variation of different parameters along with support from DFT calculations. The present report is an extensive work in this regard and the BiOCl sample developed in this work proved to be a promising visible-light assisted photocatalytic material in degrading toxic textile dyes of different types.

6.2 Experimental Details

6.2.1 Materials

$Bi(NO_3)_3 \cdot 5H_2O$ (Bismuth Nitrate Pentahydrate), 37 % HCl (Hydrochloric Acid), $C_6H_8O_7 \cdot H_2O$ (Citric Acid Monohydrate) were purchased from Merck. PVP (K30) (Poly Vinyl Pyrrolidone) was obtained from Loba Chemie. NH_3 (Ammonia solution, 25 %), IPA (Isopropyl alcohol), were from Mark Group, and EDTA-2Na (Ethylene diamine tetra acetate disodium) and *p*-BQ (*p*-Benzoquinone), $C_{28}H_{31}ClN_2O_3$ (Rhodamine B), were parched from Loba Chemie Pvt. Ltd. and PubChem, Deionized water (18.3 MΩ) and ethanol were used for all synthesis purposes.

6.2.2 Preparation of BiOCl Powders

All the reagents were of analytical grade and were used without further purification. The samples were synthesised following previous report by Zhang et al.[39] with some modifications. The precursor, the molar concentration of the reagents and the synthesis time period was modified to certain extent in the present work. Initially 3.75 mmol of $Bi(NO_3)_3 \cdot 5H_2O$ was dispersed in 22.5 mL of DI water followed by subsequent addition of 2.5 mL of HCl (37 %) into the above solution. The mixed solution (termed as solution A) was stirred vigorously at room temperature until the $Bi(NO_3)_3 \cdot 5H_2O$ was completely dissolved. A separate set of solution (solution B) was prepared by mixing 42 mL of DI Water, 50 mL of absolute ethanol (C_2H_6O), 1.16 x 10^{-4} mmol of PVP (K30) and 1.31 mmol of Citric Acid Monohydrate ($C_6H_8O_7 \cdot H_2O$) which was heated to 80 °C. 1.19 mmol of the previously prepared solution A was drop-wise added into the solution B under continuous stirring at 80 °C for 5 min to form solution C. After this, the solution C was heated at 80 °C for different time durations (0h, 1h, 3h, 6h and 18h) along with vigorous stirring. For temperature variations study, solution A was drop-wise added into solution B to form solution C which was then subsequently heated to different temperatures (40, 60, 80, 100 and 120 °C) and the system was kept under stirring for 5 min. After the reaction procedure was completed, the solution was cooled down naturally to ambient temperature; the precipitates were collected by filtration; and washed with DI water and absolute ethanol until the pH of the solution turned neutral (pH = 7). The final white coloured powdered products were obtained after overnight drying of the washed samples in an oven at 80 °C. The detailed synthesis procedure has been illustrated in Scheme 6.1. B0h/B1h/B3h/B6h/B18h refers to the BiOCl samples synthesised with 5 min stirring and

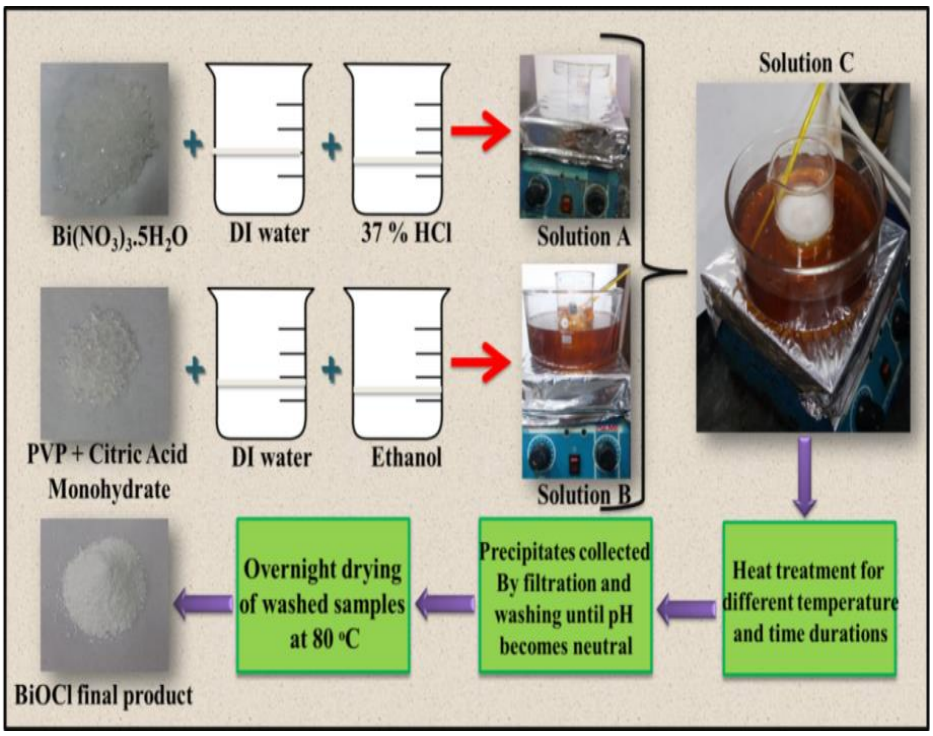

Scheme 6.1: Synthesis procedure of BiOCl samples

subsequent heating for 0, 1, 3, 6 and 18 hr. at 80 °C. B40/B60/B80/B100/B120 refers to the BiOCl sample synthesised with only 5 min stirring at 40, 60, 80, 100 and 120 °C.

6.2.3 Characterizations

The as synthesised samples were analysed by employing several characterization techniques. X-ray diffractometer (Rigaku Miniflex 600) with wavelength λ = 1.54056 Å for Cu Kα source of radiation was used at a scan rate (2Θ) of 2 °min^{-1} at 40 kV and 40 mA to study the phase formation of the powder samples. The chemical structure of the powder samples were analysed by X-ray Photoelectron Spectroscopy (XPS) using a monochromatic Al K_α X-ray source (hν = 1486.6 eV) and a hemispherical analyser (SPECS HSA 3500). The morphology of the samples was revealed from Field emission scanning electron microscopic study (FESEM, Hitachi S-4800) which was equipped with an Energy Dispersive X-ray Spectra (EDS) spectral analyser for analysing the elemental ratios of the samples and also from the High Resolution Transmission Electron Microscopic study (HRTEM, JEOL-JEM 2100). Fourier transform infrared spectroscopy (Shimadzu FTIR-8400S) revealed the presence of various chemical bondings. Raman analysis of the powder samples was carried out by Witec Raman spectrophotometer excited at 532 nm. UV-visible diffuse reflectance spectra (DRS) of the powder samples were carried out by UV–Vis spectrophotometer (Shimadzu UV-3600) using barium sulphate as a reflectance standard.

6.2.4 Photocatalytic Activity Measurement

Photocatalytic activity of the as-synthesized BiOCl samples was measured at ambient temperature at a pH of 7. In order to maintain the temperature of the catalytic reactor system at a constant value, a double-walled glass beaker was used with continuous flow of cold water in-between the two walls. To measure the photocatalytic activity of the as-prepared BiOCl samples, 30 mg of the catalysts were dispersed in 40 mL of 10^{-5} mol/L RhB dye solution. The catalyst dispersed solution was vigorously stirred for 1 hour under complete dark condition to ensure proper adsorption-desorption equilibrium of the dye on the catalyst surface. After this, the system was placed under a 400 W high pressure mercury lamp (Phillips-HPL-N G/74/2, MBF-400W, 200-250V) covering the complete range from 365 nm to 679 nm which was used as a visible-light source. A UV cut off filter (λ > 400 nm) was employed to negate the UV emission. Similarly for the UV light source, two 40 W UV tubes (Phillips) with an emission wavelength of 254.6 nm (UVC) was used. 3 mL of the reaction solution was withdrawn from

the suspension at regular time intervals which was immediately centrifuged to remove the catalyst; and the concentration of the RhB dye was monitored by using an UV−Vis absorption spectrophotometer.

6.2.5 Electrochemical Measurement

The Mott-Schottky and the Nyquist plots were analysed by Electro-chemical impedance measurement performed by PGSTAT302N AUTOLAB in a three electrodes system. Prior to the measurement, Ni foam of 1 cm X 1 cm was properly cleaned with diluted HCl solution followed by a mixture of ethanol. The working electrode was prepared by mixing 40 mg of the as synthesised BiOCl samples with 5 mg PVDF and 5 mg carbon black along with drop-wise addition of a small amount of NMP solution to prepare black coloured slurry which was stirred for 4 hours. The slurry was then uniformly applied on the clean Ni foam to prepare the electrode for measurement. The Pt electrode was used as the counter electrode whereas the reference electrode was typical calomel electrode (Ag/AgCl). 0.2 M Na_2SO_4 was used as the electrolyte solution. The Nyquist measurements were taken at a stable frequency of 100000 Hz whereas the Mott-Schottky measurements were carried out at two frequencies of 2000 Hz and 2500 Hz.

6.2.6 Theoretical Method

The first principles calculations were carried out using Vienna ab-initio Simulation Package (VASP)[40-42] with projector-augmented-wave (PAW)[43] approach. The contribution from the exchange-correlation terms were dealt with Perdew-Burke-Ernzerhof (PBE)[44] functional within the generalised gradient approximation (GGA). Plane wave basis sets up to an energy cut-off 500 eV were implemented in all the calculations. As sufficiently large cells were considered for the study of both water and Rhodamine B (RhB) adsorption process on various BiOCl surfaces, the Brillouin zone integrations were performed using (1×1×1) k-point mesh centered at the Γ point. The structures were allowed to relax until the total energies converged below 10^{-5} eV/ atom. All the calculations were performed in spin unrestricted manner and the corrections due to dispersive forces were incorporated via the PBE + D2 force field method (Grimme's method)[45] as implemented in VASP. During the relaxation of the BiOCl surfaces and composite structures a vacuum slab of 24 Å was deployed perpendicular to the surface to ward off any spurious interaction. Water or (RhB) adsorption ability of various BiOCl surfaces was determined comparing the adsorption energy values which were determined using the following formula:

$$E_{Ads} = E_{Compo} - E_P - E_{W/Rho-b} \quad (6.1)$$

where,

E_{Compo} = is the energy of the water or RhB adsorbed BiOCl surface,

E_P = is the energy of the pristine BiOCl surface and

$E_{W/Rho-b}$ = is the energy of the free water or RhB molecule.

Lower values of adsorption energies, as obtained from the above, implies stronger adsorption.

6.3 Results and Discussion

6.3.1 XRD Analysis

The XRD diffraction pattern of the as-synthesised BiOCl samples is shown in Figure 6.1(a) and Figure 6.1(b). The peaks at 12.10, 24.25, 26.00, 32.70, 33.62, 36.67, 41.04, 46.82, 49.90, 54.30, 55.14, 58.76 and 60.64 ° corresponds to (001), (002), (101), (110), (102), (003), (112), (200), (113), (211), (104), (212) and (114) lattice planes accordingly[46], which are in conformation to the tetragonal matlockite structure (space group-P4/nmm) (JCPDS Card No. 85-0861). The highest intensity peak for the B0h/B80 sample is situated at 32.70 ° which corresponds to the (110) crystal facets whereas for the other samples, the intensity of this (110) peak is more or less comparable to those of the (101) and (102) planes. This indicates the dominant exposure of the particular plane in case of B0h/B80 sample. This result is also evident from the texture coefficients (TC) analysis of all the time and temperature varied samples given in Figure 6.1(c) and Figure 6.1(b) along with the details of the TC analytical techniques.

The texture coefficients of all the time and temperature varied BiOCl samples for 9 lattice planes have been calculated from XRD data following the equation (6.2):

$$TC_{hkl} = \frac{I_{(hkl)} / I_{0(hkl)}}{\frac{1}{n}\sum_{i=1}^{n} I_{(hkl)}/I_{0(hkl)}} \qquad (6.2)$$

where,

TC = is the texture coefficient for (hkl) plane,

$I_{(hkl)}$ = is the intensity of the (hkl) planes as calculated from the XRD data of BiOCl samples, $I_{0(hkl)}$ = is the standard intensity of the (hkl) planes as taken from the JCPDS data and

'n' = is the number of XRD peaks taken into consideration during the calculation of TC.

It is evident from the bar graphs that the B0h/B80 sample shows the maximum value of texture coefficient (1.75) along the (110) lattice plane. It is known that the deviation of texture coefficient from unity indicates the preferential growth of the plane in that particular direction[1]. Thus the maximum value of TC along the (110) direction for the B0h/B80 sample suggests the dominant orientation along that particular plane as compared to the other time and temperature varied samples.

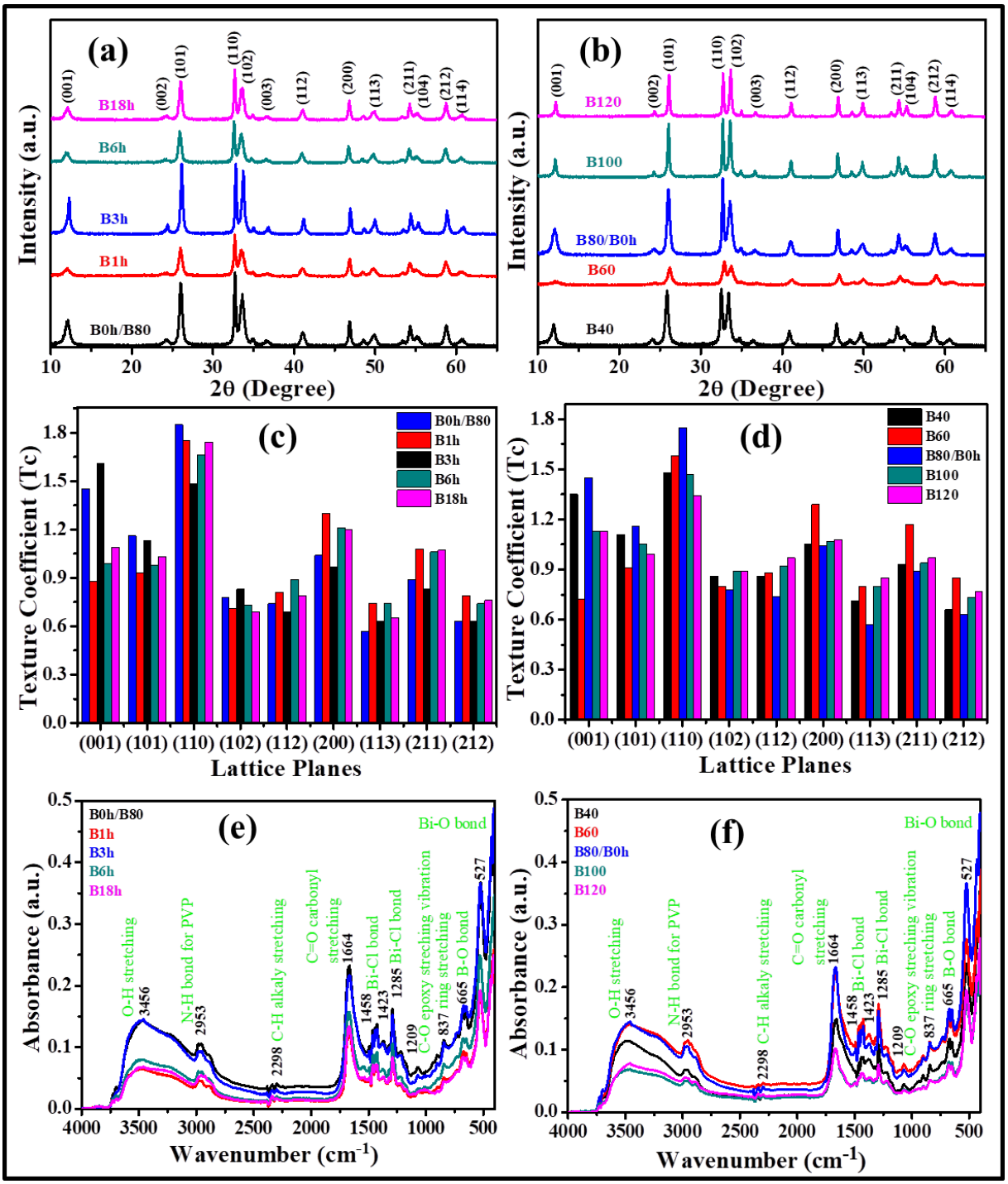

Figure 6.1: XRD pattern of (a) time varied and (b) temperature varied samples, Texture coefficients along different lattice planes of (c) time and (d) temperature varied BiOCl samples, FTIR spectra of (e) time varied and (f) temperature varied samples

6.3.2 FTIR Analysis

The FTIR (Fourier transport infrared spectroscopy) spectra of the as-synthesised time and temperature varied pure BiOCl hollow microsphere samples are shown in Figure 6.1(e) and Figure 6.1(f) respectively. The peak appearing at 527 cm^{-1} is due to the A_{2u}-type symmetrical vibrations of Bi-O bond, the large band at 1664 cm^{-1} arises due to C=O carbonyl stretching vibration and the weak band occurring at 665 cm^{-1} is due to the Bi-O bond, the band for ring stretching vibration occurs at 837 cm^{-1}, whereas the stretching vibration for C-O epoxy bond arises at 1209 cm^{-1}. The peaks at 1285, 1423 and 1458 cm^{-1} can be attributed to the Bi-Cl bonds, and that at 2298 cm^{-1} occurs for C-H alkali stretching vibration. The small hump at 2953 cm^{-1} occurs due to N-H bond for PVP and the broad hump at 3456 cm^{-1} arises due to O-H stretching mode of vibration. The presence of all the characteristic peaks confirms the successful production of highly pure BiOCl nano-materials.

6.3.3 XPS Analysis

X-ray photoelectron spectroscopic (XPS) study was executed to analyse the different chemical bonds present in the samples with respect to binding energy and the corresponding spectra are shown in Figure 6.2(a-d).

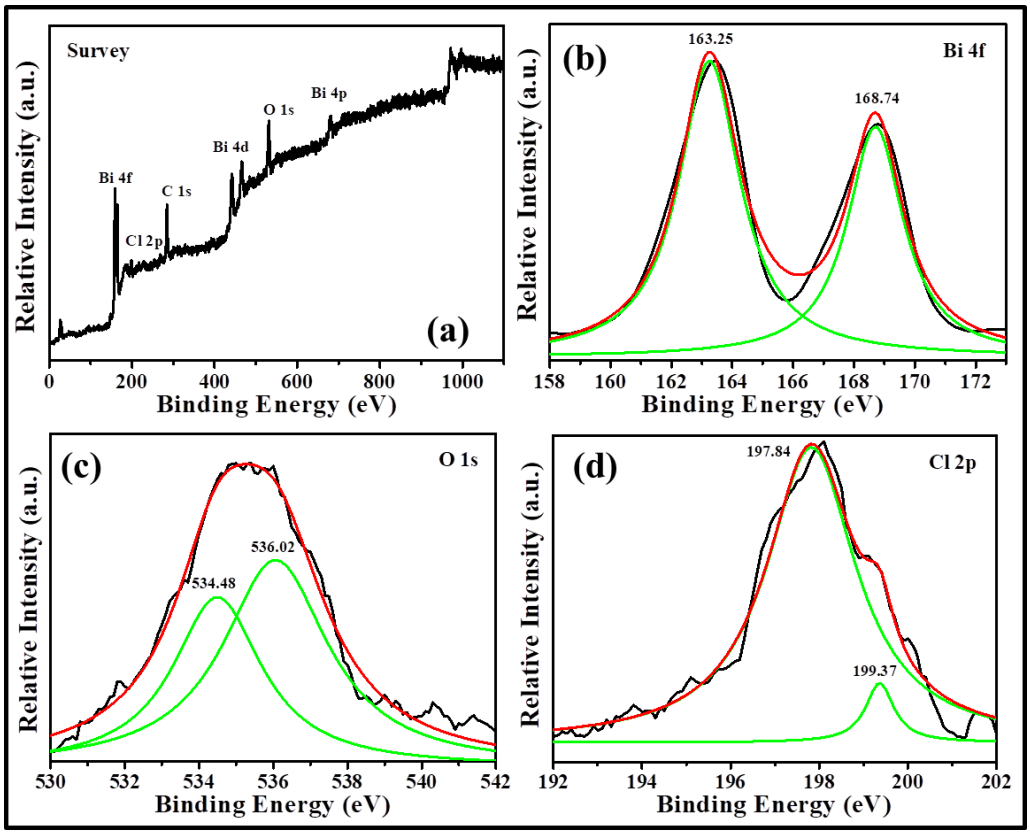

Figure 6.2: (a) XPS elemental survey scan; (b) Bi 4f spectra (c) O 1s spectra; (d) Cl 2p spectra of B0h/B80

In Figure 6.2(a) represents the elemental survey scan revealing the existence of the Bi, O, Cl and C in the as-synthesised samples. The C1s peak at 284.6 eV occurs due to the presence of atmospheric carbon. The strong peaks at 163.25 and 168.74 eV shown in Figure 6.2(b) can be ascribed to Bi $4f_{7/2}$ and Bi $4f_{5/2}$ respectively. As evident from Figure 6.2(c), the O1s peak can be deconvulated into two peaks corresponding to at 534.48 and 536.02 eV. The 1st peak can be assigned to the O_2 or O^{2-} of the Bi-O bond whereas the other peak can be primarily associated to H_2O or OH^- attached on the surface of the sample. The Cl 2p spectra shows two deconvulated peaks at 197.84 and 199.37 eV in Figure 6.2(d) belonging to Cl $2p_{3/2}$ and Cl $2p_{1/2}$ respectively which corresponds to Cl^- of the Bi-Cl bond. Hence the XRD and XPS evaluation approve that the as-synthesised samples are pure BiOCl[47].

6.3.4 Morphological and EDS Analysis

The morphology of the as-prepared B0h/B80 sample along with the magnified image taken at 100 nm is shown in Figure 6.3(a) and Figure 6.3(b) respectively. The FESEM (Field emission scanning electron microscopy) images of all other time and temperature varied samples are given in Figure A1(a-h) (Appendix) and Figure A2(a-h) (Appendix) respectively. It is evident from the images that all the samples exhibit hollow microspheres like structure.

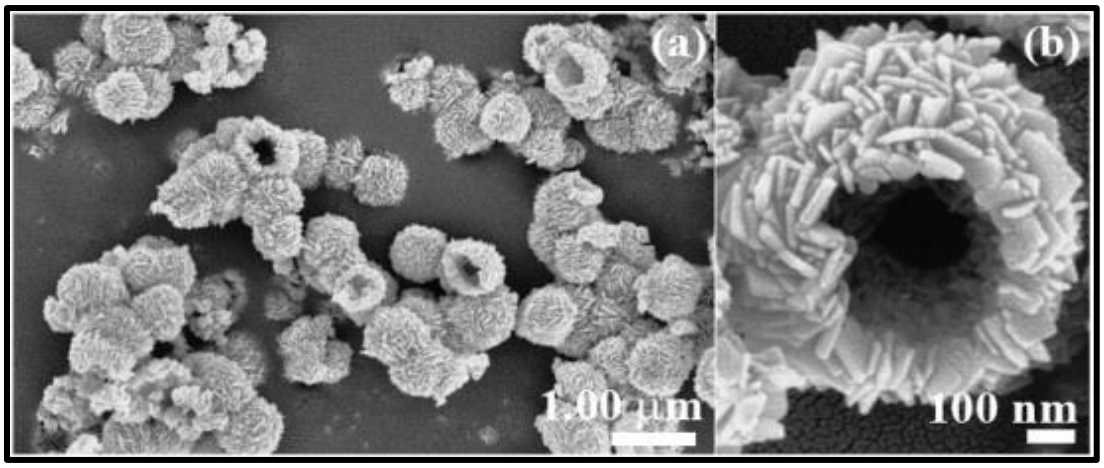

Figure 6.3: FESEM images of (a) B0h/B80, (b) higher magnified image of B0h/B80 sample

The FESEM image of the B0h/B80 sample reveals that the thickness of the walls of the hollow microsphere is narrower than the other samples thus making the hollow more pronounced in case of B0h/B80. The average inner diameter of hollow sphere is about 200 nm and the outer diameter is around 580 nm as calculated for the B0h/B80 sample. For the B120 sample, the thickness of the walls is increased thus making the internal diameter of the hollow sphere minimum. The uniform distribution of the hollow spheres was significantly disturbed for the time varied BiOCl samples. The hollow

microspheres are composed of small units having average length around 25 nm ~ 100 nm and thickness about 10 nm ~ 25 nm. The small units are uniformly arranged in all the as-synthesised BiOCl samples and significant changes in grain/crystalline sizes and particle dimensions are not observed.

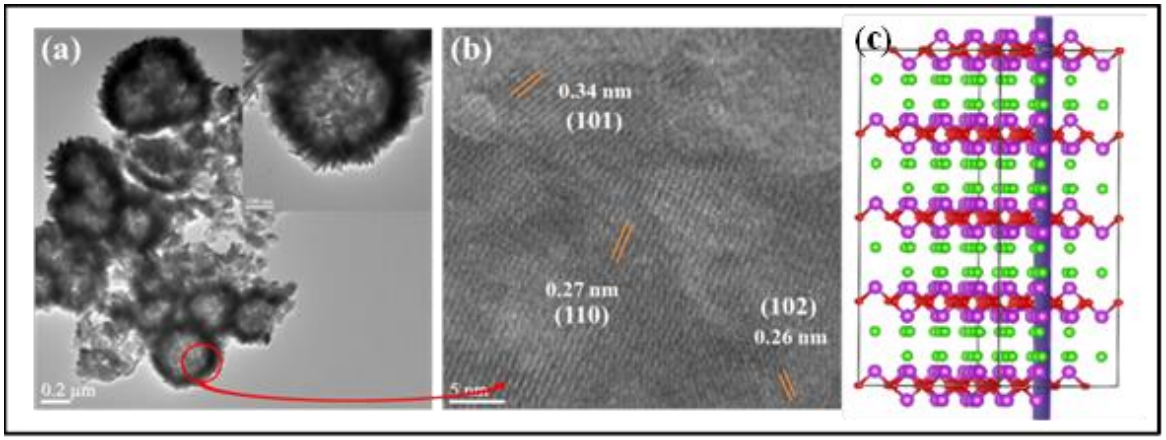

Figure 6.4: TEM image (a) and HRTEM image (b) of B0h/B80 sample, schematic representation of the BiOCl crystal structure (c) and the blue slab indicating the (110) facet of the BiOCl supercell

The TEM and HRTEM image of the as-synthesised B0h/B80 pure BiOCl sample is shown in Figure 6.4(a) and Figure 6.4(b) respectively. The images conform that the as-synthesised samples exhibit hollow micro-spherical morphology. The distinct lattice fringes are observed from Figure 6.4(b) which suggests the highly crystalline nature of the sample and the corresponding high intense (110) planes along with the other two intense planes (101) and (102) are assigned. This finding is in accordance with the XRD results which reveals that the highest intensity peak of BiOCl corresponds to the (110) plane. The scheme representation of the BiOCl crystal structure is shown in Figure 6.4(c) where the blue slab indicates the (110) facet of the BiOCl supercell.

Figure 6.5(a) shows the Energy Dispersive X-ray Spectra (EDS) of B0h/B80 which reveals the existence of Bi, O and Cl elemental peaks. Figure 6.5(b-d) shows the corresponding elemental mapping images. The weight and atom percentages of the respective elements of all the samples are given in Table A1 (Appendix). The atomic ratios of the elements of the as-synthesised BiOCl samples are approximately stoichiometric, according to the classical formula unit.

6.3.5 Raman Spectra Analysis

Figure 6.6(a) and Figure 6.6(b) shows the Raman Shift of the as-synthesised time and temperature varied pure BiOCl samples. Pure BiOCl shows three peaks corresponding to the A_{1g}, B_{1g} and E_g Raman active modes. The asymmetric vibrations modes show less intensity as compared to the symmetric vibrations. The most active band at 148 cm^{-1} (also called A_{1g} band) is attributed to the Bi-Cl internal

stretching mode of vibration whereas the weak band at 104 cm^{-1} is assigned to the external A_{1g} band arising due to 1st order scattering[48].

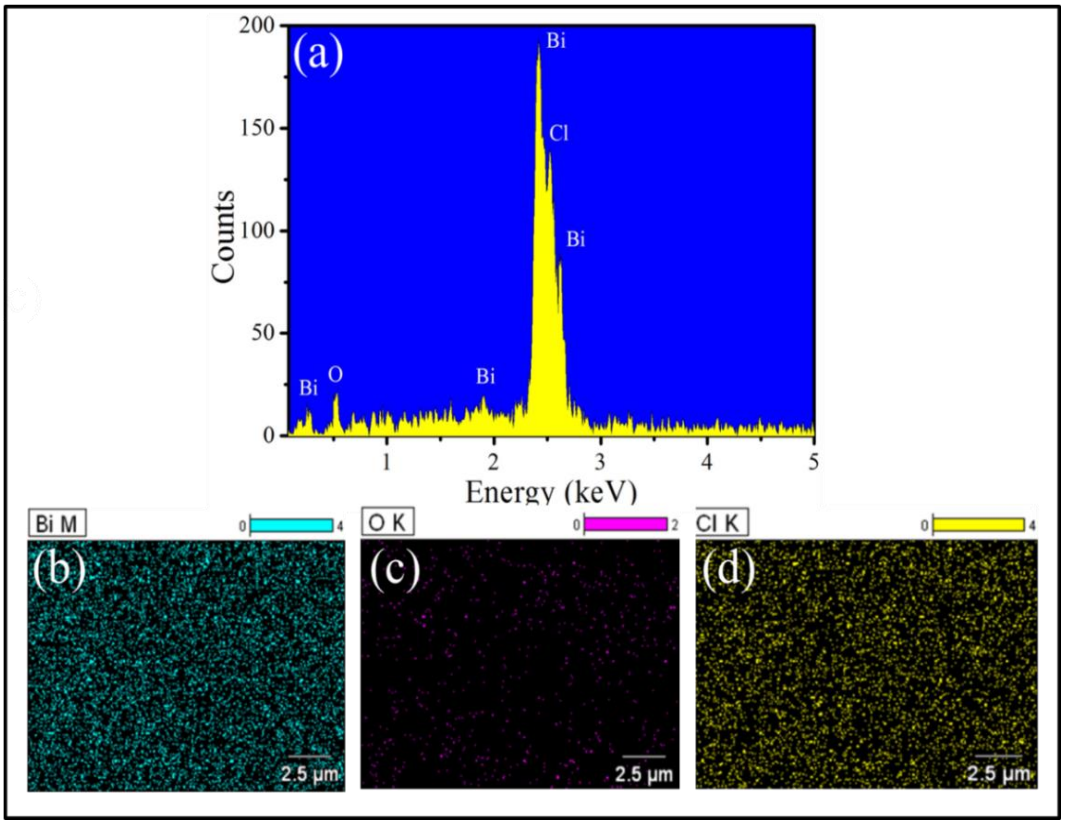

Figure 6.5: The EDS pattern (a) of B0h/B80, (b), (c) and (d) elemental mapping of Bi, O and Cl materials

The other strong band at 204 cm^{-1} (called the E_g band) occurs due to the Bi-Cl internal stretching mode of vibration. The weak band at 484 cm^{-1} can be assigned as the E_g and B_{1g} band which arises due to the motion of the O^{2-} atoms. This peak is difficult to observe. Moreover, no peak shifting has been observed in both the time and temperature varied samples.

6.3.6 BET Analysis

The measurement of the surface area, porosity and distributions of pore size of the as-synthesised B0h/B80 sample is evaluated from the nitrogen adsorption-desorption isotherm obtained from BET analysis. Figure 6.6(c) shows the nitrogen adsorption-desorption isotherms Figure 6.6(d) reveals the pore size distribution of the B0h/B80 sample. The calculated surface area is 27.108 m^2g^{-1} and the pore volume is 0.055 cm^3g^{-1} whereas the average pore diameter is 8.56 nm as measured by applying the BJH (Barret Joyner Halenda) technique. The obtained results indicate that the hollow microsphere like morphology of B0h/B80 has a significant surface is to volume ratio that is important for the photocatalytic application[47].

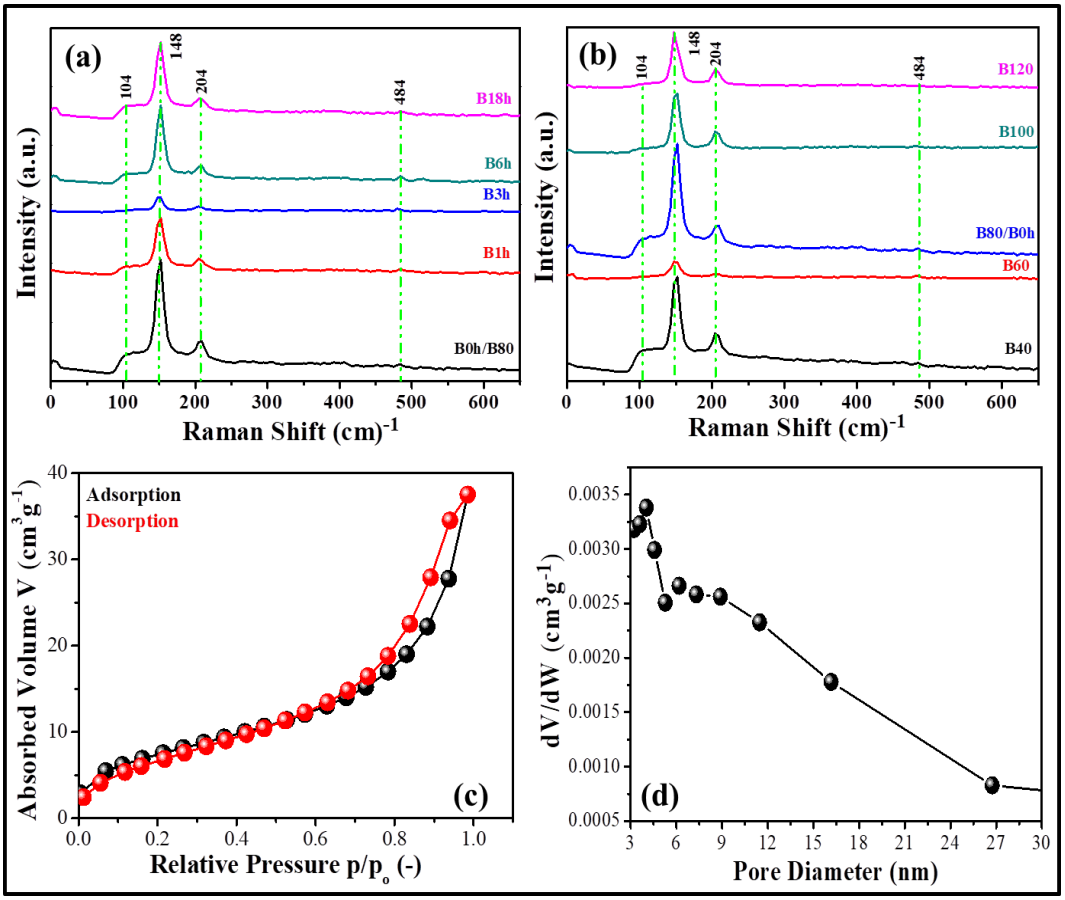

Figure 6.6: Raman spectra of (a) time varied and (b) temperature varied samples, (c) Nitrogen adsorption-desorption isotherms and (d) Pore size distributions of B0h/B80

6.3.7 Optical Property Analysis

The diffuse reflectance spectra (DRS) taken in the range of 220 to 700 nm for all the as-synthesised time and temperature varied white coloured powder samples are displayed in Figure 6.7(a) and Figure 6.7(b) respectively. $BaSO_4$ has been used as the standard for the reflectance measurement. It can be observed that all the samples exhibit very high reflectance around 93 % and a sharp fall occurs near 320 nm wavelength. The indirect band gaps of the as-synthesised samples have been calculated from the diffuse reflectance spectra by employing Kubelka-Munk method and the corresponding plots of Kubelka-Munk function vs. photon energy (hν) are shown inset of Figure 6.7(a) and Figure 6.7(b). The indirect band gaps as calculated lie in the range of 3.46 to 3.59 eV and the corresponding values are given in the inset of Figure 6.7(a) and Figure 6.7(b).

The energy band gap diagram for the time and temperature varied samples are shown in Figure 6.7(c) and Figure 6.7(d) respectively. The electronic band structures are necessary to describe the excitation and transition of photogenerated charge carriers that occurs during the photocatalytic activity. The band

diagrams determine the position of the conduction band (CB) and the valence band (VB) which is used to describe the series of redox reactions taking place during photocatalysis.

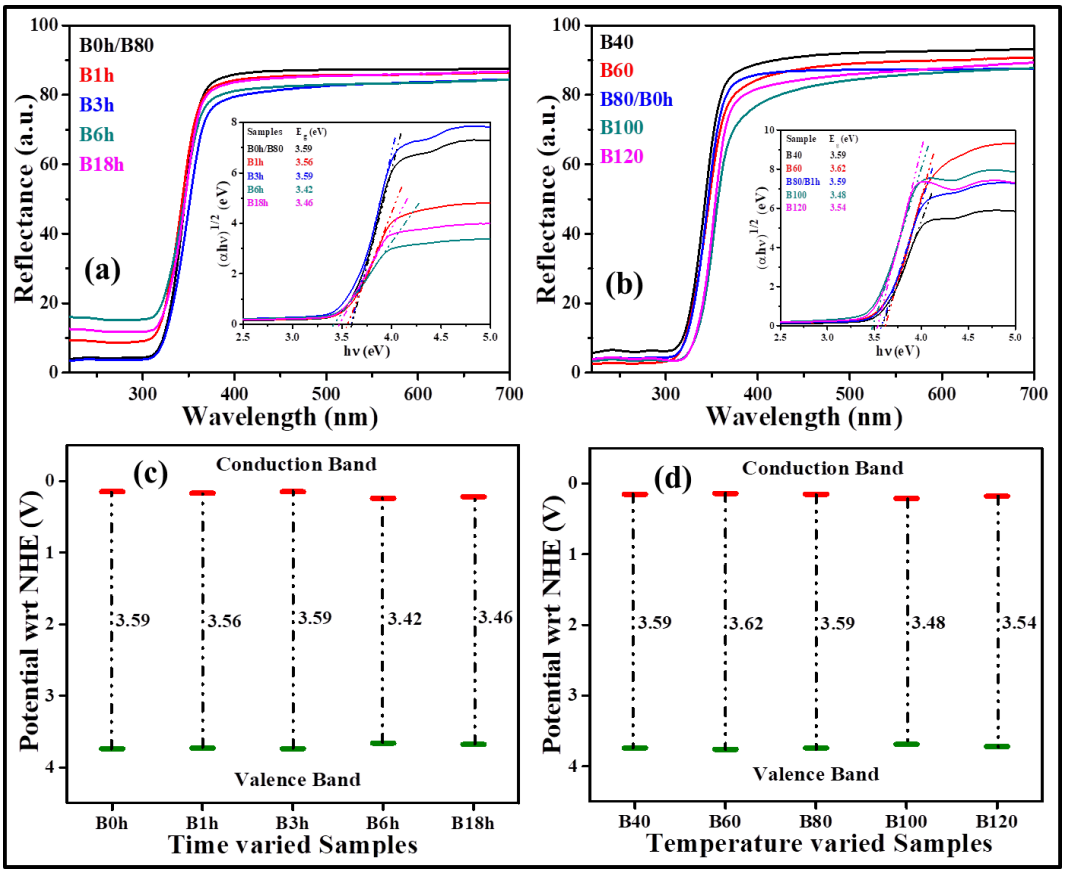

Figure 6.7: Diffuse Reflectance Spectra of (a) time varied and (b) temperature varied BiOCl samples and inset: Kubelka-Munk plots for calculation of indirect band gaps, energy band diagrams of (c) time and (d) temperature varied samples

The conduction band edge and the valence band edge potentials can be calculated by a set of equations as described by the Mulliken's electronegativity theory[49],

$$E_{VB} = \chi_{Semiconductor} - E^e + 0.5E_g \qquad (6.3)$$

where,

E_{VB} = the valence band (VB) edge potential,

$\chi_{Semiconductor}$ = the electronegativity of the semiconductor,

E^e = the energy of the free electrons of hydrogen scale (ca. 4.5 eV) and

E_g = the band gap energy of the semiconductor.

The VB edge potentials can be calculated from the above equations. The corresponding CB edge potentials are evaluated by subtracting the VB edge potentials from the electronic band gaps as measured from DRS.

6.3.8 Mott-Schottky and Nyquist Analysis

The Mott-Schottky plots of the B0h/B80 BiOCl sample measured in two frequencies is shown in Figure 6.8(a). The $1/C^2$ vs. potential plots shows the existence of negative slopes which indicates the 'p' type characteristics of the semiconductor. The Mott-Schottky plots of the other time and temperature varied BiOCl samples are given in Figure A3(a-h) (Appendix).

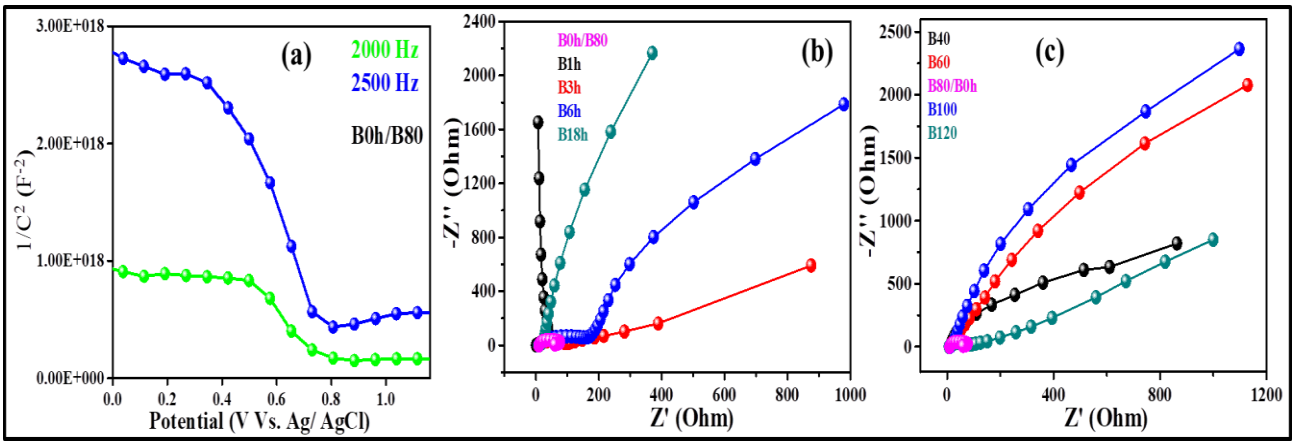

Figure 6.8: (a) Mott-Schottky plot of B0h/B80 sample at frequencies of 2000 Hz and 2500 Hz; Nyquist plots of (b) time and (c) temperature varied samples

The electrochemical impedance spectroscopy (EIS) was recorded in the semi-circular Nyquist graphs. It is a known fact that the smaller semi-circular arc of the Nyquist plots indicates the efficient separation of the charge carriers. The Nyquist plots of the as-synthesised time and temperature varied BiOCl samples are shown in Figure 6.8(b) and Figure 6.8(c). The B0h/B80 sample exhibits the smallest arc radius as compared to all other samples which determines the impressive separation efficiency of the charge carriers along with inferior charge transfer resistance. This observation establishes the B0h/B80 sample to be an effective photocatalyst owing to its superior interfacial charge transfer capability.

6.3.9 Photocatalytic Activity of BiOCl Samples

The photocatalytic activity of as-synthesised time and temperature varied BiOCl samples were evaluated by the degradation of aqueous solution of Rhodamine B (RhB) Dye under visible light irradiation. The absorbance spectra of the dye in presence of different catalysts are shown in Figure 6.9(a-i) from which it can be observed that all the samples were almost able to degrade the dye completely within significantly less time. The best sample B0h/B80 showed about 99 % degradation efficiency within only 6 minutes of visible-light irradiation.

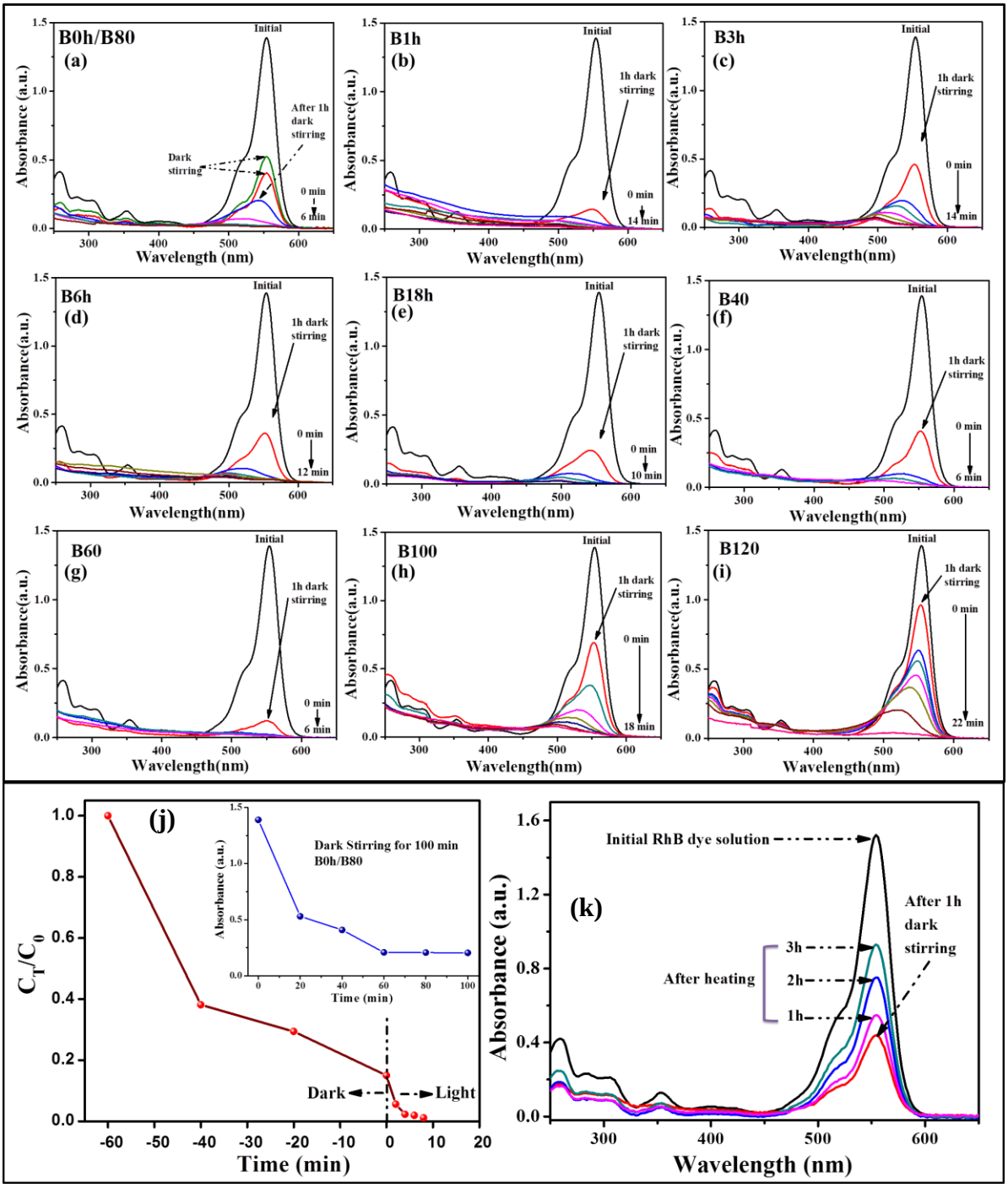

Figure 6.9: (a-i) Absorbance spectra of RhB dye in presence of as synthesized BiOCl catalysts, (j) C_T/C_0 plot of B0h/B80 sample showing adsorption under dark stirring and subsequent degradation after visible-light irradiation, (inset j) change in intensity of RhB dye solution in presence of B0h/B80 during 100 min of dark stirring and (k) RhB dye adsorption and subsequent desorption after heating up to 3 hours at 60 °C.

The reaction kinetics of the degeneration of RhB dye performed under visible light irradiation by different time and temperature varied BiOCl samples been calculated following equation (6.4).

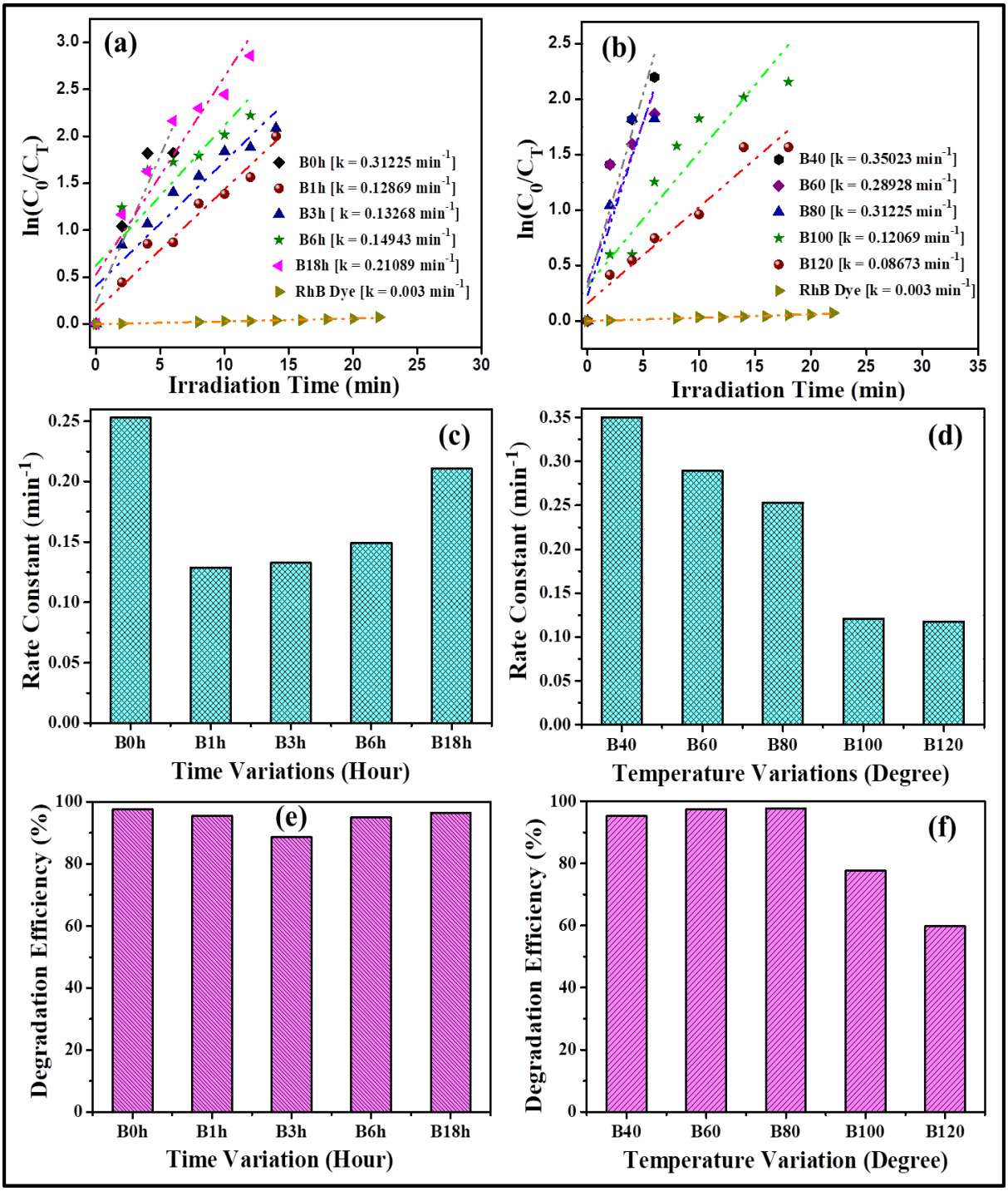

Figure 6.10: First order kinetics plots of (a) time varied and (b) temperature varied samples, rate constant bar graphs of (c) time varied and (d) temperature varied samples, degradation efficiency of (e) time varied and (f) temperature varied samples

As evident from the plots, the photocatalytic reaction rates follow first order kinetics and the corresponding rate constant values are calculated and tabulated in Table 6.1.

$$\ln\left({C_0}/{C_T}\right) = k_{app}T \qquad (6.4)$$

where,

C_0 = initial concentration of RhB dye,

C_T = concentration of RhB dye at time 't',

k_{app} = apparent 1st order rate constant and

T = time.

The k_{app} value was calculated from the slope of $\ln(C_0/C_T)$ vs. time plots as shown in Figure 6.10(a) and Figure 6.10(b) for the time varied and the temperature varied samples respectively.

The bar graphs shown in Figure 6.10(c) and Figure 6.10(d) depict the first order rate constant values of the time and temperature varied BiOCl samples respectively.

Table 6.1: Rate constant values of time and temperature varied samples

Samples name	R^2 values	*k* values (min^{-1})	Degradation efficiency %
B0h/B80	0.8920	0.3423	98.92
B1h	0.9613	0.1286	95.41
B3h	0.8866	0.1326	88.65
B6h	0.7215	0.1494	94.95
B18h	0.8688	0.2109	96.49
B40	0.8304	0.3502	95.33
B60	0.7046	0.2892	97.48
B100	0.8689	0.1206	77.73
B120	0.9398	0.0867	59.86

The degradation efficiency of the as prepared samples has been calculated from equation (6.5) and the corresponding bar graphs shown in Figure 6.10(e) and Figure 6.10(f) depicts the calculated degradation efficiency of the time and temperature varied BiOCl samples respectively.

$$\eta\ \% = \frac{\eta_0 - \eta_T}{\eta_0} \times 100 \qquad (6.5)$$

where,

η = degradation efficiency,

η_0 = initial concentration of RhB dye and

η_T = concentration of RhB dye at any time 't'.

All the samples show impressive efficiency in degrading toxic RhB dye, however, the B0h/B80 sample proved to be the most effective catalyst having degradation efficiency of about 99 %.

The stability of the as prepared BiOCl catalysts in degrading the RhB dye under visible light irradiation was studied by recycling the catalyst up to three cycles. It can be observed from Figure 6.11(a) that the degradation efficiency of the B0h/B80 BiOCl sample remains more or less unchanged even after reusing for three cycles which suggests that no photo-corrosion occurs and this in turn establishes the significant stable nature of the catalyst.

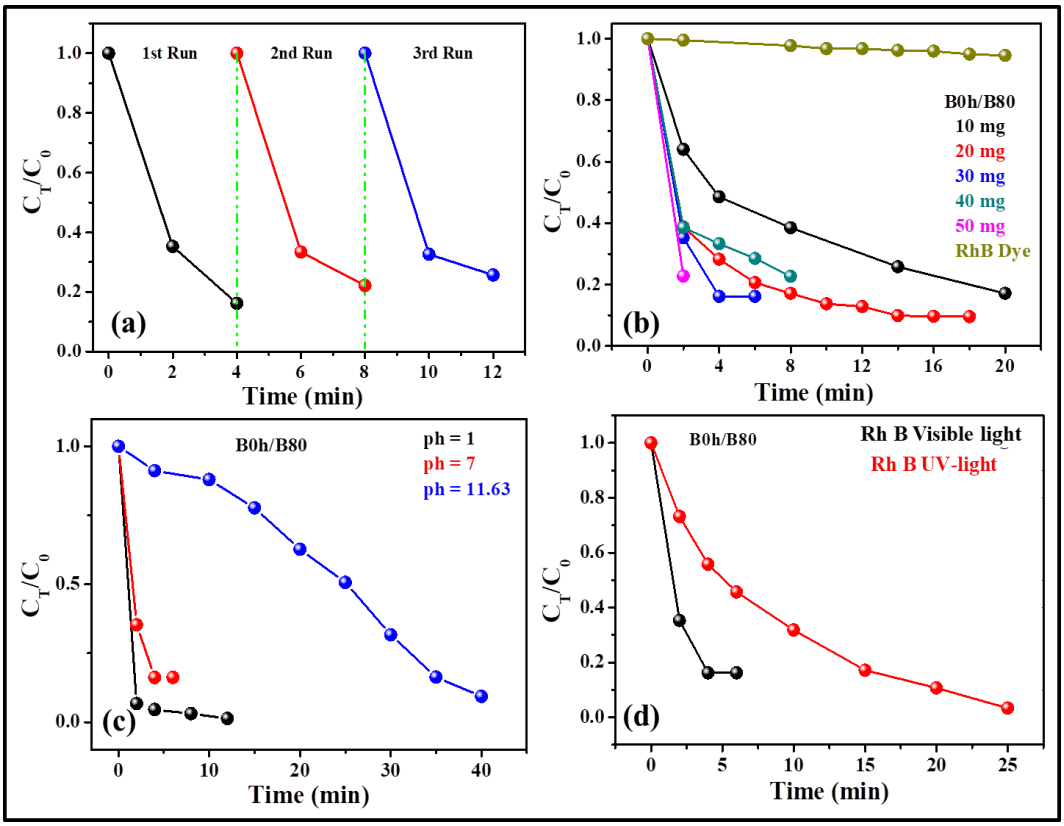

Figure 6.11: (a) Reusability of the B0h/B80 sample up to three cycles, (b) Effect of catalyst dosage on photocatalytic activity, (c) Effect of pH on the photocatalytic activity of B0h/B80 and (d) Photocatalytic activity of B0h/B80 under visible and UV light irradiation

The effect of catalyst dosage on degrading RhB dye was studied by varying the amount of catalyst and irradiating the sample under visible light. Different amount (10, 20, 30, 40 and 50 mg) of time and temperature varied BiOCl (B0h/B80) catalyst was added into the same concentration of RhB dye solution and the photocatalysis procedure was carried out following the same procedures. It can be observed from Figure 6.11(b) that with increase in the catalyst loading the photocatalytic activity improved to a great extent and the corresponding degradation efficiency improved from 70 % to 99 %.

This can be attributed to the fact that with increase in the amount of catalyst, there is a subsequent increase in the number of active sites which in turn ameliorates the rate of degradation. The dosage amount of 30 mg has been considered the optimum catalyst loading and the degradation rate is 98.92 % in only 6 minutes of irradiations.

The effect of pH on the catalytic dye degradation was studied by varying the pH of the catalyst-dye solution from acidic to basic. It can be observed from Figure 6.11(c) that the photocatalytic activity of the B0h/B80 sample increased to a great extent at acidic pH, whereas, the reaction rate got drastically hindered at a basic pH. The '*k*' values calculated for the three pH variations are given in Table 6.2. The B0h/B80 sample showed only 45 % degradation efficiency at a basic pH whereas the degradation efficiency at an acidic pH is nearly 100 % for the same irradiation time.

Table 6.2: Rate constant values of B0h/B80 sample at different pH conditions

pH values	R^2 values	*k* values (min^{-1})	Degradation efficiency at 6 min
pH = 1	0.6351	0.2903	99.95 %
pH = 7	0.8920	0.3423	98.92 %
pH = 11.63	0.8445	0.0564	44.17 %

The effect of the light source on the photocatalytic activity was studied by irradiating the catalyst-dye solution with both UV light source and visible light source. It can be observed from Figure 6.11(d) that under UV light irradiation the photocatalytic rate decreased significantly and the corresponding rate constant values are given in Table 6.3. The wavelength in the UV range thus proved to be quite insufficient in carrying out the photocatalytic reaction as compared to the visible light wavelength.

Table 6.3: Rate constant values of B0h/B80 under visible and UV light irradiation

Light variations	R^2 values	*k* values (min^{-1})	Degradation efficiency at 6 min
Visible light	0.8920	0.3423	98.92 %
UV-light	0.9764	0.1246	43.58 %

Figure A4 (Appendix) shows the zeta potential graph of B0h/B80 for surface charge calculation. The negative surface charge obtained for the sample makes it potential for degrading positive cationic dyes like RhB. The cationic dye being positive in nature adsorbs significantly on the negatively charged surface of BiOCl which in turn facilitates its easy degradation.

It is a known fact that the photo-induced electrons, holes, hydroxyl radicals and superoxide anions are the primary classes of active radicals that participate in the photocatalytic reactions to effectively degrade the toxic dyes into non-toxic end products. The existence of these radicals can be confirmed

from the free radicals trapping procedure[50]. The activity of the photocatalytic degradation of RhB dye under visible light irradiation by B0h/B80 BiOCl sample in the presence of different scavengers like *p*-benzoquinone (*p*-BQ), isopropyl alcohol (IPA), t-butanol and ethylene diamine tetra acetate disodium (EDTA-2Na) has been studied by adding the requisite amounts of these scavengers during the photocatalysis procedure followed by studying the effect of their addition in the reaction kinetics. The corresponding C_T/C_0 plots are shown in Figure 6.12(a) from which it can be clearly observed that the degradation efficiency got significantly hindered upon addition of *p*-BQ and EDTA-2Na whereas no significant changes were observed upon addition of IPA and t-butanol. It is to be noted that *p*-BQ acts as a scavenger of superoxide anion radical. The IPA and t-butanol are scavengers of hydroxyl radicals, whereas EDTA-2Na acts as photogenerated holes scavenger. Since in dye-sensitization induced photocatalytic activity there are no chances of formation of photogenerated holes, hence the observations prove that the superoxide anions are the main active radicals which participate in the photocatalytic reactions.

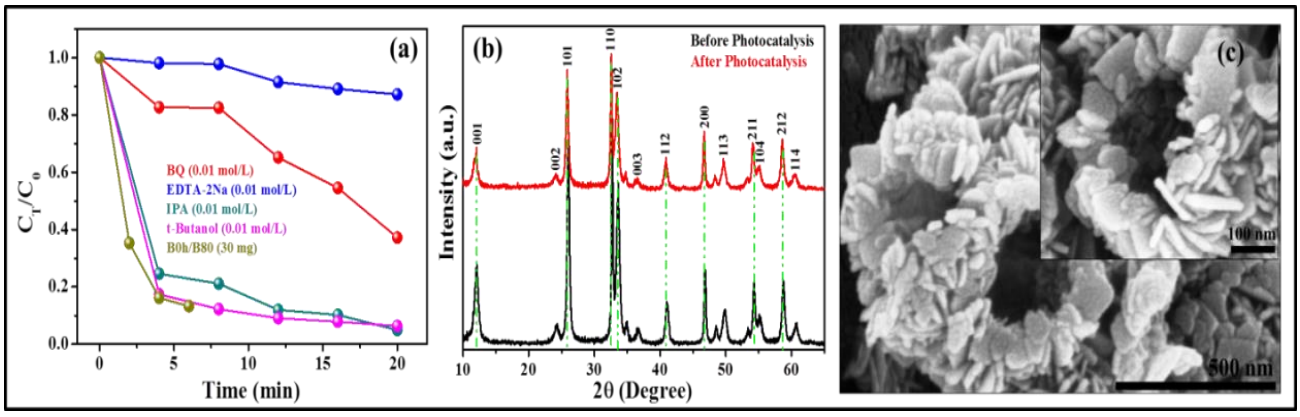

Figure 6.12: Scavenger test (a), XRD pattern of before and after photo-catalysis (b) and after photo-catalysis FESEM image (c) of B0h/B80

The XRD plots of B0h/B80 catalyst before photocatalysis and after photocatalysis are shown in Figure 6.12(b). The catalyst sample does not undergo any phase changes after the catalytic reactions take place. All the characteristics peaks are present in the reused sample with no additional peaks or absence of any peaks.

The FESEM image of the used catalyst B0h/B80 sample is shown in Figure 6.12(c) which reveals the exact same morphology that was observed before the photocatalytic reactions. These observations prove the stability of the catalyst in degrading toxic organic dyes and thereby establish its practical feasibility.

6.3.10 Plausible Photocatalytic Mechanism

Scheme 6.2 represents the plausible photocatalytic mechanism in degrading RhB dye by B0h/B80 catalyst under visible light irradiation. The photocatalytic activity of BiOCl samples were examined by decomposition of toxic organic dyes under visible light irradiation at ambient temperature and pH. The gradual decoloration of the RhB dye from deep pink to light pink and finally to completely colourless within 6 minutes of visible light irradiation in the presence of BiOCl catalyst occurs due to de-ethylation of RhB and the associated absorbance spectra has already been illustrated in Figure 6.9(a-i). Figure 6.9(j) shows the intensity ratio (C_T/C_0) plot with respect to irradiation time for the B0h/B80 sample showing significant adsorption of RhB dye (about 85 %) on the catalyst surface during one hour of dark stirring. Further dark stirring led to the saturation of the adsorption of dye which can be seen from inset of Figure 6.9(j). The rest 15 % of the dye could not be degraded without light irradiation. In order to establish the achievement of proper adsorption-desorption of dye on the BiOCl surface, the dye solution was subjected to uniform heating at 60 °C after sufficient adsorption has taken place during the one hour dark stirring. The absorption spectra were taken at regular intervals up to 3 hours of heating and it was found that the absorption intensity increased with increasing in heating time suggesting the desorption of the dye molecules from the catalyst surface. The corresponding absorption spectrum is given in Figure 6.9(k). Additionally no other new absorption peaks originate in the total spectral range of the RhB dye. It is to be noted that though the band gaps of the as-synthesised BiOCl samples lie in the UV range (3.46-3.59 eV), however, B0h/B80 sample could degrade only 68 % of RhB dye under UV light irradiation for 10 min whereas 99 % of RhB dye was degraded in lesser amount of time under visible-light irradiation. The high level of adsorption of the dye along with better photocatalytic activity under visible light irradiation than under UV light suggest the probability of dye-sensitised photocatalytic activity of BiOCl. Moreover, the hollow spherical morphology of B0h/B80 sample with an inner and outer diameter of about 200 nm and 580 nm respectively and the BET surface area of about 27.108 m^2g^{-1} is also one of the probable reasons for the superior photocatalytic activity of BiOCl. Additionally from the XRD data of the B0h/B80 sample, it can be observed that the (110) plane is the most intense among all other planes whereas for the other temperature varied samples, the peak corresponding to the (110) plane is more or less comparable with the other XRD peaks; and for the B120 sample, its intensity decreases than that of the (102) plane. The texture coefficient values as calculated from XRD data also reveals the highest value of TC (1.75) along the (110) plane for the B0h/B80 sample which suggests the preferential growth of the sample along this direction. Moreover, the FESEM image of the B0h/B80 sample reveals that the thickness of the walls of the hollow

microsphere is narrower than the other samples thus making the hollow more conspicuous in case of B0h/B80. For the B120 sample, the thickness of the walls is increased thus making the internal diameter of the hollow sphere minimum. This may be the reason behind the decreased photocatalytic activity of the B120 sample as compared to B0h/B80.

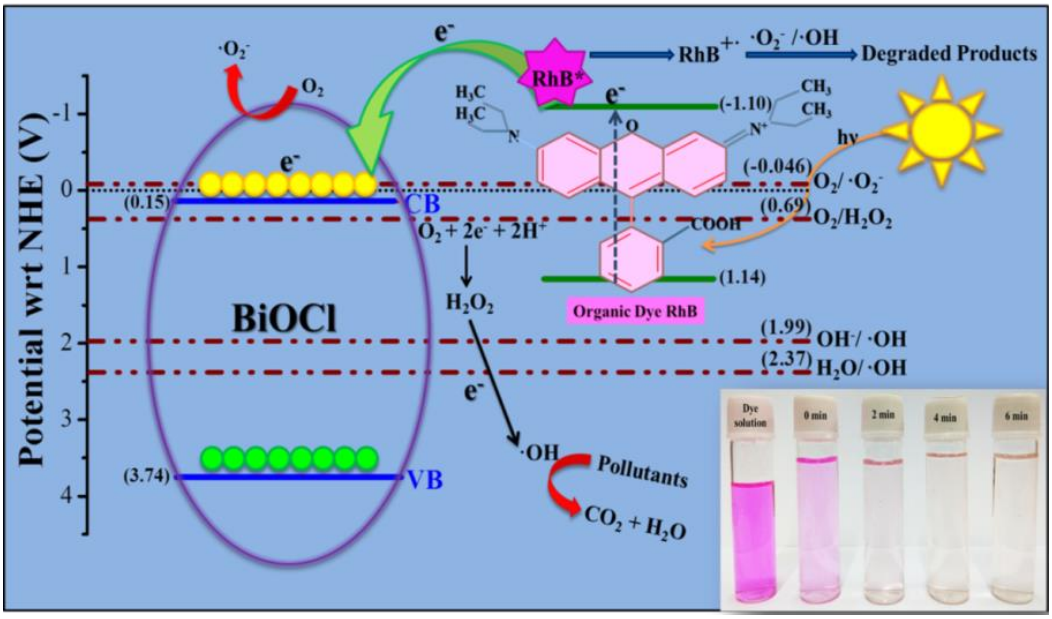

Scheme 6.2: Schematic representation of the mechanism of photocatalytic activity of B0h/B80 material under visible light irradiations

Based on the above facts and with special weightage on the fact that hollow micro-spherical BiOCl samples as-synthesised in the present work exhibited visible-light assisted degradation of RhB dye in-spite of having band gaps in the UV range, suggest the probable conclusion of dye self-sensitised degradation phenomenon occurring in presence of visible-light source. Moreover the significant adsorption of RhB on the BiOCl surface leads to the transfer of photogenerated electrons between activated RhB* and BiOCl catalyst along with recombination of charge carriers between the RhB dye and the catalyst[51]. Generally photogenerated charge carriers are produced under visible light irradiation with a wavelength equivalent to the band gap of the catalyst. The electrons travel to the conduction band leaving behind holes in the valence band. However, in the present study, due to the large band gap of BiOCl, visible-light irradiation is not sufficient to excite the material and no photogenerated charge carriers are produced. But the visible light energy proves to be adequate in exciting the RhB dye molecules adsorbed on the catalyst surface thereby forming an active species RhB*. It is also to be noted that the LUMO and HOMO of RhB lies at -1.10 V and 1.14 V (Vs. NHE)[52] whereas the CB minima and the VB maxima of BiOCl lies at 0.15 V and 3.74 V (Vs. NHE) respectively. Due to the

more negative LUMO potential of RhB than the CB edge of BiOCl, electrons will be transferred from the LUMO of RhB to the CB of BiOCl. After donating an electron RhB* gets converted to the active species $RhB^{+\bullet}$.

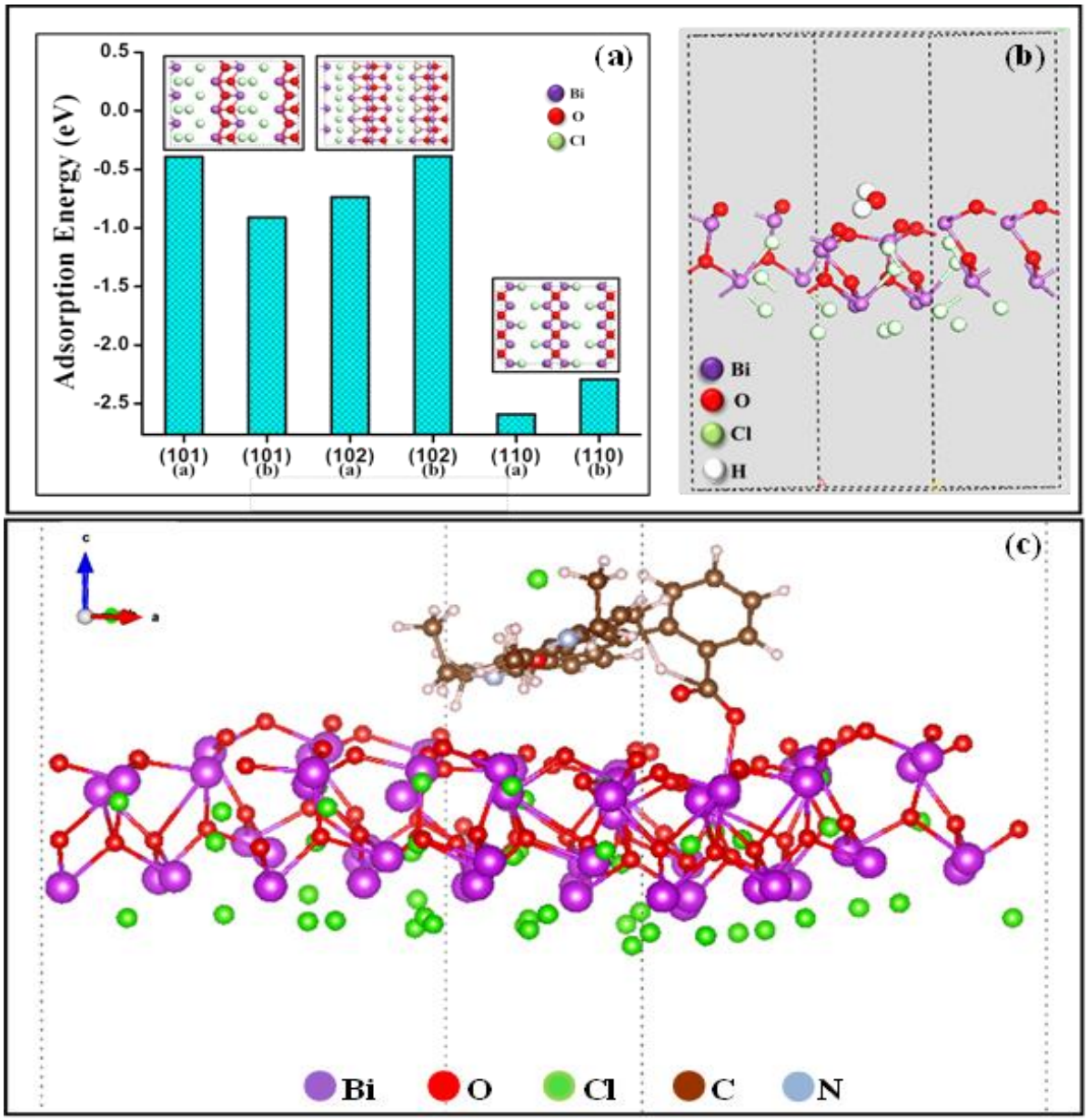

Figure 6.13: (a) Adsorption energies of water adsorbed on different planes of BiOCl. The plane indices are shown along the x axis. The top view of each surfaces are shown in the inset. (b) Optimised structure of water adsorbed on BiOCl (110) plane. (c) Optimised structure of RhB on BiOCl (110) plane

The hydroxyl active radical is produced by some intermediate reactions taking place in the CB of BiOCl where O_2 reacts with electrons (injected from RhB*) and H^+ ions to form H_2O_2. Since the redox potential of this reaction is more positive (0.69 V wrt NHE) than the CB of BiOCl, hence this reduction

reaction occurs more feasibly where H_2O_2 gets reduced to •OH in presence of electrons. The hydroxyl anion thus produced helps in the degradation of the organic pollutants to CO_2 and H_2O. The $RhB^{+\bullet}$ can also effectively degrade the toxic dye to non-toxic products in presence of the active radicals.

Figure 6.13(a) shows the bar graph plot of adsorption energies of water on different planes of pristine BiOCl as obtained from first principles calculation. For each BiOCl planes, two different water adsorption sites are considered which are denoted as (hkl) (a/b). The lowest adsorption energy value (-2.59 eV) for water adsorption is observed for the (110) (a) plane of BiOCl as revealed from the bar graph. The optimised geometry of water adsorbed in its most favourable condition is shown in Figure 6.13(b). This proves that the (110) plane of BiOCl is most beneficial for the adsorption of water. Due to the efficiency of the (110) surface to adsorb water, we further studied the adsorption mechanism of RhB dye on this surface. The optimised structure of RhB adsorbed on the (110) plane is shown in Figure 6.13(c). This calculation corroborates the dependency of the superior photocatalytic activity of BiOCl on the most intense (110) crystal plane. The (110) exposed facet of BiOCl shows the presence of large density of edge terminated oxygen atoms as observed from Figure 6.13(c) rendering an anionic nature in the sample. This proves to be immensely beneficial for the adsorption of cationic RhB dye along the particular plane assisted with accumulation of photogenerated charge carriers transferred from the LUMO of RhB dye.

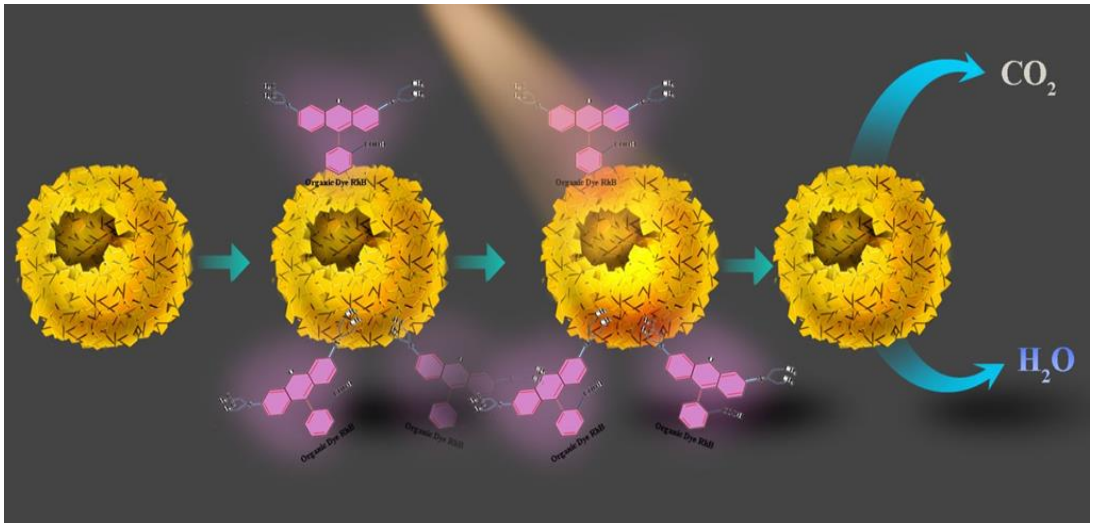

Scheme 6.3: Degradation of RhB dye by hollow micro-spherical morphology of BiOCl catalyst with exposed (110) crystal facet

The series of reactions that occur during the photocatalytic activity under visible light irradiation are given as follows:

$$RhB_{(ads)} + h\nu \rightarrow RhB^{*}_{(ads)} \quad (6.6)$$

$$RhB^{*}_{(ads)} + BiOCl \rightarrow BiOCl(e^{-}_{CB}) + RhB^{+\bullet}_{(ads)} \quad (6.7)$$

$$O_2 + e^{-} \rightarrow \bullet O_2^{-} \quad (6.8)$$

$$O_2 + 2H^{+} + 2e^{-}_{CB} \rightarrow H_2O_2 \quad (6.9)$$

$$H_2O_2 + e^{-}_{CB} \rightarrow \bullet OH \quad (6.10)$$

$$\bullet OH + RhB_{(ads)} \rightarrow CO_2 + H_2O \quad (6.11)$$

$$RhB^{+\bullet}_{(ads)} + \bullet OH/\bullet O_2^{-} \rightarrow CO_2 + H_2O \quad (6.12)$$

Hence it can be concluded that upon adsorption of RhB dye on BiOCl catalyst surface, an effective RhB/BiOCl interface is formed due to the existence of the significant energy level offset between them. This in turn leads to the thermodynamically favoured rapid transfer of photogenerated electrons from LUMO of dye to CB of catalyst resulting in effective separation of photogenerated charge carriers, which is an important requisite for photocatalytic activity[51].

Scheme 6.2 depicts the plausible photocatalytic mechanism of hollow spherical BiOCl samples in degradation of toxic organic dyes. Additionally Scheme 6.3 represents the adsorption of RhB on BiOCl surface and consequent facilitation of the enhanced photocatalytic activity owing to the unique morphology of the catalyst[53].

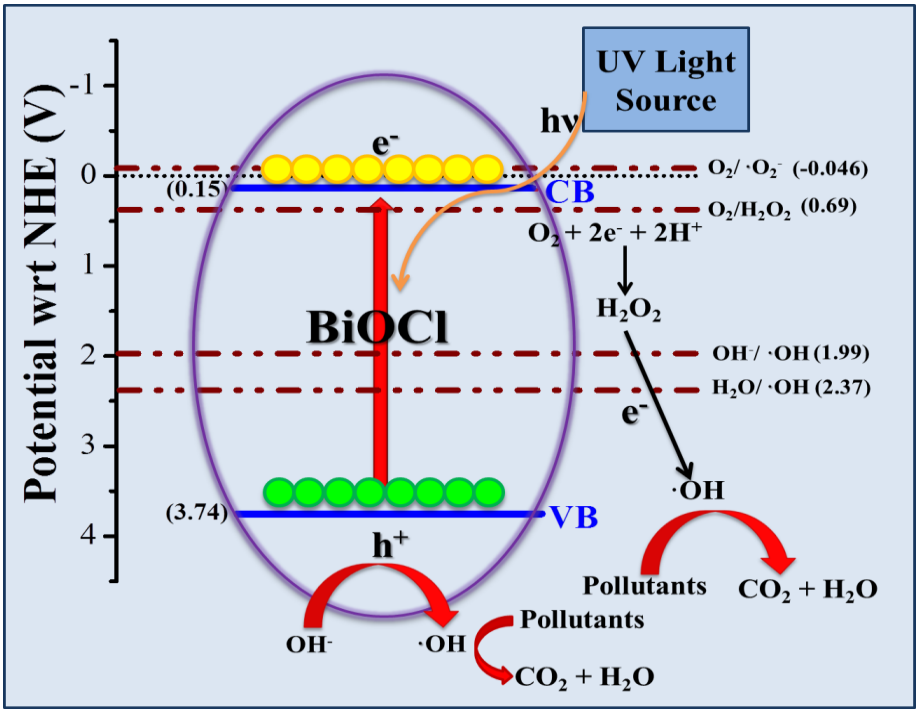

Scheme 6.4: UV-light assisted degradation of RhB dye by hollow micro-spherical BiOCl catalyst with exposed (110) crystal facet

The plausible mechanism that took place under UV light irradiation is given in Scheme 6.4. In this case, due to the favourable band gap of the BiOCl, excitation of the material occurs under UV light with subsequent generation of electrons in the CB and holes in the VB of BiOCl. The CB of BiOCl (0.15 V vs. NHE) is more positive than the redox potential of $O_2/•O_2^-$ (-0.046 V vs. NHE) hence the reduction reaction to form the superoxide anion is not feasible in the CB of BiOCl. However, the more positive redox potential of O_2/H_2O_2 (0.69 V vs. NHE) favours the formation of hydroxyl active radical (•OH) by reduction of H_2O_2 in presence of electrons. The VB of BiOCl (3.74 V vs. NHE) is more positive than the redox potential of $H_2O/•OH$ (2.37 V vs. NHE), hence the oxidation reaction of OH^- to •OH in presence of photogenerated holes occurs at the VB of BiOCl. The •OH active radical can subsequently reduce RhB dye to CO_2 and H_2O.

A list of all the reported pure BiOCl catalysts in degradation of RhB dye is tabulated in Table A2 (Appendix) which reveals the superior nature of the catalyst reported in the present work in terms of degradation time and reaction rate constant value.

6.4 Conclusions

A facile chemical synthetic procedure for the development of pure BiOCl samples by varying some synthetic parameters like time and temperature duration has been reported in the present work. The synthesised samples were characterised by different sophisticated techniques. The samples were finally utilised for the effective photocatalytic degradation of toxic organic dye. The best sample B0h/B80 exhibited the best efficiency by completely degrading the dye within very short time of visible light irradiation. Several parameters like catalyst dosage, pH and light source were varied to observe their effects on the reactions. The catalyst was able to be reused up to 3 cycles which proved its practical feasibility. The effect of the most intense (110) plane of BiOCl on the superior catalytic activity was further demonstrated from first principles calculations which confirmed the (110) plane to be the most suitable adsorption site. The high adsorption of cationic dye RhB on the anionic catalyst BiOCl along with exhibition of superior catalytic activity under visible-light irradiation in-spite of having band gaps in the UV range indicated the dye sensitised photocatalytic phenomenon. In conclusion, the as prepared BiOCl samples emerged to be highly efficient catalysts in degrading organic pollutants which establish them as potential candidates for water remediation related applications.

References

[1] I.K. Konstantinou and T.A. Albanis, *Applied Catalysis B: Environmental*, 49(1), 2004, 1-14.
[2] V. Rajagopalan, *Scientific Reports*, 6(1), 2016, 38606.

[3] R. Leena and R.D. Selva, *African Journal of Biotechnology*, 7(18), 2008.
[4] G.L. Baughman and T.A. Perenich, *Environmental Toxicology and Chemistry: An International Journal*, 7(3), 1988, 183-199.
[5] X. Chen and S.S. Mao, *Chemical Reviews*, 107(7), 2007, 2891-2959.
[6] H. Dong, G. Zeng, L. Tang, C. Fan, C. Zhang, X. He and Y. He, *Water Research*, 79, 2015, 128-146.
[7] K. Chen, J. Li, W. Wang, Y. Zhang, X. Wang and H. Su, *Materials Science in Semiconductor Processing*, 15(1), 2012, 20-26.
[8] S. Peng, Y. Huang and Y. Li, *Materials Science in Semiconductor Processing*, 16(1), 2013, 62-69.
[9] A. Ishikawa, T. Takata, T. Matsumura, J.N. Kondo, M. Hara, H. Kobayashi and K. Domen, *The Journal of Physical Chemistry B*, 108(8), 2004, 2637-2642.
[10] J. Sato, N. Saito, Y. Yamada, K. Maeda, T. Takata, J.N. Kondo, M. Hara, H. Kobayashi, K. Domen and Y. Inoue, *Journal of the American Chemical Societ*, 127(12), 2005, 4150-4151.
[11] K. Maeda, K. Teramura, D. Lu, T. Takata, N. Saito, Y. Inoue and K. Domen, *Nature*, 440(7082), 2006, 295.
[12] Q. Wang, J. Hui, Y. Huang, Y. Ding, Y. Cai, S. Yin, Z. Li and B. Su, *Materials Science in Semiconductor Processing*, 17, 2014, 87-93.
[13] Y. Wang, Z.Q. Shi, C.M. Fan, X.G. Hao, G.Y. Ding and Y.F. Wang, *International Journal of Minerals, Metallurgy, and Materials*, 19(5), 2012, 467-472.
[14] C.R. Michel, N.L.L. Contreras and A.H. Martínez-Preciado, *Sensors and Actuators B: Chemical*, 160(1), 2011, 271-277.
[15] X. Zhang, Z. Ai, F. Jia and L. Zhang, *The Journal of Physical Chemistry C*, 112(3), 2008, 747-753.
[16] H. Sopha, Z. Spotz, J. Michalicka, L. Hromadko, R. Bulanek, T. Wagner and J.M. Macak, *ChemElectroChem*, 6(2), 2019, 336-341.
[17] G. Li, B. Jiang, S. Xiao, Z. Lian, D. Zhang, C.Y. Jimmy and H. Li, *Environmental Science: Processes & Impacts*, 16(8), 2014, 1975-1980.
[18] Z. Jiang, F. Yang, G. Yang, L. Kong, M.O. Jones, T. Xiao and P.P. Edwards, *Journal of Photochemistry and Photobiology A: Chemistry*, 212(1), 2010, 8-13.
[19] Y. Wang, K. Deng and L. Zhang, *The Journal of Physical Chemistry C*, 115(29), 2011, 14300-14308.
[20] Y. Li, Y. Zhao, G. Wu, H. Ma and J. Zhao, *Materials Research Bulletin*, 101, 2018, 39-47.
[21] J. Pan, J. Liu, S. Zuo, U. A. Khan, Y. Yu and B. Li, *Materials Research Bulletin*, 103, 2018, 216-224.
[22] B. Pare, B. Sarwan and S.B. Jonnalagadda, *Applied Surface Science*, 258(1), 2011, 247-253.
[23] S. Shamaila, A.K.L. Sajjad, F. Chen and J. Zhang, *Journal of Colloid and Interface Science*, 356(2), 2011, 465-472.
[24] S.Y. Chai, Y.J. Kim, M.H. Jung, A.K. Chakraborty, D. Jung and W.I. Lee, *Journal of Catalysis*, 262(1), 2009, 144-149.
[25] Y. Liu, W.J. Son, J. Lu, B. Huang, Y. Dai and M.H. Whangbo, *Chemistry–A European Journal*, 17(34), 2011, 9342-9349.
[26] K. Xu, X. Fu and Z. Peng, *Materials Research Bulletin*, 98, 2018, 103-110.
[27] Q. Yang, Y. Zhai, X. Li and H. Li, *Materials Research Bulletin*, 106, 2018, 409-417.
[28] X. Hu, G. Zhang, C. Yin, C. Li and S. Zheng, *Materials Research Bulletin*, 119, 2019, 110559.
[29] X. Zhang, X.B. Wang, L.W. Wang, W.K. Wang, L.L. Long, W.W. Li and H.Q. Yu, *ACS Applied Materials & Interfaces*, 6(10), 2014, 7766-7772.
[30] X. Li, C. Zhu, Y. Song, D. Du and Y. Lin, *RSC Advances*, 7(17), 2017, 10235-10241.

[31] X.C. Du, W.W. Zhao, Y.W. Liu, X.P. Huang and F. Mao, *In Advanced Materials Research*, 487, 2012, 841-844.
[32] R. Zhao, X. Li, Y. Zhai and Q. Li, *Journal of Advanced Oxidation Technologies*, 18(2), 2015, 353-360.
[33] D.S. Bhachu, S.J. Moniz, S. Sathasivam, D.O. Scanlon, A. Walsh, S.M. Bawaked, M. Mokhtar, A.Y. Obaid, I.P. Parkin, J. Tang and C.J. Carmalt, *Chemical Science*, 7(8), 2016, 4832-4841.
[34] J. Li, Y. Yu and L. Zhang, *Nanoscale*, 6(15), 2014, 8473-8488.
[35] H. Peng, C.K. Chan, S. Meister, X.F. Zhang and Y. Cui, *Chemistry of Materials*, 21(2), 2008, 247-252.
[36] H. Zhang, L. Liu and Z. Zhou, *Physical Chemistry Chemical Physics*, 14(3), 2012, 1286-1292.
[37] A. Huizhong, D.U. Yi, W.A.N.G. Tianmin, W.A.N.G. Cong, H.A.O. Weichang and J. Zhang, *Rare Metals*, 27(3), 2008, 243-250.
[38] Z. Wan and G. Zhang, *Scientific Reports*, 4(1), 2014, 6298.
[39] K. Zhang, J. Liang, S. Wang, J. Liu, K. Ren, X. Zheng, H. Luo, Y. Peng, X. Zou, X. Bo and J. Li, *Crystal Growth & Design*, 12(2), 2012, 793-803.
[40] G. Kresse and J. Hafner, *Physical Review B*, 47(1), 1993, 558.
[41] G. Kresse and J. Hafner, *Physical Review B*, 49(20), 1994, 14251.
[42] G. Kresse and J. Furthmüller, *Computational Materials Science*, 6(1), 1996, 15-50.
[43] P.E. Blöchl, *Physical Review B*, 50(24), 1994, 17953.
[44] J.P. Perdew, K. Burk and M. Ernzerhof, *Physical Review Letters*, 77(18), 1996, 3865.
[45] S. Grimme, *Journal of Computational Chemistry*, 27(15), 2006, 1787-1799.
[46] J. Hou, K. Jiang, M. Shen, R. Wei, X. Wu, F. Idrees and C. Cao, *Scientific Reports*, 7(1), 2017, 11665.
[47] G. Cheng, J. Xiong and F.J. Stadler, *New Journal of Chemistry*, 37(10), 2013, 3207-3213.
[48] S. Weng, B. Chen, L. Xie, Z. Zheng and P. Liu, *Journal of Materials Chemistry A*, 1(9), 2013, 3068-3075.
[49] L. Kong, Z. Jiang, H.H.C. Lai, T. Xiao and P.P. Edwards, *Progress in Natural Science: Materials International*, 23(3), 2013, 286-293.
[50] M. He, D. Zhao, J. Xia, L. Xu, J. Di, H. Xu, S. Yin and H. Li, *Materials Science in Semiconductor Processing*, 32, 2015, 117-124.
[51] D.H. Wang, G.Q. Gao, Y.W. Zhang, L.S. Zhou, A.W. Xu and W. Chen, *Nanoscale*, 4(24), 2012, 7780-7785.
[52] C. Chuaicham, R. Pawar and K. Sasaki, *Catalysts*, 9(3), 2019, 235.
[53] P. Cui, J. Wang, Z. Wang, J. Chen, X. Xing, L. Wang and R. Yu, *Nano Research*, 9(3), 2016, 593-601.

Chapter 7

Grain size dependent catalytic mechanism of sheet like BiOCl nanoparticle dye degradation under UV-light

7.1 Introduction

BiOCl is one of the new age semiconductors showing remarkable applications in different fields. Starting from traditional semiconductor aspects to novel green cleaning technology, BiOCl has shown its promising properties. Several studies based on the modifications of crystalline structure[1], transport properties[2], photovoltaic applications[3] are already performed on this material via variation of synthesis parameters, impurity doping etc.

One of the most common solutions for enhancing different properties of this material is to tune up properties in low dimension. Synthesis of BiOCl nanostructure is therefore popular among the researchers in this field. So far, BiOCl has been studied in low dimensional structures like nanorods, nanoparticles, nanoballs etc. However, fabrication of hierarchical nanostructure of BiOCl may lead to much enhanced opto-electrical properties. Such hierarchical structures often include the facilities of very low dimensional (nano) building units as well as bulk form of the same materials. Fabrication of nano-BiOCl has been attempted via in situ topo-tactic synthesis technique[4], Microwave synthesis method[5] and other popular chemical routes. These routes may result in desired nanostructure of appropriate shape and size but may require costly precursors[6], too much sophisticated instrumental set-up[7], poor yield and other drawbacks. In addition, many chemical routes often release harmful residue or by-products which may include additional barriers in future commercialisation of the same.

Even if appropriate nanostructures with desired shape and dimension are fabricated via any particular method, in absence of prior anticipation of the electronic band structure of the resulting product, an entire work may be useless. Incorporation of foreign dopant in target material has often been prescribed as a probable key for enhanced properties. This has been attempted in similar photocatalyst systems in several instances. Doping or physical attachment of novel metal nanoparticles in classic photocatalysts have been proven as a remarkable remedy in this direction[8]. Doping by other appropriate elements was also attempted in many cases[9]. But such a procedure again may require costly fabrication set up and may result in poor yield. It may also often cause stoichiometric imbalance of the hosts' structure. The only way out is to vary the constituent elements in appropriate ratio with prior anticipation of the resulting optoelectronic behaviour. For example, Kong et al.[10] has shown a wide variation of electronic band structure of BiOCl via well planned change of constituents' proportions. They have clearly shown that considerable variation of carrier concentration in BiOCl can be expected if the inherent ratio of Bi and Cl is altered. Variation of the stoichiometric proportion of constituent elements normally does not require any additional component in popular fabrication route, rather simple variation of precursor and experimental parametres in general suffice. Moreover, this normally allows a wide range of variation of

the carrier concentration of the host without affecting its crystal structure considerably. This work proposes a suitable fabrication of BiOCl nanostructure in appropriate hierarchical form via cost effective simple hydrothermal technique. The resulting products were properly characterised with appropriate tools to investigate crystal structure, morphology and spectroscopic properties. Finally, the samples were characterised for detailed photocatalytic activity under UV-Visible excitation.

The variation of photocatalytic activities were correlated with the electronic band bending of the samples. The variation of the morphology was directly associated with the synthesis time whereas the morphology was correlated with electronic band configuration which is the key factor governing the catalytic behaviour of the sample.

7. 2 Experimental Details

7.2.1 Chemicals

The Merck Group provided $Bi(NO_3)_3 \cdot 5H_2O$ (Bismuth nitrate pentahydrate), $C_6H_8O_7 \cdot H_2O$ (Citric Acid Monohydrate) and HCl (Hydrochloric acid, 37 %). The polyvinylpyrrolidone (PVP, K30) was purchased from Loba Chemie Pvt. A solution of 25 % ammonia and IPA (Isopropyl alcohol) were provided by Mark Group. In addition to EDTA-2Na (Ethylene diamine tetra acetate disodium) and *p*-BQ (*p*-Benzoquinone) were obtained from Loba Chemie Pvt. The samples were synthesised using absolute ethanol (99.99 %) and DI water.

7.2.2 Synthesis Method of BiOCl

There was no further purification of the reagents, all of which were analytical grade. The samples were synthesised according to the methodology reported[11]. A solution of 3.75 mmol of $Bi(NO_3)_3 \cdot 5H_2O$ was initially dissolved in 22.5 mL of DI water, followed by the addition of 2.5 mL of HCl (37 %) to the solution in question. A vigorous stir was carried out at room temperature with the mixed solution (called solution A) until the $Bi(NO_3)_3 \cdot 5H_2O$ was completely dissolved. Separately, 42 mL of DI Water was mixed with 50 mL of absolute ethanol, 1.16 x 10^{-4} mmol of PVP, and 1.31 mmol of Citric Acid Monohydrate that was heated to 80 °C. After adding 1.19 mmol of solution A to the solution B drop by drop, it was stirred continuously at 80 °C for 5 minutes to form solution C. The solution C was then heated at 80 °C for six hours, eighteen hours, and twenty-four hours while vigorously stirring for each time period. It was allowed to cool to ambient temperature naturally after the reaction procedure was completed. As the solution became neutral (pH = 7) filtration and washing with DI water and absolute ethanol was applied to collect the precipitates. After drying the washed samples overnight at 80 degrees

Celsius, white powdered products were obtained. The samples B6h, B18h, and B24h were prepared by stirring for 5 minutes at 80 °C for 6, 18 and 24 hours.

7.2.3 Characterizations

Several characterisation techniques were employed to evaluate the synthesised samples. To determine the phase formation of the powder samples, a X-ray diffractometer (BRUKER D8) was used under 40 kV and 40 mA with a wavelength (λ = 1.54056 Å) for a Cu K_α source of radiation. With an Al K_α X-ray source ($h\nu$ = 1486.6 eV) and a hemispherical analyser (SPECS HSA 3500) monochromatic source was utilised the chemical structure of the powder samples by X-ray Photoelectron Spectroscopy (XPS). An Energy Dispersive X-ray Spectroscopy (EDS) spectral analyser was installed on the Hitachi S-4800 for analysing the elements in the samples. In addition, the samples were studied by High Resolution Transmission Electron Microscopic (HRTEM, JEOL-JEM 2100) to reveal their morphology. Powder samples were measured by FESEM using carbon tape, while aqueous dispersion samples were analysed by TEM by drop casting on copper meshes that were coated with carbon. A Witec Raman spectrophotometer excited at 532 nm was used to analyse the powder samples. A Shimadzu UV-3600 spectrophotometer was used to obtain the UV-visible diffuse reflectance spectra of the powder samples using $BaSO_4$ as a reflectance standard.

7.2.4 Photocatalytic Activity Measurement

A standard photocatalytic setup was used to study dye degradation properties of RhB dye. An ordinary experiment would use the RhB stock solution of 10^{-5} M. Independently, 30 mg of each of the samples was added to this test solution and stirred for 60 minutes in dark conditions. In the photocatalysis experiment chamber, each powder sample solution was exposed to UV irradiation after stirring at night. In the photocatalysis experiment chamber were a quartz beaker with a 50 mm thickness that served as the active medium for photocatalysis and a sample stirrer that gave up to 450 rpm stirring speed. Keeping the radiation distance constant at 15 cm was the solution to the radiation distance problem. The stirring solution system was exposed directly to the 254.6 nm wavelength UV-rays from two 40 W tubes (Philips). A rectangular encapsulation is used on the whole system to prevent additional incident wavelengths from surrounding the device. In the catalysis process, the UV exposure was applied for different durations and parts of the solutions were filtered and collected after different times for subsequent spectroscopic analysis. Various time intervals of solution collection were used to record the time-evolved absorption spectra.

7.2.5 Electrochemical Measurement

Electrochemical impedance measurements were conducted for three electrodes in PGSTAT302N AUTOLAB in order to analyse the Mott-Schottky plots. To prepare the foam for measuring, diluted HCl solution was applied followed by ethanol mixture following cleaning with Ni foam of 1 cm X 1 cm. In order to prepare a working electrode by mixing 40 mg of the as synthesised BiOCl samples with 5 mg PVDF and 5 mg carbon black sprinkled with NMP solution drop-by-drop to create a black coloured slurry which was stirred for four hours. As the electrode was prepared for measurement, the slurry was applied uniformly on the clean Ni foam. Using a Pt electrode as the counter electrode and a typical Ag/AgCl electrode as the reference electrode, the experiments were carried out. The electrolyte solution was 0.5 M Na_2SO_4. A frequency of 1000 Hz was chosen for the Mott-Schottky measurements.

7.3 Results and Discussion

7.3.1 Crystallinity of BiOCl Analysis

The PXRD patterns of as-prepared BiOCl materials were demonstrated by Figure 7.1(a). All the diffracted peaks were well coordinated to the crystal structure of tetragonal phase (P4/nmm) and JCPDS Card No. 06-0249 by the sharp distinctive peaks were originated at 2θ of 11.96, 25.9, 32.56, 33.48, 40.92, 46.66, 49.74, 54.1 and 58.66 ° with corresponds the lattice planes (001), (101), (110), (102), (112), (200), (113), (211) and (212) respectively.

The materials grain sizes were evaluated by Scherer's formula from the respective PXRD patterns. The Scherer's formula given below:

$$D = {}^{0.89\lambda}/_{\beta cos\theta} \qquad (7.1)$$

where,

λ = the wavelength of incident X-ray,

β = the diffracted peak broadening and

θ = diffracted angle.

Generally β was indicated as:

$$\beta = \sqrt{\beta_{exa}^2 - \beta_{instru}^2} \qquad (7.2)$$

where,

β_{exa} = the examine FWHM,

β_{instru} = the broadening of instrument.

The broadening factor of instrument BRUKER D8 XRD was constructed to be 0.1323 ° and 0.89 was the shape factor.

According to the equations (7.1) and (7.2) have been used for the correction of grain sizes, Table 7.1 provides the corrected grain sizes for all the samples. It was estimated that the largest grain size for the B18h sample was greater than the other samples. And the bar plots of grain size vs. different lattice plane was demonstrated in Figure 7.1(b).

Table 7.1: Calculated value of grain size and d-spacing of the samples from XRD pattern

Samples Name	Grain size (D) for the lattice planes (nm)				d-spacing for lattice planes (Å)			
	(001)	(101)	(110)	(102)	(001)	(101)	(110)	(102)
B6h	1.9687	3.6618	7.761	2.5924	7.44	3.4395	2.7488	2.6754
B18h	2.8179	5. 1701	9.8463	3.7174	7.39	3.4418	2.7503	2.677
B24h	2.5011	3.5609	6.7986	3.0444	7.343	3.4351	2.7466	2.6779

7.3.2 Raman Spectra Analysis

The Raman spectroscopy's spectrum to approve from the phonon dynamics to the coordination of the phases demonstrated in Figure 7.1(b) in range at 0-500 cm^{-1} of the as-prepared time varying BiOCl at 80 °C. From PXRD the iso-structure of BiOCl was a tetragonal structure (PbFCl) with P4/nnm space group[12]. For this a structural space group of D_{4h}^{7}, by the two molecular functions for each unit cell and the active modes of Raman are A_{1g}, B_{1g} and E_g. The analysing interacting methods for the respective structure and the optical methods are delivered towards by Zhang et al.[13] as following:

$$\Gamma = 2A_{1g} + 2A_{2u} + B_{1g} + 3E_g + 2E_u \qquad (7.3)$$

where,

g = Raman active modes and

u = IR active modes.

The Raman spectrogram consists of two high bands (136.5 and 195.2 cm^{-1}) and two weak bands (79.8 and 382.4 cm^{-1}) are demonstrated. The symmetrical vibration generally presented to acceleration of higher excessive Raman band than asymmetrical vibration, the bands at 79.8 cm^{-1} and at 136.5 cm^{-1} are carried out to A_{1g} internal stretching mode of vibration of Bi-Cl bonds, the band at 195.2 cm^{-1} allotted to E_g internal stretching mode of vibration of Bi-Cl and the weak band at 382.4 cm^{-1} evaluated by the oxygen atoms motion and also known as B_g band. In Figure 7.1(b), the bands intensity and

wavenumber are increased by the duration of synthetic time and directly proportional relation with time.

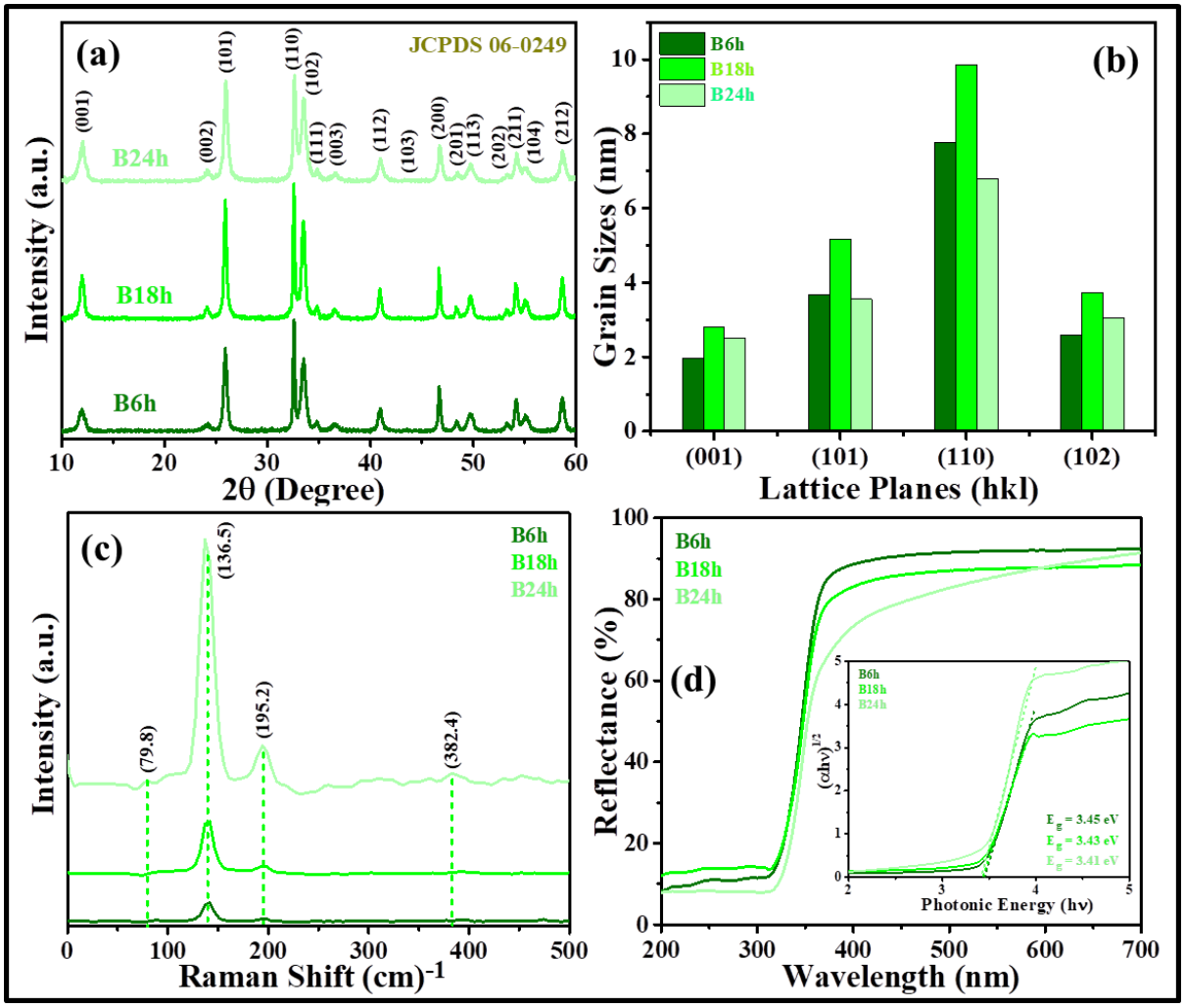

Figure 7.1: The PXRD pattern (a), the grain sizes along different lattice planes (b), Raman spectrum (c), DRS spectrum (d) and inset: of calculated indirect band gap by Kubelka Munk function of all samples

7.3.3 UV-vis DRS Analysis

The Ultraviolet visible diffuse reflectance spectroscopy (UV-vis DRS) was utilised to describe the electronic configuration of as-synthesised materials. In Figure 7.1(c) demonstrated that all the as-synthesised time dependent BiOCl materials reflectance, which are decreases to the reflectance by increasing duration of time, that suggested the duration of time can be carried out as a band gap controlling operator for constructing nanomaterials to efficiently decreased the reflectance as well as falling ratio. The band gap energy of as-synthesised samples is evaluated by Kubelka Munk function using following equation:

$$(\alpha h\upsilon)^{1/n} = k\left(h\upsilon - E_g\right) \quad (7.4)$$

where,

α = reflectance coefficient,

hν = photonic energy (eV),

k = constant of proportionality,

E_g = samples band gap energy and

n = characterizing index that depends on nature direct or indirect of the transition of energy band. The graph $(\alpha h\upsilon)^{1/2}$ vs. $h\upsilon$ was demonstrated in Figure 7.1(d), that presented the deduced intercepted to the evaluated E_g of the respective materials. The respective optical band gap energy of the as-synthesised BiOCl materials is 3.45, 3.43 and 3.41 eV, which is completely ultraviolet range and also efficient to promote the photocatalysis activity.

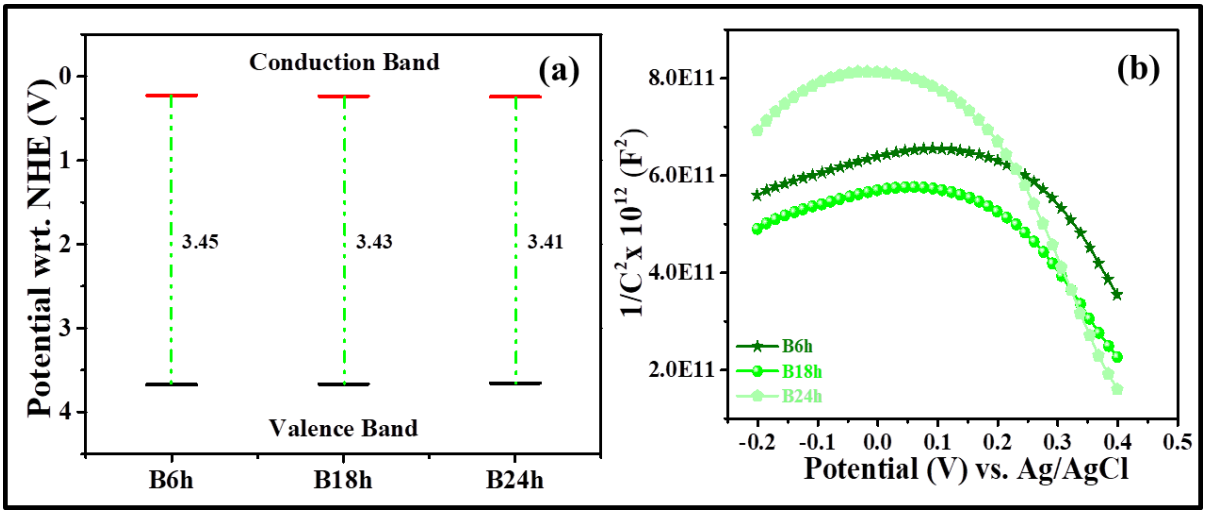

Figure 7.2: The energy band diagrams (a) and Mott-Schottky plot at the frequency 1000 Hz of all time varied BiOCl samples (b)

As shown in Figure 7.2(a), each time variable energy band gap diagram has been plotted. A description of the process of photocatalysis would not be complete without discussing the electronic band structures. In a photocatalytic reaction, the band diagram guides the description of how the conduction band (CB) and the valence band (VB) are distributed. Mulliken's electronegativity theory[11] describes a set of equations that can be used to compute the conduction band edge and valence band edge potentials.

$$E_{VB} = \chi_{Semiconductor} - E^e + 0.5E_g \quad (7.5)$$

where,

$E_{VB} = edge\ potential\ of\ valence\ band,$

$\chi_{Semiconductor} = electronegativity\ of\ the\ semiconductor,$

$E^e = free\ electron\ energy\ of\ H_2\ scale\ (4.5\ eV)\ and$

$E_g = band\ gap\ energy\ of\ semiconductor.$

From the above equations, one can calculate the VB edge potentials. The VB edge potentials, as measured by DRS, are subtracted from electronic band gaps, to obtain the CB edge potentials.

7.3.4 Mott-Schottky Analysis

Figure 7.2(b) shows the Mott-Schottky plot of the all BiOCl samples that were measured in the 1000 Hz frequency range. In the $1/C^2$ Vs. potential plots, there are negative slopes, which indicate the semiconductor is of the 'p' type.

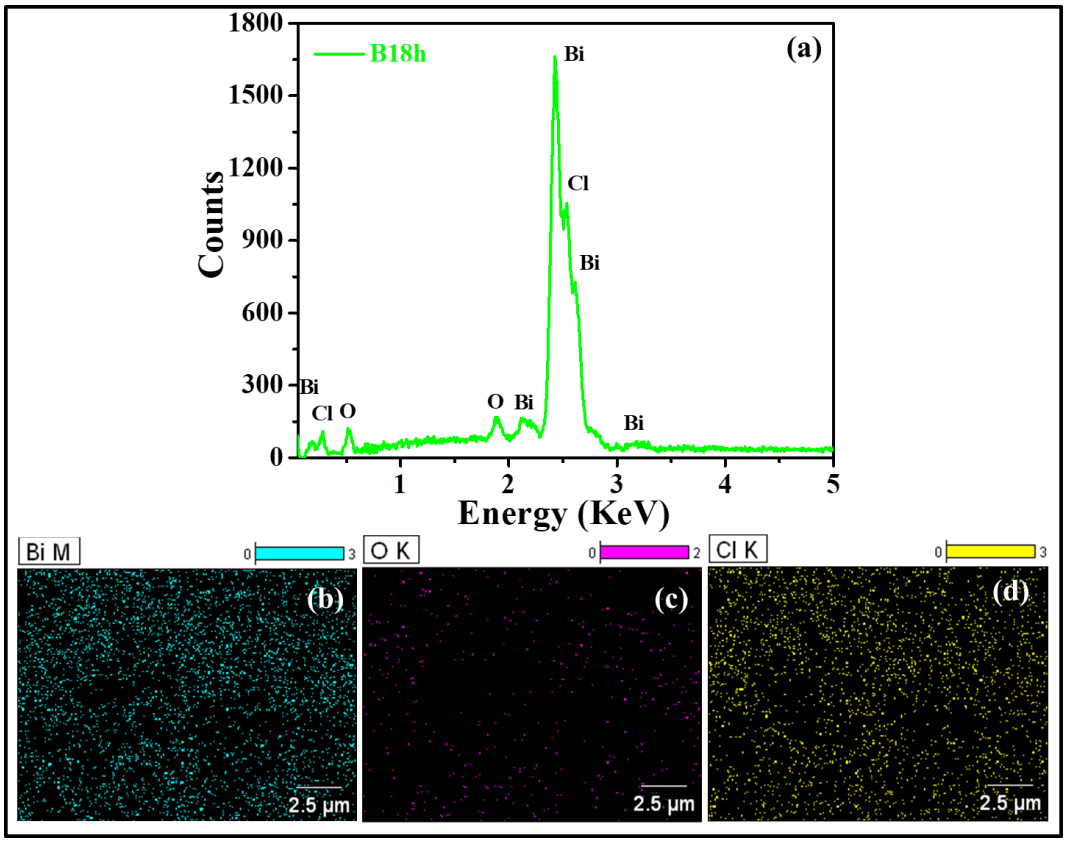

Figure 7.3: The EDS pattern (a) of B18h sample, (b), (c) and (d) elemental mapping of Bi, O and Cl materials

7.3.5 EDS Analysis

The Energy Dispersive X-Ray Spectra (EDS) of B18h sample was shown in Figure 7.3(a), revealing the presence of elemental peaks for Bi, O, and Cl. The elemental mapping of the sample was demonstrated in Figure 7.3(b-d). Each sample is given its weight and atom percentage in Table 7.2. As

synthesised BiOCl samples, their atomic ratios are approximately stoichiometric, based on the classical formula unit.

Table 7.2: Quantitative results of all samples are obtained from EDX analysis

Materials	Quantitative Result	Bi	O	Cl
B6h	Weight %	80.46	9.08	10.46
	Atom %	30.86	45.48	23.66
B18h	Weight %	80.86	6.18	12.96
	Atom %	33.97	33.92	32.10
B24h	Weight %	82.01	6.21	11.77
	Atom %	35.27	34.89	29.84

7.3.6 XPS Analysis

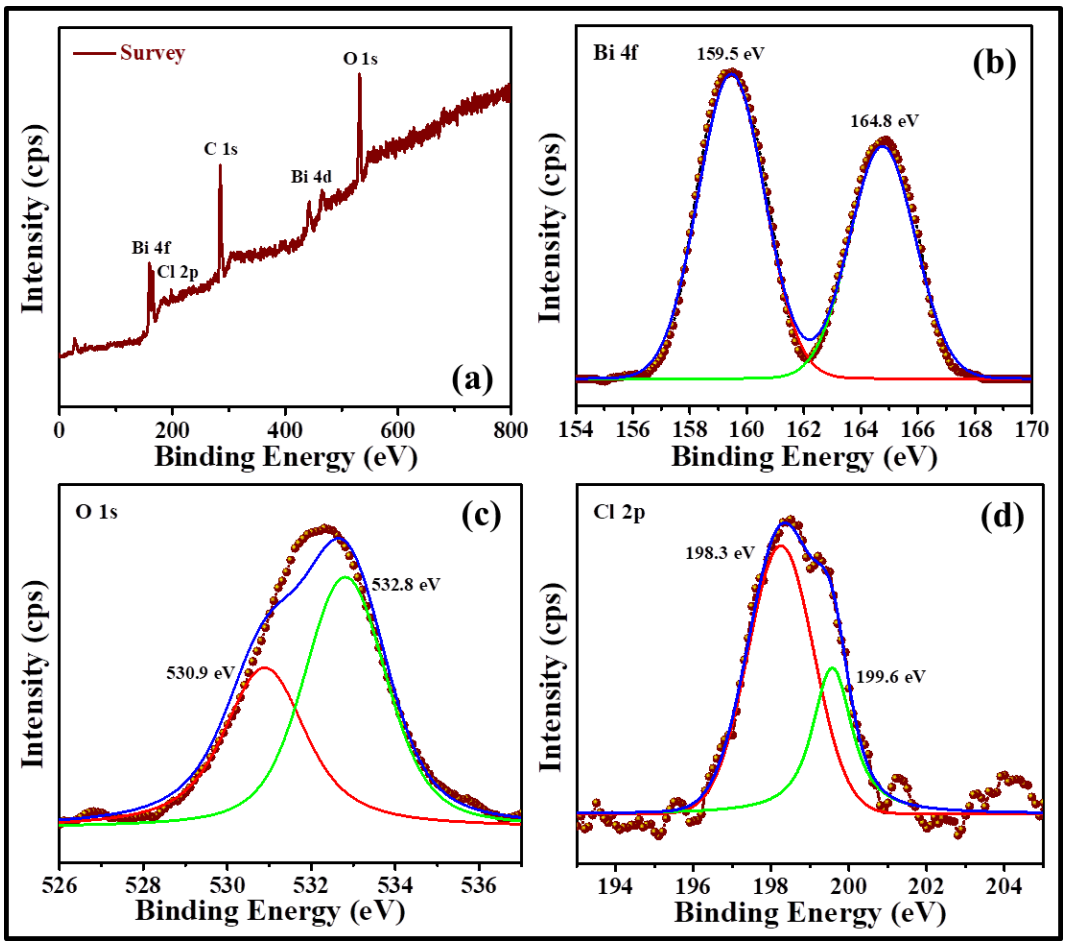

Figure 7.4: The photoelectron spectroscopy by elementally survey (a), Bi 4f spectrum (b), O 1s spectrum (c) and Cl 2p spectrum (d) of B18h sample

The X-ray photoelectron spectroscopy (XPS) analysis on the sample to determine the strength of the bond based on binding energy, and have demonstrated different spectra for the different bonds in Figure 7.4. According to the elemental survey scan in Figure 7.4(a) reveals the presence of Bi, O, Cl, and C in the as-synthesised samples. The presence of atmospheric carbon is responsible for the peak of C 1s at 284.6 eV. In Figure 7.4(b), the sharp peaks at 159.5 and 164.8 eV can be attributed to $4f_{7/2}$ and $4f_{5/2}$ of Bi. Using Figure 7.4(c), the deconvoluted peaks at 530.9 and 532.8 eV can be separated from the O 1s peak. It can be assumed that the first peak results from the presence of O^2 or O^{2-} in the Bi-O bond, while the second peak originates principally from the presence of H_2O or OH^- on the surface of the sample. There are two deconvoluted peaks in the Cl 2p spectrum demonstrated in Figure 7.4(d), at 198.3 and 199.6 eV that correspond to Cl^- of the Bi-Cl bond. The XRD and XPS analysis support the purity of the as-prepared samples[14].

7.3.7 Morphology Analysis

Figure 7.5(a-c) shows the FESEM (Field emission scanning electron microscopy) images taken at 100, 100 and 500 nm with respect to the morphology of the samples as prepared. The images clearly indicate that all of the samples exhibit nanosheet-like structures. Each sheet is around 25 ~ 100 nm in length and about 10 ~ 25 nm in thickness. There is no significant difference in the grain size or crystalline nature of the as-synthesised BiOCl samples. The small units are uniformly arranged.

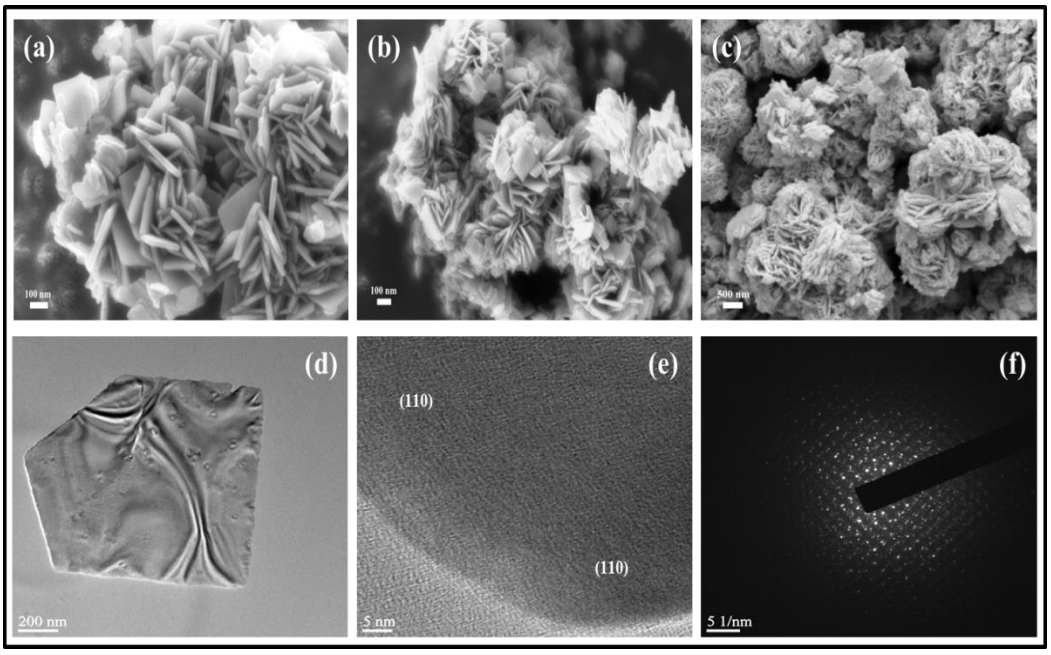

Figure 7.5: FESEM images of B6h (a), B18h (b), B24h (c); and TEM image (d), HRTEM image showing with lattice fringes (e) and the SAED pattern (f) of B18h sample

As-synthesised TEM and HRTEM images of a pure BiOCl (B18h) sample are depicted in Figure 7.5(d-f). According to these images, the as-synthesised samples exhibit morphology similar to that of sheets. According to Figure 7.5(e), the sample is highly crystalline, as indicated by the large number of bright planes assigned (110) to the sample. The SADE pattern demonstrated in Figure 7.5(f), which conforms to the as-synthesised sample was polycrystalline. These results are consistent with those of XRD, which indicate that BiOCl's highest intensity peak occurred in the (110) plane.

7.3.8 Photocatalysis Performance Analysis

The catalytic activities of the as-prepared materials were analysis by using the deterioration of Rhodamine B (RhB) dye in aquatic solution. In presence of UV-light irradiation the absorbance spectrum was demonstrated in Figure 7.6(a-c), for all samples.

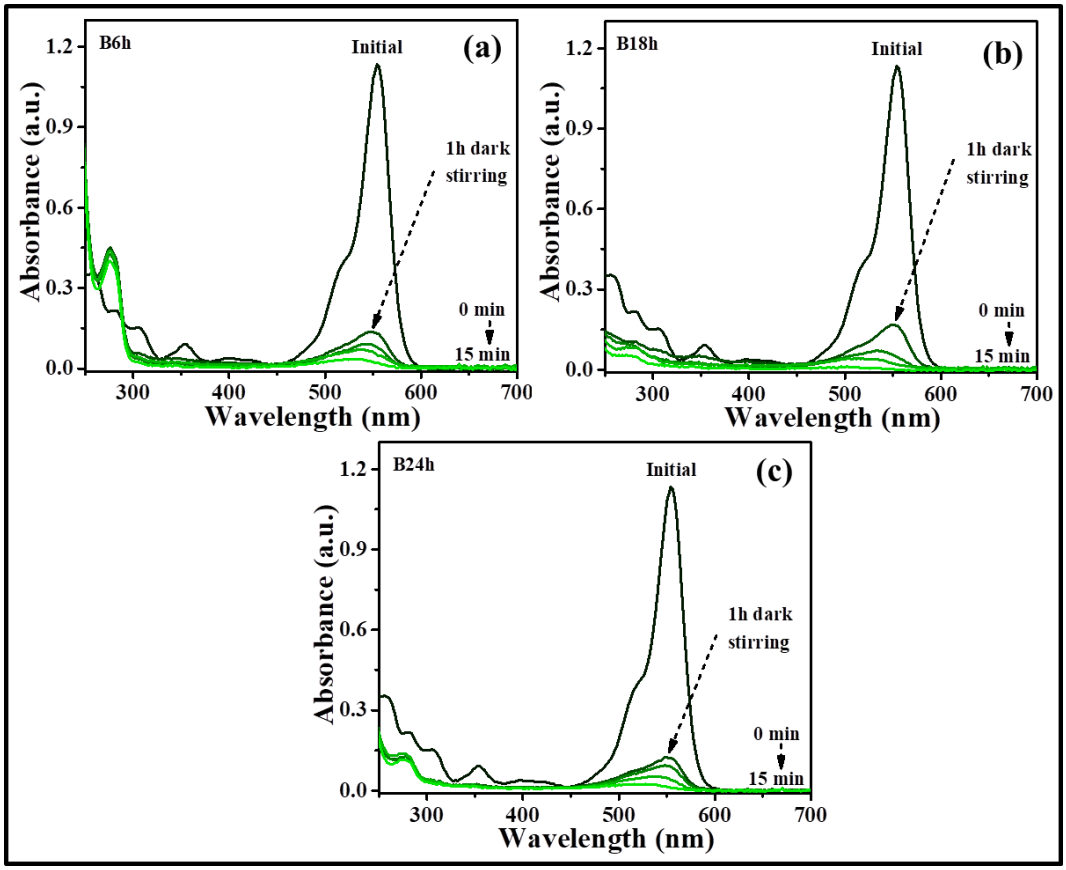

Figure 7.6: The Absorbance spectra of B6h (a), B18h (b) and B24h (c) under UV-light irradiations

Figure 7.7(a) and Figure 7.7(b) were demonstrated that C/C_0 vs. irradiation time and the $\ln(C_0/C)$ vs. irradiation time that also known as Langmuir-Hinshelwood pseudo 1st order rate kinetics of all time varied nanomaterials in presence of UV-light irradiations that analysis by following equation:

$$\ln\left(C_0/C\right) = kt \qquad (7.6)$$

where,

C_0 = initial concentration of dye with catalyst,

C = final concentration of dye with catalyst,

k = the apparent constant and

t = irradiation time.

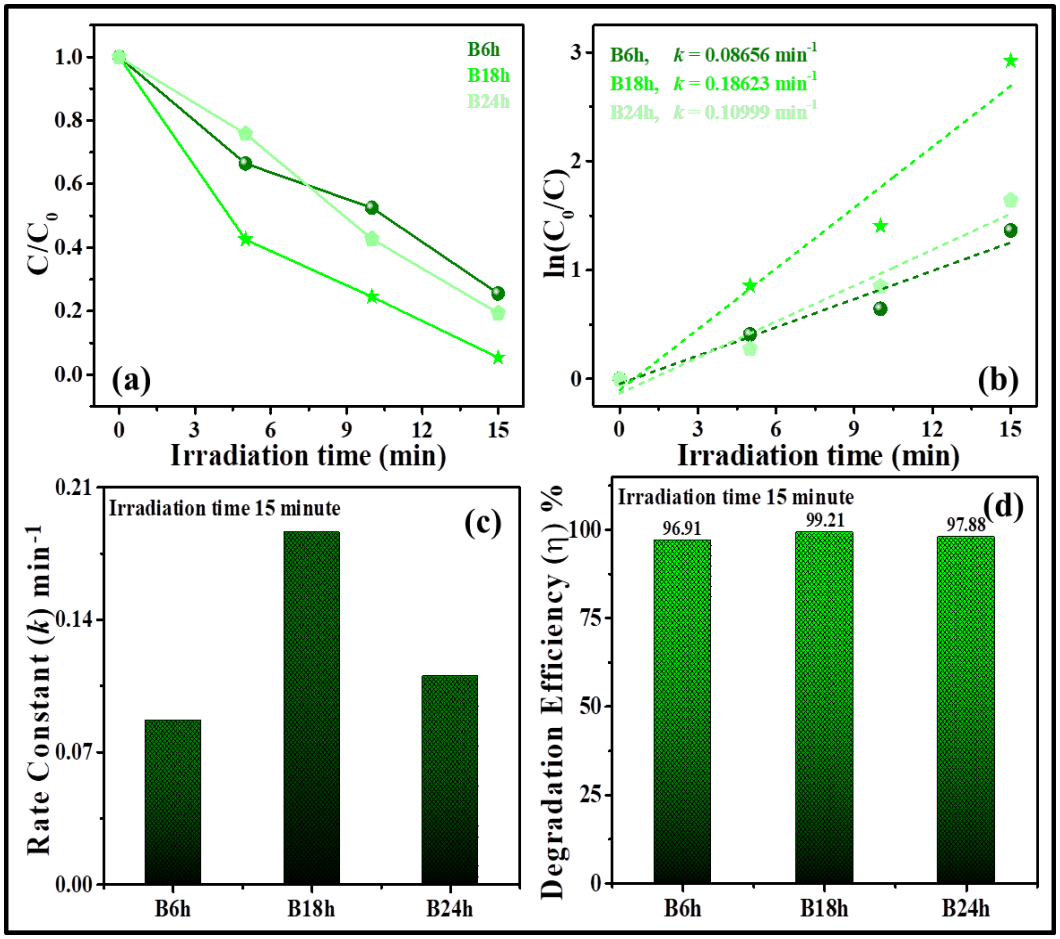

Figure 7.7: (a) The C/C_0 vs. irradiation time (min) plots, (b) $\ln(C_0/C)$ vs. irradiation time (min) plots, (c) the bar graphs of 1st order rate constant and (d) catalytic degradation efficiency for all the samples

From Figure 7.7(c) was shown the bar graphs of 1st order rate constant (k) and Figure 7.7(d) was demonstrated the bar plots of degradation efficiency (η) vs. irradiation time at only 15 minutes of all the nanomaterials. The catalytic degradation efficiency was evaluated by following equation:

$$\eta\ \% = \frac{D_0 - D_t}{D_0}\ X\ 100 \qquad (7.7)$$

where,

η % = catalytic degradation efficiency,

D_0 = initial absorption and

D_t = final absorption.

The catalytic degradation in the dark condition was demonstrated in Figure 7.8(a).

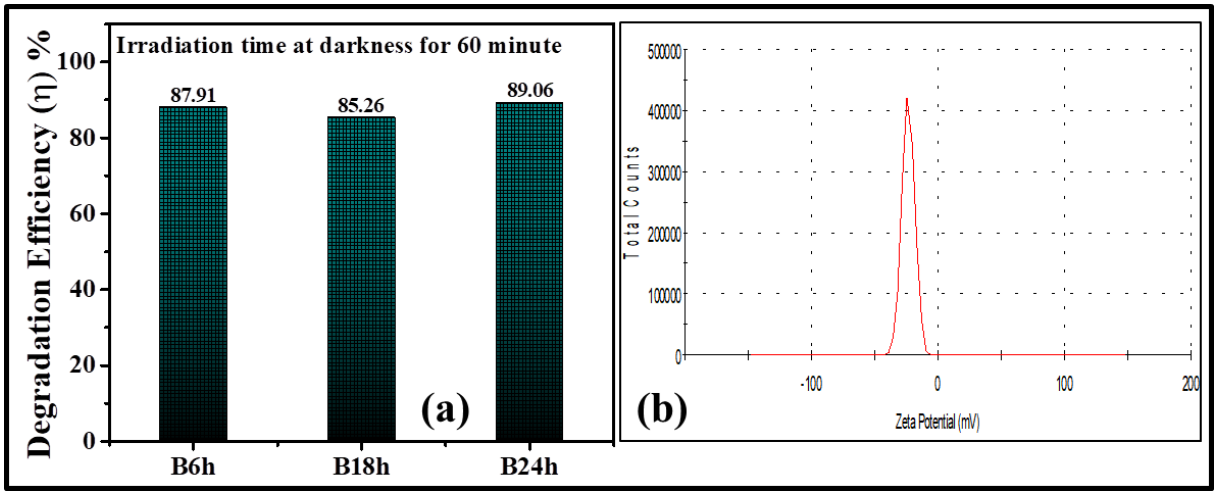

Figure 7.8: The degradation efficiency of adsorption spectra of all samples under 60 minute in dark conditions (a) and the Zeta Potential distribution of the B18h sample (b)

The all BiOCl samples were demonstrated efficient degradation performance under UV-light irradiation within 15 minutes that the best sample performed at 99.21 %. The ratio of R^2, Rate constant values and degradations efficiency of different catalytic samples of Rhodamine B (RhB) dye in presence of UV light irradiation were demonstrated in Table 7.3.

Table 7.3: R^2, Rate constant values and degradations efficiency of different catalytic samples of Rhodamine B (RhB) dye

Samples name	R^2 values	*k*-values (min^{-1})	Degradation efficiency (η %)
B6h	0.92937	0.08656	96.91
B18h	0.93692	0.18623	99.21
B24h	0.93667	0.10999	97.88

The surface charge calculation of the best sample demonstrated in Figure 7.8(b). The zeta potential graph of B18h sample shows the -23.5 mV charge. The positive cationic dyes such as RhB are susceptible to degradation by the sample due to its negative surface charge. In addition to being

positively charged, cationic dyes adsorb significantly on negatively charged BiOCl surfaces, that facilitating the significant degradation.

All the samples were efficiently performed the decolourization under UV light irradiations, apart from this the best sample demonstrated excellent degradation activity about 100 % only 15 minutes. The doses variations of the best sample were demonstrated in Figure 7.9(a). Variations in catalyst dosage and irradiating the sample under ultraviolet light were studied to determine their effect on degrading RhB dye. The photocatalysis procedure was carried out using different amounts of catalyst (0, 15, 30 and 45 mg). According to the degradation efficiency, that improved between about 2 to 100 % with an increase in the catalyst loading. As the catalyst concentration increases, the number of active sites increases, and this, in turn, improves the rate of degradation. In only 15 minutes, 99.21 % of the catalyst has been degraded by irradiating with 30 mg of the catalyst.

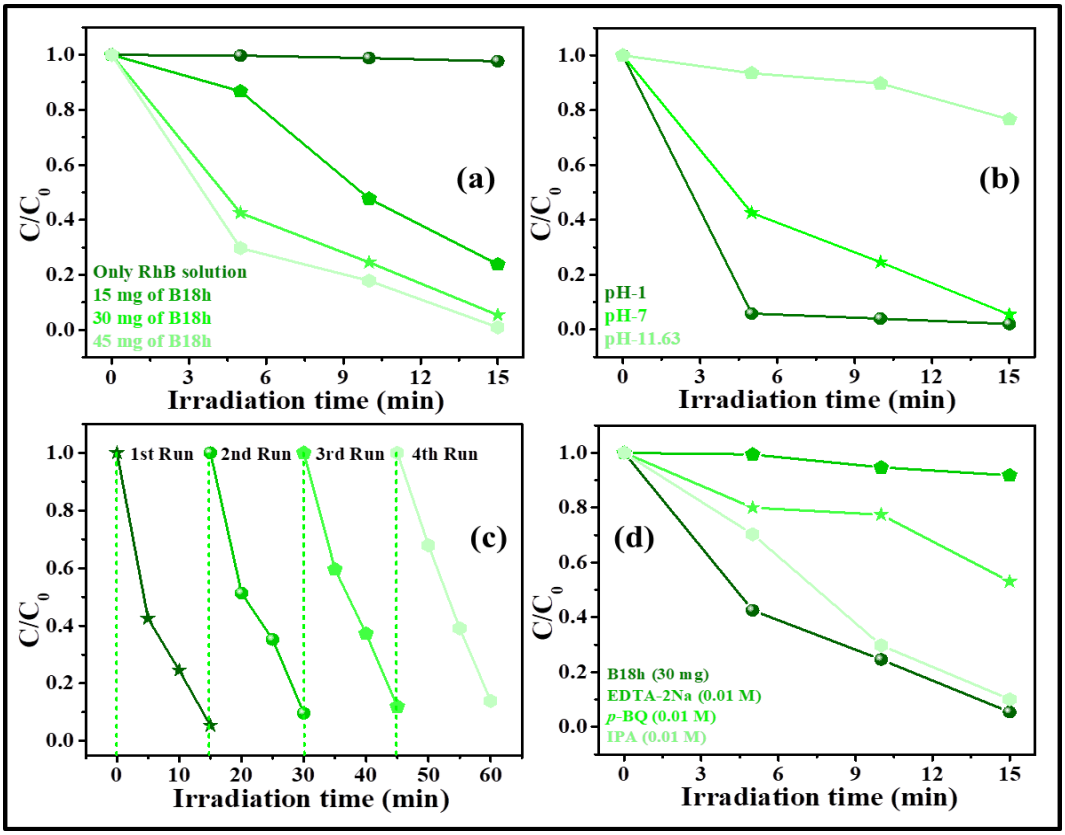

Figure 7.9: The doses variation graphs were demonstrated (a), pH variation of the medium (b), recycle test up-to 4th photocatalytic runs (c) and the scavenger test (d) for the best B18h catalyst

Variations in the pH of catalyst-dye solutions were used to study the effect of pH on catalytic dye degradation. Figure 7.9(b) shows that the B18h sample exhibited a higher photocatalytic activity at an acidic pH, whereas it exhibited a steeper decrease in reaction rate at a basic pH. On the other hand,

when the B18h sample was placed at an acidic pH, its photocatalytic activity increased greatly, whereas the rate of reaction became high.

In order to determine how stable the BiOCl catalysts were at degrading RhB dye under UV light irradiation, they were recycled four times. According to Figure 7.9(c), even when the B18h sample is reused three times, the degradation efficiency remains roughly the same, suggesting there wasn't any photo-corrosion and this proves the catalyst to be highly stable.

In order for the photocatalytic processes to efficiently degrade toxic dyes into non-toxic end products, photoactivated electrons, holes, hydroxyl radicals, and superoxide anions are necessary. In the free radical trapping procedure[15], it is possible to confirm that these radicals exist. By adding the requisite amounts of scavengers during the photocatalytic procedure, followed by determining the effect of their addition on the reaction kinetics, the photocatalytic degradation of RhB dye under visible light irradiation by B18h BiOCl sample has been studied in the presence of scavengers such as *p*-BQ, IPA and EDTA-2Na. In Figure 7.9(d), C/C_0 plots illustrate the effect of adding *p*-BQ and EDTA-2Na upon degradation efficiency. In contrast, adding IPA resulted in no visible change. Among the compounds studied, *p*-BQ acts as a radical scavenger, IPA acts as a radical scavenger of hydroxyl radicals, and EDTA-2Na acts as a radical scavenger of photogenerated holes. Due to the lack of possibility of photographic holes being formed the induced photocatalysis; this study proves that unpaired superoxide ion radicals are the primary active radicals in photocatalysis.

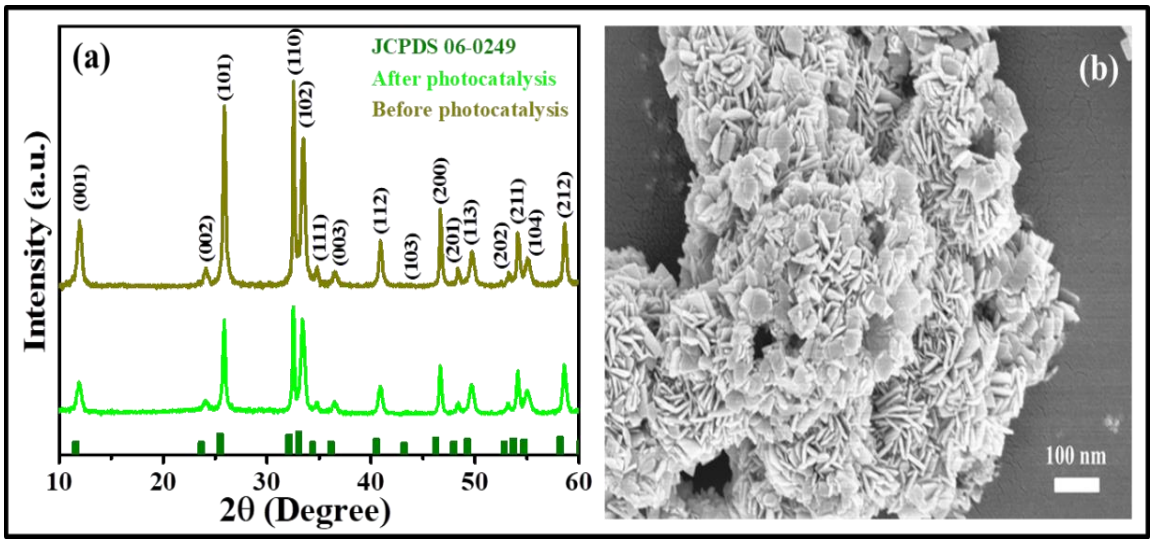

Figure 7.10: The PXRD pattern of B18h sample before and after photocatalysis (a), and as well as the FESEM image following the photocatalysis process (b)

Figure 7.10(a) demonstrates the PXRD plots of B18h catalysts before and after photocatalysis. After the catalysis reaction takes place, there is no change in phase of the catalyst sample. The reused sample is unchanged, and all peaks are present. Additionally, none of the peaks are absent. As can be seen from Figure 7.10(b), the FESEM image of the respective catalyst displays the exact morphology that existed before the catalytic reaction. In determining the feasibility of the catalyst, these observations demonstrate its stable degrading of toxic organic dyes.

7.3.9 Plausible Photocatalytic Mechanism Analysis

The schematic representation of what happened under UV irradiation in Scheme 7.1. Under ultraviolet light, because of the favourable band gap of BiOCl, electrons are generated in the CB of the material and holes are generated in the VB.

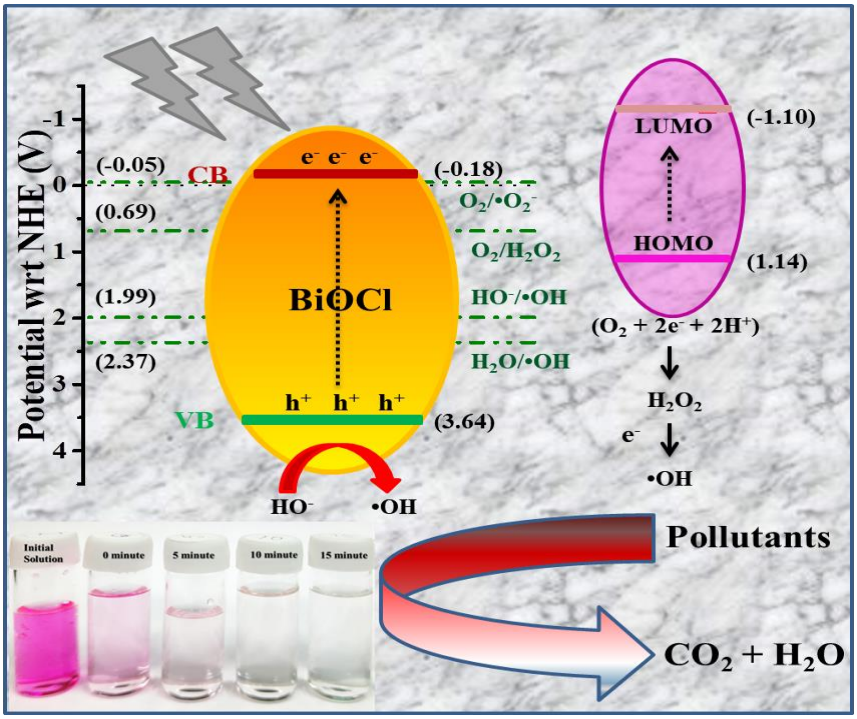

Scheme 7.1: A schematic illustration of the photocatalysis mechanism of B18h materials upon UV light exposure

In contrast, in the case of BiOCl (-0.18 V vs. NHE), the redox potential is more negative than the redox potential of $O_2/•O_2^-$ (-0.05 V vs. NHE). This renders the reduction reaction in order to form the superoxide anion impossible. In the presence of electrons, however, the higher redox potential for O_2/H_2O_2 (0.69 V vs. NHE) favours the formation of the hydroxyl radical (•OH) by reduction of H_2O_2. In presence of photogenerated holes, BiOCl oxidizes OH^- to •OH in a more positive manner than

H_2O/•OH (2.37 V vs. NHE) at its VB (3.64 V vs. NHE). RhB dye can be reduced to CO_2 and H_2O by an active radical with the formula •OH.

$$BiOCl \rightarrow h^+ + e^- \quad (7.8)$$

$$H_2O + h^+ \rightarrow H^+ + \bullet OH \quad (7.9)$$

$$\bullet O_2^- + 2H^+ + e^- \rightarrow H_2O_2 \quad (7.10)$$

$$H_2O_2 + e^- \rightarrow \bullet OH + OH^- \quad (7.11)$$

$$OH^- + h^+ \rightarrow \bullet OH \quad (7.12)$$

$$(\bullet OH, h^+) + Organic\ pollutants\ (RhB) \rightarrow CO_2 + H_2O \quad (7.13)$$

The results clearly show that the chlorine enrich sample (B18h) responded most efficiently in photocatalysis experiment. It could degrade the pollutant fastest and also responded positively in pH variation and load variation tests. On the other hand, the scavenger test indicated that OH^-/•OH radicals are the major catalysis agent in the entire process. The generation of •OH radicals are directly related to the hole concentration of the catalyst system. The electron-hole pairs are generated by incidence of UV irradiation, due to the low dimension of the samples, the separation of electron and holes is facilitated preventing the instantaneous recombination of the same. Thereafter, these photo induced electron and holes participate in degradation process. These steps are common for all the samples synthesised in this work. Also, concentration of holes has been identified as the major factor of catalytic process here. Hence, an additional input of holes within the system may boost up the entire catalytic activity of the host catalyst. This is what happened in case of B18h sample. As per the report by Kong et al., enhanced Cl content directly increases the hole concentration[10] in BiOCl system. In case of BiOCl, the chlorine content is maximum and thus it already possess higher hole concentration, This, together with photogenerated holes enhance the catalytic activity compared to other samples like B6h and B24h. If the inherent hole concentration is identified as a key factor for photocatalysis, the dark stirring should also comply with the same. The degradation performance studied for dark stirring {presented in Figure 7.8(a)} also supported this explanation of better photocatalytic performance of BiOCl samples.

In addition to the above discussion, another minor factor regarding the photocatalytic performance of the samples may be mentioned here. The grain size of the samples, as determined from XRD studies (demonstrated in Figure 7.1(b)) can also influence the catalytic activity. It can be inferred that the B18h samples exhibited highest grain size. The other samples, exhibiting grains less than 5 nm in size could also exhibit higher amount of lattice defects. Such lattice defects can act as trapping sites for

photogenerated e^-/h^{+16}. Having lesser probability of being trapped, these photogenerated e^-/h^+ can contribute to catalytic performance of B18h sample making it a superior catalyst.

7.4 Conclusions

Here, a simple synthetic procedure is outlined for developing grain size dependent pure BiOCl samples by altering synthetic parameter like time. Based on the PXRD analysis, the phase formation was confirmed and the most intense peak corresponded with the (110) plane, indicating that the facet was dominant. A detailed understanding of chemical bonding was obtained from XPS and Raman measurements that were used to analyse the chemical structure. Elements were determined using the EDS, whereas sheet-like morphology was determined using FESEM. Based on HRTEM images, it was found that the (110) plane is the most intense plane, and the lattice fringes confirm the highly crystalline nature of the samples. Following Mulliken's electronegativity theory, measurements of the electronic band edge potentials of the samples are based on the band gaps measured by DRS. By measuring the Mott-Schottky characteristics, the BiOCl semiconductors were found to be p-type semiconductors. Photocatalytic degradation of organic cationic dyes of toxic nature was finally achieved with the samples. By irradiating the dye with UV light for a very short period of time, sample B18h exhibited the best degradation efficiency. In order to examine the effects of changing certain parameters, such as catalyst dosage and pH, several analyses were performed. After being utilised for degradation of catalysts, the B18h sample was able to be recycled up to three times, supporting its practicality. BiOCl samples as prepared were highly effective catalysts for the degradation of organic pollutants, making them potential candidates regarding water remediation.

References

[1] C. Huang, J. Hu, S. Cong, Z. Zhao and X. Qiu, *Applied Catalysis B: Environmental*, 174, 2015, 105-112.
[2] Y. Zhang, X. Xu, Y. Xing, H. Wang, H. Fu, X. Lin and J. Wang, *Advanced Materials Interfaces*, 2(12), 2015, 1500194.
[3] S. Wu, J. Xiong, J. Sun, Z.D. Hood, W. Zeng, Z. Yang, L. Gu, X. Zhang and S.Z. Yang, *ACS Applied Materials & Interfaces*, 9(19), 2017, 16620-16626.
[4] Y. Shi, X. Xiong, S. Ding, X. Liu, Q. Jiang and J. Hu, *Applied Catalysis B: Environmental*, 220, 2018, 570-580.
[5] J. He, J. Wang, Y. Liu, Z.A. Mirza, C. Zhao and W. Xiao, *Ceramics International*, 41(6), 2015, 8028-8033.
[6] Y. Ma, C. Lv, J. Hou, S. Yuan, Y. Wang, P. Xu, G. Gao and J. Shi, *Nanomaterials*, 9(3), 2019, 322.
[7] S. Wang, J.H. Yun, B. Luo, T. Butburee, P. Peerakiatkhajohn, S. Thaweesak, M. Xiao and L. Wang, *Journal of Materials Science & Technology*, 33(1), 2017, 1-22.

[8] M.Z. Shahid, R. Mehmood, M. Athar, J. Hussain, Y. Wei and A. Khaliq, *ACS Applied Nano Materials*, 4(1), 2020, 746-758.
[9] J. Yu, B. Wei, L. Zhu, H. Gao, W. Sun and L. Xu, *Applied Surface Science*, 284, 2013, 497-502.
[10] B. Kong, T. Zeng and W. Wang, *Physical Chemistry Chemical Physics*, 23(35), 2021, 19841-19853.
[11] R. Sarkar, D. Das, B.K. Das, A. Mitra, N.S. Das, S. Sarkar and K.K. Chattopadhyay, *Materials Research Bulletin*, 125, 2020, 110778.
[12] R. Sarkar, D. Das, A. Mitra, S. Sarkar and K.K. Chattopadhyay, *Materials Today: Proceedings*, 18, 2019, 1086-1095.
[13] K. Zhang, J. Liang, S. Wang, J. Liu, K. Ren, X. Zheng, H. Luo, Y. Peng, X. Zou, X. Bo and J. Li, *Crystal Growth & Design*, 12(2), 2012, 793-803.
[14] G. Cheng, J. Xiong and F.J. Stadler, *New Journal of Chemistry*, 37(10), 2013, 3207-3213.
[15] M. He, D. Zhao, J. Xia, L. Xu, J. Di, H. Xu, S. Yin and H. Li, *Materials Science in Semiconductor Processing*, 32, 2015, 117-124.
[16] I.J. Badovinac, R. Peter, A. Omerzu, K. Salamon, I. Šarić, A. Samaržija, M. Perčić, I.K. Piltaver, G. Ambrožić and M. Petravić, *Thin Solid Films*, 709, 2020, 138215.

Chapter 8

Grand Conclusions and Future Prospects of Bismuth Oxyhalide

8.1 Grand Conclusions

Bismuth oxyhalide and its catalytic applications are the focus of this thesis and a detailed review in this regard has been provided. An introduction to nano science and technology has been provided in the first section of the thesis. Furthermore, nanomaterials are introduced along with their classifications, properties, and applications. Additionally, a brief overview of researchers' past works and a discussion of the current project have been presented. The third chapter of this thesis covers various characterization tools and their applications. Main research work has been described in fourth, fifth, sixth and seventh chapters. Following are the conclusions drawn as a result of the investigation:

1. In conclusion, the BOC-GO nanosheet-like composite material was successfully synthesised by hydrothermal method. The various properties such as identification of phases and chemical structures were successfully verified by sophisticated techniques such as XRD, XPS, Raman, FTIR, UV-Vis DRS, BET, FESEM and HRTEM analysis. As demonstrated in this study, the nanocomposite photosynthesised the harmful organic dye Rhodamine B (RhB) within a short period of time under visible light irradiation. The degradation efficiency of the material was 99.59 %, demonstrating its highly active nature. A variety of parameters were also analysed in order to discover how they affected the photocatalytic activity of the nanomaterial, such as the amount of catalyst and pH. The catalytic degradation procedure by BOC-GO can also be governed by a feasible mechanism that can explain the reactions occurring during the process. Therefore, the catalyst effectively removes poisonous substances from aqueous ecosystems and thus can be employed in the wastewater treatment process.
2. Using citric acid as a capping agent, the morphology of the BiOCl samples can be tuned and modified by hydrothermal method. In the presence of visible light, the samples were effective in degrading toxic dye Rhodamine B (RhB). The degradation efficiency was impressive for the best sample. The catalysts' performance was also observed by varying parameters such as the catalyst dosage, pH, and irradiation sources. Electrochemical measurement of the pure material was performed in an acidic medium and the material was used as an electrocatalyst for hydrogen evolution. As for the best nanomaterial (CA-2), the Tafel slope was demonstrated at about 72 mV/dec.
3. A simplified chemical heating technique for generating pure BiOCl samples was developed by varying certain synthetic parameters such as time and temperature duration. A very short time of visible light irradiation completely degraded the organic textile dye by the best sample. To

measure the effects of different parameters on the reactions, such as catalyst dosage, pH and light source, the as-synthesised catalyst materials were utilised in several experimentations. Additionally, the best (B0h/B80) catalyst was able to degrade a mixture of dyes and was reusable up to three times, demonstrating the practicality of the product. First principles calculations confirmed that the (110) plane was the best adsorption site for superior catalytic activity since this was the most intense plane of BiOCl. An increase in cationic dye adsorption on the anionic catalyst BiOCl when irradiated with visible light was associated with the dye-sensitised photocatalytic phenomenon despite the band gaps being in the UV range. As prepared, pure BiOCl samples were found to be highly efficient catalysts in the degradation of organic pollutants, which makes them potential candidates for use in water treatment.

4. Pure BiOCl samples were produced following a simple synthetic procedure by modifying parameters such as time duration of synthesis. These samples were ultimately capable of photocatalytic degradation of the toxic organic cationic dyes. In the case of the best sample (B18h), the dye showed the best degradation efficiency after being irradiated with UV light for a short period of time. Multiple experiments were performed to examine how different parameters, such as catalyst dosage and pH, impacted the results. The sample can be recycled up to three times after being utilised for degradation of catalysts, providing evidence that it is practically usable. As synthesised pure BiOCl samples functioned extremely well as a catalyst to degrade organic pollutants and therefore provide an excellent opportunity for water remediation.

The different morphologies of BiOCl arise due to the variation in the concentration of the precursors and different synthesis conditions. The main precursors used during synthesis of BiOCl are citric acid (CA) and Poly Vinyl Pyrrolidone (PVP), apart from the $Bi(NO_3)_3$ and HCl. CA is a structure-directing agent which induces the growth of different morphological architectures, whereas PVP is a surfactant which helps in the typical attachment of the nanomaterials to assemble into different morphologies like hollow, nut or nest-like structures of BiOCl. This type of PVP-induced attachment is termed as imperfect oriented attachment. CA is also an important biological chelating agent for metal ions, forming strong complexes with Bi^{3+}, Al^{3+}, Ca^{2+}, Fe^{3+}, Zn^{2+} and Mg^{2+}.

Final thoughts: After reviewing its catalytic properties, different morphology of the as-synthesised pure and composites of bismuth oxychloride were highly effective in any catalytic applications and also very useful for wastewater remediation and water-treatment applications.

8.2 Future Prospects of Bismuth Oxyhalide

This thesis focused on the catalytic and energy harvesting applications of pure bismuth oxychloride and its composite with graphene oxide. The catalytic experiments were performed under visible and UV light irradiations. Although extensive research is underway to develop effective catalytic applications for wastewater remediation, their applicability must still be improved with some perquisite improvements. In this section we try to discuss its application in various other fields in the near future.

1. Here we have mostly described pure BiOCl and its composite with graphene oxide as a highly efficient catalytic sample. An even better and faster catalytic response may be obtained if foreign booster candidates, such as novel metal nanoparticles, are attached to the surface of catalyst nanostructures.

2. One of the most successful technological achievements in this thesis was the implementation of branched nanostructures for photocatalytic activity and hydrogen evolution with impressive stability. In the future, different composites can be synthesised in a similar way, which may be much more effectively designed for performance testing.

3. The efficient dye-sensitised photocatalysis application was much more efficient to degrade any organic textile dye, which was useful for wastewater remediation. In the same way, any pure or composite material can be fabricated for water remediation.

4. BiOCl nanomaterial exhibited effective catalytic performance using UV light irradiation also. So, BiOCl based pure or composite material can easily be designed for better catalytic performance for wastewater treatment.

Appendix

Appendix

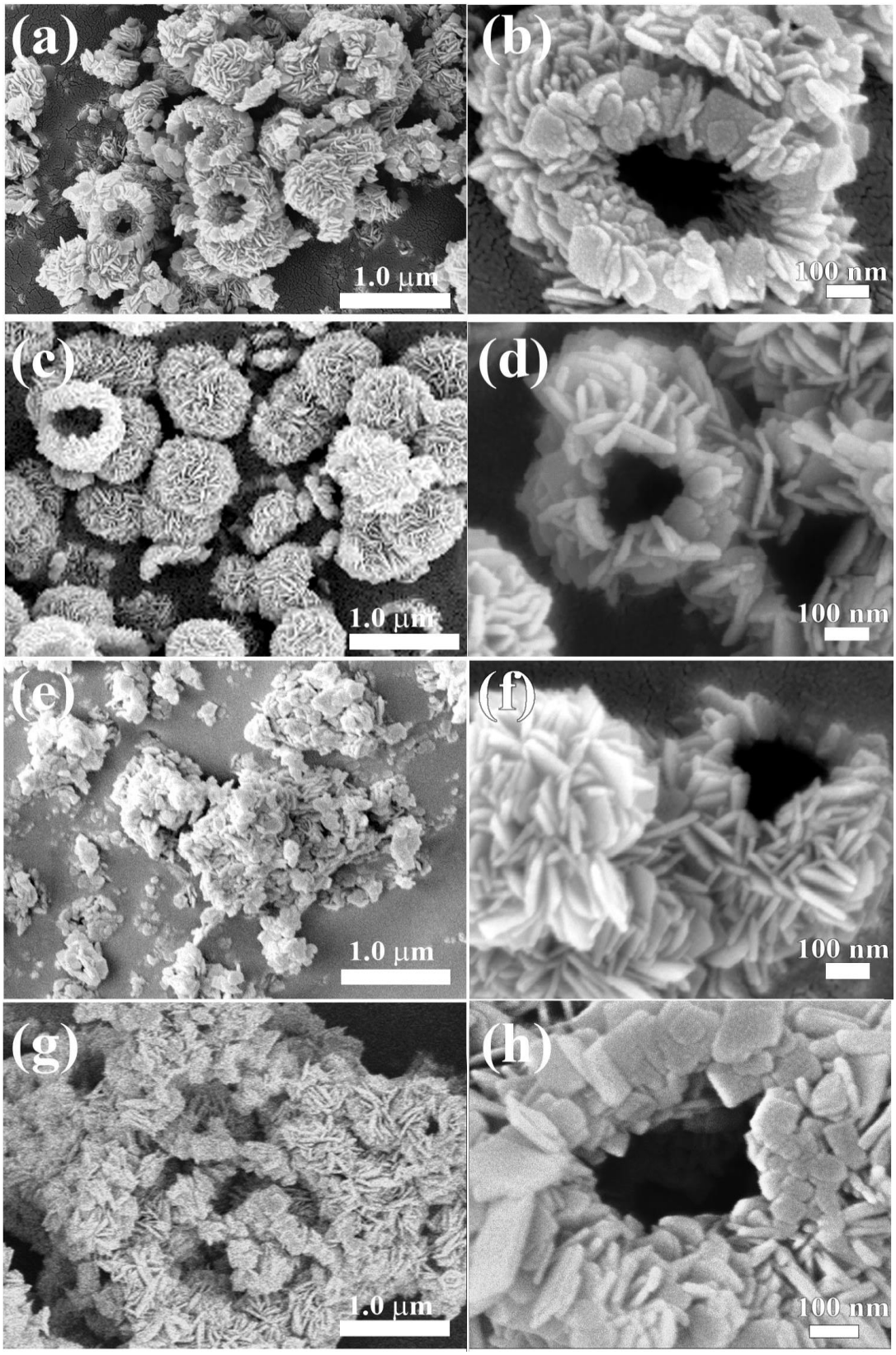

Figure A1: FESEM images of (a & b) B1h, (c & d) B3h, (e & f) B6h and (g & h) B18h time varied BiOCl samples

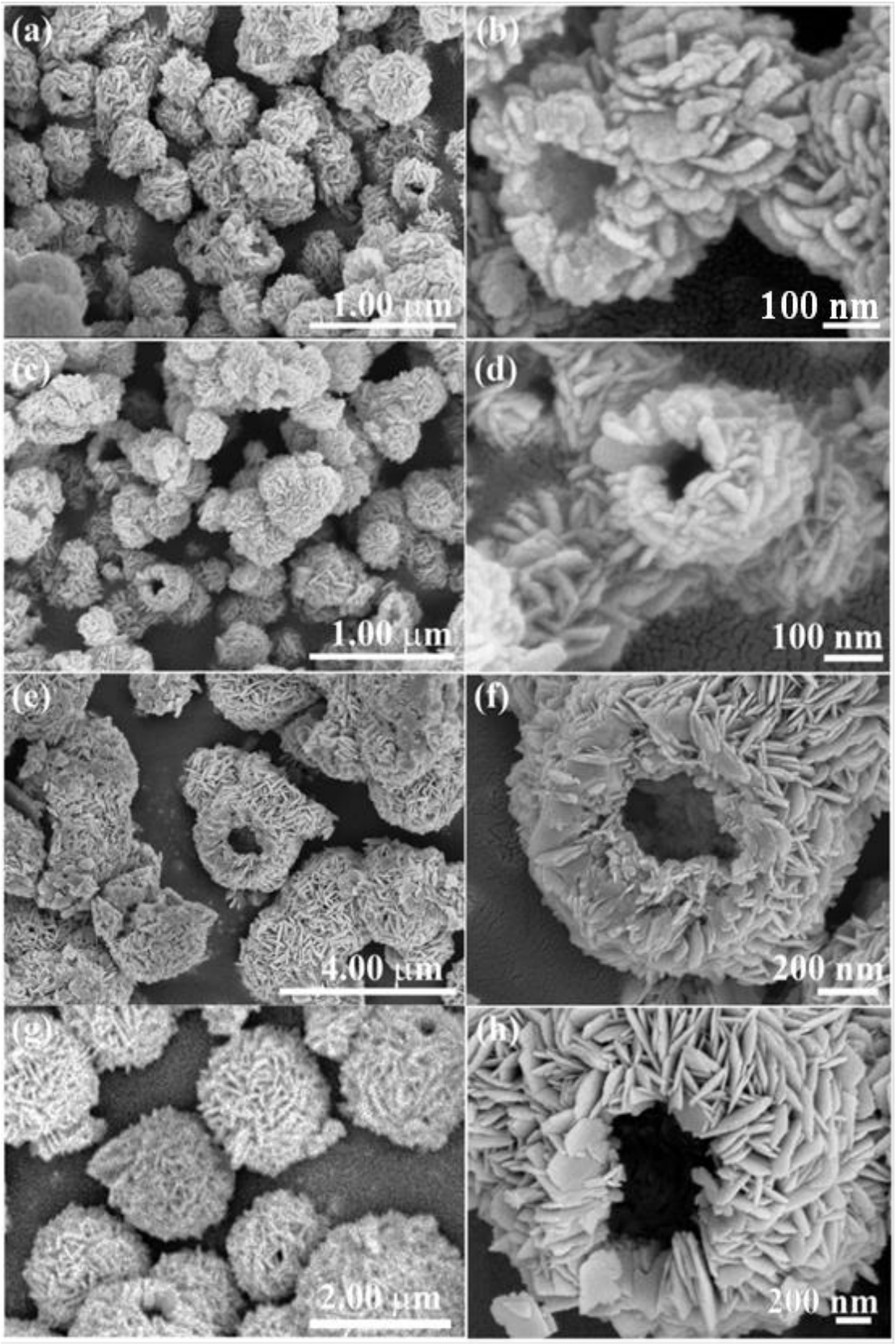

Figure A2: FESEM images of (a & b) B40, (c & d) B60, (e & f) B100 and (g & h) B120 temperature BiOCl samples

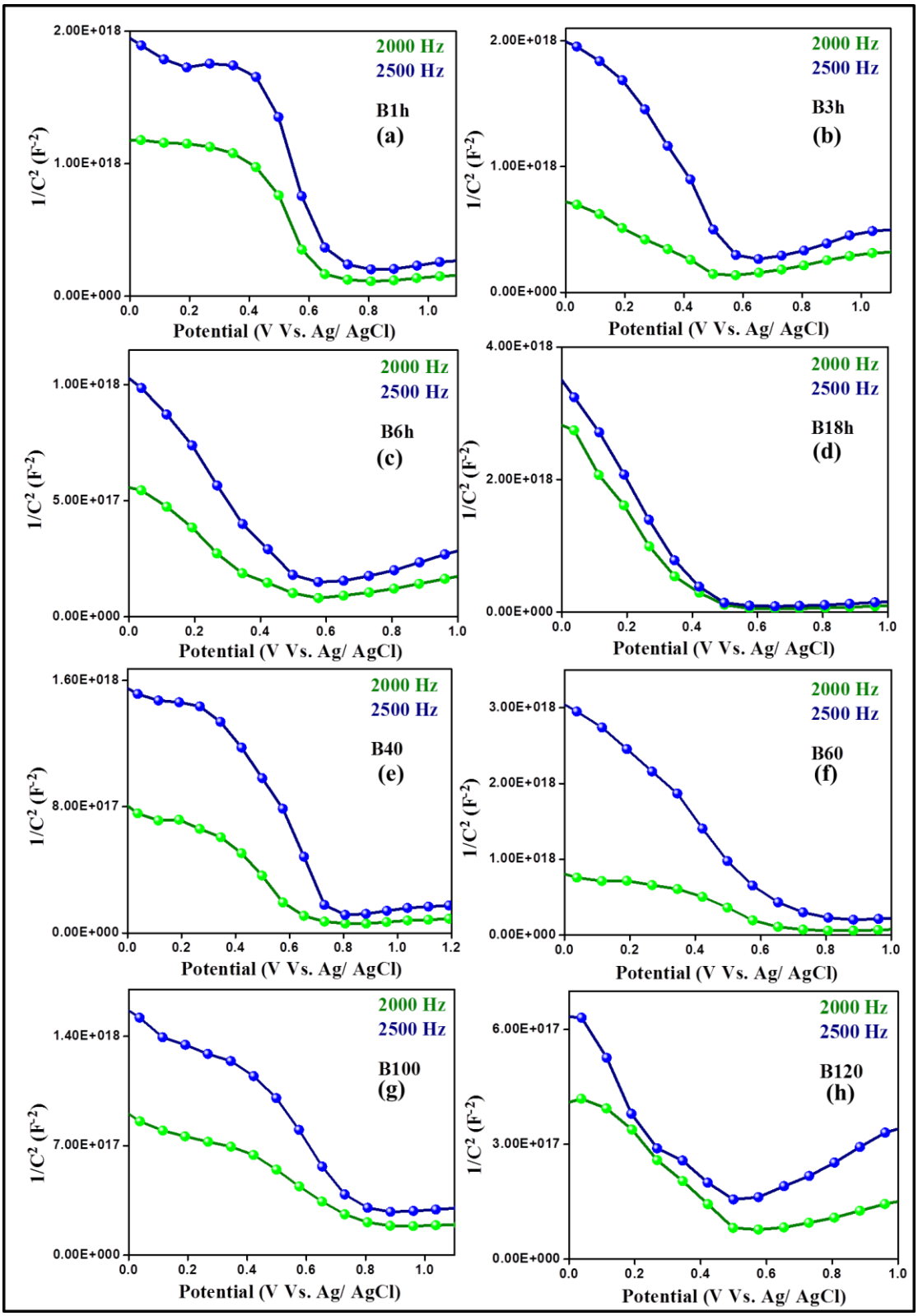

Figure A3: (a-h) Mott-Schottky plots of time and temperature varied BiOCl samples

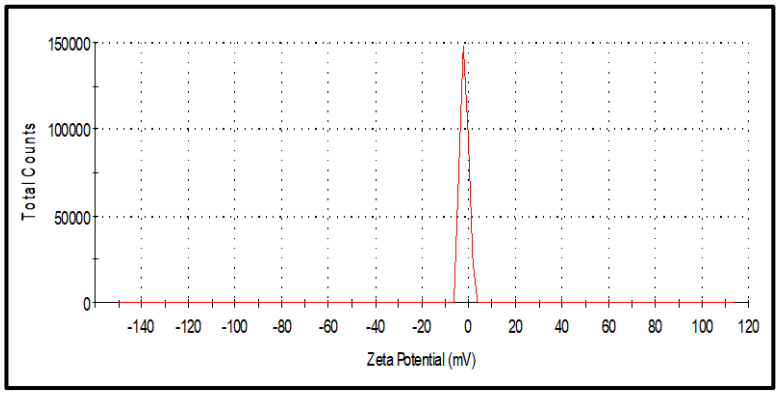

Figure A4: Zeta potential plot of B0h/B80 sample

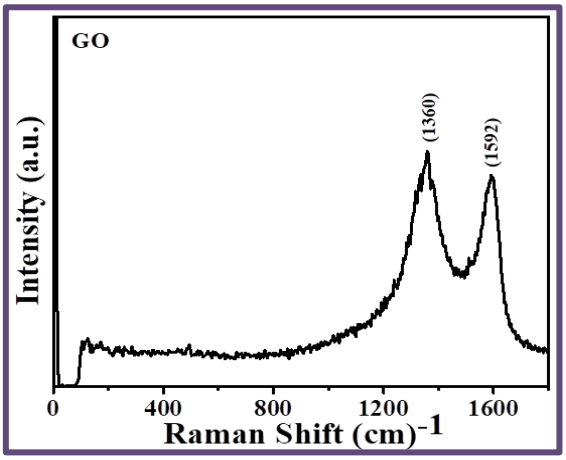

Figure A5: The Raman spectra of pure GO (graphene oxide)

Table A1: Quantitative results as obtained from EDS analysis

Materials	Quantitative Result	Bi	O	Cl
B40	Weight %	84.58	3.26	12.16
	Atom %	42.54	21.40	36.06
B60	Weight %	78.51	7.53	13.96
	Atom %	30.29	37.97	31.75
B100	Weight %	81.88	4.30	13.81
	Atom %	37.31	25.60	37.09
B0h/B80	Weight %	80.46	6.09	13.45
	Atom %	33.62	33.24	33.14
B1h	Weight %	72.67	14.32	13.02
	Atom %	21.60	55.59	22.81
B3h	Weight %	78.19	9.27	12.55
	Atom %	28.62	44.31	27.07
B6h	Weight %	77.73	8.90	13.36
	Atom %	28.49	42.63	28.88
B18h	Weight %	77.77	7.68	14.55
	Atom %	29.48	38.03	32.50

Table A2: Comparison of photocatalytic activity of different reported pure BiOCl catalysts

Name of Catalyst	Dye degraded and Concentration of Dye	Degradation Time (min)	Catalyst Dosage in 100 mL DI (g)	Source of Irradiation	$k_{relative}$ (min^{-1})	$k_{absolute} = k_{relative}$/Catalyst Dosage ($min^{-1}$)
BiOCl [2]	RhB (4.17 x 10^{-4} M)	120	0.1	Visible light	0.0670	0.6704
BiOCl [3]	RhB (1.39 x 10^{-3} M)	120	0.067	Visible light	-	-
BiOCl NS [4]	RhB (1.04 x 10^{-3} M)	20	0.05	Visible light	-	-
BiOCl [5]	RhB (4.17 x 10^{-4})	75	0.1	UV-light	0.0589	0.589
BiOCl HNS [6]	RhB (10^{-5} M)	15	0.01	Visible light	-	-
BiOCl [7]	RhB (2.08 x 10^{-4} M)	32	0.02	UV-light	0.0255	1.275
BiOCl [8]	RhB (2.08 x 10^{-4} M)	60	0.5	Visible light	0.061	0.122
BiOCl [9]	RhB (10^{-5} M)	4	0.1	Visible light	-	-
BiOCl [10]	RhB (8.35 x 10^{-4} M)	110	0.06	Visible light	0.01574	0.2623
BiOCl [11]	RhB (10^{-6} M)	60	0.05	Visible light	0.112	2.24
BiOCl [12]	RhB (10^{-5} M)	20	0.02	Visible light	0.272	13.6
BiOCl [This Work]	RhB (10^{-5} M)	6	0.075	Visible light	0.3423	4.564

References

[1] M. Kumar, A. Kumar and A.C. Abhyankar, *ACS Applied Materials & Interfaces*, 7, 2015, 3571-3580.
[2] Q. Wang, J. Hui, Y. Huang, Y. Ding, Y. Cai, S. Yin, Z. Li and B. Su, *Materials Science in Semiconductor Processing*, 17, 2014, 87-93.
[3] X. Zhang, X.B. Wang, L.W. Wang, W.K. Wang, L.L. Long, W.W. Li and H.Q. Yu, *ACS Applied Materials & Interfaces*, 6, 2014, 7766-7772.
[4] X. Li, C. Zhu, Y. Song, D. Du and Y. Lin, *RSC Advance*, 7, 2017, 10235-10241.
[5] K. Zhang, J. Liang, S. Wang, J. Liu, K. Ren, X. Zheng, H. Luo, Y. Peng, X. Zou, X. Bo and J. Li, *Crystal Growth & Design*, 12, 2012, 793-803.
[6] J. Xiong, G. Cheng, F. Qin, R. Wang, H. Sun and R. Chen, *Chemical Engineering Journal*, 220, 2013, 228-236.
[7] L. Ye, L. Zan, L. Tian, T. Peng and J. Zhang, *Chem Commun*, 47, 2011, 6951-6953.
[8] L. Ye, K. Deng, F. Xu, L. Tian, T. Peng and L. Zan, *Physical Chemistry Chemical Physics*, 14, 2012, 82-85.
[9] J. Xiong, G. Cheng, G. Li, F. Qin and R. Chen, *RSC Advance*, 1, 2011, 1542-1553.
[10] R. Liu, Z. Wu, J. Tian, C. Yu, S. Li, K. Yang, X. Liu and M. Liu, *New Journal of Chemistry*, 42, 2018, 137-149.
[11] K. Shen, M.A. Gondal, A.A. Al-Saadi, L. Li, X. Chang and Q. Xu, *Research on Chemical Intermediates*, 41, 2015, 2753-2766.
[12] D.H. Wang, G.Q. Gao, Y.W. Zhang, L.S. Zhou and A.W. Xu, W. Chen, *Nanoscale*, 4, 2012, 7780-7785.

Ratna Sarkar

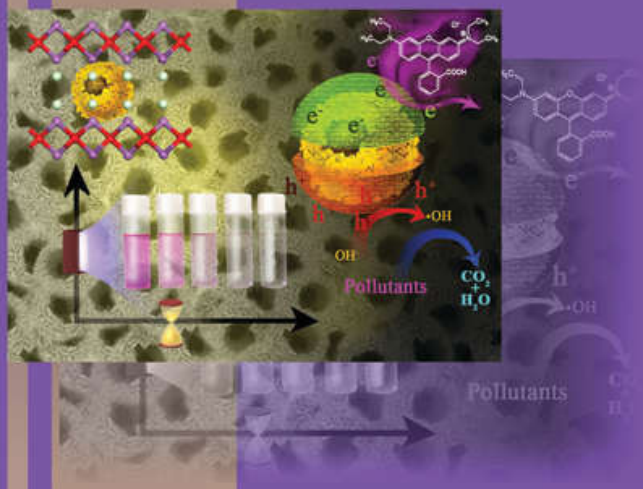
Pollutants
CO_2 + H_2O
•OH
OH⁻

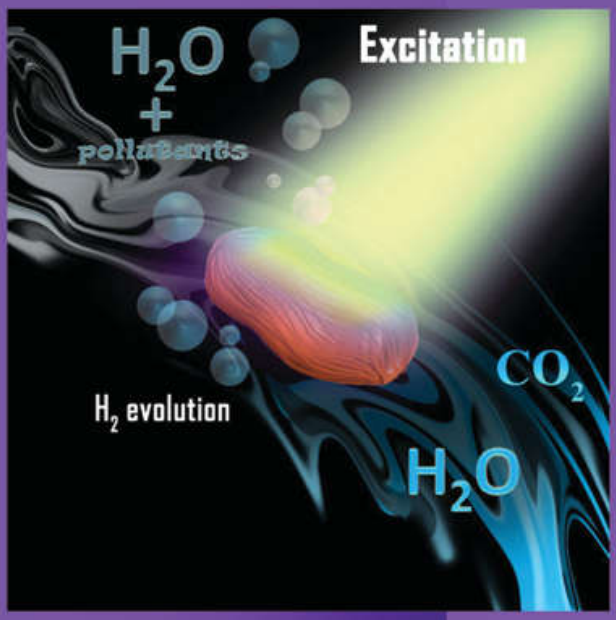
H_2O + pollutants
Excitation
H_2 evolution
CO_2
H_2O

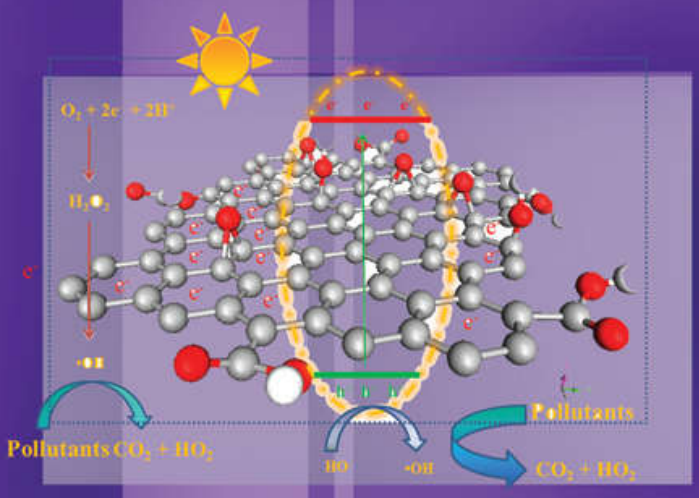
$O_2 + 2e^- + 2H^+$
H_2O_2
•OH
Pollutants $CO_2 + HO_2$
HO
•OH
Pollutants
$CO_2 + HO_2$